Doctoral Dissertation
Doctoral Program in Energy and Nuclear Science and Technology

POLITECNICO
MILANO 1863

Development of innovative transcritical power cycles working with CO_2 mixtures for concentrated solar power applications

PhD Thesis of

Ettore Morosini

* * * * * *

Supervisors
Prof. Giampaolo Manzolini, PhD
Gioele Di Marcoberardino, PhD

Tutor
Prof. Paolo Chiesa, PhD

Examination Committee
Prof. Andreas Werner, PhD, Technische Universität Wien
Prof. David Sanchez, PhD, Universidad de Sevilla

Politecnico di Milano, Italy
June 30th, 2023

I hereby declare that the contents and organisation of this dissertation constitute my own original work and does not compromise in any way the rights of third parties, including those relating to the security of personal data.

Ettore Morosini
Milano, June 30th, 2023

Summary

This work proposes a methodology to characterize binary mixtures based on CO_2 to be used as working fluids in transcritical power cycles.

Due to the penetration in the grid of cheap and renewable non-dispatchable energy sources, it becomes crucial to develop innovative cycles, suitable for various applications and able to efficiently work at high maximum temperatures.

The focus of this work is on the development of power cycles models for hot climates with air-cooled heat rejection units: under these circumstances the good performance of pure sCO_2 cycles cannot be guaranteed due to the drastic increase of the compression power occurring far from the critical temperature of CO_2, for cycle minimum temperatures over 45-50 °C.

A few innovative mixtures are proposed as working fluid for power cycles under these conditions, investigated with equations of states fitted on experimental data available in literature, or eventually taken within this work. At first, the performances of these cycles are showed and compared to the ones of sCO_2 cycles, showing the benefits in cycle efficiency. Then, numerical in-house tools are developed to analyse the various cycle components: suitable literature correlations for the heat transfer coefficients and the pressure drops of mixtures are included, particularly for the VLE region.

Given the tools developed and the ones already available, the power cycle performances were simulated for a set of case studies, evidencing both the cycle off-design behaviour operating in sliding pressure and the cycles integration in state-of-the-art and next gen CSP plants, an application of interest in this thesis.

The results proposed in this thesis can potentially be of interest to researchers involved in the development of innovative categories of efficient power cycles, at high maximum temperatures and characterized by a wide and flexible range of operating conditions, adaptable to any ambient temperature.

Acknowledgments

The author of this thesis is grateful for the opportunity to develop new knowledge within the framework of two European H2020 projects, the SCARABEUS and the DESOLINATION project.

From a personal point of view, a special thank goes to Giampaolo Manzolini and the other colleagues at Politecnico di Milano, including Gioele Di Marcoberardino and Marco Binotti, among the many. It has been demonstrated that research is possible even during a pandemic, while still having fun (not always, but at least in most of the occasions).

Another very special thank is also given to Dario Alfani and Riccardo Simonetti: without the two of them these years would have not passed very easily, for a lot of different reasons.

The author is also thankful to the many master students that have cooperated in this research, with Enrico and Guglielmo at the top of the list, and the colleagues from Università degli Studi di Brescia.

Finally, the author is grateful to the colleagues met during the period abroad of the PhD programme in Fontainebleau Mauro Riva, Paolo Stringari and all the others at CTP, for their very gentle attitude.

Contents

List of Tables

List of Figures

Introduction

Motivation of the PhD thesis

A sharp growth of dispatchable and renewable power generation installed capacity is foreseeable in the near future, coping with the imminent necessity of decarbonising the power generation sector and the need of regulating the grid with new energy systems, complementary to conventional and unpredictable renewable power generation technologies.

Two widely proposed solutions to balance the electrical grid are represented by batteries and by power-to-fuel systems, as the production of green hydrogen from electrolysis. Both solutions are developed to absorb the excess electricity produced by wind and photovoltaic systems, the fraction not instantaneously requested by the grid, by store it or convert it for its exploitation in the future. At the current state of the art, however, batteries are associated with high capital costs and fast degradation during the plant lifetime, along with the intrinsic exploitation and depletion of resources such as lithium, cobalt and rare earth elements [1]. On the other hand, power to fuel solutions like electrolysers are affected by high capital costs and low conversion efficiencies.

Together with the ability of reaching good dispatchability levels, a second important feature of future renewable power plants is represented by their capability to run efficiently at partial load, exploiting fast transients. This is not normally possible with solar photovoltaics or wind turbines, if not coupled with electrochemical storage systems, while it is inherently achievable with power cycles.

Amid a plethora of possible solutions this category of renewable energy systems, concentrated solar power (CSP) represents a promising dispatchable power generation technology, potentially efficient at partial load and intrinsically capable of storing energy. State-of-the-art CSP systems are proposed with large thermal energy storages (normally above 8 equivalents hours) to store thermal energy during the hours of the day with the highest radiation levels: this way the plant can run when the electric demand is the highest, decoupling the electricity production and the availability of primary energy (irradiation), as originally intended, while using wind or photovoltaic plants coupled with electrochemical storage.

According to the state-of-the-art of the CSP plants installed nowadays and effectively running, conventional steam Rankine cycles represent the only solutions adopted as power cycles. Their characteristics normally lead to conversion efficiencies slightly lower than the ones of conventional steam cycles for fossil fuels applications: in fact, limits on the maximum pressures at 100-150 bar and the maximum temperatures at 530-550 °C are usually set, correctly

matching the temperature of the hot source (molten salts at maximum temperatures around 565 °C). In addition, the plant layout of steam cycles is intrinsically complex, including reheaters, multiple regenerative bleedings, deaerators, steam drums, a sub-atmospheric condensation of the working fluid and sub-atmospheric conditions in the hotwell.

Literature works dealing with large-scale Rankine cycles for CSP applications suggest net electric power block efficiencies around 39% when air-cooled, at ambient temperatures of 30 °C [2], strongly penalized by the auxiliary consumption of the condenser [3]. Moreover, the cycle efficiency can be penalized by up to 1.5% when the ambient temperature moves from 30 °C to 40 °C and can increase only by 0.8% with an ambient temperature of 20 °C. Importantly, this significant penalization in terms of cycle efficiency is also experienced by air-cooled Rankine cycles for any other application, such as nuclear plants or heat recovery systems.

Finally, fast transients (both for ramp-up and ramp-down) and start-ups are not favoured in steam cycles, which are penalized by heat exchangers with high weight per unit of surface area and thus high thermal inertia, in addition to the low average density of the working fluid and the large turbomachinery. For dispatchable and renewable energy applications, a sluggish load regulation might compromise the overall competitiveness of the system itself, independently from the primary energy exploited, especially if competing with electric batteries.

Given the various limitations of steam cycles, in the last decade countless scientific literature works pointed to supercritical CO_2 (sCO_2) as a possible innovative working fluid for power cycles to overcome the limits of steam cycles [4], evidencing its good behaviour also in the field of waste heat recovery [5], gas turbine bottom cycles [6], coal [7] and nuclear [8] [9] plants, other than CSP.

A sCO_2 cycle can work efficiently when the fluid condition at the inlet of the compressor is close in temperature and pressure to the critical point of the working fluid itself (31 °C, 73.8 bar), exploiting the real gas effects during the compression step. Moreover, a relevant simplification of the power block layout is possible with sCO_2 cycles when compared to the steam Rankine cycle, effectively similar to the cycle architecture of internally fired gas cycles, with the sole addition of recuperators.

Another crucial advantage of sCO_2 cycles with respect to steam cycles is their inherent capacity to operate in part load with fast transients and start-ups, given by the power block limited footprint, the high average density of the working fluid and smaller turbomachinery with fewer stages. Finally, given the supercritical nature of the working fluid across the whole process, these categories of power cycles are efficient if the cycle maximum temperature is substantially higher than the compressor inlet temperature, similarly to conventional gas turbines for power generation working with air.

The main drawback of sCO_2 cycles is the drop in cycle efficiency when the compressor inlet temperature increases: this condition occurs when a cooling medium at low temperature (i.e. below 20 °C) is not available to cool the

sCO_2 flow close to the critical temperature in the heat rejection unit (HRU) of the power cycle [10]. Notably, in arid locations where the ambient temperature can be up to 40 °C during peak summer days, the adoption of air-cooled HRUs is usually the only reasonable solution: at these conditions, the compressor inlet temperature increases and the higher average compressibility factor of the CO_2 along the compression step leads to drastic drops in cycle efficiency, depending on the conditions. In addition, since the compressor is designed to work with a supercritical fluid, the power cycle cannot be adaptable to cold sinks at very low temperatures (below 15 °C), as the absence of liquid droplets must be ensured at the intake of the compressor: in fact, cycle minimum temperatures around 33 °C to 35 °C represents the lower bound of this technology.

A possible innovative idea to overcome the limits of sCO_2 cycles for high minimum temperature applications is to adopt CO_2-based binary mixtures as working fluids, substituting pure CO_2 in the power block: the rationale behind this approach is to increase the critical temperature of the working fluid in the range between 70 °C and 120 °C by adding a certain amount of specific dopants, carefully selected, hence turning the supercritical cycle into a transcritical one. Consequently, it is possible to use a pump for compressible liquids instead of a compressor for supercritical fluids. The selection of suitable dopants for these CO_2 mixtures must consider different aspects: among them, the thermal stability is the most crucial, along with a good compatibility with the materials and the dopant solubility with CO_2.

Transcritical cycles with CO_2-mixtures (tCO_2-mixtures cycles) inherit the good characteristics of sCO_2 cycles in high temperature applications (an extremely simplified power block layout and a good capability to responsively follow the electric demand), and, depending on the dopant and the operating conditions, can significantly exceed the performance of sCO_2 cycles.

By maintaining the fluid during the whole compression step in liquid conditions, no efficiency drops are foreseeable for air-cooled cycles at very high ambient temperatures, marking a crucial difference between sCO_2 and tCO_2-mixtures cycles. Moreover, as the critical temperature of the working fluid is far from the operating conditions of the pump, the operating conditions of these cycles are not limited by the critical temperature of the working fluid: they can operate in off-design at any cycle minimum temperature, potentially down to levels not achievable by steam cycles, experiencing clear efficiency increments when the cycle minimum temperature decreases. In this regard, the operating range of the power cycles extensively widen with respect to sCO_2 cycles, both at high ambient temperatures and especially at the lowest ambient temperatures.

Considering the potential of tCO_2-mixtures cycles in applications like CSP, briefly summarized Table 1, this work proposes a methodology to investigate these innovative power cycles, focusing on a handful of CO_2-mixtures.

Table 1. Qualitative comparison of power cycles potentialities for CSP

		Steam Cycle	**sCO_2 Cycles**	**tCO_2-mixtures Cycles**
Dispatchable power production		Yes	Yes	Yes
Fast transients and regulation		No	Yes	Yes
Power block complexity		High	Low	Low
Power cycle		Subcritical	Supercritical	Transcritical
Maximum temperatures		390-550 °C	Over 550 °C	Over 390 °C
Efficiency in climates:	Hot (T_{amb}> 35 °C)	Low	Good	High
	Warm (15 °C <T_{amb}< 35 °C)	Good	High	High
	Cold (T_{amb}<15 °C)	Good	-	High

Introduction to sCO_2 cycles

The supercritical state of a fluid is usually defined as the thermodynamic condition where both temperature and pressure are above the critical conditions of the fluid, a region where no phase-change can occur. The definition in principle holds true for any working fluid, including mixtures, at pressures above the cricondenbar.

At conditions close to the critical point, in the supercritical state, for any fluid a drastic variation of thermodynamic properties occurs. Among them, the heat capacity at constant pressure (C_P) is the most affected by this effect, as it can vary easily by an order of magnitude within a very narrow range of temperature and pressure. The locus of the points where the C_P presents its maximum, at various pressures, is generally referred to as the "Widom line" [11]: it defines a change in the behaviour of the working fluid, distinguishing a region where the supercritical fluid is considered "liquid-like" (with low compressibility factors (Z) and limited temperature differences across a compression step), and a region defined as "gas-like", with the opposite characteristics.

While dealing with pure carbon dioxide, its critical point is located at a temperature around 31 °C and a pressure of 73.8 bar. Analysing the properties of pure CO_2, Figure 1 shows the drastic variations of the density (ρ) and Z in the supercritical region near the critical point, adopting the Span and Wagner equation of state (EoS) [12]: the figure depicts also the trend of isentropic conditions, a representation that can be useful in the estimation of compressions of the supercritical fluid, especially of interest in the field of sCO_2 cycles. As noticeable from the figure, the Widom line is also proposed, and it coincides with the trend of one particular isentropic line depicted.

In conclusions, while considering supercritical compressions of CO_2 near the critical point, at least for isentropic processes, it is possible to approximate the fluid behaviour to iso-choric compressions, while a drastic variation of density and compressibility factor is found across the Widom line.

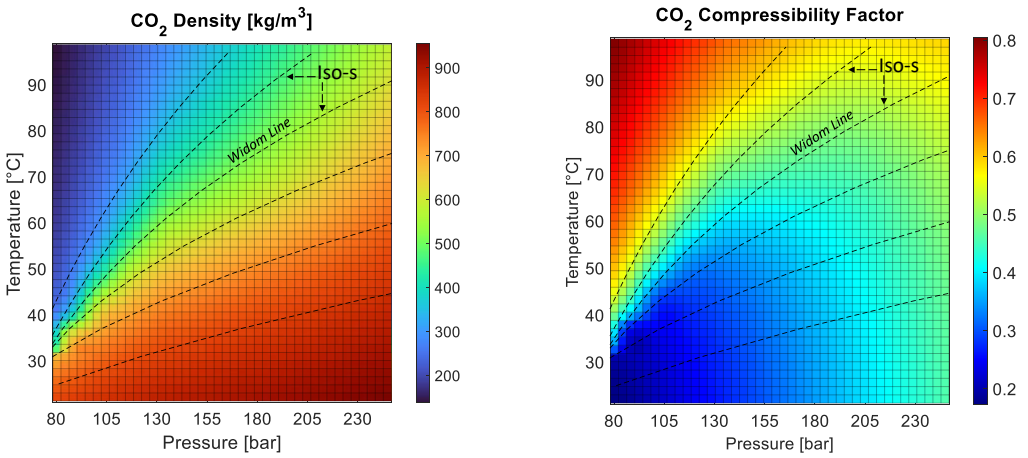

Figure 1. Properties of CO_2 – Dotted lines represent iso-entropic conditions

The key advantage of a sCO_2 cycle with respect to a conventional gas cycle (adopting ambient air as working fluid) lies in the thermodynamic region where the compression occurs. In fact, the critical temperature of CO_2 is normally a value close to the ambient temperature: as such, a sCO_2 cycle can ideally be suitable in conditions where the cold sink of the power cycle is either a water stream or air at low ambient temperature (around 15 to 20 °C): under both conditions, running an sCO_2 cycle with a compressor inlet temperature close to the critical point (35 °C) is possible and effective. With such compressor inlet temperatures, the optimal compressor inlet pressure is typically found around 80 to 85 bar, with densities around 750 kg/m^3 and compressibility factors in the order of 0.3. Therefore, as the compression work is inversely proportional to the density, a limited mechanical work is foreseeable (around 15 to 20% of the expansion work). Unfortunately, the design of turbomachinery sensitive to small variation in working fluid temperature and pressure presents technological challenges. In fact, efficient compressors are ideally possible, but manufacturers face non negligible challenges due to the limited volumetric flow rate (an important issue especially for small plants, strongly affected by scale effects), densities drastically different than the ones of conventional air compressors and overall uncertainties about sharp oscillations of thermodynamic properties. The most relevant problem is related to the onset of liquid droplets of CO_2 at the rotor leading edge, a problem caused by the acceleration of the fluid causing a drop in pressure (entering in the two-phase region) [13]. A work of Romei [14] proposed suitable correlations for the estimation of compressors efficiencies as function of the pressure ratio and the size of the machinery, evidencing that total-to-total efficiencies over 86% are possible for large scale power cycles with low compression ratios.

On the other hand, as expected in a hot environment with air-cooling, if the compressor minimum temperature is in the range of 45 to 50 °C, the density can be in the order of 350 kg/m^3 and the optimal cycle minimum pressure increases,

up to over 100 bar: in this thermodynamic region the real-gas effects of the working fluid are more limited (as visible in Figure 1), and the cycle efficiency is badly affected. Nevertheless, no major issues related to the operation of the compressor near the critical region can be predicted under these circumstances.

Detailing the power cycle performances under these two extreme conditions, Figure 2 presents the trend of the cycle efficiency and the heat source temperature difference of an sCO_2 cycle. The cycle is modelled with the recompression power block, considered the most promising for high temperature applications [15], assuming a cycle maximum temperature of 700 °C, literature values for cycle non-idealities and modelling the power cycles with the Span and Wagner EoS.

As evidenced in literature [16], the effect of the variation in cycle minimum temperature is significant: moving from a cycle minimum temperature of 33 °C at design conditions to 50 °C, a 7% of power production is lost and the exploitation of the hot source (i.e. its temperature difference) declines by 22%, with a significant negative impact on the heat recovery of the cycle, or on the coupling between the power cycle and the HTF of the CSP plant, in solarized cycles.

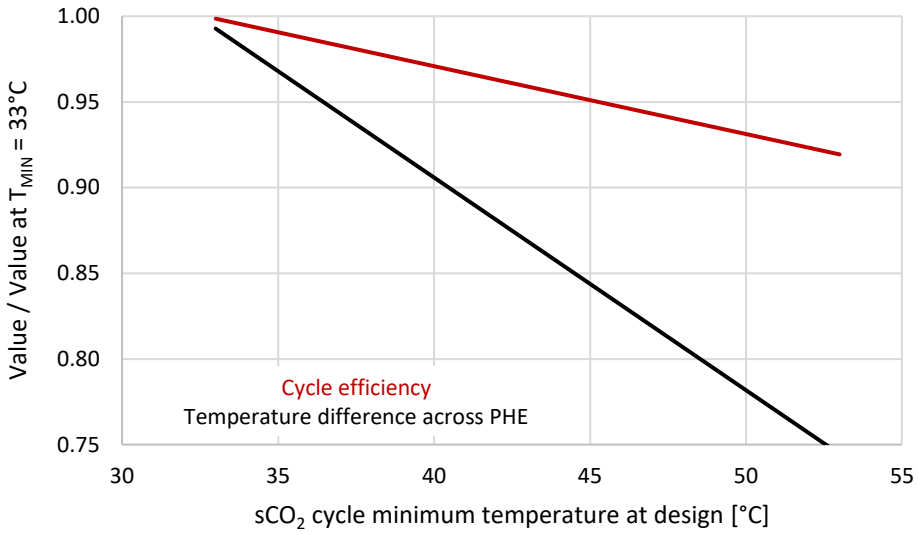

Figure 2. Sensitivity of sCO_2 cycle performances on the design cycle minimum temperature for a typical CSP plant

State of the art of CSP and future trends

Concentrated solar power is widely renowned as a suitable technology to provide clean and dispatchable electric power to the grid. However, a limited number of CSP plants is nowadays in operation worldwide (around 140), with an overall electricity production around 14.5 TWh_{el} in 2020 [17], 56 times lower than photovoltaics (PV), in the same time span. Nevertheless, projections up to the end of the current year evidence a large relative growth in the energy production, with

more than 23 TWh_{el} produced across 2023, considering the more than 8 GW_{el} of installed power in operation [18].

On the economic perspective, CSP is penalized with respect to other renewable technologies, both by its high financial costs (mainly due to the perceived early-stage maturity of the technology itself) [19] and by the modest net electric conversion efficiencies of the power blocks in operation, based on steam cycle technology, with values around 34% for conventional parabolic through system adopting synthetic oil as HTF and around 40% for the state-of-the-art solar tower systems using solar salts (60% $NaNO_3$, 40% KNO_3) as HTF [20]. Specific capital costs for large scale solar tower plants can approximately span in a range from 5000 $\$/kW_{el}$ and 7000 $\$/kW_{el}$, depending both on the location and the storage capacity (hence the foreseen capacity factor of the solar plant) [21].

State-of-the-art solar tower CSP plants adopt direct storage layouts (where the HTF coincides with the storage medium), while in case of advanced HTF literature works consider also the possibility to exploit indirect storage systems, by keeping separated the HTF and the storage section, as shown in Figure 3.

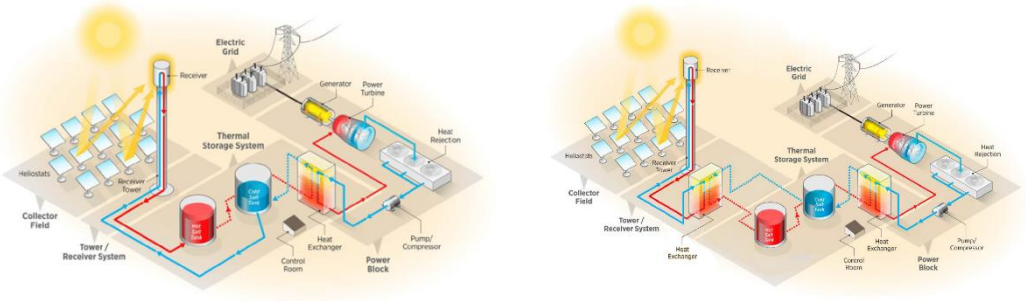

(a) (b)

Figure 3. Direct (a) and indirect (b) storage layouts for solar tower CSP [22]

While no revolutionary innovations are foreseen for next generation CSP plants regarding the technology for the solar field (heliostats), both on the receiver and on the storage side a series of so-called “pathways” are evidenced by the US Department of Energy (NREL) to set new standards for the innovative plants [22], positively achieving the goal of converting and storing heat for power cycles with maximum temperatures up to 700 °C (coherent with the sCO_2 cycle technology).

A possible pathway is represented by gas-phase receivers, even if it represents a solution with a relatively low success across the scientific literature. Other most promising pathways are listed in Table 2: the first is the so-called liquid pathway, where either advanced molten salts or liquid metals are adopted as HTF in conventional tubular receivers (detailed reviews of this pathway can be found in literature [23]). The second solution is represented by using solid particles as heat medium, falling by gravity in a cavity receiver while being heated by the concentrated radiation, then stored directly without the necessity to use HTF.

Table 2. Brief overview of the possible pathways for next-gen CSP plants

Next generation CSP plants – Cycle TIT up to 700 °C		
Advanced molten salts	**Liquid metals**	**Solid media**
Tubular receiver	Tubular receiver	Falling particles receiver
Indirect or direct storage (2 tanks system)	Indirect storage, with advanced salts as media (2 tanks system)	Direct storage, with solid particles in a thermocline

Within this work only the liquid pathway is considered for high temperature CSP plants, performing the overall design, off-design and economic analysis of the solar plant. As no detailed nor extensively tested thermal models are available, to the best knowledge of the author, for falling particles receivers, the analysis of this pathway to run a 700 °C power cycle is not presented in this work: nevertheless, it can be the focus of future works dealing with the coupling between tCO_2-mixtures power cycles and innovative CSP plants.

Between the two possible liquid pathways, the one adopting sodium as HTF is investigated in this work: in principle, advanced molten salts can be also considered as an alternative to sodium, but previous literature works underlined the good performances of sodium with respect to these alternatives [24] [25]. In fact, sodium as HTF is widely proposed in literature within the state-of-the-art of high temperature tubular receivers: its main advantage is the high thermal conductivity, a factor that helps limiting the temperature gradient on the tube circumferential direction, therefore limiting the mechanical stresses [26]. While adopting state-of-the-art nickel-based alloys for the receiver tubes, limiting the mechanical stresses becomes vital to increase the lifetime of the receiver.

Thesis objective and outline

As the state-of-the-art of CSP plants and the current state of the research on sCO_2 cycles for any category of high temperature application clearly pose limitations in terms of conversion efficiency and economic competitiveness of the overall plants, this work focuses on detailing the characteristics and the performances of innovative CO_2-based mixtures as working fluids for high temperature power cycles, along with considering the competitiveness of such power cycles in particular for solar applications.

The research carried out in this work is developed mainly across the following four different macro-steps:

- The selection of the appropriate CO_2-dopants on the basis of their thermal stability, compatibility and the respective efficiency of the power cycle adopting the mixture as working fluid.

- The modelling of the CO_2-based mixtures, detailing both thermodynamic properties and transport properties. As the lack of experimental data is a major problem for mixtures, a few sets of additional experimental data on promising mixtures are taken in this work.
- The integration of the power cycle with the solar plant: numerical tools help in describing the design and off-design of the solar plant, proposed to be correctly coupled with the cycle depending on the mixture characteristics.
- The design of each cycle component and the modelling of the cycle off-design behaviour in steady state, potentially for any application, considering as variables the thermal input and the ambient conditions.

The analysis will be carried out taking into account few CO_2-mixtures. However, the most relevance will be given to the CO_2+C_6F_6 mixture: for this working fluid it will be proposed a coherent narrative covering the complete analysis, up to the off-design performances of the power cycle. Nevertheless, the methodology described and applied only to the CO_2+C_6F_6 mixture can easily be extended to any other CO_2-mixture.

To summarize, a simplified overview of the methodology adopted in this work to characterize the performances of the innovative cycles is depicted in Figure 4.

	Methodology	*Tools*	*Outcome*
Dopant selection	Literature review on dopants properties to identify effective CO_2-mixtures	Power cycles preliminary computed with simple equations of state	Identification of dopants, focusing on thermal stability and feasibilty
Mixture modeling	Selection of EoS by fitting experimental data	Models in ASPEN Plus and Matlab. (Experimental campaign on some mixtures)	Thermodynamic and transport properties of the mixtures
CSP plant modeling	Optimization and sensitivty analysis on the CSP plant main parameters	CSP optical and thermal efficiency evaluated with referenced models	Design of cost-effective CSP configurations, adapted to the innovative cycles
Cycle design and off-design	Sizing of the cycle components, description of the system at variable boundary conditions	Cycle components modelled in MATLAB. 1-D models for HX	Cycle performances based on the solar resources and the residual load to follow

Figure 4. Overview of the work carried out in this thesis

According to the thesis aims and scope, the next chapters will be organized as follows:

- In Chapter 1 is proposed a literature review of sCO_2 cycles and cycles adopting CO_2-mixtures, and the required characteristics of suitable CO_2-dopants are discussed.
- In Chapter 2 the explored CO_2 mixtures are presented and modelled with EoS already available in literature, focusing on the use of experimental data in the EoS modelling.
- In Chapter 3 the performances of the innovative power cycles are analysed, detailing some specific cases for high temperature applications.
- In Chapter 4 are described the numerical tools developed in MATLAB to design all the power block components working with the innovative mixtures, including the modelling of their off-design behaviour.
- In Chapter 5 the various models for the solar plant design and off-design are listed and briefly described, including the necessary cost functions for all the components of a CSP plant. Only models from literature are adopted in this thesis for the solar plant characterization.
- In Chapter 6 a complete case study is reported, evidencing the performances of the innovative cycles considering a CSP application in Las Vegas.
- In Chapter 7 is described the methodology adopted for the off-design characterization of the innovative power cycles.
- In Chapter 8 a case study is proposed, detailing the off-design performances of a transcritical cycle working with the CO_2+C_6F_6 mixture for state-of-the-art CSP plants.

1. Literature review of sCO_2 and CO_2-mixtures power cycles

1.1 Literature review of sCO_2 cycles for high temperature applications

Typical configurations of cycles for high temperature applications based on sCO_2 employs at least a compressor, internal recuperators, a primary heat exchanger (PHE), at least a turbine and a gas cooler, also referred to as heat rejection unit (HRU). Figure 5 shows some of the most adopted plant layouts in literature. The design of the piping between the various components is rarely detailed, due to the compactness of the power cycle.

Moreover, a crucial component for the operation of the power block is the inventory tank of the working fluid: the overall quantity of working fluid flowing across the cycle, referred to as "inventory", can be stored in a dedicated vessel, externally to the cycle loop, to introduce and remove the working fluid mass in off-design conditions, regulating the cycle minimum pressure. Configurations of sCO_2 cycles with no inventory control are possible, but they don't generally allow for flexible nor efficient operations.

Across the literature of sCO_2 cycles for high temperature applications some general considerations are commonly reported:

- The maximum allowable pressure of the cycle is usually set around 250 bar, to match the technological constraints: as such, all simulations in literature usually assume cycle maximum pressure this upper bound, exploiting the highest-pressure ratio and the highest efficiency.
- The minimum cycle pressure is variable in a range between 80 bar and 110 bar: it is optimized to maximise the cycle efficiency and strongly depends on the compression inlet temperature (the actual trend of the optimal minimum pressure mimics the Widom curve, proposed in Figure 1).
- The simplest cycle layout, the simple recuperative cycle (shown in Figure 5), is not a suitable solution for a highly efficient power block:

in fact, modifications and variations are always considered (adding splitters, multiple recuperators and compression steps).

- Considering CSP as application, the cycle maximum temperatures usually considered are 550 °C and 700 °C, to match with 2nd generation CSP plants (adopting solar salts as HTF) and 3rd generation of CSP (with either sodium as HTF or adopting solid particles for the heat introduction). As the coupling with the CSP plant introduces some important boundary conditions on the HTF temperature range (influencing both the thermal efficiency of the receiver and the electric consumption of the HTF pump), plant layouts that focus on improve the cycle efficiency by reducing the hot source exploitation (as the cycle with multiple re-heatings) are usually not investigated.

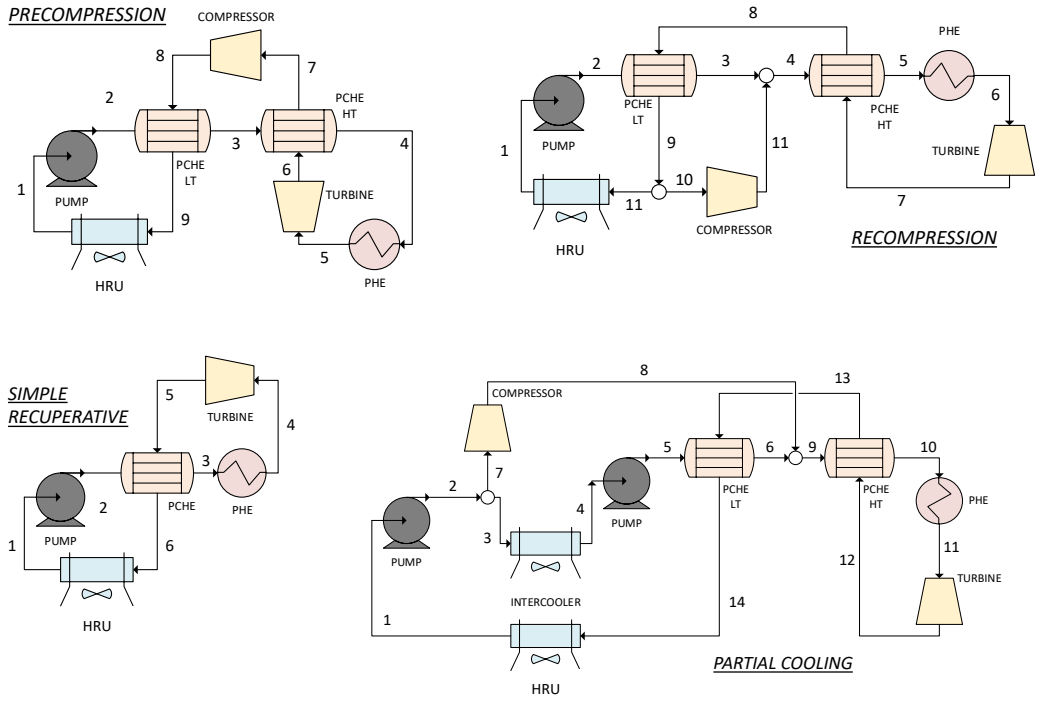

Figure 5. Typical plant layouts of sCO_2 cycles studied in literature for high temperature applications

Regarding the technical solutions adopted in literature for the heat exchangers of sCO_2 cycles, the following considerations can be drawn:

- PHE are usually designed as shell-and-tubes (S&T) heat exchangers: they represent the simplest solutions dealing with molten salts, appositely flowing on the shell-side to avoid clogs, solidifications of the HTF and hot spots that can otherwise eventually occur inside the tubes. An adopted technical solution in the CSP industry is to tilt the PHE with respect to the horizontal position, in order to drain by

gravity possible impurities and solidifications of the solar salts through the clearance between the baffles and the shell.

- Recuperators for these cycles are generally modelled as Printed Circuit Heat Exchanger (PCHE), the gold standard for compact heat exchangers dealing with high-pressure flows on both sides of the HX.
- HRU are normally composed of multi-pass tubes, always finned on the air side to increase the area wetted by the air, where the working fluid and the air are positioned in a crossflow configuration.

The materials usually adopted for the HXs include carbon steel or copper for the condenser tubes, optimal for CO_2 at low temperatures, with fins in aluminium or others low-cost materials with high thermal conductivity. At intermediate temperatures, stainless steel is commonly adopted up to its maximum limit set by creep failure, at around 550 °C. Over 550 °C, nickel based allows are proposed as a higher quality material for a better compatibility with CO_2 under extreme conditions. As such, SS316L is normally chosen for recuperators (developed as PCHE), and Inconel 617 is renowned for the tubes of the S&T PHE.

Finally, concerning the cycle characteristics at design conditions, the typical values of non-idealities related to the power block includes:

- Isentropic efficiencies of the turbine between 85% and 93%, depending on the plant size, with isentropic efficiencies of compressors between 80% and 90%.
- Pressure drops around 0.5 to 2 bar for the recuperator on the low-pressure slide, while the pressure drops in the high-pressure side of the recuperators are normally 35% of the one at low pressure, due to the higher densities and lower velocities.
- Pressure drops on the PHE between 2 to 4 bar: they are inherently higher than the ones across the high-pressure side of the recuperators, since PHE are characterized by a lower heat exchange area per unit of volume, and they are made of more noble materials.
- Pressure drops on air-cooled heat rejection units in the range of 1 to 2 bar, while can be considered negligible for water cooled HRU.
- Minimum internal temperature differences for the recuperators typically between 5 °C and 10 °C, and never lower than the technological limit (at around 2 °C for PCHE). Other approaches found in literature account for the effectiveness of the recuperator (usually set at around 95%), or the adimensional size of the recuperator expressed as $\frac{UA_{PCHE}}{Q_{IN}}$.
- Efficiencies of the motor of the compressors and generator of the turbines in the range within 97-99%, depending on the size.
- The auxiliary consumption of the air-cooled HRU is defined by a trade-off between an increment in the air temperature difference and a

reduction in heat transfer area of the HRU. Values around 0.8% of the heat rejected can represent the electric consumption of HRU in literature, while for steam Rankine cycles this value is around 2%.

Some literature studies and review works evidenced the actual performances of sCO_2 cycles for various applications [15] [27], also when applied to CSP. In addition, as correctly pointed out by Crespi [28], the crucial trade-off to consider while selecting a plant layout of a sCO_2 cycle for CSP is between the cycle efficiency and the temperature difference of the HTF (or storage fluid) across the cycle PHE. According to the trend of the ideal cycle efficiency (Lorenz cycle), plant layouts exploiting higher HTF temperature differences will inevitably have a lower cycle efficiency, as the optimal trade-off between the two aspects can only be only found with an overall techno-economic analysis. An example of a comparison between the cycle performances of various sCO_2 power cycles with different plant layouts can be found in literature in another work of Crespi [29], quickly recalled in Table 3.

Analogously, a work of Binotti [30] compared with the same approach various sCO_2 cycle configurations for CSP, evidencing a trade-off between the cycle efficiency and the HTF temperature difference across the receiver while adopting realistic assumptions on the cycle non-idealities. The analysis, reproposed in Table 4, evidenced that with a cycle maximum temperature and minimum temperature of 700 °C and 50 °C, respectively, adding an intercooling to the main compressor of the recompression layout would lead to a higher cycle efficiency.

Table 3. Examples of sCO_2 cycle layouts comparison adapted from literature [29]. Results refer to a cold environment with 15 °C of ambient temperature

Plant layout	**Relative cycle efficiency difference**	**Relative HTF temperature difference**	**Relative CSP plant cost difference**
	With respect to the simple recuperative layout		
Precompressed	+10%	-12%	+2%
Recompressed	+10%	-24%	+7%
Partial Cooling	+11%	0	-8%

Table 4. Sensitivity on the sCO_2 power block layout of the efficiency of a CSP plant, adapted from literature [30]

Plant layout	**Cycle efficiency [%]**	**HTF temperature difference**
	Assuming $T_{min} = 50\ °C$ and $T_{max} = 700\ °C$	
Recompressed (+ Interc)	47%	185 °C
Recompressed	45.6%	200 °C
Partial Cooling	46%	160 °C

Considering the results presented in this form, analogous analysis will be carried out within this thesis, with the aim of comparing the performances of the sCO_2 cycles with the innovative power cycles working with tCO_2-mixtures.

1.2 Introduction to CO_2-mixtures cycles

The adoption of CO_2-mixtures as working fluids in thermodynamic cycles is already investigated in literature, including reversed cycles such as heat pumps. Moreover, focusing on power cycles and depending on their application (ranging from geothermal, heat recovery, biomass plants or nuclear plants) both supercritical CO_2-mixtures cycles and transcritical CO_2-mixtures cycles are proposed, mainly depending on the dopant. In fact, dopants as noble gases, nitrogen and light hydrocarbons are often considered for supercritical cycles, while more unconventional dopants are exploited for transcritical cycles, as the ones proposed in this work.

In both cases, the status of the literature is at a relatively preliminary stage: works usually focus on the calculation of the locus of critical points, adapting the cycle conditions (and the composition of the mixture) to the application specified, while rarely considering the effects of the mixture on the design of the cycle or by going into details on the cycle off-design.

1.2.1 Literature review of supercritical CO_2-mixtures power cycles

Regarding sCO_2-mixtures power cycles, literature works consider them as valid candidates for CSP and nuclear applications, predominantly: they are not adopted at conditions with low temperature difference between the cycle maximum temperature and the minimum one, as for geothermal applications.

Reviewing literature works, two solutions are proposed for these cycles, as seen in Table 5, characterized by different approaches to restore at various temperatures the near-critical conditions that pure CO_2 experiences around 35 °C, in order to benefit the cycle efficiency.

Table 5. Classification of literature works covering sCO_2-mixtures cycles

	Dopants with T_{crit}<31 °C	**Dopants with T_{crit}>31 °C**
Reason	To work in near-critical conditions (exploiting real-gas effects)	To work in near-critical conditions (exploiting real-gas effects)
Cycle minimum temperature	20-30 °C	Above 50 °C
Dopants	Noble gases, N_2, O_2	Hydrocarbons, H_2S, SO_2, SF_6

Considering the first category, a work by Guo [31] considers Xenon as CO_2-dopant proposing a comprehensive analysis of a CSP plant with conventional solar salts as HTF: the results consider the possibility to have cycle minimum temperatures down to 30 °C (possible due to the adoption of Xenon as dopant), and present thermal efficiencies of the overall system increased by 1 to 2% with respect to the plant adopting sCO_2 cycles.

Focusing on nuclear applications with sodium fast-cooled reactors, Jeong [32] investigated the recompression power block working with CO_2 doped by some light gases and noble gases (Argon, Xenon, Helium, Krypton, Oxygen and Nitrogen) with the aim of reducing the critical temperature of the supercritical cycle: a higher flexibility and a wider operating range are possible with respect to the conventional sCO_2 cycle due to the above-mentioned difficulties regarding the compression stability at near-critical conditions. The results showed that Helium, as a dopant, can allow for higher cycle pressure ratios than sCO_2 and a higher cycle efficiency (by around 2%) when low temperature coolants are available, mainly due to the decrement in critical pressure of the mixture leading to lower optimal minimum pressures.

An example of a study to increase the critical temperature of the working fluid can be found in the work of Tafur-Escanta [33], where H_2S, NH_3, SO_2 and COS were proposed as possible dopants, for cycles with a minimum and maximum temperature of 50 °C and 700 °C: the resulting increments of cycle efficiency with respect to the sCO_2 plants are fairly limited and the adoption of such problematic dopants are not entirely justified, if working in supercritical conditions.

Analogously, a work by Zheng [34] identified the necessity to theoretically tune the critical point of the working fluid to the ambient temperature in a solarized cycle, proposing a solution that intra-day can vary the composition of the working fluid, adopting a storage of working fluid to add or remove a single compound from the loop. The authors evidenced the good performances of the cycle with H_2S as dopant, among some hydrocarbons analysed.

About the hydrocarbon family, propane and butane are usually suggested as CO_2 dopants: nevertheless, they are sometimes considered without considering their thermal stability limits [35] [36], especially in works dealing with CSP plants. In a detailed and ambitious work of Liu [35] the authors assumed to work with a compression inlet temperature 1 °C higher than the critical temperature of the mixture: in these conditions, propane and H_2S were again evidenced as promising dopants, while all the cycles with CO_2 mixtures are shown to have higher specific works than the sCO_2 counterpart. Interestingly, the authors also performed a rapid analysis on the heat transfer coefficients (HTC) and pressure drops in the recuperator of the cycle, evidencing good performances of the mixtures in terms of HTC and negative ones for the pressure drops with respect to sCO_2 cycles.

Overall, across the various literature works mentioned, the approach already developed for the analysis of sCO_2 cycles is reproposed: the degrees of freedom of the cycle simulations (split ratios, pressures, recuperators size, working fluid composition, etc.) are usually optimized to obtain the maximum cycle efficiency. In addition, not much consideration is given to sensitivity analyses on the equation of state adopted for the modelling of the mixtures, and the fitting between the equation of state selected and the experimental data of the mixture (if present) is normally not included in the analysis.

1.2.2 Literature review of transcritical CO_2-mixtures power cycles

Transcritical cycles for these applications normally operate with the entire compression step in the liquid region, both at inlet and outlet: at pump inlet the fluid is normally taken from the hotwell at bubble condition or slightly subcooled with an additional HRU, then it is pumped up to a subcritical temperature and supercritical pressure, in the liquid region. Given the high reduced conditions at pump inlet (with reduced temperatures over 0.9), the liquid is compressible and the pumping work is still significant: the temperature increment across the process is reduced with respect to supercritical cycles (sCO_2 cycles) but it is not negligible as in power cycles working with incompressible liquids, as steam cycles. On this regard, Table 6 provides a quick comparison between the three technologies focusing on the cycle compression work, assuming propane as CO_2-dopant in a simple recuperative cycle.

Table 6. Example of compression processes in different thermodynamic cycles for CSP applications with T_{max} = 550 °C and T_{min} = 51 °C [37].

	Steam Rankine Cycle	**Recompressed sCO_2 Cycle**	**Transcritical CO_2+Propane cycle**
Compression work [% of Expansion work]	3%	34%	15%
Compression ΔT	<0.01 °C/bar	0.4 °C/bar	0.15 °C/bar

The main consequence of adopting transcritical cycles instead of supercritical ones is usually a simplification of the plant layout, achieved while still maintaining sufficiently high cycle performances (even above the levels of sCO_2 cycles with more complex layouts).

Regarding low temperature applications, literature works as the ones reported in Table 7 focus both on low temperature bottom cycles and geothermal cycles, performant with CO_2-dopants of the hydrocarbon family. Generally, the thermodynamic properties of these mixtures are modelled within the ASPEN Plus environment, either with the case specific EoS developed in Refprop [38] (for common mixtures such as CO_2+Propane) or more approximately with the standard Peng Robinson EoS [39].

This category of transcritical cycles present large efficiency (or power) increments while comparing sCO_2 and tCO_2-mixtures configurations, mainly favoured by the low temperature difference between the minimum and maximum cycle temperature, imposing themselves as direct competitors to ORCs.

Table 7. Outline of some literature works dealing with tCO_2-mixtures cycles adopting hydrocarbons and refrigerants as dopants

Reference	CO_2-dopant	Power cycle	Notes
Siddqui [40]	n-pentane, cyclopentane, cyclohexane	Simple recuperative, T_{min} = 40 °C	TIT = 200 °C, Efficiency gain 18% vs 13% (sCO_2)
Shu [41]	R32, R161	Preheated recuperative	TIT = 270 °C, ICE bottom cycle
Wu [42]	R161	Simple cycle, T_{min} = 30 °C	TIT = 150 °C, Geothermal plant, Power production gain + 23% (vs sCO2)
Feng [43]	Propane, iso-butane	Simple cycle, T_{min} = 30 °C	TIT = 180 °C, Efficiency gain +29% (sCO_2)
Siddiqui [44]	Toluene	Recompressed, T_{min} = 50 °C	TIT = 400 °C, Efficiency gain +8% (sCO_2)

For high temperature applications, assuming cycle maximum temperatures above 300 to 400 °C, the selection of the dopant turns out to be a pivotal choice for the cycle designer, as the thermal stability of the dopant can put a limit on the efficiency of the hypothetical power cycle.

These category of power cycles, similar to the one of interest for work, are more likely to adopt perfluorocarbons and siloxanes, among the many dopant categories: perfluorocarbons are characterised by good solubility into CO_2, high molecular complexity, low-toxicity and low-flammability and they are potentially thermally stable and chemically inert at temperatures higher than 400 °C [45],[46],[47]. On the other hand, also siloxanes present good thermal stability, due to the strong silicon bond, potentially up to 400 °C [48],[49]. Nevertheless, few works antecedent to this did not reach a sufficient level in terms of cycle maximum temperatures to be efficiently applied to CSP: for example, an experimental study was proposed for the CO_2 mixture with C_6F_{14} [50], a working fluid proposed as good candidate to compete with high temperature ORC in the 350 °C range of maximum temperature.

The idea of high-temperature dopants for CO_2 in tCO_2-mixtures cycles is proposed and fully investigated in the EU H2020 project SCARABEUS [51], to which this work is partially dedicated to. Nonetheless, before the research developed within the SCARABEUS project itself, some preliminary studies were conducted to understand the concept potentiality up to cycle maximum temperatures above 550 °C: for example, CO_2 dopants as $TiCl_4$ (a strongly reactive metal halide which decomposes in HCl in contact with air) or N_2O_4 (a dissociating gas that decomposes at high temperature and recombines at lower temperatures) were investigated [52]–[54]. Even if these mixtures clearly lead to an improvement in cycle efficiency with respect to sCO_2 cycles at 700 °C and 550 °C of maximum temperature (assessed with a limited knowledge on the mixture thermodynamic behaviour), their high toxicity levels and the substantial chemical reactivity makes their handling very difficult from a technical standpoint, as small leakages are normally unavoidable in power plants.

In particular, these works evidenced that assuming to work with a simple recuperative power block the goal of gross cycles efficiencies over 50% and 44% are possible for cycle maximum temperature of 700 °C and 550 °C, respectively. The same ideas were reproposed within the SCARABEUS project by subsequent works, such as the one of Crespi [55]. A tentative experimental analysis started, with the aim of investigating the VLE behaviour of the CO_2+$TiCl_4$ mixture (and potentially the CO_2+$SnCl_4$ mixture) [56], but difficulties in handling the strongly reactive fluid were encountered, suspending the campaign with the goal of improving the experimental procedures to effectively analyse this mixture.

In conclusion, it is possible to identify a literature gap within the abovementioned considered power cycles at very high temperature for CSP applications: this is represented by the identifications of CO_2-dopants which are easy to manage, store and process. Accordingly, this work has the aim to consider these strong limitations to the research and identification of CO_2-dopants.

In detail, particular attention should be given to the following characteristics of the hypothetical innovative CO_2 dopants: i) a low toxicity and a low flammabilty of the dopants itself, ii) the dopant high thermal stability (at least above 550 °C) must be taken for granted, or eventually experimentally analysed, iii) the dopants should not be reactive with air, water, CO_2 nor metals, and must be chemically stable, iv) a good mixing behaviour with CO_2 must be ensured. The analysis proposed in the next section will focus on detailing these requirements for CO_2 dopants.

1.3 Definition of the dopant characteristics for high temperature cycles

A qualitative analysis of each CO_2 dopant must be proposed based on its characteristics as pure fluid, as done in this work in the next chapter.

Nevertheless, to effectively be exploited as working fluid, the following general considerations on the dopant characteristics can be drawn:

- The dopant thermal stability is either taken as a reference value from literature or experimentally determined: alternatively, it can be at first assumed based on the molecule structure, the strength of the chemical bonds and the similarity with more familiar chemical compound. Considerations on the thermal stability are presented accounting for the stability of the compound on a long-term horizon (for over 100 hours, as determined in the SCARABEUS project by partners at University of Brescia [57]). Moreover, the compatibility of the fluid with the metals is also evidenced, since more noble materials (as Inconel with respect to

Stainless steel) are expected to have a more limited interaction with the fluid, increasing its stability and resistance to any chemical interaction. Finally, no distinction between static and dynamic thermal stability is proposed, and both categories of experimental analysis in literature are considered equivalently valid to determine the fluid stability under a thermal stress. Additional details on the experimental campaigns carried out by University of Brescia (UNIBS) are found in Appendix A.1.

- The dopant flammabilty is assessed according to conventional parameters as the fluid flash point, the autoignition temperature or its concentration in air necessary to cause a spontaneous ignition. It can also be determined with a lumped parameter index, following the NFPA scale [58].
  Nevertheless, mixing a flammable fluid with CO_2 is per se an effective protection measure to reduce the flammability of the overall working fluid in case of a leakage, assuming a homogeneous mixture composition across the whole circuit of the power plant, since CO_2 is conventionally adopted as inert fluid in fire-extinguishers.
  Limiting the leaks from the power plant are crucial to cope with the flammabilty issues. In fact, leaks can occur: i) across the flanges of the piping of the loop, ii) from the turbomachinery sealings, iii) from the hotwell, while varying the fluid inventory from the working fluid storage vessel, iv) from the working fluid storage vessel itself.
  Safety measurements as dry gas seals can be adopted to handle the leaks from the power plant, nevertheless other mature technologies, such as ORC, nowadays can employ various flammable organic fluids. At the current technological level, in fact, it is possible to safely handle flammable working fluids in closed cycles, as evidenced in various studies on ORC [59]. For these reasons, any consideration regarding the fluid flammabilty is certainly of interest, but do not represent factors as critical as the fluid thermal stability in determine the potentiality of the respective CO_2-mixture in power cycles.

- A good solubility of the dopant in CO_2 is ensured for all the mixtures proposed, and any component not easily miscible in CO_2 (as water) are not included in the analysis.

- The toxicity level of the dopants has to be considered in the analysis. As mentioned, while describing the issues related to flammabilty, the handling of problematic working fluids is already done in state-of-the-art ORC plants, for example adopting toluene. With respect to the flammabilty, it is also important to determine the physical state of the dopants at ambient conditions, when in contact with the environment. In fact, a toxic dopant with a high normal boiling temperature and a low volatility is not easily dissolved in air at relatively high concentrations to

damage humans. On the other hand, gaseous dopants in normal conditions can cause more damages in case of a leakage, even if per unit of volume their lethal concentration is higher. Accordingly, it is possible to adopt the lethal concentration (LC50) indicator to characterize the dopants toxicity: the indicator refers to the concentration of the vapor in air (in ppm) that is likely (with a probability higher than 50%) to cause death when inhaled for a given period. Alternatively, the IDLH index can be used, indicating the concentration of immediate danger to life or health, or the STEL index, representing the short-term acceptable exposure limit. The combination of the lethal concentration and the actual volatility of the fluid at ambient temperature and pressure is hence a comprehensive indicator of the fluid toxicity.

- Finally, importance is given to the dopant chemical reactivity, particularly with air, the air moisture and the metals adopted in the loop. In case of leakages and while filling or removing the working fluid in its storage vessel, the consequences of the fluid toxicity and flammabilty can be easily controlled. On the other hand, in case of reactive dopants, a complete inert environment must be developed. These aspects are not particularly studied in the state-of-the-art of commercial power cycles, as reactive working fluids (contrarily to toxic and flammable fluids) are not normally considered. In fact, internal communications with industrial partners of the SCARABEUS projects underlines that it is undoubtedly preferrable to work with toxic non-reactive fluids than with reactive non-toxic fluids. Consequently, reactive compounds represent the biggest technological challenge to face for these systems, among the many challenges related to the fluids characteristics.

In the next chapter the proposed CO_2-dopants are listed and described: they are selected to enhance the performance of sCO_2 cycles, but importance to their characteristics as pure fluids is given according to the desired characteristics evidenced in this section.

2. tCO_2-mixtures for power cycles

A series of possible dopants for CO_2-mixtures as working fluids in high temperature power cycles are evidenced in this chapter: the list proposed does not represent an exhaustive pool of all the possible mixtures, as the research on this topic is continuously in progress. In fact, the identification of a plausible dopant is a delicate and difficult task, where the thermal stability of the fluid poses by far the most relevant obstacle to overcome. Moreover, preliminary calculations of the cycle efficiency in various conditions must be continuously carried out for each mixture investigated, in order to justify its promising characteristics.

2.1 Dopants selected for tCO_2-mixtures in power cycles

2.1.1 Hexafluorobenzene

Hexafluorobenzene (C_6F_6) belongs to the perfluorocarbon family, a class of fluids already well known for their thermal stability. In particular, C_6F_6 is selected as its aromaticity makes it the best candidate for achieving higher temperature stability, a concept already evidenced in literature [60]. The fluid is characterised by a high critical temperature and molecular complexity: before the work carried out within this thesis, no experimental data on the fluid thermal stability were available in literature except for static and dynamic analysis revealing that a mixture of C_6HF_5 and C_6F_6 (with a molar composition of 60% and 40%, respectively) can work continuously at around 480 °C [61].

Considering the promising premises, an experimental analysis of the thermal stability of the CO_2+C_6F_6 mixture was carried out within the SCARABEUS project [57], evidencing the working fluid thermal stability for 100 hours in a stainless-steel vessel up to 550 °C, and up to 600 °C in an Inconel 625 vessel.

These levels of resistance to thermal stresses have certainly projected the mixture to be a promising working fluid for power cycles in the future. In addition, the fluid is mildly flammable (its flash point is around 10 °C) and it has a low toxicity: in fact, it is liquid at ambient conditions and does not cause damages to the skin when put in contact. Interestingly, the fluid is also adopted in the medical field as reported probe in MRI [62].

Table 8 gathers the characteristics of C_6F_6, where the information on the thermal stability is intended for the mixture with CO_2 in an Inconel vessel.

Table 8. Characteristics of hexafluorobenzene (C_6F_6)

CAS	Critical point	Boiling temperature	Molar mass	Flammability	Toxicity	Chemical stability	Thermal Stability
392–56-3	243 °C, 32.8 bar	81 °C at 1 atm	186.06 kg/kmol	Low Risk (Flash point 10 °C)	Low (LC 50 = 12488 ppm/2h)	Inert	Over 550 °C

Experimental data of the thermodynamic and transport properties of C_6F_6 are extensively available in literature, including the saturated liquid density and heat capacity for a wide range of temperature, the vapor pressure, the enthalpy of evaporation, the surface tension and the liquid conductivity and viscosity. All the experimental data and the respective literature reference can be found in the database Thermo Data engine (TDE), implemented in ASPEN Plus v.11 [63], developed by NIST at the Thermodynamics Research Center (TRC).

Within this work, the CO_2+C_6F_6 mixture is modelled with two different thermodynamic models: the first is the standard Peng Robinson, optimized with a binary interaction parameter mainly on the available VLE data already available in literature [64] for this mixture and the ones collected by the author of this work [57]. The second EoS adopted for this mixture is the PC-SAFT, optimized within this work in ASPEN Plus v.11 on the experimental data of the pure compounds [37], presenting good fitting capabilities with the experimental VLE data.

2.1.2 Sulphur dioxide

Sulphur dioxide (SO_2) is an inorganic gas used in numerous industrial applications, such as a bleaching agent in the pulp, paper and textile industries, to produce sodium hydrosulfite or for the removal of chlorine from wastewater and chlorinated water. Moreover, since the mixture CO_2+SO_2 has been already studied as a mixture of interest in the carbon capture and storage field, a larger amount of experimental data are available with respect the CO_2 + C_6F_6 mixture, enabling a more detailed optimization procedure of the EoS on experimental data.

Finally, even if its toxicity is very high, the fluid does not pose issues in terms of flammabilty nor chemical reactivity with other compounds.

SO_2 is selected as a promising working fluid due to its thermal stability even at high temperatures: as a matter of fact, it is usually produced during combustion of coal in coal-fired power plants and can be produced during volcanic eruptions, two conditions where the exhaust gases reach very high temperatures. From a molecular point of view, it presents two strong S-O double bond (having 522 kJ/mol as average bond energy), a chemical bond considered stronger than the C-F bond (which has 485 kJ/mol as bond energy). For these reasons, in this work the CO_2 + SO_2 mixture is investigated up to 700 °C, where the CO_2 + C_6F_6 is not considered thermally stable.

Table 9 describes the characteristics of SO_2: with respect to C_6F_6, SO_2 is considered a widely known fluid, as experimental data of the pure fluid are available for any thermodynamic variable in a wide range of conditions.

Table 9. Characteristics of sulphur dioxide (SO_2)

CAS	Critical point	Boiling temperature	Molar mass	Flammability	Toxicity	Chemical stability	Thermal Stability
7446-09-5	157.5 °C, 78.8 bar	-10 °C at 1 atm	64.06 kg/kmol	Not flammable	High (IDLH = 100 ppm)	Inert	700 °C

2.1.3 Silicon tetrachloride

Silicon tetrachloride ($SiCl_4$) is proposed in this work as an alternative to $TiCl_4$ and $SnCl_4$ for very high temperatures power cycles. In fact, within this thesis and the SCARABEUS project, the author observed the reactivity of these three compounds, leading to dissociation of chlorine in air to form HCl, reacting with the air moisture. Under these circumstances, $SiCl_4$ presented by far the lowest tendency to decompose and the slowest reaction time: accordingly, it is studied in this work. $SnCl_4$ and $TiCl_4$, on the other hand, presented extremely quick decomposition, fuming in air forming HCl. The fluid must be stored in completely anhydrous environments, nonetheless.

$SiCl_4$, along with the other two metal-tetrachloride components, presents very high thermal stability, due to their tetrahedral molecular structure and their very strong metal-chlorine chemical bond. In fact, these components are adopted in industrial processes up to 1000 °C. For example, $SiCl_4$ can be used as a reactant to produce high purity silicon for the manufacturing of PV cells and in the semiconductor industry.

Finally, the fluid is liquid at ambient conditions and it is not flammable. It can be properly mixed with CO_2 for the purposes of this work, having a high critical temperature and molar mass: Table 10 proposes an overview of the compound characteristics.

Table 10. Characteristics of Silicon tetrachloride ($SiCl_4$)

CAS	Critical point	Boiling temperature	Molar mass	Flammability	Toxicity	Chemical stability	Thermal Stability
10026-04-7	234.9 °C, 35.9 bar	57.6 °C at 1 atm	169.9 kg/kmol	Not flammable	Reacts with water	Produces HCl in air	Over 700 °C

Available experimental data of this fluid includes: the vapor pressure trend, few data of saturated liquid densities, the thermal conductivity in both vapor and liquid conditions, the vapor viscosity and the heat capacity at bubble conditions in a wide range of temperature.

2.1.4 Tetrachloroethylene

Tetrachloroethylene (C_2Cl_4) is another fluid investigated as a candidate for medium temperature power cycles (with maximum temperatures in the range of 300-350 °C). With respect to the dopants previously mentioned, C_2Cl_4 is a more conventional working fluid: it is liquid at ambient conditions, it is not flammable nor reactive. As C_6F_6, also C_2Cl_4 can get in contact with the skin without damaging it. Its thermal stability, while mixed with CO_2, is studied at UNIBS within the framework of the H2020 EU project DESOLINATION [65], showing no signs of decompositions up to 375 °C. In fact, even if it is a commonly adopted fluid, little information about its thermal stability was available in literature [66].

The fluid has plenty of commercial applications, such as being a dry-cleaning agent for textiles and an excellent solvent for organic materials: in fact, it is still nowadays massively produced worldwide. The fluid characteristics are proposed in Table 11.

Table 11. Characteristics of Tetrachloroethylene (C_2Cl_4)

CAS	Critical point	Boiling temperature	Molar mass	Flammability	Toxicity	Chemical stability	Thermal Stability
127-18-4	345 °C, 47.6 bar	121 °C at 1 atm	165.82 kg/kmol	Not flammable	Low (STEL = 275 mg/m3 (8h))	Inert	Over 350 °C

Easily available experimental data for this pure fluid include a set of densities and heat capacities at bubble conditions, enthalpies of vaporization, vapor pressures at any temperature, viscosities and thermal conductivity in liquid conditions.

2.1.5 Other innovative dopants

A few additional CO_2 dopants are considered in this thesis, mainly expanding the pool of dopants for power cycles at maximum temperatures around 550 °C. Accordingly, the two following fluids have good potentialities due to their characteristics, as they are not toxic and completely inert:

- Octafluorocyclobutane (C_4F_8): this fluid belongs to the fluorocarbon family as C_6F_6. It is gaseous under normal conditions and it is not toxic. It is preliminary assumed to be thermally stable up to 550 °C according to literature [67], even if this aspect needs to be furtherly investigated. Table 12 details its characteristics: literature data are available for this fluid describing the density and heat capacity at bubble conditions, the vapor pressures and the transport properties as viscosity and thermal conductivity in liquid conditions. Unfortunately,

among all the fluids mentioned, C_4F_8 is the more difficult to find on the market.

Table 12. Characteristics of Octafluorocyclobutane (C_4F_8)

CAS	Critical point	Boiling temperature	Molar mass	Flammability	Toxicity	Chemical stability	Thermal Stability
115-25-3	115.2 °C, 27.7 bar	-6 °C at 1 atm	200.0 kg/kmol	Not flammable	Not Toxic	Inert	Over 500 °C

- Acetonitrile (C_2H_3N): it is considered of interest for CO_2-mixtures due to its very high critical temperature, very low molar mass and simple molecular structure. In fact, it is the only CO_2-dopant considered in this work with a molar mass lower than CO_2, a feature that helps limiting its concentration in the mixture, particularly in weight terms. Its thermal stability is preliminary assumed at 550 °C according to literature [68], but a more specific experimental characterization is necessary. The pure fluid is highly flammable but mixing it with a large quantity of CO_2 would curb this risk drastically. Table 13 presents the fluid characteristics: even if it does not present a high risk in toxicity, it is essential to keep under control its thermal decomposition, since it thermally decomposes in HCN. Any categories of data on the thermodynamic and transport properties of C_2H_3N are available in literature.

Table 13. Characteristics of Acetonitrile (C_2H_3N)

CAS	Critical point	Boiling temperature	Molar mass	Flammability	Toxicity	Chemical stability	Thermal Stability
75-05-8	270 °C, 48.3 bar	82 °C at 1 atm	41.05 kg/kmol	Highly flammable	Low (LC 50 = 7551ppm/8h)	Inert	Over 500 °C

Other working fluids which potentially are interesting for tCO_2-mixtures power cycles can be perfluoro-2-methyl-3-pentanone or 1,2-dichlorobenzene. The first one, known for its commercial name NOVEC 649, is an artificial compound with ideal characteristics in terms of compatibility, toxicity, flammabilty and chemical stability, available on the market at a relatively low cost. It is used as HTF or as a refrigerant, and it is even proposed in mixture with CO_2 to replace SF_6 for the electric insulation of medium to high voltage electric equipment [69]. The thermal stability of the CO_2+Novec 649 mixture for the application in power cycles is preliminary set up to 475 °C [69], even if it is examined at compositions not representative of a working fluid for power cycles. Dichlorobenzene, instead, is a dopant representing the family of aromatic C-H-Cl compounds, it is relatively safe if properly adopted as working fluid and it can be suitable for power cycles at temperatures in the range of 300-350 °C.

These fluids are two examples of a wider pool of possible CO_2-dopants considered within the research period of this work, investigated with the collaboration of few master students who worked with the author of this thesis within the framework of the SCARABEUS project.

Accordingly, other CO_2-dopants are briefly listed in Appendix A.2: they are not examined in this thesis in power cycles due to all the combination of possible limitations (low thermal stability, high toxicity, strong reactiveness, low cycle efficiency), but are proposed to show the potential vastness of the research field.

2.2 Experimental data of the selected CO_2 mixtures

In order to characterize at best the thermodynamic behavior of mixtures experimental data are considered necessary: in fact, the accuracy of the equations of state must be assessed on their fitting capabilities on experimental data.

In general, the most important category of experimental data for mixtures are VLE data: for their application in transcritical power cycles these data are even more crucial, as the knowledge of the VLE behavior of the mixture allows to accurately estimate the pressure in the hot well, at pump inlet and along the whole low-pressure side of the cycle. In addition to VLE, densities are commonly adopted as indicators for robust modelling by the EoS, if accurate fitting capabilities are proven. Other experimental data related to calorimetric variables such as heat capacities and speed of sounds are useful to determine the ability of the EoS to compute different derivatives of the various properties (for example, in the calculation of the speed of sound the derivative of pressure with respect to density must be computed).

The experimental data already available in literature for the mixtures of interest are summarized in Table 14. For the CO_2+C_6F_6 mixture a set of bubble points are presented by Dias [64], while for the CO_2+C_2H_3N mixture lots of literature studies investigated the mixture VLE behavior from 25 °C to 100 °C [70]–[73]. The CO_2+SO_2 is also already studied since, as said, it is of interest in the carbon capture and storage field: experimental data of VLE in the (P, x, y) form are available from Coquelet [74], along with densities and VLE in the (P, ρ, T) form from Gimeno [75], while additional densities, data on speed of sound, inversion curves and pseudo experimental residual specific heat are taken from Nazeri [76].

Table 14. Experimental data for the mixtures already available in literature

Mixture	VLE	Densities	Other data
CO_2+C_6F_6	Available from 20 °C to 80 °C	-	-
CO_2+SO_2	Available from -10 °C to 60 °C	Available in liquid region from x_{CO2} of 80% to 90%	C_p , speed of sounds, inversion curves
CO_2+C_2H_3N	Available from 25 °C to 100 °C	-	-

To expand the pool of experimental data available on mixtures, and to allow a more precise characterization of their efficiency adopted in power cycles, experimental data for three mixtures are taken by the author of this PhD thesis, within this work. They are briefly summarized in Table 15, and more details on the experimental campaigns are proposed in Appendix A.3. Unfortunately, no experimental data on the CO_2+C_4F_8 mixture are available nor measured within this work.

Table 15. Experimental data of CO_2-mixtures taken in this work by the author

Mixture	VLE	Densities
CO_2+C_6F_6	From 50 °C to 90 °C	-
CO_2+$SiCl_4$	From 35 °C to 70 °C (only bubble points)	From 40 °C to 80 °C, from 73% to 91% molar CO_2
CO_2+C_2Cl_4	-	From 40 °C to 80 °C, from 70% to 93% molar CO_2

Regarding VLE data, the most important category of experimental data for the application of mixtures in power cycles, it is crucial that they are available at temperatures in the range from 50 °C to 80 °C, to properly be exploited for the power cycle modelling.

2.3 CO_2 mixtures modelling with EoS

The modeling of mixtures with EoS proposed in this work exploits the robust and performant thermodynamic packages already available in commercial software, like ASPEN Plus [63] or Refprop [38]. In recent years, also the tool TREND was developed for this purpose with promising results [77].

The calculations are carried out in the next chapters with the specific version of ASPEN Plus v.11 and Refprop v.10. In principle, high fidelity in-house thermodynamic models can be studied and developed for some of the mixtures of interest: nevertheless, this approach has not been adopted in this work, focusing on aspects related to tCO_2-mixtures for closed power cycles more oriented to the actual characteristics of the overall power plant.

An example from literature of a detailed in-house study of EoS for CO_2-mixtures (including mixtures of interest for this work) is presented by Neumann [78]: the work is included in the Refprop set of equations of state for the modelling of some mixtures, including CO_2+SO_2. Neumann's work expands the already existing equation of state, explicit in the Helmholtz free energy, of Kunz and Wagner (also known as GERG 2008 EoS [79]) with additional adjusted reducing function and specific departure function for various mixtures of relevance in the CCS field.

Regarding the mixtures of interest for this work, the following chapters will briefly describe the mixture modelling with EoS and give some indications of their predictive performances.

As already mentioned, most of the importance will be given to the modelling of the CO_2+C_6F_6 and the CO_2+SO_2 mixtures. The CO_2+C_6F_6 mixture is proposed as one of the most promising innovative working fluids for the state-of-the-art CSP plants (adopting solar salts as HTF) within the EU H2020 project SCARABEUS, and it will be tested in an experimental loop at Technische Universität of Wien (TUW, partner of the SCARABEUS project) in late 2023, at a maximum temperature coherent with the expected temperature levels in power cycles for CSP plants. For this specific mixture, some details about the modelling of the transport properties will be additionally indicated. On the other hand, the CO_2+SO_2 mixture is also particularly under scrutiny in this work, since it has been selected as working fluid for the 1.7 MW_{el} pilot power block that will be built within the EU H2020 DESOLINATION project, in 2025. Also in this case, the respective EU project suggests the working fluid as promising alternative to pure CO_2 for the next generation of very high temperature CSP plants.

2.3.1 Modelling of mixtures with simple and advanced EoS

Equations of state can compute any thermodynamic property "π", of pure fluids and mixture, with different accuracy, as reported in Equation (1):

$$\pi(T,P,x) = \pi_{ideal}(T,P,x) + \Delta\pi_{residual}(T,P,x) \quad (1)$$

where the term $\pi_{ideal}(T,P,x)$ is the property computed in the ideal gas state, while the term $\Delta\pi_{residual}(T,P,x)$ is the residual property, both evaluated at the same given temperature and pressure (and composition, in case of mixtures). The prediction of the real fluid behaviour, thus the residual quantities, strongly affects the power cycle modelling.

If a cubic equation of state is employed, as well as in any other model where the solution of the EoS is expressed in the form $v = f\,(T,P)$, the residual quantities of the main thermodynamic variables such as enthalpy, entropy and specific heat can be calculated analytically as:

$$\Delta h_{residual}(T,P,x) = \int_0^P \left(v - T\left(\frac{\partial v}{\partial T}\right)_P\right)_T dP \quad (2)$$

$$\Delta s_{residual}(T,P,x) = \int_0^P \left(\frac{R_g}{P} - \left(\frac{\partial v}{\partial T}\right)_P\right)_T dP \quad (3)$$

$$\Delta C_{P_{residual}}(T,P,x) = -\int_0^P T\left(\left(\frac{\partial^2 v}{\partial T^2}\right)_P\right)_T dP \quad (4)$$

Considering that specific works of CO_2-based mixtures power cycles are very low (in the range of 80-120 kJ/kg), the accuracy in enthalpy calculation is fundamental: as a matter of fact, an enthalpy error of 5 kJ/kg in the calculation of any thermodynamic points of the cycle has a relevant impact on the assessment of the cycle efficiency, while this is not true for traditional steam Rankine cycles that are characterised by a specific work of an order of magnitude higher (around a thousand of kJ/kg). For this exact reason, before moving to the analysis of the EoS on the investigated CO_2-based mixtures, a qualitative comparison of the predictive capabilities between the cubic EoS and Refprop models on known mixtures is briefly presented, highlighting the benefits and drawbacks related to the adoption of a cubic EoS. In particular, among the many cubic EoS and their variations, the PR EoS (with the proper $k_{i,j}$ values fitted on VLE data of each mixture) is selected because it is the standard choice for many cycle simulations.

As the ideal gas properties are not affected by the property models, a deviation in the calculation of the residual quantities translates directly in a deviation of overall quantities. Focusing on enthalpy, which is the most crucial variable in modelling of power cycles and in the determination of their efficiency, Figure 6 presents a comparison between the residual calculations of PR and Refprop. In particular, the comparison is done on two known CO_2-based mixtures potentially representative of transcritical cycles, whose modeling is possible with the Refprop models: CO_2+Propane (C_3H_8) and CO_2+Toluene (C_7H_8) [37].

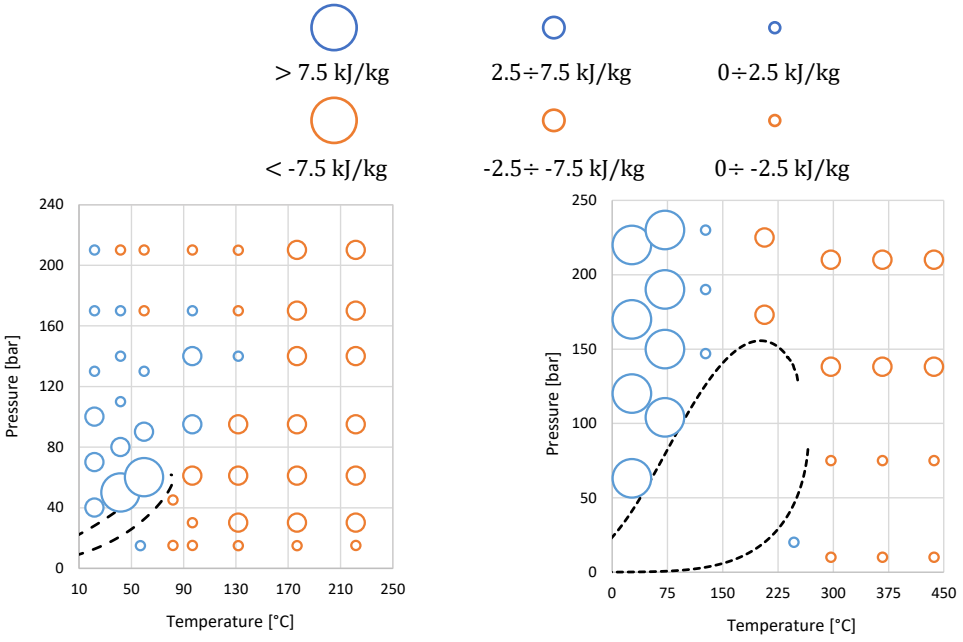

Figure 6. Differences between residual enthalpy computed with PR and Refprop: CO_2+Propane (x_{CO2}=30%) on the left, CO_2+Toluene (x_{CO2}=50%) on the right [37]

From the figure it is possible to notice a significant positive deviation (blue bubbles) of the enthalpy computed by PR in the liquid region for both the mixtures; on the other hand, a slight negative deviation (orange bubbles) can be seen in supercritical conditions. As these two contributions have an opposite sign, an enthalpy difference calculation between two points in these two different regions (from liquid to supercritical zones) has a big impact on the evaluation of the cycle efficiency. For example, in a simple recuperative transcritical cycle an error in the calculation of the enthalpy at the outlet of the pump, which is also the inlet of the recuperator at the high-pressure side, will influence the estimation of the recuperated heat, thus the cycle efficiency. Consequently, the resulting efficiency of the cycle can be affected by a significant uncertainty, even if an optimized binary interaction parameter is known and used on the cubic EoS, assuming the results from Refprop as a reference for the modeling of the mixture.

The good predictive capability of cubic EoS on VLE calculations is widely known from literature, especially for PR, and it can be almost taken for granted if a solid optimization procedure of the binary interaction parameters is carried out on experimental data. Nevertheless, as reported, this approach can still lead to inaccuracies in terms of cycle calculations. For this reason, at least in principle, advanced EoS are more of interest for the applications studied in this work, with respect to conventional cubic EoS. Since the categories of experimental data necessary to develop and to fit complex EoS are not always available in literature, this work will present both approaches on the basis of the CO_2+C_6F_6 mixture and the CO_2+SO_2 mixture. In particular, with the sulfur dioxide mixture, a detailed characterization of the EoS is done based on experimental data, while in the other case, when hexafluorobenzene is considered as dopant, the EoS optimization is less detailed, due to the lack of useful experimental data.

2.3.2 Modelling of the CO_2+C_6F_6 mixture

The mixture is preliminary analysed with some commonly adopted models for mixtures available in ASPEN Plus, fitted on the experimental bubble points proposed by Dias [64] through binary interaction parameters. The EoS selected are: (i) the standard PR EoS with soave alpha function and VdW mixing rules, (ii) the same model with the Boston-Mathias alpha function [80], (iii) the Predictive Soave-Redlich-Kwong (PSRK) EoS [81], which is an extension of the RKS equation of state, iv) the virial model LK-PLOCK [82], [83] and (v) the PC-SAFT EoS [84].

The PC-SAFT EoS is based on the perturbation theory, according to which a molecule is modelled as a chain molecule with freely joined spheres. PC-SAFT requires three pure component parameters known as segment number (m),

segment diameter (σ) and segment-segment interaction energy (ε/k): an additional binary interaction parameter (k_{ij}) can be included, as for the other simpler EoS.

The calculation of the three parameters of the PC-SAFT EoS on the pure C_6F_6 is carried out in this work, using experimental data of saturated liquid densities, heat capacities, vapor pressures and enthalpies of evaporation. The Peng-Robinson EoS instead, used in numerous studies in past, only requires the critical point temperature and pressure (T_{cr}, P_{cr}), the acentric factor (ω) and the molecular weight (MW) of each pure component. In addition, an optional binary interaction parameter (k_{ij}) can be used to appropriately describe the VLE properties of the selected binary mixture.

This analysis can be found in the literature produced within this work [37], along with the lists of binary interaction parameters proposed for each equation considered. It is important to note that different possible numerical tools available in literature can implement different versions of the EoS of interest: for that reason, it is important to specify that the optimization of the PC-SAFT parameters must be done from scratch in case other computational environments (different than ASPEN Plus) are adopted.

The five thermodynamic models listed can provide a first guess idea of the shape of the VLE region at any composition, shown in Figure 7 along with experimental data. Although at low temperature all equations converge on the same results, large differences can be noticed at higher temperatures where they diverge, close to the critical point, being this region the most problematic to be modelled.

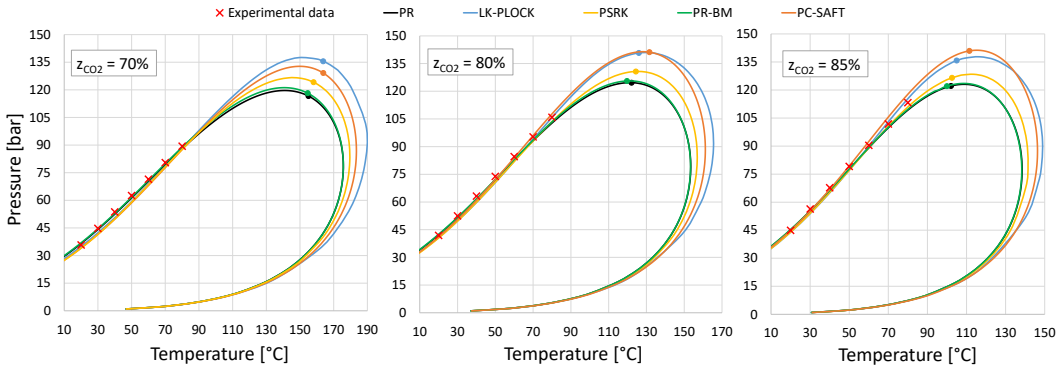

Figure 7. Examples of phase diagrams at different CO_2+C_6F_6 mixture compositions on P-T diagram. Solid lines calculated by various EoS [37]

As the comparison of EoS in Figure 7 can be considered as relatively inconclusive, the second set of VLE experimental data are analysed (listed in Table 15 and Appendix A.3.3) [57]. The results in Figure 8 depict the fitting of the PR EoS with both sets of experimental data, obtained with a temperature-dependent binary interaction parameter. The resulting refined binary interaction parameters of both the PR and the PC-SAFT EoS are shown in Table 16: in fact, PC-SAFT presents a sufficiently good fit of the VLE data, even if with a lower precision than PR.

Table 16. Binary interaction parameters (k_{ij}) for the CO_2+C_6F_6 mixture as modelled in ASPEN Plus v.11

Mixture	BIP for Standard PR	BIP for PC-SAFT
CO_2+C_6F_6	$0.163 - 0.0003951 \cdot T[K]$	$0.1023 - 0.05574/(\frac{T[K]}{298.15})$

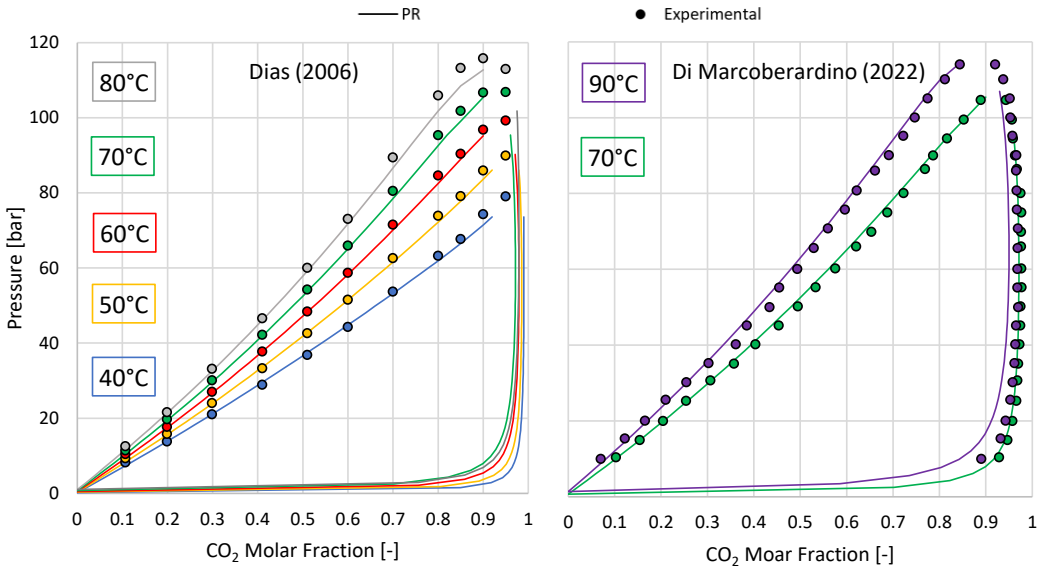

Figure 8. VLE of the CO_2+C_6F_6 mixture modelled by the PR EoS (as in this work)

The comparison between experimental and calculated data is also reported at fixed molar composition, considering CO_2 composition of interest for this work (at 80% and 85%, respectively), only for the PR EoS for the sake of brevity. Figure 9 and Figure 10 report the mixture behaviour in P-T and T-s diagrams: from the P-T diagrams a limited but clear deviation is visible between the bubble points measured by Dias and the ones measured in this work, by Di Marcoberardino. In the future, in case the CO_2+C_6F_6 mixture will be considered in literature more in detail than the analysis carried out in this work, additional VLE data are probably necessary to confirm this trend and to cover higher temperatures (above 100 °C), where the various models present large deviations (as shown in Figure 7).

The T-s diagrams evidence the large glide of the mixture at the two compositions and the trend of some isobars of interest for power cycles, along with the substantial isentropic temperature difference across a hypothetical pump to compress the liquid up to 250 bar.

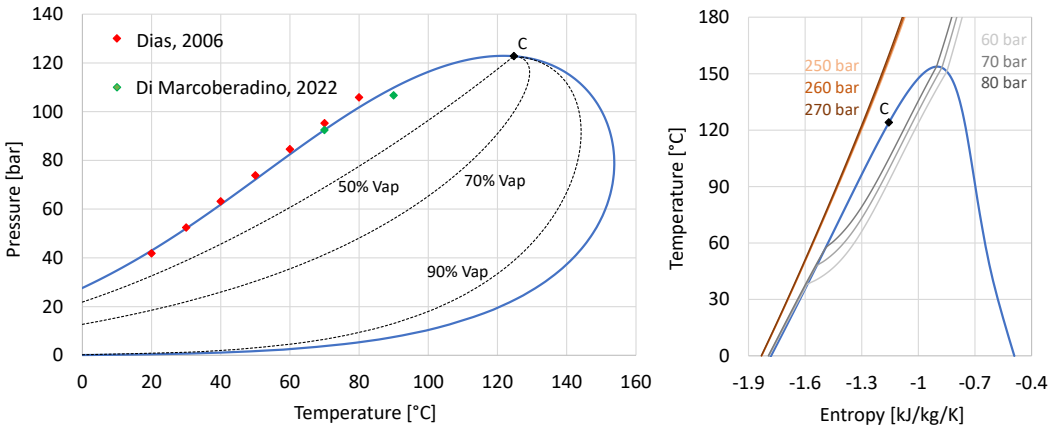

Figure 9. CO_2+C_6F_6 mixture (80% CO_2 molar) modelled by the PR EoS (as in this work)

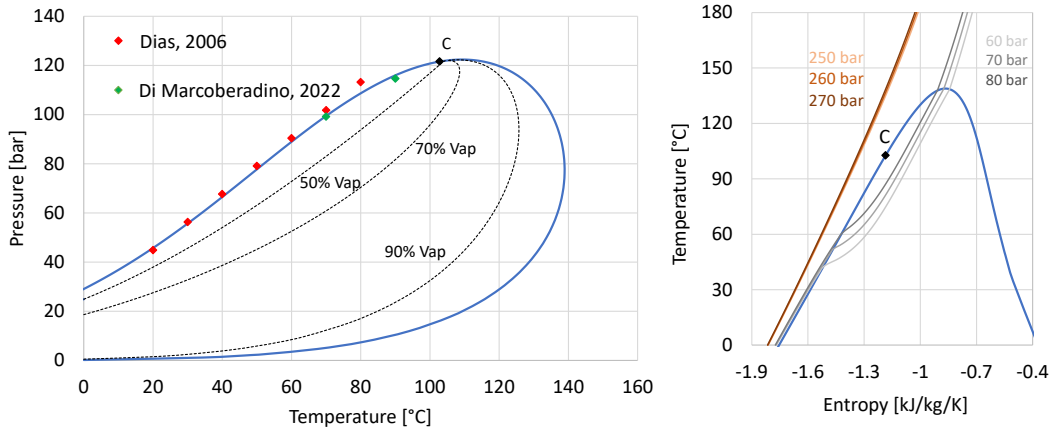

Figure 10. CO_2+C_6F_6 mixture (85% CO_2 molar) modelled by the PR EoS (as in this work)

As only VLE data are considered in this analysis, the optimization of the EoS on this mixture can allow to draw conclusions whose validity is only partial. In fact, as will be proposed in the analysis of the CO_2+SO_2 mixture, additional volumetric and calorimetric experimental data could in principle evidence inaccuracies from the calculation of cubic EoS, as reported in literature for many mixtures.

According to this analysis and the inherent uncertainties of the cubic EoS in the calculation of properties of interest for power cycles (as discussed in Figure 6), both the PR and the PC-SAFT EoS are considered in this work, equally valid to be preliminary able to model the thermodynamic properties of the CO_2+C_6F_6 mixture.

In addition to the optimization of thermodynamic properties for this mixture and given the large importance of the CO_2+C_6F_6 mixture for this work, some considerations are also developed, regarding the calculation of the mixture transport properties, useful to properly characterize the heat exchangers of the power cycles, to propose their sizing and to estimate their off-design performances.

The models have been developed as in-house MATLAB codes by the SCARABEUS partners at UNIBS, before being tested and applied within this work. The so-called CO_2-SUPERTRAPP model, a modification of the TRAPP (TRAnsport Property Prediction) method (from Ely and Hanley [85]), has been used for the thermal conductivity of the mixture using carbon dioxide as reference fluid to improve the matching between the CO_2-rich and the reference fluid. As the vapor phase of the investigated condensing mixture is characterized by a high molar content of the most volatile component (CO_2), the same approach has been used for the vapor phase viscosity of the mixtures; thus, the so-called CO_2-SUPERTRAPP model has been successfully adopted by Nazeri [86] for CO_2 mixtures with impurities.

On the other hand, the viscosity of the mixture liquid phase has been characterized with the general one-parameter friction theory model of Quiñones-Cisneros [87]. The critical characteristic viscosity of the pure components of the binary mixture, which is a degree of freedom of the friction theory model, is already optimized for pure CO_2, and it has been optimized for C_6F_6 fitting the experimental data of liquid viscosity for the pure fluid.

Additional information on the models adopted for the viscosity and thermal conductivity of the CO_2+C_6F_6 mixture can be found in the literature work developing these concepts [88]: interestingly, the two models have been validated by the author on a known mixture, CO_2+R1234ze(E), by comparison with the transport properties models already available in Refprop. As reported in the respective literature work, deviations lower than 4% on all transport properties (liquid and vapor phase viscosity and thermal conductivity) are computed between the Refprop models and the models of this work [88]. Therefore, the promising results on the known mixture (CO_2+R1234ze(E)) encouraged the author to adopt these models also for the CO_2+C_6F_6 mixture.

2.3.3 Modelling of the CO_2+SO_2 mixture

A literature work developed within this thesis analysed the predictive behaviour on the CO_2+SO_2 mixture of a selection of conventional thermodynamic models [89]. Among the several EoS which can be adopted, three EoS have been selected and compared: 1) the standard Peng Robinson EoS (PR) with soave alpha function [39], 2) the PC-SAFT EoS [84], 3) the REFPROP inbuilt EoS (extended GERG-2008 EoS proposed by Neumann [78]).

The selected equations of state cover a wide spectrum of options: PR is an extensively adopted cubic EoS (thanks to the limited amount of required input data and its accuracy in VLE calculations), PC-SAFT is very versatile and proved to be accurate for CO_2 mixtures and REFPROP is considered as a reference tool in many studies to predict properties of pure fluids and mixtures. The in-built Refprop model involves four parameters to compute temperature and density

reducing functions, proposed in literature [89] and not reported in this thesis for sake of brevity.

As mentioned in the literature review on CO_2 mixtures for power cycles, most of the literature studies on this topic do not consider the evaluation of the EoS accuracy, not identifying the most accurate property model. This work aims at filling this gap by comparing the properties predicted by three EoS and recommending the one which demonstrates the minimum deviations from experimental data.

The procedure developed for the selection of the optimal EoS can be summarized in the following three steps:

1) PR and PC-SAFT are calibrated on sets of VLE experimental data (P,x,y) available in literature from Coquelet [74], as they are non-predictive EoS (while the Refprop inbuilt EoS is already optimized).
2) The accuracy of the three equations of state is evaluated with reference to experimental VLE data ($P-\rho-T$), densities, speed of sounds, pseudo experimental residual heat capacities and Joule Thompson inversion curves available in literature [75], [76] for the CO_2+SO_2 mixture.
3) An overall index to identify the most accurate EoS is proposed and used.

Accordingly, the analysis is carried out starting from the VLE data from Coquelet [74]:

- The PR EoS and PC-SAFT EoS are optimized with binary interaction parameters on Coquelet data [74], as graphically presented in Figure 11, which results are presented in Table 17.

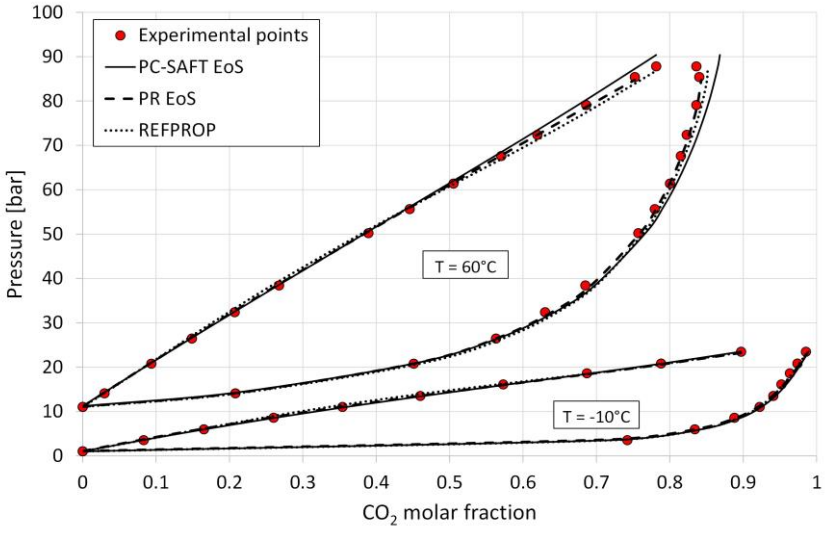

Figure 11. Comparison of predicted VLE by the selected EoS of the CO_2+SO_2 mixture with experimental data from Coquelet [74] at two temperatures

Table 17. Predictive capability of the selected EoS on the CO_2+SO_2 mixture experimental data from Coquelet [74]

EoS	Binary Parameter	Average error on P_{bubble}			Average error on y_{dew}		
		-10 °C	60 °C	Average	-10 °C	60 °C	Average
PR	0.0242	1.4%	0.6%	1.0%	0.3%	0.8%	0.5%
PC-SAFT	0.0121	0.8%	1.1%	0.9%	0.7%	1.7%	1.2%
REFPROP	Refprop	2.0%	1.3%	1.7%	0.5%	1.7%	1.1%

- Once the various EoS are adequately optimized on VLE data, other sets of data, as the $(P-\rho-T)$ along the saturation lines and the densities from Gimeno [75], densities, speed of sound, inversion curves and pseudo experimental residual specific heat from Nazeri [76] are included in the comparative analysis of the EoS. In fact, the methodology proposed will underline the EoS which reports the lower overall deviation from experimental data.

  Graphical representations of the fitting between these experimental data and the EoS are shown in Figure 12: in the charts with P-T and T-ρ curves, triangles show experimental data for 90% molar CO_2 mixture, while solid circles correspond to the 80% molar CO_2 mixture. In the charts with density and speed of sounds against pressure, the experimental data of the 80% molar CO_2 mixture are dotted, while the residual heat capacities refer to CO_2 molar content of 95%.

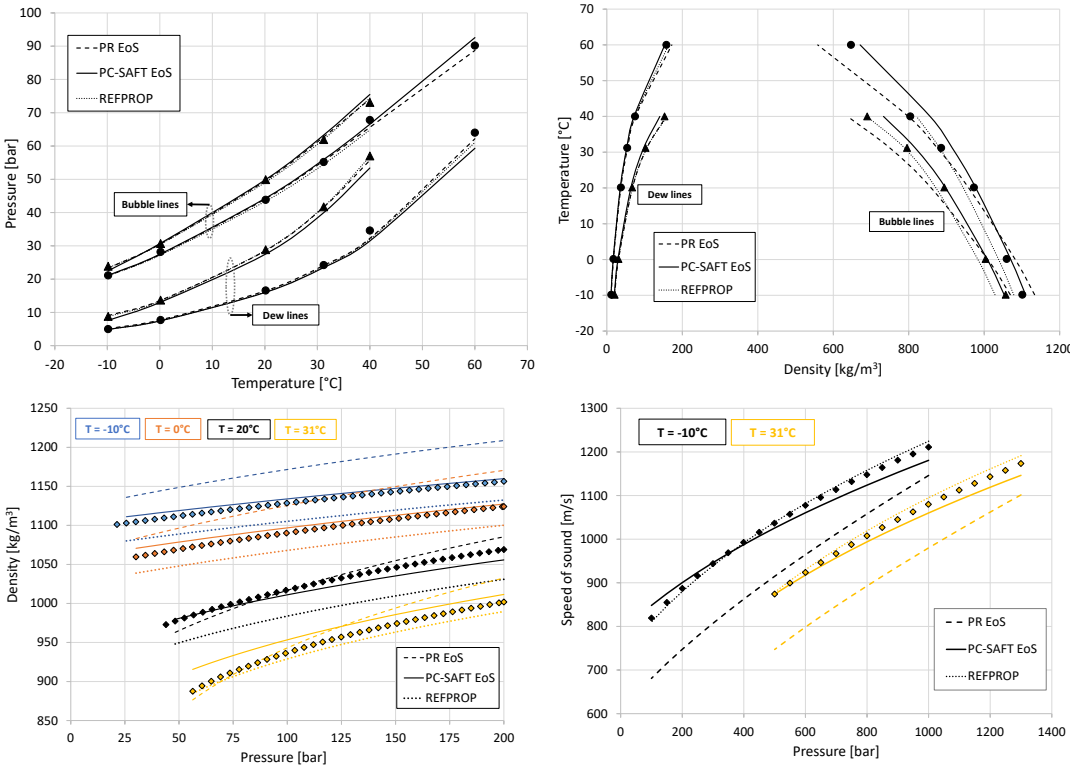

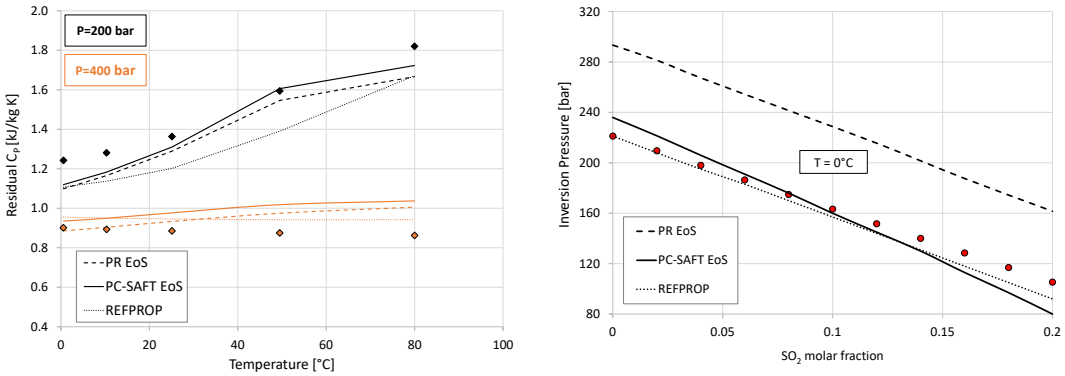

Figure 12. Comparison between experimental CO_2+SO_2 data and values computed by the EoS considered in this work for the mixture

- Finally, the scope of this procedure is to identify the most accurate EoS to be adopted for the assessment of the CO_2+SO_2 mixture used as working fluid in closed cycles. With respect to most of the approaches adopted in literature, which uses only VLE data for the EoS optimization, the comparison is extended also considering densities, data on specific heat and speed of sound. For this reason, the identification of the most appropriate EoS is more challenging, since it can be difficult to combine the predictability of many EoS at different temperatures and compositions for different set of properties. Therefore, the properties of the mixture are divided into four categories: VLE, density, speed of sound and residual specific heat. The average relative errors across these four classes of data are proposed in Table 18: according to this analysis, the PR EoS is discarded due to the poor capability of fitting some of the advanced calorimetric properties such as the speed of sound and the inversion curve of Figure 12, while both the PC-SAFT and the REFPROP EoS are proven to be adequate models for this mixture.
  Considering the results of the PC-SAFT model on the densities and the overall accuracy along the whole analysis, this model is selected as the reference EoS for this mixture: as a matter of fact, PC-SAFT is the EoS that presents the lowest average relative error indicator, justifying its choice as selected model. Regarding the VLE calculations, it must be reminded that the different relative errors on these experimental data between the three models are computed with equations fitted on the VLE quantities themselves (through the BIP): the precision of these calculations represent an upper limit of the fitting capability for each adopted model.

Table 18. Overall average relative error of the EoS with respect to different categories of experimental data of the CO_2+SO_2 mixture

EoS	Average error with experimental data				
	VLE	Densities	Speed of sound	Residual C_P	Average on all data
PR	1.1%	2.5%	10.4%	7.3%	5.3%
PC-SAFT	2.0%	1.4%	1.6%	7.2%	3.0%
REFPROP	1.5%	2.3%	0.9%	8.1%	3.2%

According to these considerations, the P-T and T-s diagrams of the CO_2+SO_2 mixture at two compositions of interest are proposed in Figure 13 and Figure 14. With respect to the P-T envelopes of the CO_2+C_6F_6 mixture of Figure 9 and Figure 10, this mixture presents a much limited extension of the VLE region, with a drastic reduction in temperature glide: this is a direct consequence of the more similar molecular structure of the CO_2 and SO_2. As it will be described in the next chapter regarding power cycle calculations, this will also have an impact on the most suitable cycle layout for this working fluid.

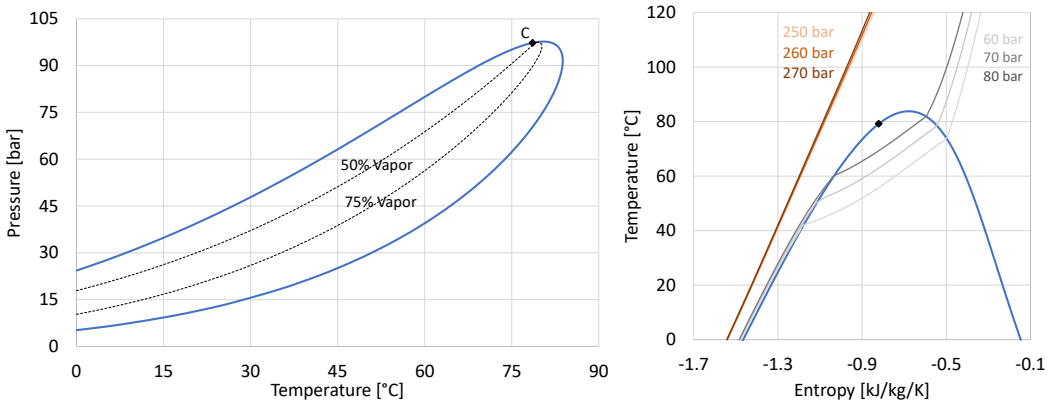

Figure 13. CO_2+SO_2 mixture (70% CO_2 molar) modelled as in this work

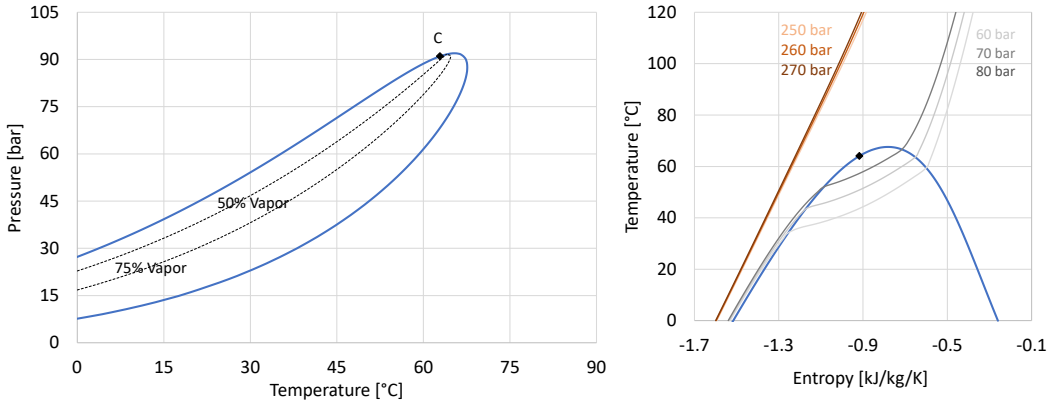

Figure 14. CO_2+SO_2 mixture (80% CO_2 molar) modelled as in this work

The methodology proposed in this chapter can clearly be exploited for any set of EoS, any mixture and any category of experimental data, and it represents a step-by-step procedure to determine the most accurate thermodynamic model for mixtures. In this case, for the CO_2+SO_2 mixture, since a comparison with the gold standard model from Refprop was included, no additional EoS were considered.

It is important to underline that the thermodynamic model proposed in this work is also adopted in the H2020 EU project DESOLINATION for the design of a pilot power cycle, running with the CO_2+SO_2 mixture, to be applied to a CSP-like environment.

Finally, as no considerations about the transport properties of this mixture are developed in this work, the author refers to the modelling of the mixture viscosity and thermal conductivity as proposed in the Refprop model: future works can detail this aspect based on the experimental data of this mixture.

2.3.4 Modelling of other mixtures of interest

This chapter reports a quick characterization from the thermodynamic point of view of the mixtures previously mentioned and different than CO_2+C_6F_6 and CO_2+SO_2, representing the fluid behaviour in P-T and T-s diagrams.

The mixtures CO_2+$SiCl_4$, CO_2+C_2H_3N, CO_2+C_4F_8 and CO_2+C_2Cl_4 are modelled in Aspen Plus with the standard PR EoS, exploiting an optimized binary interaction parameter only for the first two mixtures, as experimental VLE data are available. The diagrams in Figure 15 are reported highlighting molar compositions of interest for application in air-cooled power cycles, referring to the location of the critical point (particularly for the temperature, between 70 °C and 100 °C) as main indicator.

In the T-s diagrams is also depicted the trend of the isobars of interest, to emphasize the extension of the temperature glide and the temperature difference across the pumping process.

As evidenced during the analysis of the CO_2+C_6F_6 and CO_2+SO_2 mixtures, very different shapes of the VLE region can be obtained by different mixtures. Mixtures like CO_2+SO_2 and CO_2+C_4F_8 have limited glides, with both the cricondenbar and the cricondentherm very close to the critical conditions, given the very high volatility of both dopants (proposed in Table 9 and Table 12 through the information of the normal boiling temperature). The other dopants with a low volatility are instead expected to show a large extension of the VLE region in the P-T chart of the mixture, even at pressures above the critical one. This characteristic has a large impact on the choice of the plant layout that is the most suitable for each working fluid.

Moreover, mixtures with large glides adopted as working fluid in power cycles are normally characterised by the partial condensation of the working fluid in the recuperator (for any plant layout), on the hot side (low pressure side). This feature improves the performance of the respective power cycles, even for the simplest layouts, but introduces a technological challenge given by the possible maldistribution of the two-phase flow at the outlet of the recuperator and the inlet of the condenser. This issue has been anticipated and preliminary discussed also within the DESOLINATION EU project: as a consequence, for the pilot plant of the project, a working fluid with low glide and dry conditions along the whole recuperator is selected.

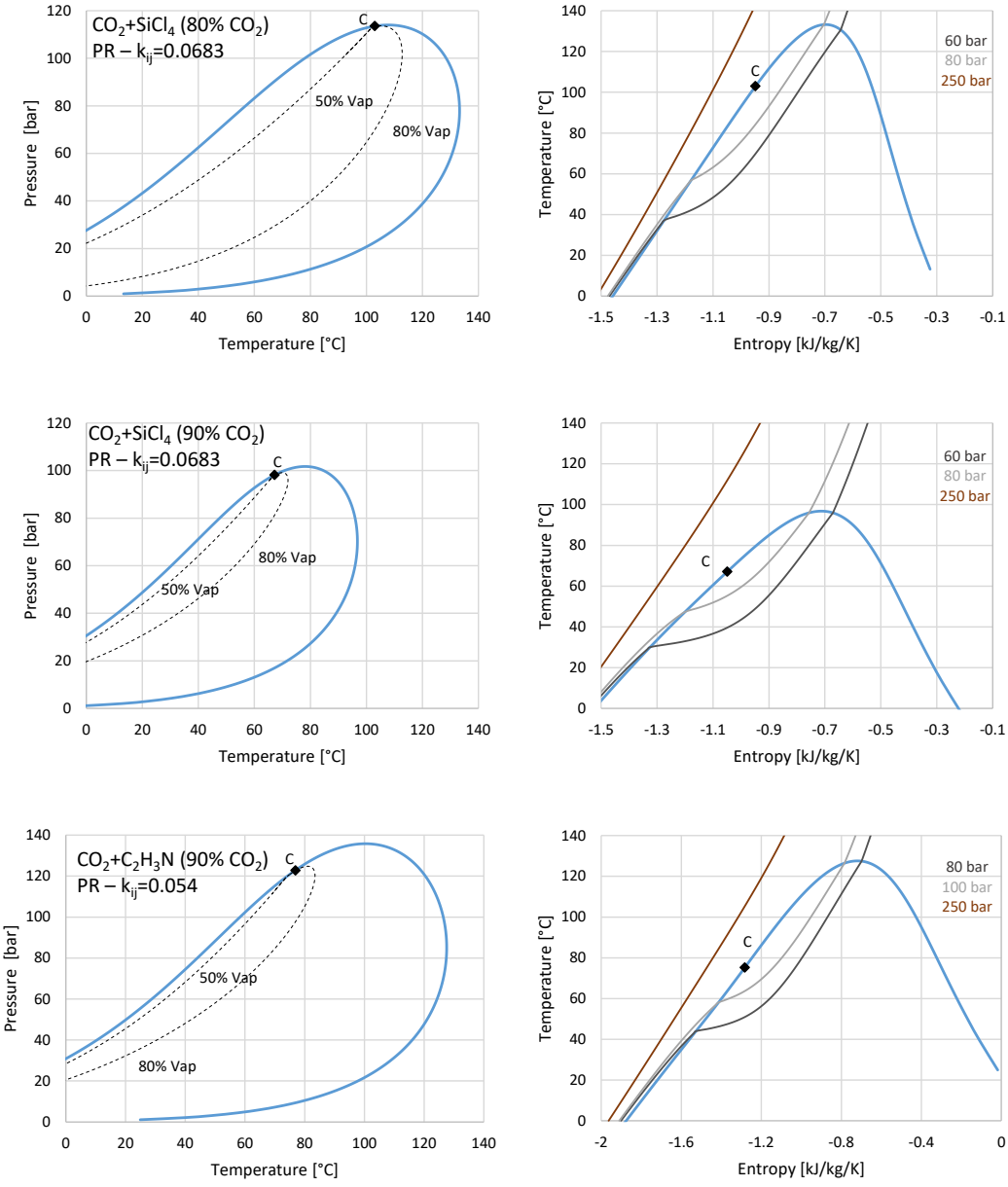

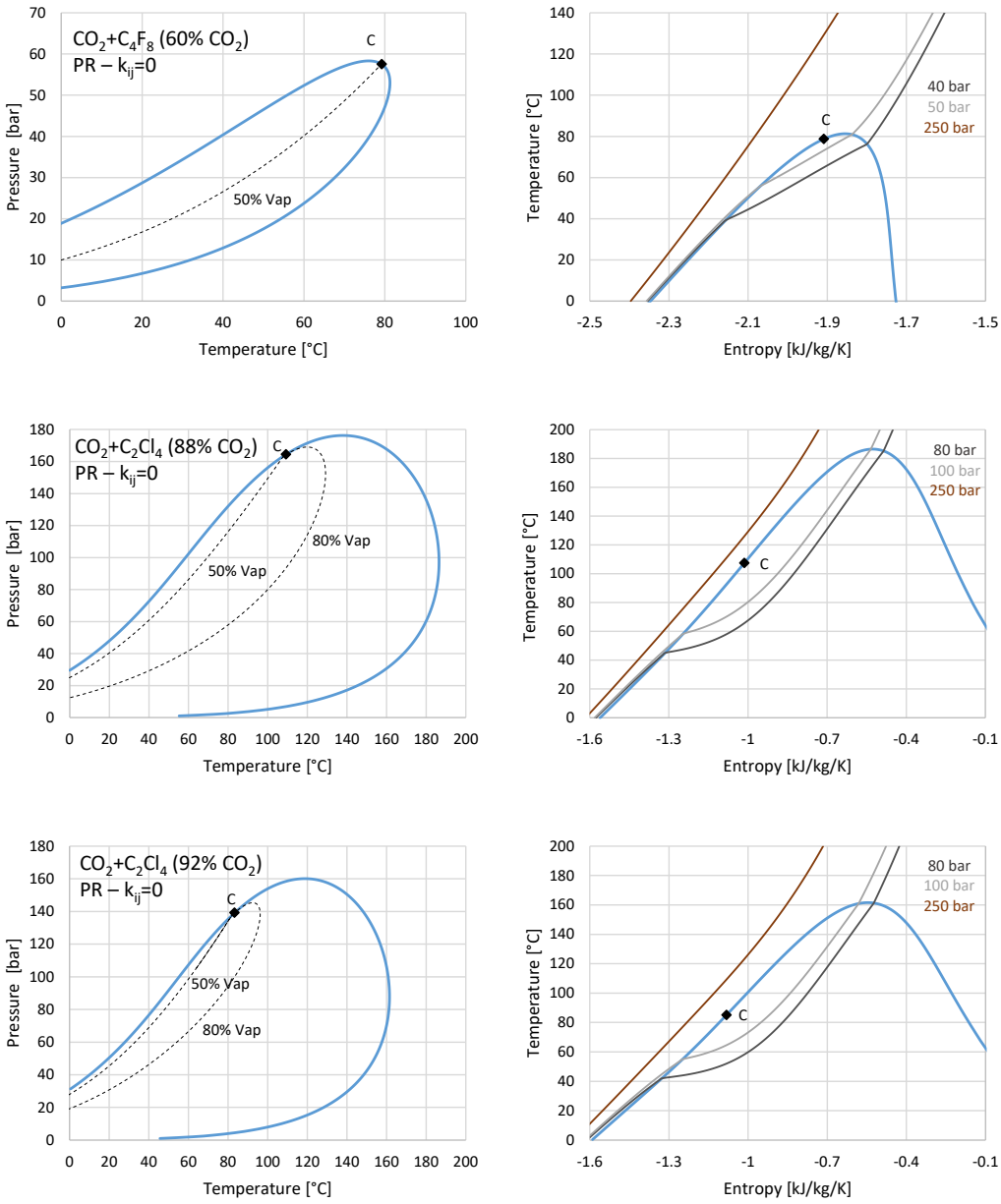

Figure 15. P-T and T-s diagrams of some CO_2-based mixtures. Each set of diagram reports the CO_2 molar content and the binary interaction parameter adopted for the cubic EoS

3. Innovative cycles performances

The outcome of this work is to demonstrate the effectiveness and techno-economic attractiveness of the innovative mixtures to be adopted as working fluids in closed cycles. As a first step, the performances of the innovative cycles must be assessed, even before considering the implementation of the cycle in a specific application (like CSP, nuclear power, high temperature waste heat recovery, etc…).

This chapter will present some of the characteristics of the innovative cycles in conditions of interest for high temperature applications.

Among the sets of cycle simulations carried out for the various mixtures, a complete and detailed analysis will be presented for the CO_2+SO_2 mixture when used as working fluid: nevertheless, the methodology proposed for this mixture can be applied to any other mixtures at any condition for the power cycle.

The analyses are proposed computing the performances of the various cycles underlining the efficiency improvements with respect to the sCO_2 power block, considering it a benchmark technology for this study.

3.1 Sensitivity on plant layouts and working fluid compositions

While analyzing a new working fluid for power cycles in a specific application, it becomes crucial to properly select the most appropriate power block layout, as any working fluid presents specific trends of the efficiency for each different plant layout adopted. Considering transcritical cycles with binary mixtures, as done in this work, one of the distinctive features that can be used to identify the most appropriate plant layout is the extension of the VLE region in terms of temperature and pressure. As a matter of fact, depending on the CO_2 dopant and its molar mass, molecular complexity and its normal boiling point, the VLE region can be extended for more than a hundred degrees in temperature (for the mixture composition of interest), and the cricondentherm can be located well over fifty degrees above the critical temperature. On the other hand, also the opposite is possible, while mixing two components with similar volatility: in this case the cricondenbar and cricondentherm can be found very close to the critical point, and the glide during condensation is very limited, down to ten or twenty degrees. These two different trends are particularly evident in the results of Figure **15**.

Regarding pure CO_2 cycles, in recent years many studies of various applications evidenced different optimal cycle layouts. For example, when waste

heat recovery is explored, the simple recuperative layout with bypass or the cascade layout have been identified as optimal configurations [90], while the recompression layout is usually proposed as highly performant for CSP applications, mainly due to the high cycle efficiency [15]. Nevertheless, this solution comes at the cost of a very poor heat recovery from the hot source, entailing a working fluid temperature difference across the PHE between 120 °C to 180 °C. A wide selection of possible plant layouts for CO_2-based cycles are visible in Figure 16.

The thermodynamic characteristics of pure CO_2 in a pressure-temperature diagram can be considered similar to the one of a CO_2-based mixture with a volatile dopant, where very low glides are experienced: in this work it is possible to refer to the CO_2+C_4F_8 mixture (Figure 15) or the CO_2+SO_2 mixture (Figure 14) for this category of mixtures as working fluids. Considering sCO_2 cycles, the adoption of a recompression layout is favorable when the heat source has a very high average temperature. In fact, for this layout, due to the drastic variation of the C_p of the working fluid at the low-pressure side (close to the critical pressure), a splitter is adopted to balance heat capacity of the two sides of the recuperators, modifying the mass flow rate to compensate for the specific heat variation [15]. Similar considerations regarding the specific heat capacity variation, even if not as marked as in pure CO_2, can be done for the family of CO_2-mixtures with limited glides, that inevitably can have good performances when the recompression cycle is considered.

On the other hand, for the mixtures with large VLE regions (as the CO_2+C_6F_6 mixture), the recompression layout is not adopted for two main reasons. At first, the inlet conditions of the recompressor (point #10 in Figure 16 (d)) must be on vapor phase: this is not normally possible, again due to the VLE region extension, unless a sub-optimal solution in terms of split ratio is considered. Secondly, the C_p of the vapor mixture above the dew point does not present large variations, and it is almost constant with respect to temperature: therefore, it is not necessary to balance the heat capacity of the two sides of the recuperator.

For this reason, simpler plant layouts (as the simple recuperative layout or the recompression layout) are suggested for these mixtures.

In addition to the plant layout, also the mixture composition can be considered as a degree of freedom to be optimized in the definition of the tCO_2-mixture cycles characteristics at design. The approach developed in this work is to fix the mixture composition according to the condition that maximizes the cycle efficiency at design point for that layout, not considering the performance of different mixture compositions during the off-design and part load simulations of the cycle. Interestingly, the optimizations of the plant layout and the mixture composition are intertwined: for the same mixture and the same cycle boundary conditions it is possible that certain cycle layouts present the best performance for

a given mixture composition, while other layouts can allow for their maximum cycle efficiency at different nominal value of the mixture composition.

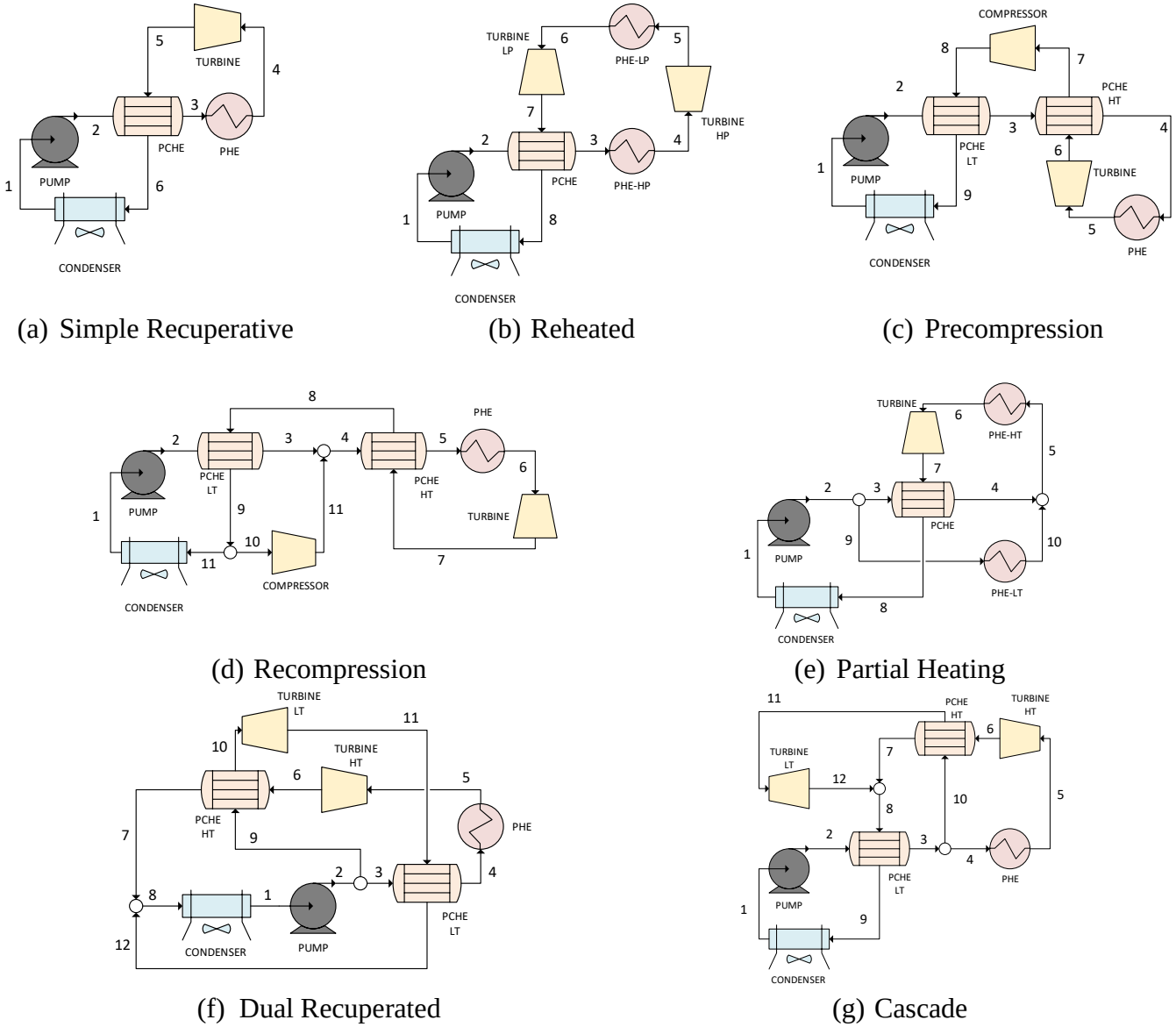

(a) Simple Recuperative (b) Reheated (c) Precompression

(d) Recompression (e) Partial Heating

(f) Dual Recuperated (g) Cascade

Figure 16. Possible power block layouts for transcritical power cycles working with CO_2-mixtures

3.2 Key thermodynamic indicators for the analysis of power cycles

The important performance indicators for the thermodynamic analysis of the power cycles are the cycle efficiency, the specific work, the working fluid

temperature at the PHE inlet and the relative size of the recuperators of the power cycle.

Considering the gross cycle specific work, it is normally computed with respect to the mass flow rate $\dot{m}_{Compression}$ during the compression phase to make a consistent comparison between all the plant layouts, including the ones characterized by two turbines. The only exception being the recompression cycle, where two compression steps and only one expansion are present: in this case the specific work can be computed with respect to the mass flow rate expanded in the turbine $\dot{m}_{Expansion}$.

The cycle specific work is important in closed cycles since it accounts for: i) the overall working fluid inventory (leading to an extra cost when non-conventional working fluids are adopted), ii) the mass flow rate of the cycle itself (high mass flow rates increase the size of the cycle components and their cost), iii) the environmental impact of any leakage of the working fluid in case of leakages or damages.

Overall, the cycle efficiency is considered as the most important descriptor of a thermodynamic cycle. This is true especially in solarized cycles, where it determines the size of the solar field itself, and therefore it is strictly related to the specific CAPEX of the overall power plant.

The third key performance parameter, the working fluid temperature at the inlet of the primary heat exchanger, is another crucial indicator of costs and thermodynamic performances for high temperature applications, since the lower the temperature of heat introduction, the higher the temperature difference of the hot source exploited. In CSP plants, a large temperature differences of the HTF across the PHE would result in: i) an increment of the receiver thermal efficiency, due to a corresponding reduction of thermal losses between the receiver and the environment, ii) a lower HTF flow rate at constant thermal input, thus reducing the size and cost of the TES and the electric consumption of the HTF pump. Nevertheless, following the trend of the Carnot efficiency, a lower temperature at the PHE inlet inevitably leads to a drop in cycle efficiency.

The last parameter, the relative size of the PCHE, expressed as $UA_{PCHE}/\dot{Q}_{IN}$, accounts for the physical dimensions of all the recuperators: since the various plant layouts present significant differences between each other, this parameter gives an indication of the recuperators size for each condition, and consequently their cost.

The calculations of the cycle components are carried out as in Equations from (5) to (10) and the performance indicators of the cycles are defined as in Equations from (11) to (13).

$$\dot{W}_{Compression} = \dot{m}_{compression} \cdot \left(h_{iso-s}^{outlet,compression} - h^{inlet,compression}\right)/\eta_{iso,compressor} \quad (5)$$

$$\dot{W}_{Expansion} = \dot{m}_{expansion} \cdot \left(h^{inlet,expansion} - h_{iso-s}^{outlet,expansion}\right) \cdot \eta_{iso,expander} \quad (6)$$

$$\dot{Q}_{IN,PHE} = \dot{m}_{PHE} \cdot \left(h^{outlet,PHE} - h^{inlet,PHE}\right) \quad (7)$$

$$\dot{Q}_{PCHE} = \dot{m}_{PCHE,HP} \cdot \left(h^{outlet,PCHE\ HP} - h^{inlet,PCHE\ HP}\right) = \dot{m}_{PCHE,LP} \cdot \left(h^{inlet,PCHE\ LP} - h^{outlet,PCHE\ LP}\right) \quad (8)$$

$$\dot{Q}_{Condenser} = \dot{m}_{condensed} \cdot \left(h^{inlet,condenser} - h^{outlet,condenser}\right) \quad (9)$$

$$UA_{PCHE} = \frac{\dot{Q}_{PCHE}}{\Delta T_{ML,PCHE}} \quad (10)$$

$$\eta_{gross,cycle} = \frac{\dot{W}_{Expansion} - \dot{W}_{Compression}}{\dot{Q}_{IN,PHE}} \quad (11)$$

$$w_{Specific,Cycle}\ [kJ/kg] = \frac{\dot{W}_{Expansion} - \dot{W}_{Compression}}{\dot{m}_{Cycle}} \quad (12)$$

$$UA_{PCHE}/\dot{Q}_{IN}\ [1/K] = \frac{\sum UA_{PCHE,i}}{\dot{Q}_{IN,Cycle}} \quad (13)$$

According to the key performance parameters defined it can be possible to compare different cycle configurations adopting the same working fluid or comparing different working fluids in the same cycle layout. An analysis on the performance of the sCO_2 cycles can be also carried out, to evidence if the most effective plant layouts and the trends of the main thermodynamic variables are comparable to the results of the tCO_2-mixture power cycles, or, on the other hand, if the latter can be exploited in circumstances different than the ones usually of sCO_2 cycles.

Many thermodynamic analyses on the innovative CO_2-based mixtures are carried out within the SCARABEUS H2020 project, mainly by partners from University of Seville. In the following sub-chapters of this work will be proposed a single large case study, detailing the performances of the CO_2+SO_2 mixture as working fluid across a wide range of operating conditions, while the performance of the other mixtures in power cycles will be shown with a lower level of details. For additional investigations on tCO_2-mixture cycles the author refers to the available literature works of the SCARABEUS project [91], [55], [92].

3.3 Performance analysis of the CO_2+SO_2 mixture: a case study

This chapter will propose an analysis of the performances of the cycles with the CO_2+SO_2 mixture assuming the component non idealities of Table 19: in particular, the simulations are run for an application with 700 °C of cycle maximum temperature, representative of next generation CSP plant or very high temperature heat recovery, and a cycle minimum temperature of 51 °C, assuming an air-cooled power cycle in hot locations.

Table 19. Cycle characteristics of the case study presenting the performances with the CO_2+SO_2 mixture

Cycle characteristic	Value at design conditions
Cycle minimum temperature [°C]	51
Cycle maximum temperature [°C]	700
Compression inlet pressure [bar]	Optimized for sCO_2, at bubble point for mixtures
Recuperator MITA [°C]	5
Turbine isentropic efficiency [%]	92
Pump isentropic efficiency [%]	88
Primary HX pressure drops [%]	2
Condenser/HRU pressure drops [%]	2
PCHE pressure drops (LP) [%]	1.5
PCHE pressure drops (HP) [%]	0.3

The resulting trends of the four thermodynamic key performance parameters are shown from Figure 17 to Figure 20. A wide sensitivity analysis is depicted across this case study, showing the cycle performance of different: i) power block layouts, ii) cycle maximum pressures, and iii) mixture compositions.

Considering the results in Figure 17 it can be observed that the adoption of the mixture in the simple recuperative layout and in the reheated layout does not provide significant improvements on the sCO_2 cycles from a cycle efficiency perspective.

The most significant improvement of the CO_2+SO_2 mixture with respect to supercritical CO_2 in terms of cycle gross efficiency occurs for the recompression layout, with an increase of 2.1% (overcoming the 50% threshold) when the maximum pressure is 250 bar. In addition, the temperature of heat introduction decreases by 40 °C, the relative size of the PCHE decreases by more than 20% and the specific work increases by more than 25%. Combining these four aspects, the overall thermodynamic analysis on the recompression cycle suggests that the adoption of the mixture, with respect to the sCO_2 configuration, would allow significant improvements in the technoeconomic performances of the power cycle and of the power plant in which the cycle is employed.

Similar considerations can be made for the precompression layout, where the mixture shows a 0.5% cycle efficiency growth, a 40% reduction of the PCHE size and a 25% growth of specific work with respect to pure sCO_2. Notably, the specific work of the precompression cycle is the highest between the various

layouts, since it is the only configuration where the expansion ratio of the turbine is higher than the pump compression ratio.

On the other hand, when it becomes necessary to increase the exploitation of the hot heat source, plant layouts from the heat recovery family can be also exploited (reported in Figure 16 (e), (f) and (g)). As the recompression cycle permits only a 150-200 °C of temperature difference of the working fluid in the PHE, heat recovery cycle configurations, instead, have 420 to 480 °C of temperature difference, three times higher, as presented in Figure 18.

The dual recuperated and the cascade cycle present comparable results in terms of cycle efficiency: depending on the layouts, these two heat recovery cycles achieve efficiencies between 41.0% and 41.5% for maximum pressures of 250 bar and between 42.0% and 42.5% for maximum pressures of 300 bar. The most considerable improvement that the mixture can bring with respect to the pure sCO_2 cycle is in the heat introduction temperature, which can be up to 100 °C lower than the one of sCO_2 cycle, assuming the same heat recovery plant configuration. This difference can be mainly attributed to the lower temperature difference in the compression step of the transcritical cycle with respect to the compression of pure CO_2, that occurs in the supercritical phase.

The cycle efficiencies computed in various conditions also permit to identify the optimal mixture composition: under this perspective, the composition of the CO_2+SO_2 mixture equal to 85% of CO_2 molar content is selected as the optimal one since it reaches the highest cycle efficiency in all configurations while, unfortunately, increases the recuperator relative sizes and reduces the specific work of the cycle. These last two characteristics are mainly caused by the trend of the mixture molar mass, which decreases at high CO_2 content and at low working fluid complexity.

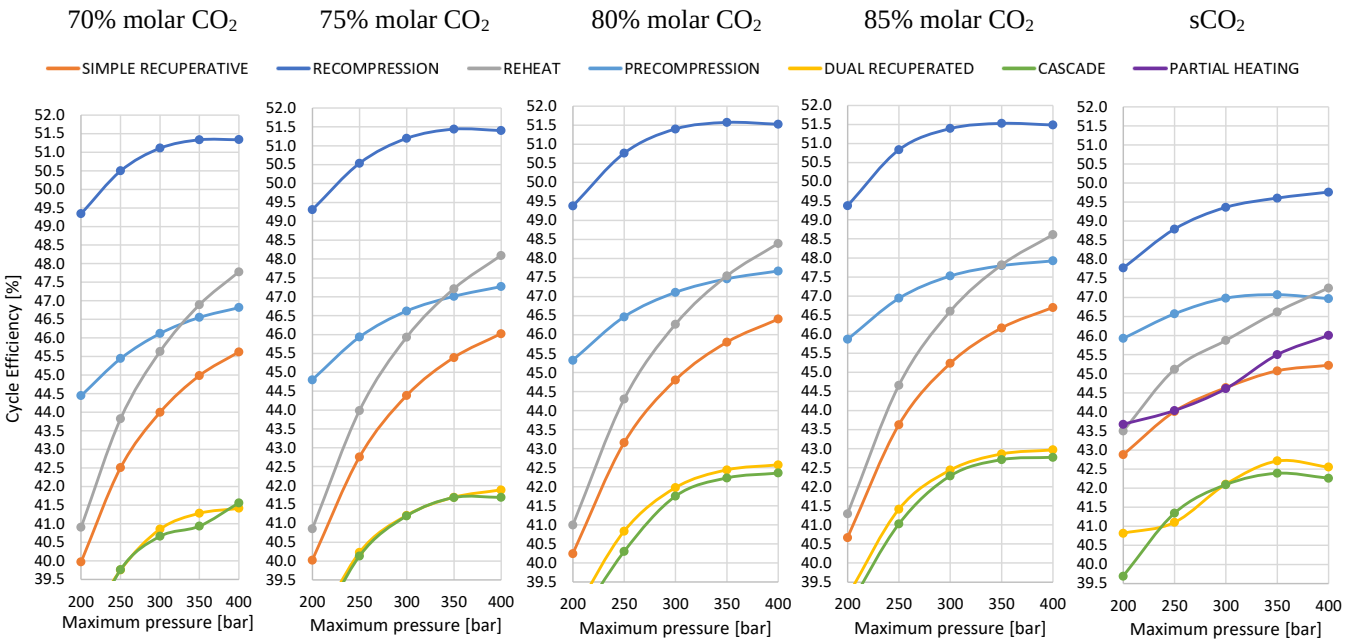

Figure 17. Gross cycle efficiencies in the various conditions considered, referring to the case study of Table 19

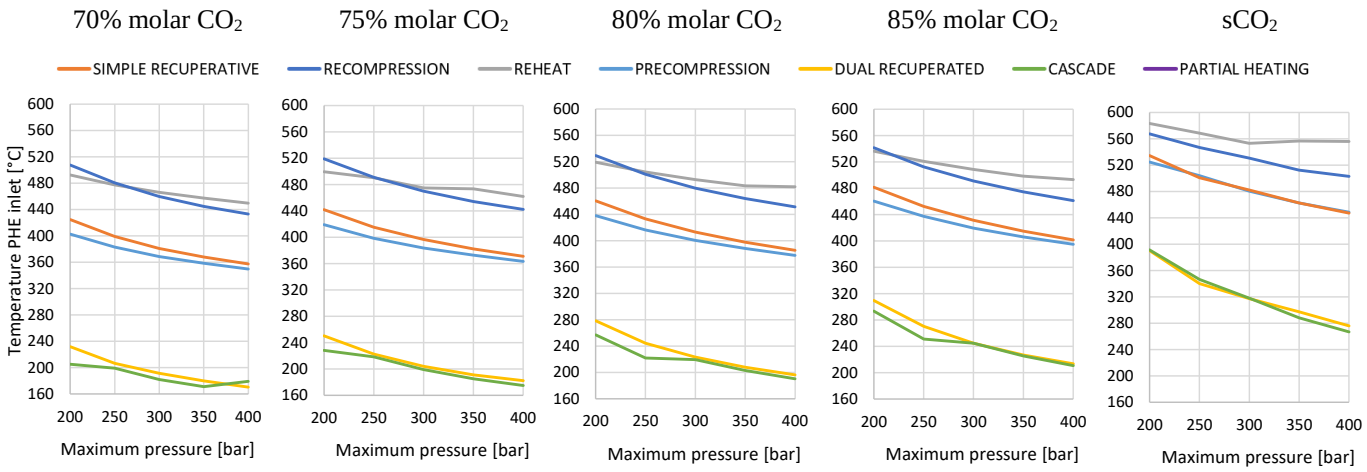

Figure 18. Working fluid temperature at the inlet of the PHE in the various conditions considered, referring to the case study of Table 19

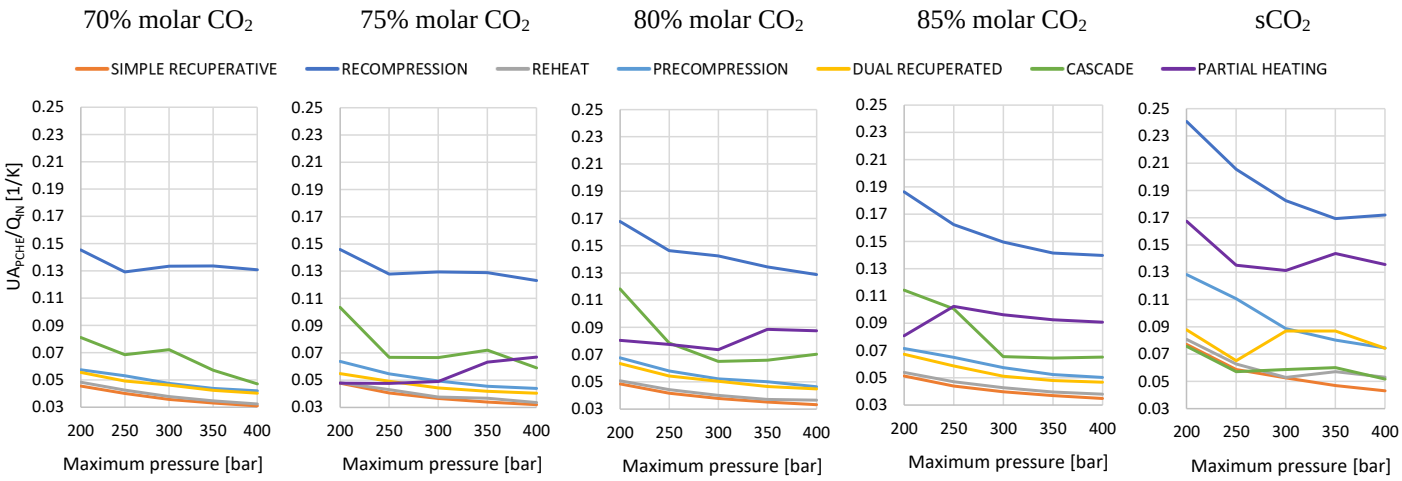

Figure 19. Relative recuperators size of the power cycle in the various conditions considered, referring to the case study of Table 19

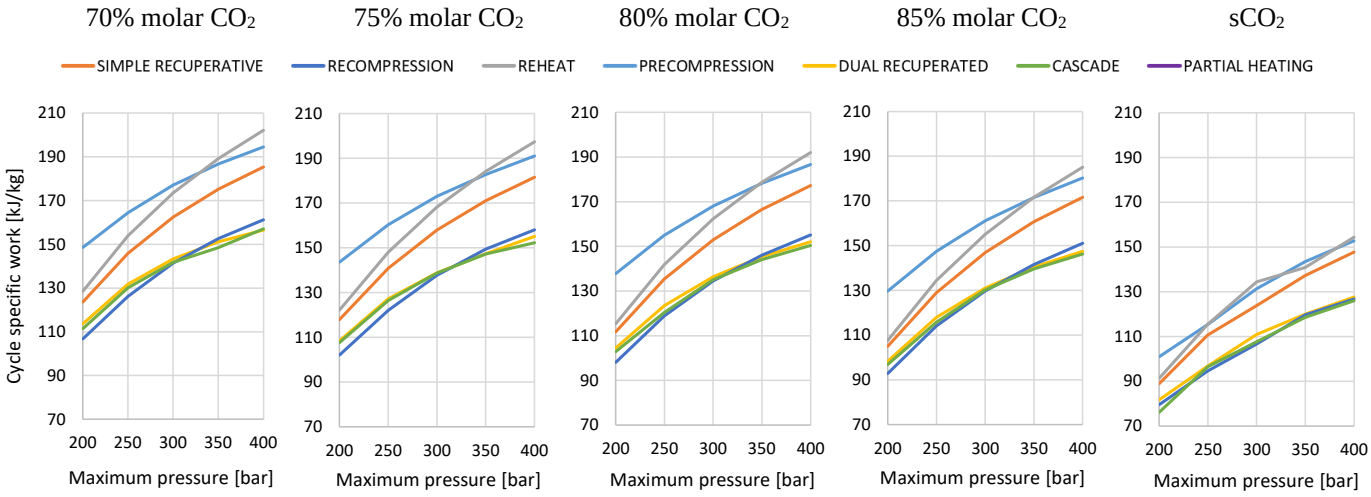

Figure 20. Cycle gross specific work for the various conditions considered, referring to the case study of Table 19

3.3.1 Cycle performance for a state-of-the-art power plant

Once the comparison between the characteristics of sCO_2 cycles and transcritical CO_2+SO_2 mixture cycles have been detailed, a more detailed analysis is proposed focusing on the most efficient molar composition, considering a CO_2 molar fraction of 85% in the CO_2+SO_2 mixture. In addition, the maximum pressure of the cycles is set at a state-of-the-art maximum value of 250 bar, representing the state-of-the-art of the CO_2-based power cycle technology, according to literature. Under these assumptions, the T-s diagrams of the power cycles considered are plotted in Figure 21: these T-s diagrams allow for a

comparison between the transcritical cycle working with the mixture and the sCO_2 cycle for each plant layout considered. In the diagrams the hot sources are also reported to illustrate the different heat introduction temperatures and the different cooling of the hot source for each configuration.

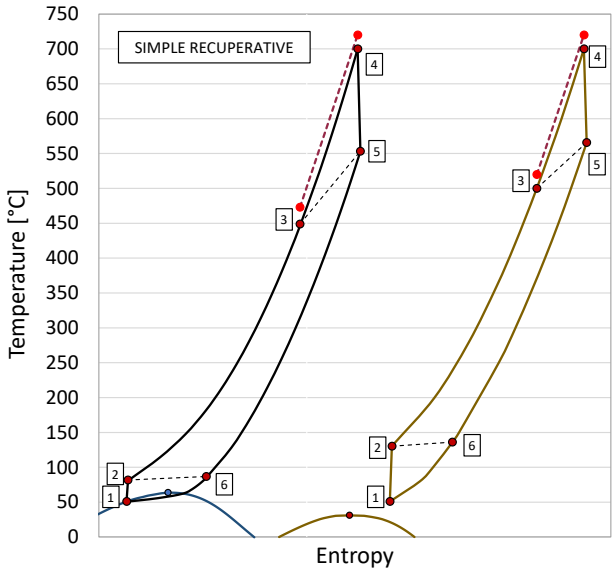

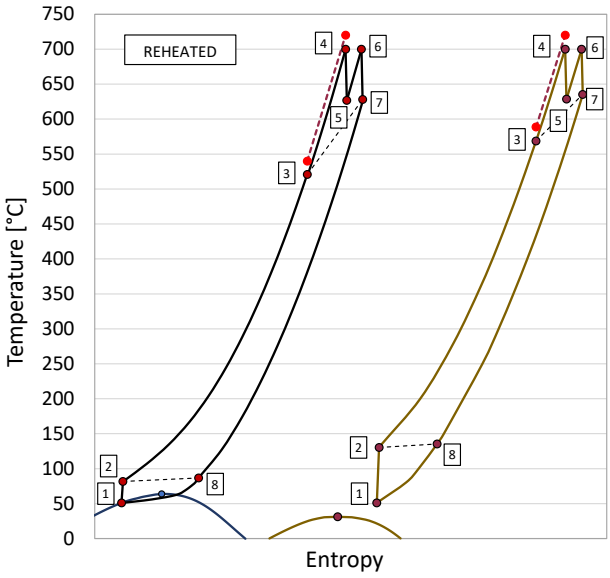

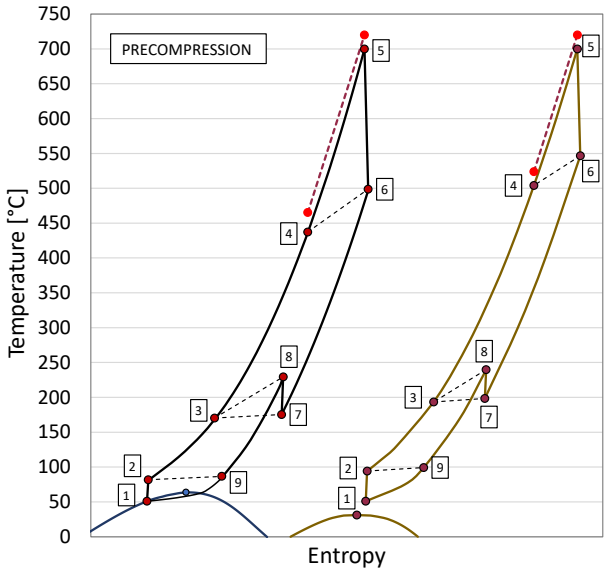

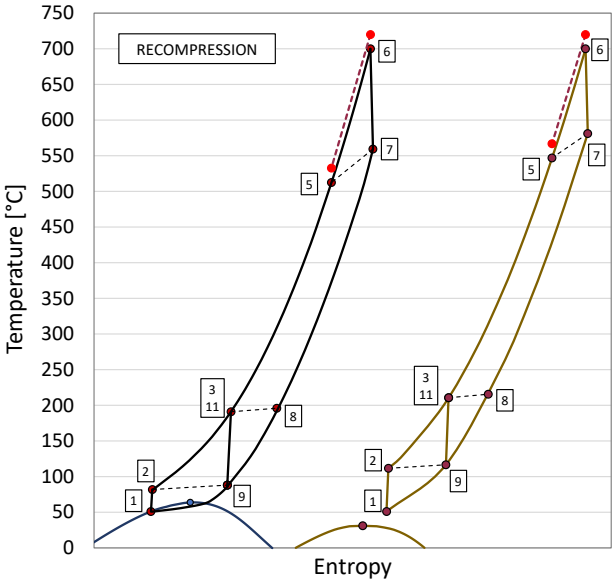

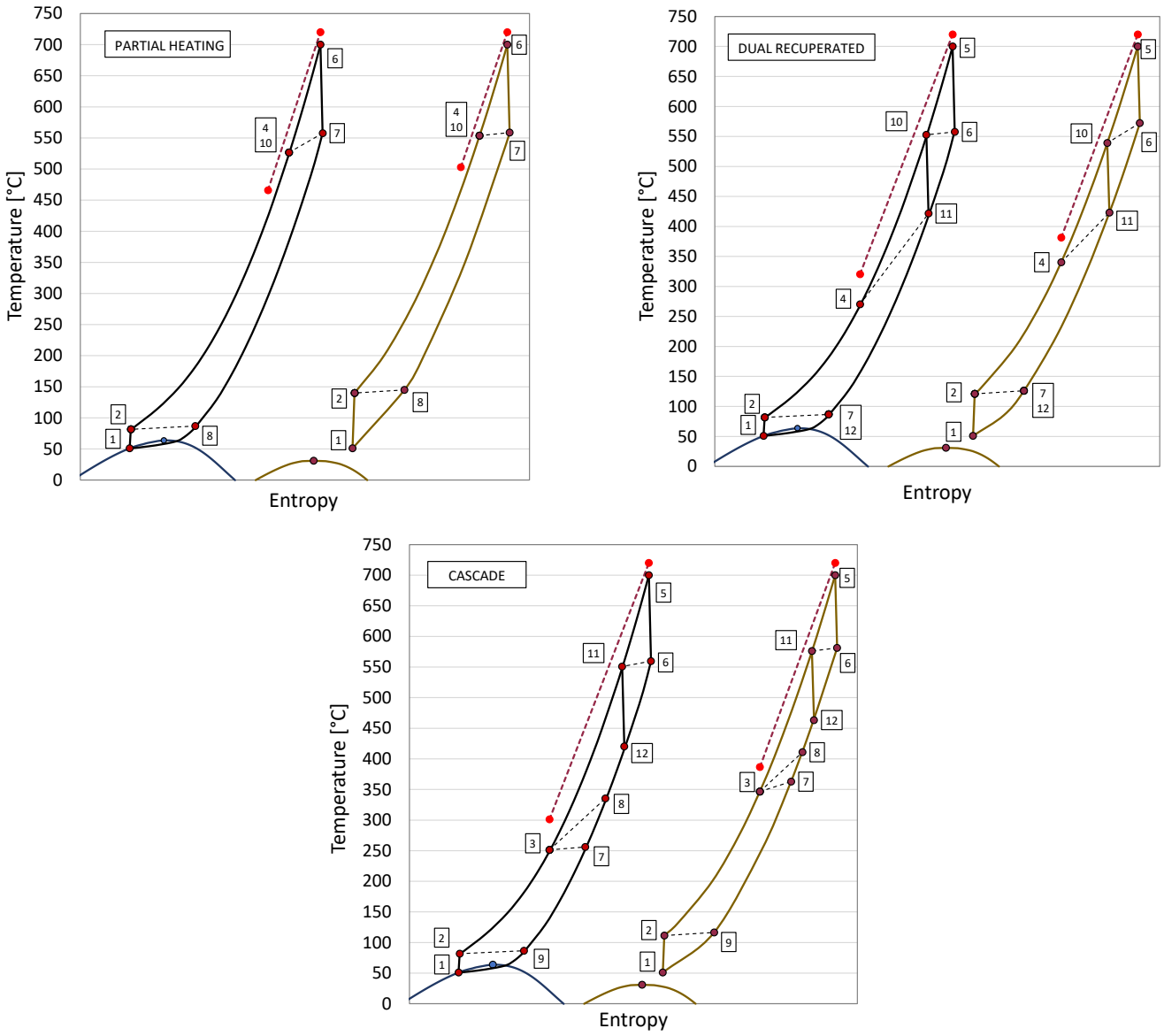

Figure 21. T-s diagrams of the selected CO_2+SO_2 mixture power cycles (left) and the respective sCO_2 cycles adopting the same plant layout (right). The dotted red line represents the hot source

In addition to the T-s diagrams, the power balance of the power cycles is reported in Table 20 and Table 21 for the innovative cycles working with the mixture and the sCO_2 cycles, respectively: the results are shown assuming 100 MW as reference cycle mechanical power.

According to the results, all cycle layouts that adopts the transcritical configurations with the CO_2+SO_2 mixture can achieve a higher net cycle efficiency than the respective sCO_2 cycles. Moreover, in case of CSP applications adopting solar towers, the net electric efficiency of the power plant would also account for the pump consumption of the HTF: this aspect is additionally beneficial for the configurations adopting the mixture, since all plant layouts

experience a higher temperature difference across the PHE and therefore a more limited mass flow rate of the HTF.

Table 20. Performance of the power cycles working with the CO_2 + SO_2 mixture under the assumptions of Table 19 and a maximum pressure of 250 bar

	Transcritical CO_2+SO_2 Cycle – 85% Molar CO_2 – P_{MAX} = 250 bar						
	Simple Recuperative	RH	Recompression	Precompression	Cascade	Partial heating	Dual recuperated
Cycle Efficiency [%]	43.62	44.66	50.84	46.94	41.02	43.62	41.41
Specific Work [kJ/kg]	129	134	114	147	116	129	118
UA_{PCHE}/Q_{IN} [1/K]	0.044	0.047	0.162	0.065	0.101	0.102	0.059
UA_{PHE} [MW/K]	9.32	11.4	9.17	8.49	7.3	11.78	7.40
Temperature at PHE inlet [°C]	453	521	513	437	251	-	270
Compression power [MW]	20.7	19.8	35.1	48.6	23.0	20.7	22.6
Expansion power [MW]	122.9	122.0	137.9	151.9	125.4	122.9	124.9
Heat rejected [MW]	132.1	126.6	99.5	116.7	147.1	132.2	144.8

Table 21. Performance of the sCO_2 cycles under the assumptions of Table 19 and a maximum pressure of 250 bar

	Supercritical CO_2 Cycle – P_{MAX} = 250 bar						
	Simple Recuperative	RH	Recompression	Precompression	Cascade	Partial heating	Dual recuperated
Cycle Efficiency [%]	44.01	45.11	48.79	46.57	41.34	44.04	41.10
Specific Work [kJ/kg]	111	115	95	115	97	112	97
UA_{PCHE}/Q_{IN} [1/K]	0.059	0.063	0.206	0.111	0.057	0.135	0.065
UA_{PHE} [MW/K]	11.7	11.3	10.6	11.2	8.6	11.75	8.6
Temperature at PHE inlet [°C]	501	569	547	504	347	-	340
Compression power [MW]	45.0	42.9	50.9	59.0	39.9	49.6	45.5
Expansion power [MW]	148.4	146.2	154.5	163.0	143.0	153.2	148.9
Heat rejected [MW]	131.4	125.6	108.7	119.2	146.3	131.5	148.1

3.4 Performance analysis of other tCO_2-mixtures power cycles

The previous chapter showed a methodology to define the most effective operating conditions of transcritical power cycles with a CO_2-based mixture, principally developing a wide sensitivity analysis on all the cycle characteristics. The performance of the cycles with the other CO_2-mixtures are mentioned in this chapter, without performing sensitivity analyses and only focusing on the comparison between the thermodynamic indicators of the innovative cycles and the ones of the sCO_2 recompression cycle.

The cycle simulations are carried out assuming the non-idealities from literature [93], analogous to the ones of Table 19, but with a cycle maximum pressure of 250 bar and adopting absolute values for the pressure losses (i.e. 4 bar

across the PHE, 2 bar on the condenser, 1 bar and 0.5 bar across all the recuperators on the low pressure and high pressure side, respectively).

According to the thermal stability of each dopant, the CO_2+C_6F_6 mixture is studied at cycle maximum temperatures of 550 °C, the CO_2+$SiCl_4$ mixture at maximum temperatures of 700 °C and the CO_2+C_2Cl_4 mixture is studied at 350 °C of cycle maximum temperature. The cycle simulations with the CO_2+C_2Cl_4 mixture can represent a retrofit of an existing first generation CSP plant (with thermal oil as HTF). The results related to the CO_2+$SiCl_4$ mixture refer instead to a next generation CSP plant and the ones of the CO_2+C_6F_6 mixture to a state-of-the-art CSP. Additional cycle simulations with other mixtures are proposed in Chapter 6, including the CO_2+C_4F_8 and the CO_2+C_2H_3N.

According to an analysis on the optimal power block layout, the precompression cycle is proposed for the CO_2+$SiCl_4$ mixture and the CO_2+C_6F_6 mixture, while the simple recuperative cycle is considered both for the CO_2+C_6F_6 and the CO_2+C_2Cl_4 mixture, emphasizing the cycle performances in the most simplified configuration.

The results of Table 22 offer a synthetical overview of the innovative cycle performances. Moreover, the graphical trends in Figure 22 are shown to provide an insight on the sensitivity of the cycle efficiency on the molar composition and the pressure at turbine outlet for the precompression layout, a plant layout with two variables of optimization. The performance of the precompression cycle is evaluated at a maximum pressure coherent with the technological limits of this technology: even if a previous work of Rodriguez De Arriba presented a flat trend in terms of cycle efficiency with the maximum pressure [91], a high value of maximum pressure is preferrable at design conditions to allow for a wider flexibility during off-design operation, when the cycle maximum pressure reduces.

Table 22. Subset of the possible combinations of tCO_2-mixtures and power blocks for efficient innovative cycles

	sCO_2	**CO_2 + C_6F_6**	**CO_2 + C_6F_6**	**CO_2 + $SiCl_4$**	**CO_2 + C_2Cl_4**
CO_2 molar fraction [%]	100	87	88	82	88
Cycle layout	Recompressed	Simple Rec.	Precompressed	Precompressed	Simple Rec.
Maximum temperature [°C]	550	550	550	700	350
Gross cycle efficiency [%]	42.6	42.0	43.3	48.9	32.4
Specific work [kJ/kg]	71.3	82.1	87.5	109.0	49.8
UA_{PCHE}/Q_{IN} [1/K]	0.195	0.140	0.182	0.126	0.218
Temperature at PHE inlet [°C]	416	402	396	479	229
Working fluid ΔT_{PHE} [°C]	134	148	154	221	121
Cycle minimum pressure [bar]	110	84	86	76	89
Compression power [MW]	52.7	24.6	43.8	37.8	39.4
Expansion power [MW]	152.7	124.6	143.8	137.8	139.4
Heat rejected [MW]	134.6	138.1	131.1	105.0	208.5

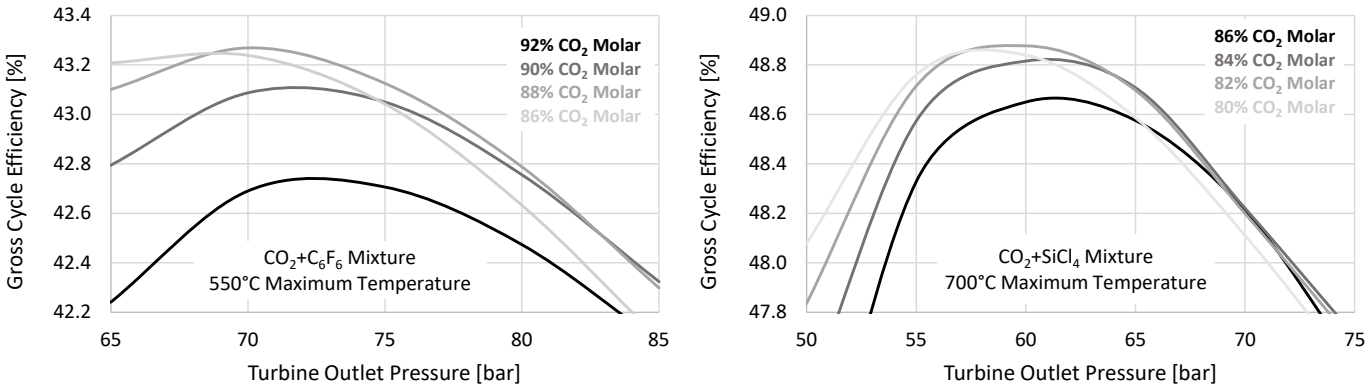

Figure 22. Details on the sensitivity analysis performed for the precompressed cycles: variable mixture composition and turbine outlet pressure

In the next chapters the core of this work will be discussed, proposing a methodology to describe the sizing of each component of the innovative power cycles, their off-design behavior and their integration in a CSP plant, proposed as a reference application for high temperature cycles.

Not all the mixtures are considered in the analyses of the next chapters. Nevertheless, even if with a limited pool of case studies, the results of Table 22 aimed at showing that most of the innovative working fluids present interesting characteristics to be exploited in power cycles.

4. Modelling of cycle components

After the impact of the innovative working fluids on the cycle performance, the methodology adopted for the design of the cycle components is the most relevant issue to investigate while dealing with CO_2-mixtures in power cycles.

As a matter of fact, since tCO_2-mixtures power cycles cover the same pressure ranges of sCO_2 cycles and present flows in single-phase across most of the cycle components and the piping connecting the cycle components, the methods adopted for the design and off-design of the components of sCO_2 cycles can be extended to tCO_2-mixtures cycles with a few exceptions, especially during mixture condensation.

An overall qualitative description of the methodology adopted for the characterization of all cycle components with in-house MATLAB models is proposed in Figure 23. At first, the thermodynamic and transport properties of the mixtures are computed as presented in Chapter 2, for the mixture of interest in this work, and are provided to the MATLAB routines in the form of a set of isobaric lookup tables, with a fine resolution both in temperature and pressure.

With the database of all thermodynamic and transport properties, the heat exchangers of the power cycles are characterized in dedicated MATLAB models, including the recuperator, the primary HX and the condenser. The turbine of the cycles is not modelled within this work, but it is possible to refer to the methodology developed by the SCARABEUS partners at City University of London, in partnership with this work for the case study discussed in Chapter 8. In addition, a case-specific definition of the pump and its behavior is not provided in this work, as the author relies on some preliminary performance maps provided by industrial partners of SCARABEUS.

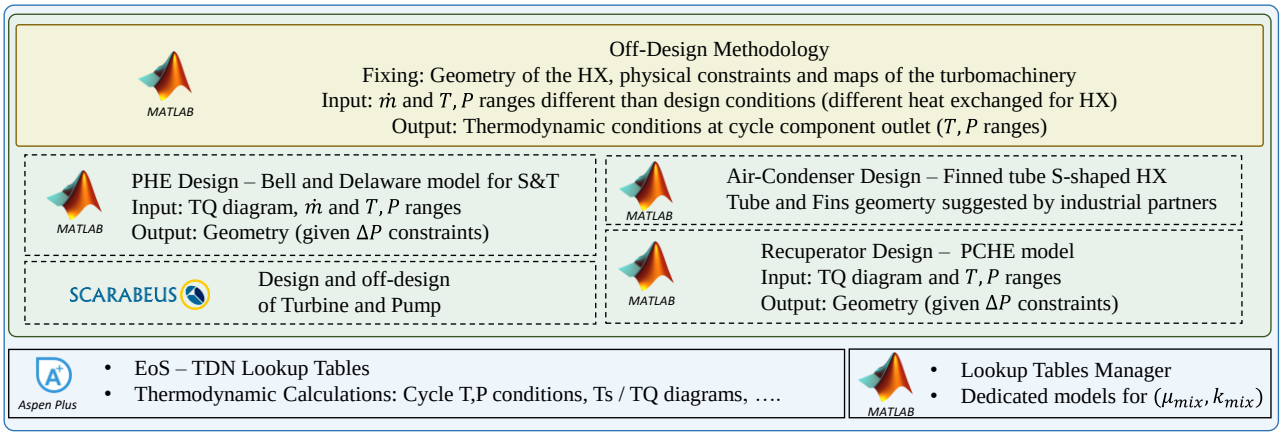

Figure 23. Overview of the design and off-design modeling of the power cycle components

The methodology adopted in the design of the cycle components, particularly for heat exchangers, is commonly proposed in literature: the geometry of the HX is initially determined assuming the conditions of the power cycle at design point (at the highest minimum temperature of the cycle and at design thermal input), afterwards the components geometry is fixed and used as input for the off-design MATLAB routines of the same power cycle components. The off-design MATLAB models of the HX are developed according to the mathematical formulations of the same models at design conditions, by exchanging some of the inputs with some of the outputs.

With respect to a large fraction of the literature works describing off-design performances of power cycles, this work does not exploit scaling laws or power laws for the estimations of the overall HTC: all the HXs are instead solved in off-design conditions along the whole geometrical domain discretized in the 1-D model.

4.1 Convective heat transfer coefficients and frictional pressure drop models for mixtures

An accurate modelling of the thermodynamic and transport properties of the innovative mixtures is crucial for modelling of the cycle components as much as the use of the appropriate convective heat transfer coefficient (HTC) correlations and models for frictional pressure drops (ΔP) across the heat exchangers.

While dealing with sCO_2 or tCO_2-mixtures in power cycles, the working fluids always develop a so called “in-tubes” or “in-channels” flow field, as plate HX are normally not considered for these applications, and shell and tubes adopts always the HTF or storage fluid on the shell-side, leaving the tube side to the working fluid.

Accordingly, the gathering of HTC and ΔP correlations for tCO_2-mixtures power cycles can be concentrated in in-tubes HTC and ΔP models for mixtures in single phase condition, and in-tubes HTC and ΔP models for mixtures in VLE conditions. Only for the single-phase region, given the very similar pressure levels and the same HX geometries, the models for pure carbon dioxide in sCO_2 cycles are directly adopted and their validity extended to mixtures.

- The in-channel convective HTC of CO_2-mixtures in single phase condition is computed according to the Gnielinski correlation [94], proposed in Equation (14), with the respective heat transfer coefficient friction factor (f_{HTC}) of Equation (15), as the validity of the correlation for sCO_2 has been underlined multiple times in literature and it represents the gold standard for 1-D solutions of HX [4].

$$Nu_{,i} = \frac{\frac{f_{HTC,i}}{8} \cdot \left(Re_{,i} - 1000\right) \cdot Pr_{,i}}{1 + 12.7 \cdot \left(Pr_{,i}^{\frac{2}{3}} - 1\right) \cdot \sqrt{\frac{f_{HTC,i}}{8}}} = HTC_{,i} \cdot \left(\frac{D_{hydr}}{k_{,i}}\right) \tag{14}$$

$$f_{HTC,i} = \left(\frac{1}{1.82 \cdot Log_{10}\left(Re_{,i}\right) - 1.64}\right)^2 \tag{15}$$

- The in-channel single phase frictional pressure drops ΔP for mixtures are also computed with conventional models. The Darcy-Weisbach equation, presented in Equation (16), is proposed in this work with the respective friction factor relative to the pressure drop (f_{DP}) of Equation (17) expressed according to the form of Chen, since it has the accuracy of the Colebrook-White correlation but it is explicit in the friction factor.

$$\Delta P_{,i} = \frac{f_{DP,i}}{2} \cdot \frac{L_{,i}}{D_{hydr}} \cdot \rho_{,i} \cdot V_{,i}^2 \tag{16}$$

$$\frac{1}{f_{DP,i}} = -2 \cdot Log_{10}\left[\frac{\epsilon}{D_{hydr} \cdot 3.7065} - \frac{5.0452}{Re_{,i}} \cdot Log_{10}\left(\frac{1}{2.8257} \cdot \left(\frac{\epsilon}{D_{hydr}}\right)^{1.1098} + \frac{5.8506}{Re_{,i}^{0.8981}}\right)\right] \tag{17}$$

- The in-channel convective HTC for mixtures in two-phase conditions is computed adopting the model of Cavallini [95], that includes a transition criterion covering all possible flow regimes during condensation of pure fluids and azeotropic mixtures in smooth tubes. The two possible flow regimes are defined by Cavallini as "ΔT dependent" and "ΔT independent", as function of the difference in convective HTC between the upper and lower part of the same cross-section of the channel where the condensation of the two-phase mixture occurs. Since this work analyses zeotropic mixtures, the Bell and Ghaly [96] resistance is included in the calculation of the internal heat transfer coefficient of Cavallini, as reported in literature [88] and suggested in the Cavallini model itself [95].

  The convective HTC model is validated by Cavallini with high accuracy on more than 1000 experimental data of various zeotropic

mixtures. In addition, within the SCARABEUS project, the HTC model has been validated with good accuracy on three sets of experimental data of a condensing mixture (the CO_2+R1234ze(E) mixture, representing a generic CO_2-based working fluid). The results of the experimental validation are presented in Figure 24: while the experimental data (on the x-axis in the figure) have been measured by partners of the SCARABEUS project in TUW (in Wien, Austria), the numerical validation (on the y-axis in the figure) has been carried out within this work, representing a validation of the Cavallini model on a CO_2-mixture with a very low average error of 5.34%. Additional details about this experimental validation can be found in the respective literature work [88].

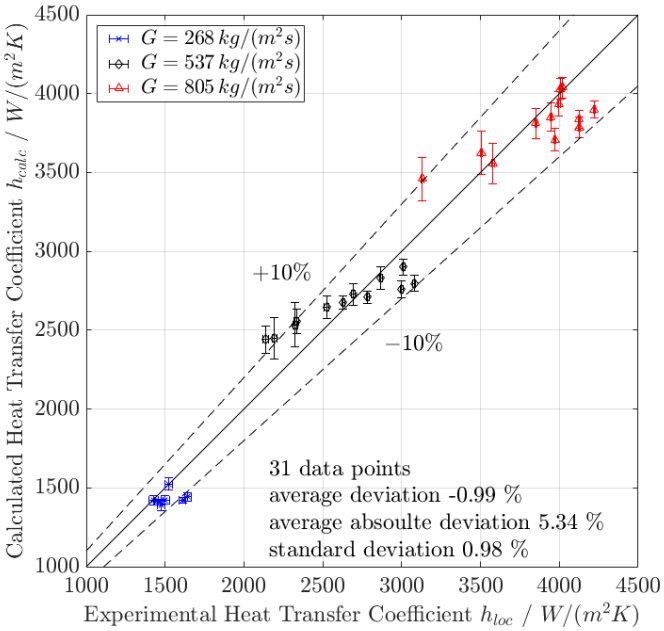

Figure 24. Comparison of the experimental convective internal HTC of the CO_2+R1234ze(E) mixture with the Cavallini model [88]

- The in-channel frictional ΔP for mixtures in two-phase conditions are computed with the model of Del Col [97]. In principle the model is an updated version of a previous frictional model by Cavallini [98] that was developed for mini channels (with diameters lower than 3 mm). However, since it is reported in literature that the predictions of the Del Col model were also in good agreement with experimental ΔP data in macro tubes (showing an average deviation of -7 %), the Del Col model is adopted in this work.

4.2 Air cooled condenser sizing

The first numerical model examined in this work for the analysis of the HXs of the innovative cycles is the one related to the air-cooled condenser.

The HX geometry is represented with an S-shaped tube, where the heat exchange between the air and the working fluid side occurs crossflow: the air flow is developed along a single direction and the mixture flows through a series of 7 rows, as evidenced in the representation of the tube layout of Figure 25. The tube is externally finned, and it has the characteristics reported in Table 23 (suggested by an industrial partner of the SCARABEUS project [88]).

Of the whole full-scale air-cooled condenser of the tCO_2-mixture power cycle, only a single tube is simulated in the 1-D MATLAB tool, since it is considered representative of all the others. In fact, even if it is assumed that the HX is composed by multiple tubes, all of them identically exchange heat and experience pressure drop on both the air and the working fluid side.

Table 23. Characteristics of the finned-tube air-cooled condenser

Tube characteristic	Value
Tube internal / external diameter [mm]	20.76 / 26.8
Number of pass / number of rows per tube	7 / 7
Tube disposition	Staggered
Longitudinal / transversal tube pitch [mm]	57.7 / 66.7
Fin type	Circular and flat
Fin spacing / height [mm]	2.52 / 15.9
Fin thickness [mm]	0.3
Porosity of the tube banks [%]	82.7
Fin efficiency [%]	77.5
Area ratio (AR) [-]	27.3
Tube material	Carbon steel
Fin material	Aluminum 1100-annealed

In the code, each row is discretized into 20 cells (and 21 nodes): across each cell the overall HTC, U, is computed relative to the external area, accounting both for the effects of the internal and the external convective resistance, along with the conductive one. The expression for the overall HTC is shown in Equation (18), where AR is the area ratio (the ratio between the external area, in contact with the air, and the internal one, in contact with the working fluid):

$$U_{cell} = \left[\frac{1}{HTC_{IN,cell} \cdot AR} + \ln\left(\frac{d_{ext}}{d_{int}}\right) \cdot \frac{d_{int}}{2 \cdot k_{steel} \cdot AR} + \frac{1}{HTC_{EXT,cell} \cdot \eta_{surf,FIN}} \right]^{-1} \quad (18)$$

In the calculation of the internal HTC with the Cavallini model already presented, the MATLAB tool reads from the lookup tables all the thermodynamic and transport properties necessary to the model from the value of temperature and pressure at the center of each cell.

Regarding the external HTC, on the air side, its value is computed with the Grimison correlation for staggered tubes [99]. Finally, the air side pressure drops are evaluated according to the Marković correlation [100], tailored to this specific configuration of a bank of staggered tubes. The air side pressure drop model has been also compared with the Robinson and Biggs model [101], specific to the fin geometry, showing deviations lower than 5% across all the range of interest.

In the calculation of both the HTC and the pressure drop on the air side, the maximum velocity of the air across the tube banks is computed. For this purpose it is necessary to compute the porosity of the tube bank according to Marković [100], reported in Table 23.

An overview of the MATLAB model adopted for the design of the condenser is shown in Figure 25. For the condenser design, the inputs of the condenser model are, in addition to the geometry of the tube and the fins of Table 23, the mass flow rate, the temperature and the pressure range on the working fluid side. The sizing is carried out at given values of ambient temperature and air face velocity, being the latter a parameter that influences both the convective HTC on the air side and the electric consumption of the fans.

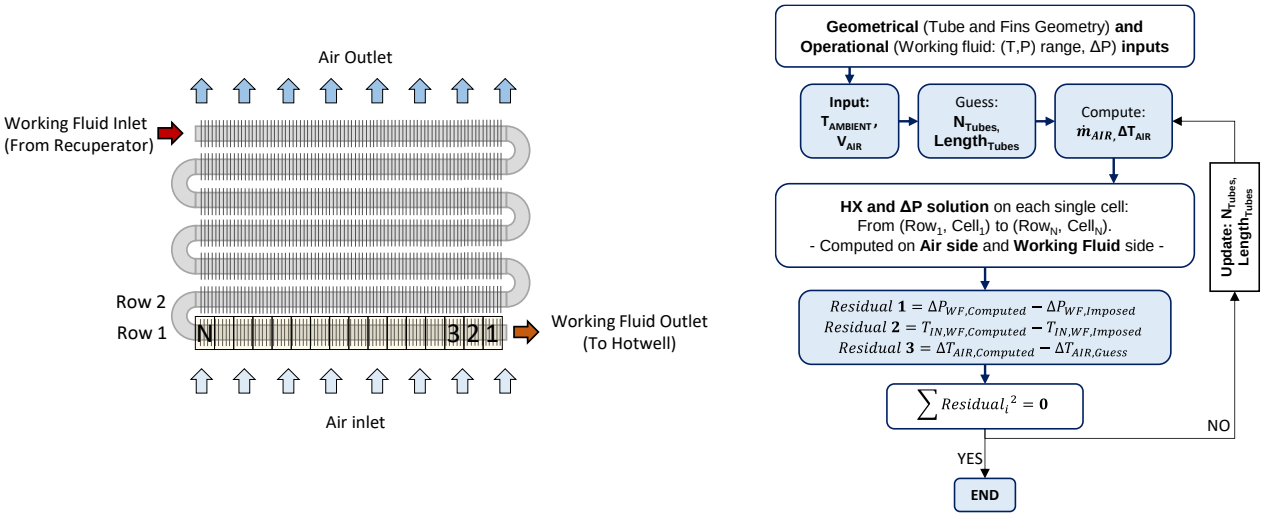

Figure 25. Methodology for the design of the finned tube of the air-cooled condenser of the power cycle

The condenser is solved iteratively for each finite volume starting from the coldest cell (at working fluid outlet), at a known temperature of both the air and the working fluid, up to the cell where the working fluid has the highest temperature, countercurrent with respect to the direction of working fluid.

In order to solve the heat balance of each cell between the air side and the working fluid side, the actual heat exchanged across the finite volume is computed accounting for the effectiveness of the cell ϵ_{cell}, defined as in Equation (19) by Navarro and Cabezas-Gomez [102]:

$$\epsilon_{cell} = 1 - \exp\left\{\frac{NTU_{CELL}^{0.22}}{CR_{cell}} \cdot [\exp(-CR \cdot NTU_{cell}^{0.78}) - 1]\right\} \quad (19)$$

The tube is solved iteratively up to convergency on the imposed i) pressure drop of the working fluid, ii) inlet temperature of the working fluid and iii) air temperature difference. The MATLAB model updates the guessed values of the overall condenser geometry (overall number of tubes and length of the tube) exploiting the *fsolve* function, converging on all the three residuals.

Once the model reaches convergency, the outputs are represented by the number of tubes (of which only one is simulated) and their length: along the tube, the model provide a complete 1-D characterization of all the thermodynamic properties of both fluids, including the two convective HTC and the heat exchanged across each finite-volume.

4.2.1 Air cooled condenser off-design

In order to compute the off-design of the air-cooled condenser, similarly to its design, all the characteristics of the flow on the working fluid side must be given as input (mass flow rate, inlet and outlet temperature, pressure range), and, at given tube geometry, the air flow field is simulated for any ambient temperature and air velocity. The flowchart in Figure 26 shows the methodology adopted to use the MATLAB code of the design of the condenser also for off-design simulations, with only marginal variations.

Guessing air face velocity at the given ambient temperature, a single run of the code is sufficient to compute the whole geometrical domain, understanding whether the temperature profile of the working fluid matches with the input. Accordingly, having a single degree of freedom (the air velocity) instead of two (the length of the tubes and the overall number of tubes), the off-design version of the condenser model is faster than the design code, from a computational point of view.

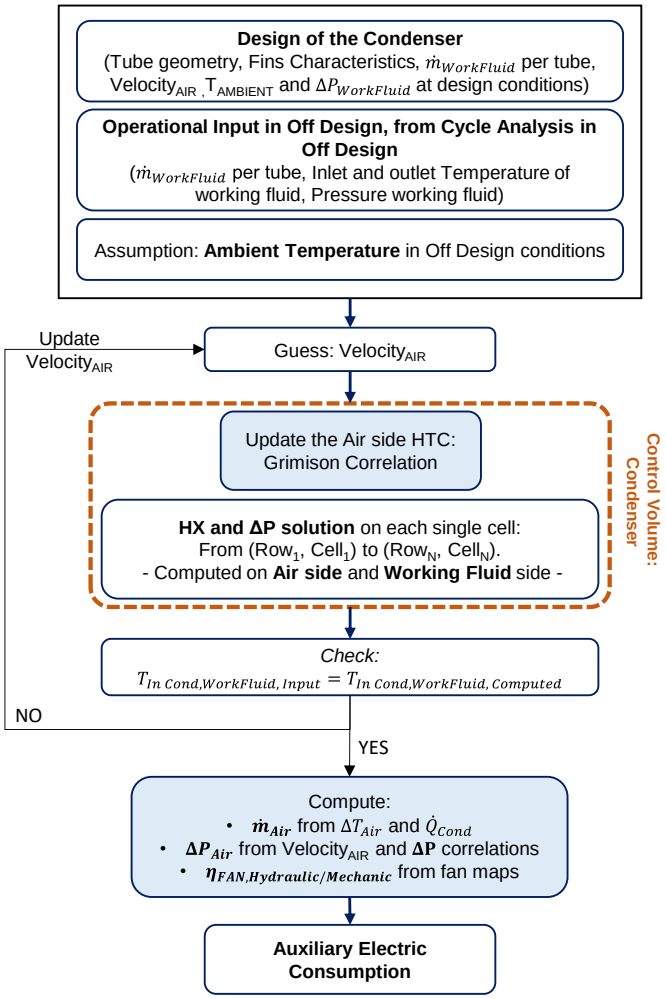

Figure 26. Methodology for the off-design modelling of the air condenser

A summary of the inputs and outputs of the MATLAB models of this work for the air-cooled condenser of tCO$_2$-mixtures cycles is proposed in Table 24.

Table 24. Inputs and outputs of this work models for the air-cooled condenser

Parameter	Air-Condenser Design	Air-Condenser Off-Design
Working fluid temperature at inlet / outlet	Input	Input
Working fluid pressure at inlet	Input	Input
Working fluid mass flow rate	Input	Input
Working fluid pressure drop	Input	Output
Air temperature	Input	Input
Tubes number and tubes length	Output	Input
Air face velocity	Input	Output
Air temperature difference	Output	Output
Air mass flow rate and pressure drop	Output	Output

Finally, the pressure losses on the air-side computed on this tube and fins geometry and the specific seven loops bank of staggered tubes are proposed in Figure 27, representing useful data for the calculation of the condenser auxiliary consumption, reported in Figure 26.

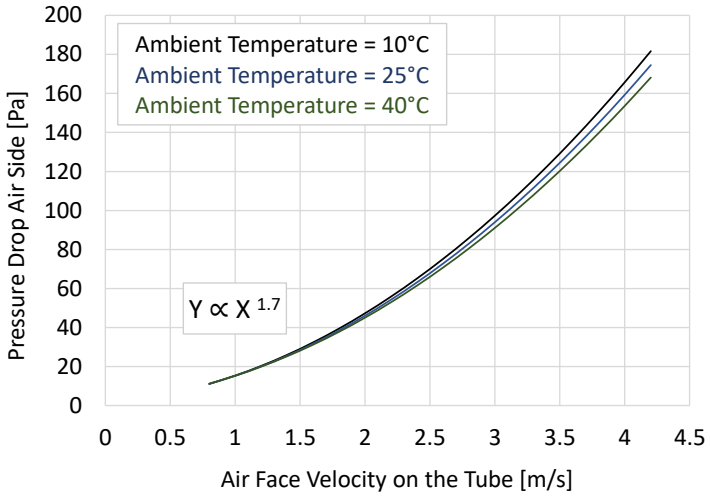

Figure 27. Air-side pressure losses on the air-cooled condenser in off-design computed for any air face velocity with literature models [100]

4.2.2 Model comparison with Xace® industrial tool

The MATLAB model of the condenser is compared in this chapter with a tool (Xace®) adopted by an industrial partner of the SCARABEUS project [88], on a tube geometry different than the one proposed in this work in Figure 25. The tube configuration proposed by the partner is shown in Figure 28 and it comprises of 7 rows, but only 3 passes: therefore the working fluid is equally splitted in three rows, twice, before mixing the flow and passing through the last row. This way, according to the SCARABEUS partner, the pressure drop at the working fluid side can decrease. The comparison of the MATLAB code and Xace® is developed at same thermodynamic and transport properties, provided as lookup tables by the author of this work to the industrial partner [88].

A full condenser is assumed at design conditions, condensing the flow from the dew point to the bubble point. Figure 28 provides the temperature and pressure range of the case study, adopting the CO_2+C_6F_6 mixture with 92% molar fraction of CO_2. Even if this mixture composition and condensation process is not representative of an efficient power cycle, it was selected by the author to model a case with a limited glide and a temperature of 51 °C at bubble point, a condensation close to the critical point for a cycle power of around 100 MW_{el}.

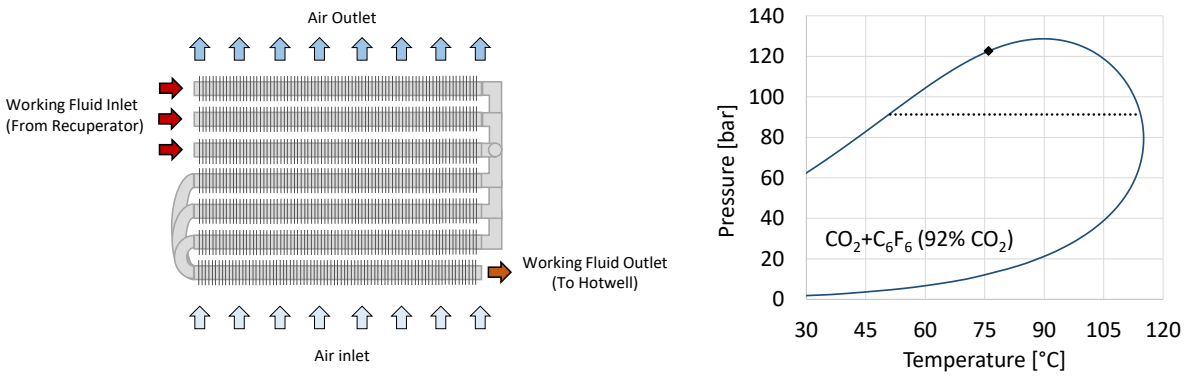

Figure 28. Tube layout of the air-cooled condenser defined by the partner of SCARABEUS (left), condensation for the case study in the P-T diagram (right)

According to internal calculations of the software Xace®, the value suggested for the air face velocity (i.e. the air velocity hitting the finned tube) in this condition is 3.23 m/s, and the value is assumed for the MATLAB model, accordingly [88]. As the validation compares two different software, different combinations of inputs and outputs are considered, shown in Table 25.

Table 25. Comparison of the I/O of the two air-cooled condenser models

Parameter	MATLAB	Xace®
Heat duty	Input	Input
Working fluid mass flow rate	Input	Input
Working fluid temperature inlet / outlet	Input	Input
Tube and fins geometry	Input	Input
Length and number of tubes	Output	Input
Ambient temperature and air face velocity	Input	Input
Air outlet temperature	Output	Output
Working fluid pressure drop	Input	Output
HTC	Output	Output

The result of the comparison is proposed in Table 26: the MATLAB model has been run in order to have an air outlet temperature similar to the one of the commercial software, eventually increasing its value in case of a lower heat transfer area (and therefore air passage area) computed, to enforce the air side mass conservation equation.

Table 26. Comparison on the validation case of the air-cooled condenser model from this work and the commercial software [88]

Parameter	MATLAB	Xace®
Working fluid (condensing mixture)	CO_2+C_6F_6 (92% molar CO_2)	
Heat duty [MW_{th}]	236	
Working fluid mass flow [kg/s]	1200	
Working fluid temperature range [°C]	From 114 to 51	
Working fluid pressure at inlet [bar]	91	

Air face velocity [m/s]	3.23	
Working fluid pressure drop [bar]	0.46	
Air ambient temperature [°C]	36	
Air outlet temperature [°C]	59.5	59.0
Number of tubes [-]	2030	2242
Length of the tubes [m]	135	128.1
Length of the pass [m]	19.3	18.3
External HX area [m^2]	487 800	499 500
Overall HTC [$W/m^2/K$]	23.0	21.6

The deviation between the results of the two models is very limited: the relative deviation on the computed area is only 2.3 %. Nevertheless, the higher deviation in tube length (around 5.4 %) and number of tubes (around 9.5 %) evidences the effect of the different HTC and pressure drop models: as a matter of fact, the two effects are almost balanced between each other and their opposite contributions tend to make the results comparable, since the relative error on the area is well below the one on tube length and number of tubes.

While dealing with commercial closed-source software, it is not immediate to retrieve the numerical models adopted. For this reason, even if accounting for the same thermodynamic and transport properties (given as input), the embedded models for HTC of both the working fluid and the air side certainly play a role. Nevertheless, the comparison has produced satisfactory results.

4.3 Recuperator (PCHE) sizing

The methodology proposed to model recuperators for the power cycles investigated relies on the Printed Circuit Heat Exchanger (PCHE) with standard straight semicircular channels as recuperators technology, in accordance with the first work of Dostal [8] on sCO_2 cycles and all the successive literature.

Thus, a single pair of channels (one on the hot and low-pressure side, the other in the cold and high-pressure side) is modelled and considered representative of all the channels in the PCHE, as the influence of a mass flow rate variation in the channel directly impacts the heat transfer coefficient and the frictional pressure drops along the channel. Table 27 includes all the main design parameters of the PCHE, assumed considering literature values of all the values among the sCO_2 cycles field [103], and Figure 29 shows a frontal view of two pairs of channels for representation purposes.

With respect to the available literature works on sCO_2 power cycles, in this work the classic PCHE 1-D model of Dostal is extended to characterize condensing flows at the low-pressure side of the recuperator, introducing the models for two-phases mixtures convective heat transfer coefficients and pressure drop.

The geometry of both channels is discretized along the axial direction with a finite volume approach, and the overall HTC for the PCHE for each axial section considered, U_i, includes the cold and hot side convective heat transfer coefficients but also the conductive term, as proposed in Equation (20).

$$U_i = \left(\frac{1}{HTC_{i,hot}} + \frac{1}{HTC_{i,cold}} + \frac{T_{thickness}}{k_{metal}} \right)^{-1} \tag{20}$$

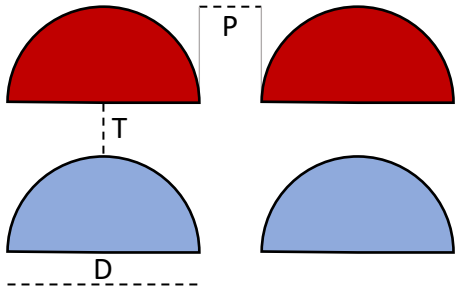

Figure 29. Two pairs of channels of the PCHE (frontal view)

Table 27. Characteristics of the PCHE for sCO_2 cycles from literature

PCHE characteristic	**Value**
Channel diameter [mm]	2
Plate thickness [mm]	0.5
Pitch between channels (center-to-center) [mm]	2.4
Internal surface roughness [mm]	0.01
Material	Stainless Steel 316
Material thermal conductivity [W/m/K]	15

The design of the PCHE is carried out given the mass velocity for each channel as input. Across each finite volume, the energy balance equation and the heat exchanger constitutive equation are solved simultaneously, after the calculation of the HTC. By means of a numerical solver, the code iterates on the in-channel mass velocity until it converges to the desired pressure drops. The main outputs of the code are the channels length, the overall number of channels and the axial profile of the main thermodynamic and heat transfer variables, including the heat transfer coefficients, the velocities, the densities and the pressure drop.

A more detailed description of the MATLAB model for the PCHE is provided in Figure 30, focusing on the model adopted to provide the design of the HX. In the design procedure, once the inputs are determined (including the channel geometry except for its length, the temperature and pressure profiles of the working fluid on both sides), the code assumes an initial mass velocity in the channels to run the first simulation. Then, the numerical domain is discretized in hundreds of finite-volumes at constant heat exchanged (i.e. enthalpy difference across the finite volumes). Once to each finite volume is associated a value of enthalpy and pressure, by means of look up tables (L.U.T) its temperature is found ($T = f(h, P)$), along with all the other thermodynamic and transport properties associated to these values of temperature and pressure ($Properties = f(T, P)$).

Then, again by means of lookup tables (having the temperature and pressure profile along all the finite volumes), the location of the dew point of the mixture at the low-pressure side (hot side) is identified, so that every finite volume can be characterized by the phase of the working fluid flowing (either in single phase or in VLE). If the mixture selected as working fluid does not present any phase-change behavior across the PCHE, this intermediate step is not performed.

Finally, the internal convective HTC and the frictional pressure drop are computed across both channels along the axial direction, adopting the appropriate models depending on the working fluid phase condition as mentioned in Chapter 4.1. Once each finite volume is characterized by the two convective HTCs, the overall HTC, U_i, is computed according to Equation (20) and the constitutive equation is solved directly, returning the value of the axial length of each finite volume, inversely proportional to the temperature difference between the two sides of the HX. The pressure drop along the channels is finally included, numerically, and eventually the code is run again, if the overall pressure drop is different than the target value, with an updated value of the working fluid mass velocity.

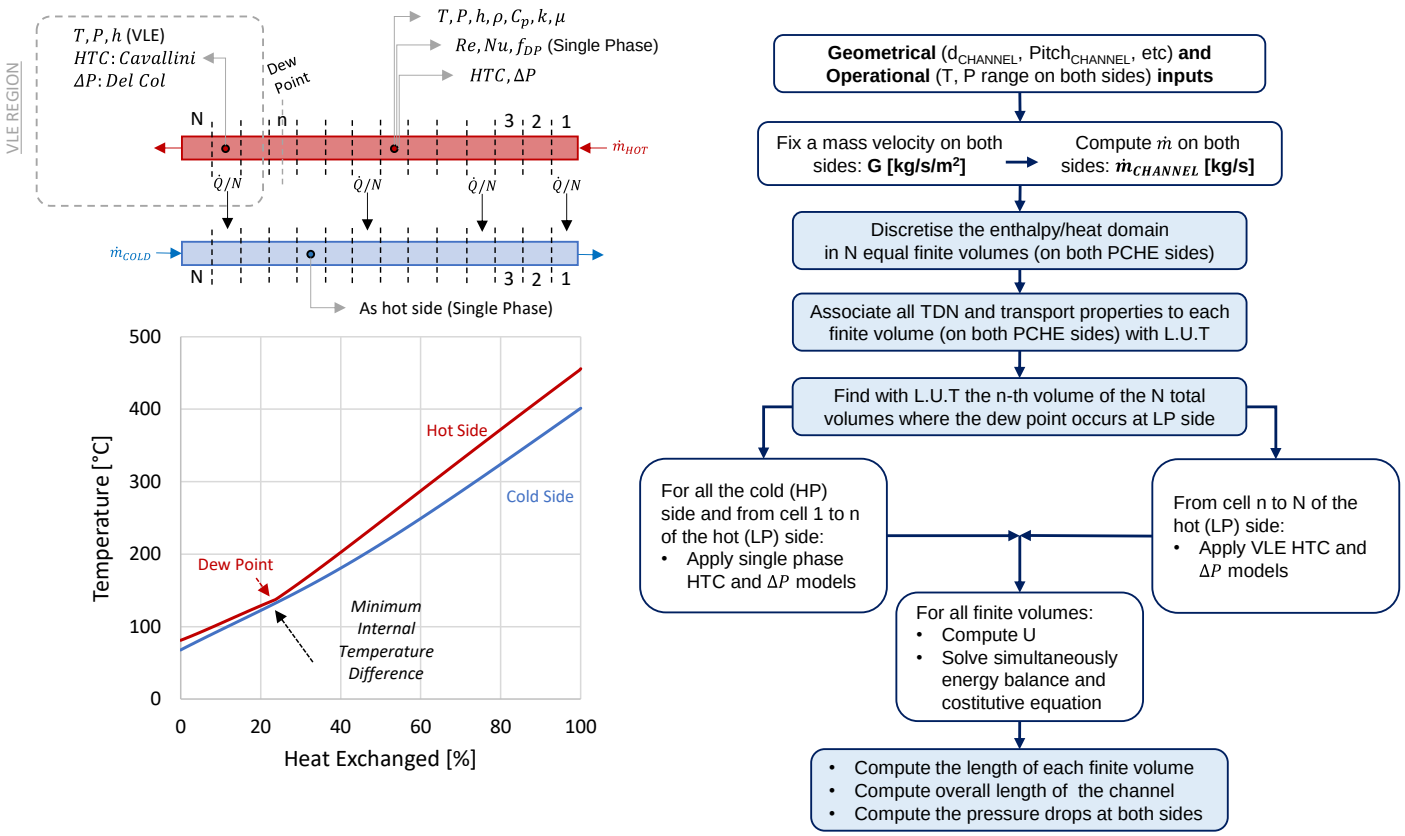

Figure 30. Methodology for the design of a PCHE with the low-pressure side occurring in the VLE region for a part

4.3.1 Recuperator (PCHE) off-design

The flowchart proposed in Figure 31 points out the methodology adopted by the MATLAB model for the PCHE off-design described in this work.

With respect to the MATLAB routine for the design of the PCHE, which discretizes the axial domain of both channels into many finite volumes according to the T-Q diagram (i.e. at constant enthalpy difference across all the finite volumes), in the off-design model of the PCHE the overall length of the channel is known and given as an input. As a consequence, the two channels are discretized in many finite volumes according to their length into finite volumes at constant geometrical dimension, but different values of heat exchanged.

The model assumes as inputs the mass flow rates of the working fluid in the channels, the pressure of the working fluid on both sides of the HX and two temperatures: the inlet temperature on the hot side ($T_{max,Hot}$) and the inlet temperature of the cold side ($T_{min,Cold}$), which, for example, is at the outlet of the pump in a simple recuperative cycle. A third temperature, the outlet temperature

of the cold side ($T_{max,Cold}$), must be initially assumed, as convergency must be reached on $T_{min,Cold}$ by varying $T_{max,Cold}$.

As for the design of the PCHE, in off-design the MATLAB model starts solving the channel from the hot end of the PCHE, where only single-phase correlations for HTC and pressure drops are adopted, down to the cold part.

The model can directly compute the dew temperature of the mixture at the pressure of the hot side of the HX, adopting look up tables in a single query.

For each finite volume, at known area, the heat balance and the constitutive equations are solved simultaneously, by computing outlet conditions of the cells (both at hot and cold side) knowing the mass flow rates and the overall HTC.

The procedure is carried out both for the single-phase region and the region where VLE occurs at the low-pressure side, up to the solution of the whole channel.

When convergency is reached on the $T_{min,Cold}$, also $T_{min,Hot}$ is computed, along with all the axial trends of the variables of interest (thermodynamic properties, Reynolds number, HTCs, etc…), and the pressure drop along the two channels can be computed by a direct numerical integration. In case the pressure drop computed along the channel deviates from the values initially assumed, a final and external iteration loop can be run, up to convergency on that value.

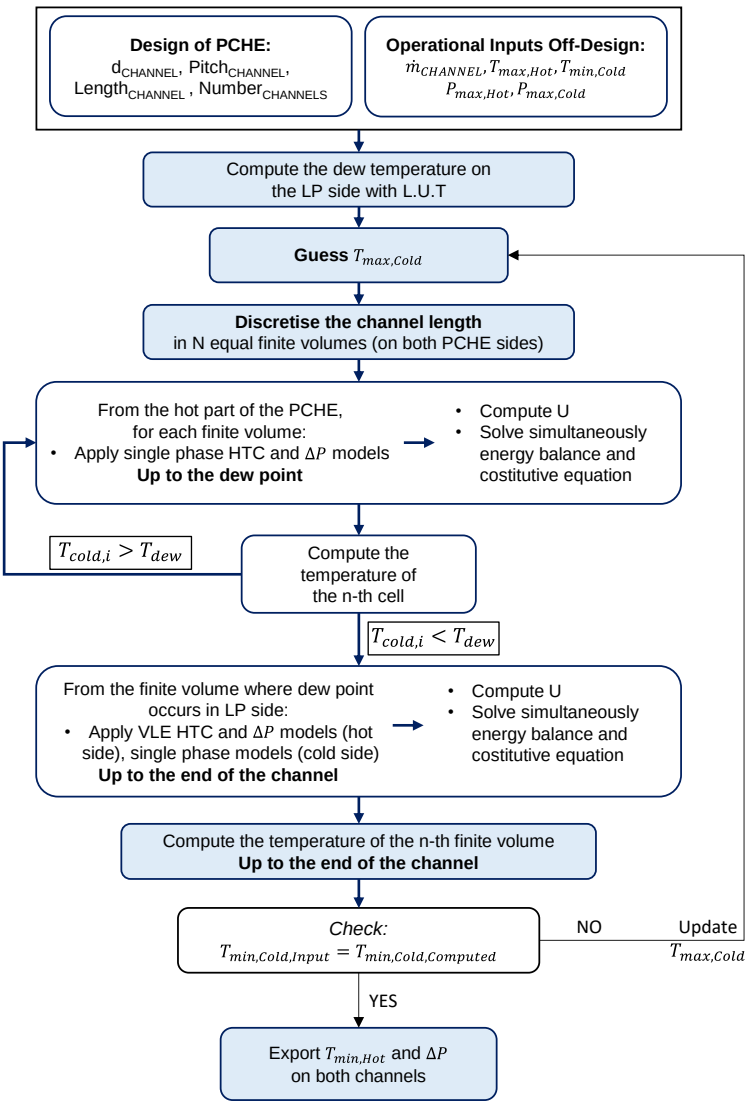

Figure 31. Methodology for the off-design model of the PCHE with the low-pressure side occurring in the VLE region for a part

4.4 Primary HX (S&T) sizing

Similarly to recuperators, always modelled as PCHE, also the primary HX (PHE) of sCO_2 power cycles are usually designed with a well-defined HX architecture, being the shell-and-tubes (S&T) HX. Accordingly, literature models of sCO_2-to-molten salts PHE are already available in literature, along with the one developed within this work, for high temperature applications of sCO_2 cycles.

In a work of Guccione [104], for example, two possible shell and tubes configurations have been implemented (a one shell pass and one tube bass, called TEMA E, and a two shell passes with two tubes passes, called TEMA F) for a sodium-to-advanced molten salts HX for next generation CSP plants, with sodium

as HTF. In addition, as correctly pointed out by the author of the work, some geometrical parameters of the S&T PHE (or S&T HTF-to-storage fluid HX) can be identified as the most relevant optimization variables, such as the tube diameter, the number of tube and shell passes and the overall number of tubes.

Together with the next generation of CSP plants, S&T are also adopted as PHE in commercial CSP plants adopting steam Rankine cycles: a work by González-Gómez [105] identified in the welded joints of the steam generator of the Rankine cycle (a shell and tube, solar salts to high pressure steam heat exchanger) the most critical source of failures in the cyclic operation of the power block related to rapid transients and frequent startups and shutdowns. Consequently, the design and the optimization of a S&T PHE is a delicate matter that has an impact on the cost of the power block and its flexibility.

Therefore, in this work a MATLAB model is developed for the design and off-design of the PHE, using the Bell and Delaware method for the calculation of the HTC and the pressure drops on the shell side, together with the other models proposed in Chapter 4.1 for the in-tube characterization of the flow field in single phase, its convective HTC and frictional pressure drops.

The in-house model considers the following assumptions: i) the Bell and Delaware model is implemented as proposed in literature by Fettaka [106], ii) the main geometric assumptions (i.e. the segmental baffle cut ratio to shell diameter, the tube pitch to outer diameter ratio, the tube arrangement angle, the tube geometry, the baffle spacing to shell diameter ratio) are taken from Kakaç [107], and iii) a set of typical values of clearances between baffles and tubes and between shell and baffles are taken from Walraven [108], along with the characterization of the tubes layout. Analogously, the abovementioned model of Guccione [104] also provided a long and detailed list of geometrical assumptions and mathematical modelling to precisely apply the Bell and Delaware model to this category of HX.

The basic schematic of the S&T PHE modelled in this work is proposed in Figure 32: solar salts are considered as hot fluid (with the thermodynamic and transport properties modelled according to literature [25]) as they represent the state-of-the-art in CSP applications. Nevertheless, the model developed is in principle valid for any innovative advanced molten salts. In the calculations the molten salts flow always in the shell side, while the working fluid of the power cycle at high pressure flows always in the tubes.

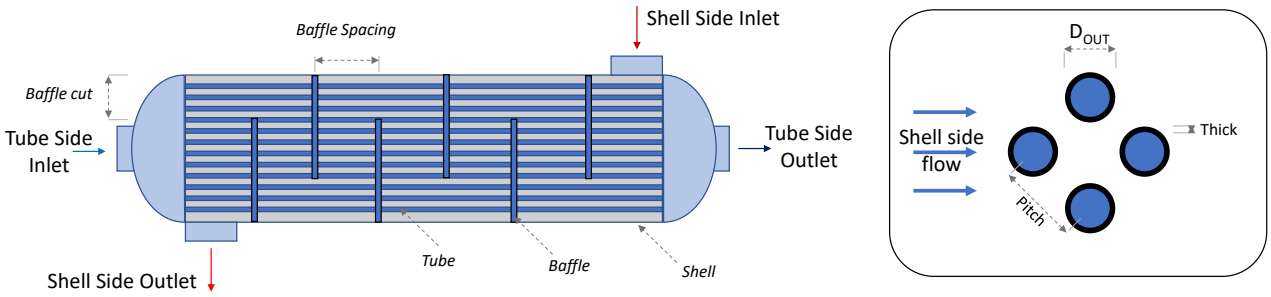

Figure 32. Shell and Tubes HX – Main geometrical characteristics of TEMA E with 6 baffles

The Bell and Delaware method for the design of S&T HX usually refers to a series of mathematical formulations adopted to compute the convective HTC of a S&T HX on the external side (on the shell side).

In this work, as presented for the condenser and the recuperator, the PHE is discretized in finite-volumes (with a 1-D axial discretization), where each finite volume corresponds to the spacing between two adjacent baffles. For each finite volume, the overall HTC, U_i, is computed assuming the external area of the tubes as reference heat transfer area following the Equation (21), neglecting any fouling and ageing effect.

$$U_i = \left(\frac{1}{HTC_{ext,i}} + \frac{D_{tube,out} \cdot \ln\left(\frac{D_{tube,out}}{D_{tube,in}}\right)}{2 \cdot k_{metal}} + \frac{1}{HTC_{int,i}} \cdot \frac{D_{tube,out}}{D_{tube,in}} \right)^{-1} \tag{21}$$

As mentioned before, the internal convective HTC is computed with the Gnielinski model and the external convective HTC with the Bell and Delaware model. A more detailed description of the Bell and Delaware method applied in this work is provided in Appendix B.1.

To solve the HX problem on each finite volume, the energy balance equation is solved simultaneously with the constitutive equation, as done in the modelling of the previous HX. Since for the S&T, differently than the PCHE, the flow field is developed partly counter-current and partly cross-flow (between the hot and cold fluid), the correction term "F" is included in the constitutive equation, as shown in Equation (22), and evaluated according to literature [106].

$$U_i = \frac{\dot{Q}_i}{\Delta T_{ML,Counter\ Current,i} \cdot F_i \cdot A_{ext,i}} \tag{22}$$

The set of information collected from literature regarding the HX geometry as input data for the PHE model are reported in Table 28.

The parameter which influences the most the calculations is the conductive thermal resistance, function of the tube internal diameter and its thickness. As convergence is reached, the MATLAB model checks the mechanical integrity of the tubes, using a correlation proposed in literature, considering an additional safety factor of 1.15 [7]. A conventional Inconel alloy is adopted as material due to its high resistance at high temperatures, a characteristic that makes it preferrable with respect to stainless steel.

Table 28. Characteristics assumed for the S&T PHE of the CO_2-based cycles

Parameter	Value
Tube arrangement angle [°]	45, Rotated square
Tube external characteristics	Flat, Unfinned
Tube pitch / Tube outer diameter ratio	1.5
Baffle spacing / Shell diameter ratio	0.5
Baffle cut / Shell diameter ratio	0.3
Tube internal roughness [mm]	0.01
Tube material	Inconel 617
Material thermal conductivity [W/m/K]	0.0185 · T (°C) + 10.25
Tube internal diameter [mm]	17
Tube thickness [mm]	3.5

After the selection of the models for the calculation of the HTC and the pressure drops of the S&T PHE, a novel procedure is developed in this work to effectively apply them, sizing the HX for the desired characteristics.

Accordingly, the flowchart in Figure 33 describes step-by-step the methodology applied for the design of the PHE, which is the novelty of this work.

The inputs of the MATLAB model are the characteristics of the hot flow and the cold flow (inlet and outlet temperatures, inlet pressures and mass flow rates) along with the number of baffles simulated and all the characteristics of Table 28. More importantly, also the temperature difference of the HTF across the first baffle spacing (at the hot end) must be first guessed ($\Delta T_{HTF,First\ Baffle}$).

The outputs of the model are the overall geometry of the S&T HX and its performances in terms of heat exchange performance: the number of tubes and their length, the shell diameter, the pressure drops on both sides and the axial trend of the overall HTC U_i, at design condition.

The MATLAB model of the S&T for the design of the PHE of CO_2-based cycles operates as follows: at first, the number of tubes and the dimension of the shell are assessed based on the outcome of the calculations carried out across the first finite volume. In fact, running the model on the first finite volume has the objective of univocally determine the shell diameter and the number of tubes, that in principle cannot be given as input: this process is possible due to the

assumption on the HTF temperature difference across the first finite volume ($\Delta T_{HTF,First\ Baffle}$).

After the calculations on the first finite volume, the S&T geometry is fixed and the remaining finite volumes (from the second to the last) are solved iteratively up to convergency on the energy balance and constitutive equation of each spacing between baffles (i.e. each finite volume). Finally, the overall energy balance and constitutive equation of the HX are checked and, if they are not satisfied, the numerical tool updates the HTF temperature difference across the first finite volume and the shell diameter until it reaches the overall convergency.

Once the S&T is sized, the pressure drop is computed on both sides: in case the tube-side pressure drop (i.e. the pressure drop on working fluid side) is not close to the target value, an external and final loop is performed, modifying the geometry parameters as input while reaching convergency on the tube-side pressure drop. In this scenario, the only parameters left to be modified to ensure the desired pressure drops are the number of baffles and the internal or external diameters of the tubes.

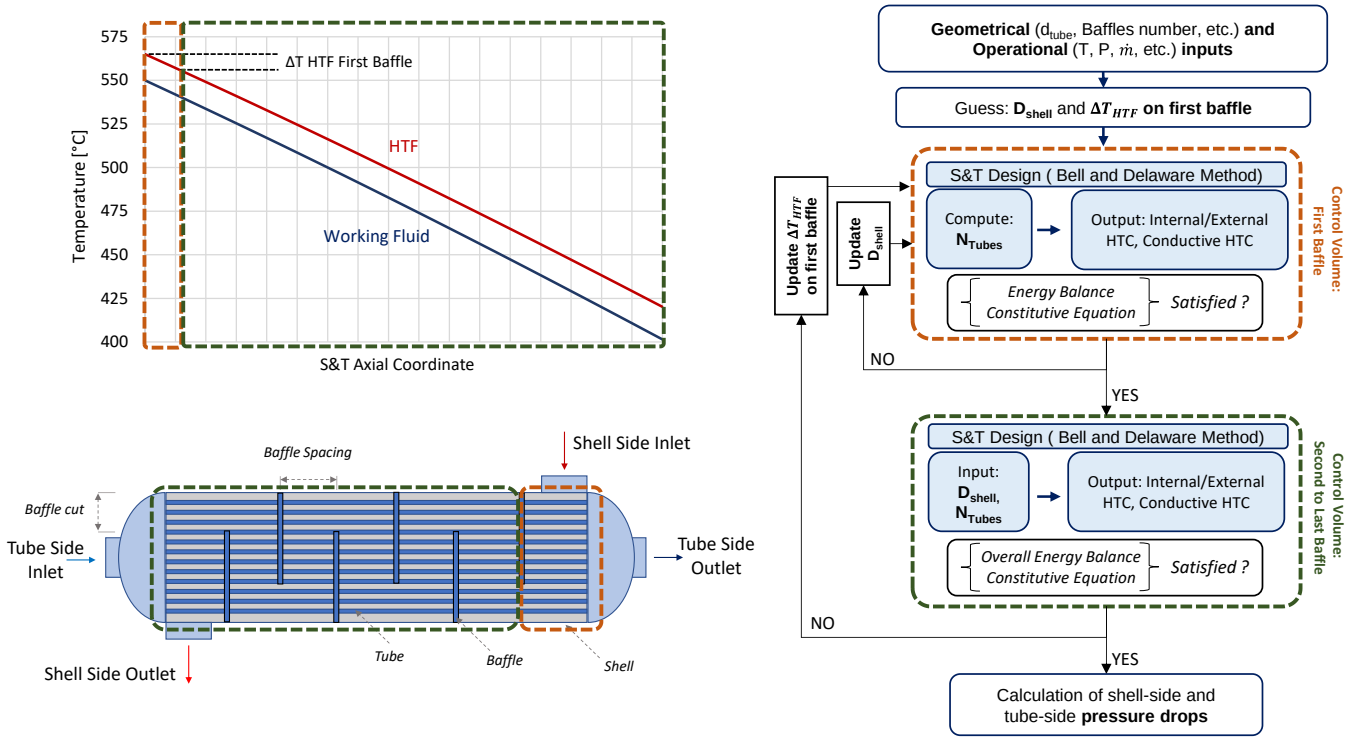

Figure 33. Methodology for the design of the S&T PHE of the CO_2-based power cycles

Given the novel sizing procedure of S&T PHEs shown in this work, a validation of the MATLAB model has been carried out considering the results of Thermoflex v.29 on some case studies: the results are shown in Appendix B.2.

4.4.1 Primary HX (S&T) off-design

The off-design model of the PHE of CO_2-based cycles can initially present some challenges, mainly related to the coupling between the hot source (the HTF or the storage fluid) and the power cycle itself.

Therefore, in this chapter, the off-design MATLAB model of the PHE is described for a stand-alone PHE, which is presumed not to be part of any power cycle, with a hot source (i.e. the HTF) which is typical of a CSP plant.

Nevertheless, in a subsequent chapter (Chapter 7.3) while describing the off-design of the CO_2-based power cycle as a system composed also by the PHE, the methodology to compute the off-design of this component will be reported again, assuming a PHE coupled with the other cycle components.

In this off-design analysis only the hot source of the PHE is fixed: the HTF mass flow rate, the HTF temperature at the inlet and at the outlet of the PHE are given as input, since their value come from the conditions of the TES of the solar plant, or from any other hot source of a different application.

Additionally, the pressure of the working fluid and the temperature of the working fluid at the inlet of the PHE are also given.

Consequently, the two outputs of the off-design model are the mass flow rate of the working fluid (crucial for the estimation of the cycle performance in off-design conditions) and the outlet temperature of the working fluid (representing the maximum temperature of the power cycle). It is important to note that the same methodology could have been also developed by fixing as an input the outlet temperature of the working fluid and leaving the inlet one as a variable to be computed: in fact, the two approaches are equivalent.

The flowchart in Figure 34 describes the overall methodology to solve the PHE MATLAB model in off-design: at first the values of the two outputs are guessed, and across each finite volume the HX problem is solved by iteratively update the value of the working fluid temperature difference.

When the S&T is completely solved, if the input value of the temperature of the HTF at the outlet of the PHE is not coherent with the one computed, the mass flow rate of the working fluid is updated. If, on the other hand, this condition is satisfied, the temperature of the working fluid at the inlet of the PHE is compared with the value given as an input. Also in this case: if the two temperature diverges, the maximum temperature of the working fluid (at the outlet of the PHE) is updated, up to convergency.

In conclusion, the overall procedure allows to compute the temperature range and the mass flow rate of the working fluid across the PHE given its pressure (a

variable that influences the thermodynamic and transport properties of the working fluid itself) and at know fixed conditions of the hot source.

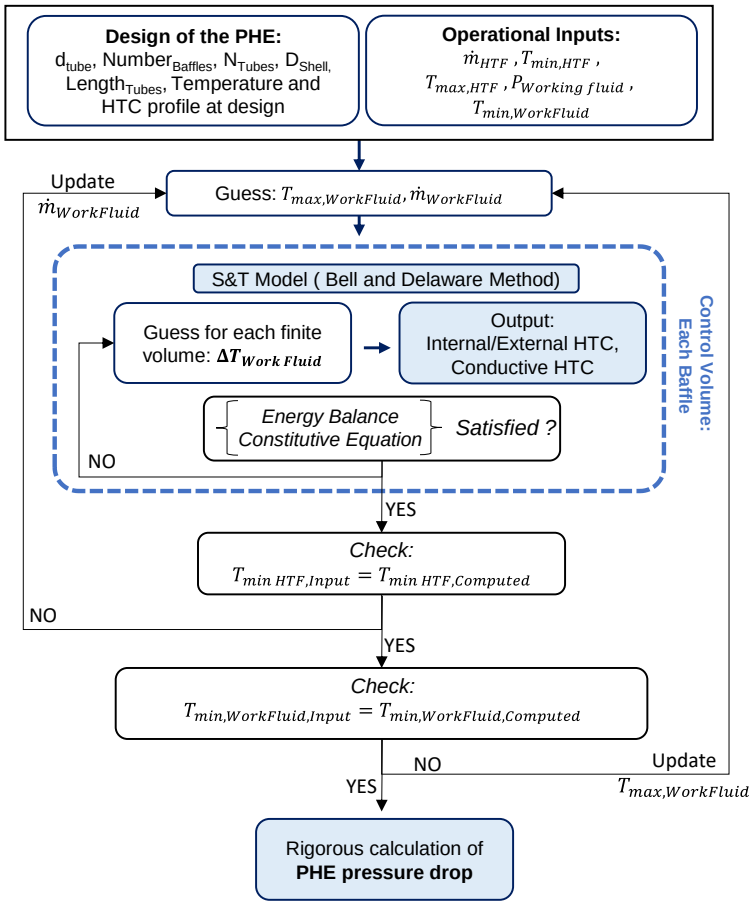

Figure 34. Methodology adopted for the off-design of the stand-alone PHE

4.5 Comparative analysis of HX with CO_2-mixtures and sCO_2

The heat transfer characteristics of some of the selected CO_2 mixtures will be analyzed in this chapter, along with their impact on the power cycles heat exchangers design and cost. The analysis proposed here can be found in literature in two works developed within this thesis [109] [88]: even if only a selection of tCO_2-mixtures is analyzed, the methodology shown can be in principle replicated to analyze additional mixtures of various compositions of the same mixture.

Cost correlations for the capital costs of sCO_2 heat exchangers are usually related to the product between the heat transfer area (A) and the overall heat transfer coefficient (U), such as in the literature references of Weiland [110] and Carlson [111].

This is a simplification, since two fundamental aspects are generally not considered: i) the dependance of the UA size parameter on the pressure drops of both sides of the HX, ii) the dependance of the UA size parameter on the actual heat exchanger material, that strongly influences the design and the costs. Regarding the HX material, a few cost functions include a temperature-dependent parameter (as the ones reported in Weiland for the recuperator) that can help to properly estimate the impact of the material on the cost, as different temperature levels entail different materials: nevertheless, this dependency is not commonly included in cost functions of all the heat exchangers. Finally, as the cost correlations are developed for sCO_2 and heat exchangers of sCO_2 cycles, they are not directly applicable to CO_2 mixtures as working fluids, since different working fluids exchange heat differently, if employed in the same heat exchanger, as both their thermodynamic and transport properties are different.

In the following analyses on the PCHE and on the S&T, the materials will be fixed: Inconel 617 will be adopted for the S&T and Stainless Steel 316L in the PCHE. Inconel 617 is expected to have good material compatibility with high temperature working fluids, but with a negative impact on costs. Stainless steel is a cheaper material already adopted for heat exchangers below 550 °C [110], nonetheless it can still be representative of a power cycle operating at high temperatures.

The effect of the working fluids pressure drops on the heat exchangers design is included in the analysis: higher pressure losses normally entail higher velocities of the fluids and therefore higher heat transfer coefficients with lower CAPEX, while compromising the cycle efficiency. For this reason, the heat transfer

performances of the two main heat exchangers will be examined in a wide range of pressure drop on the power cycle side.

On these bases, the following sub-chapters will propose a comparative analysis by designing recuperators (PCHE), PHE (S&T) and condensers of some selected CO_2-mixtures power cycles, comparing these to the results of the same HX of pure sCO_2 cycles. The study is performed specifically on the simple recuperative cycle layout with a maximum temperature of 550 °C, but the obtained results will be extended also to the other cycle layouts. The analysis proposed in this chapter is schematized in Figure 35: the analyzed fluids are sCO_2, the CO_2+C_6F_6 mixture, the CO_2+C_4F_8 mixture and the CO_2+C_2H_3N mixture, with molar compositions identified by the conditions of maximum cycle efficiency, to represent at best the working fluid of the innovative power cycles. Even if not all the CO_2-based mixtures are considered (as the ones with SO_2 or $SiCl_4$ as dopant, for example) the focus of the analysis is devoted to proposing a methodology that can in principle applied to any conditions.

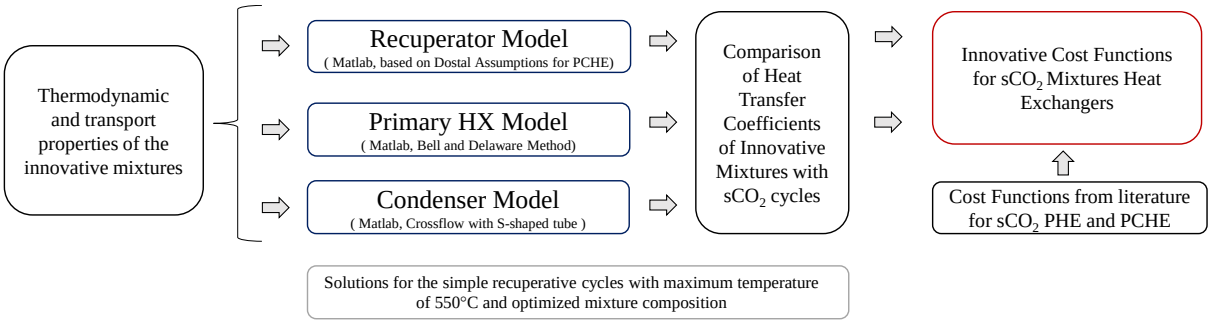

Figure 35. Methodology adopted to compare heat transfer performances of CO_2 mixtures

4.5.1 Heat transfer performances of PCHE with CO_2-mixtures

Following the methodology reported in Figure 35 for the recuperators, four sets of simulations of PCHE recuperators (one for the sCO_2 cycle and three for the cycles working with the three mixtures) are designed with the MATLAB model developed in this work.

The design temperature and pressure ranges on the two sides of the recuperators for the four cases are listed in the reference literature work [109], resulting in similar temperature ranges, same high pressure and different low pressures. While the pressure at the low-pressure side of the sCO_2 cycle is optimized to maximize cycle efficiency, the low-pressure side of the transcritical cycles working with CO_2 mixtures is set by the bubble conditions of each mixture at the cycle minimum temperature. The four sets of PCHEs have been designed in

a wide frictional pressure drop range on the hot-side channel (modifying the mass flow rate flowing in the single channel).

The trends of the overall HTC of the PCHEs as function of the pressure drop for the different CO_2 mixtures are reported in Figure 36: the results show a reduction of about 18% and 30% of the overall heat transfer coefficient with respect to pure CO_2 for the CO_2+C_6F_6 and the CO_2+C_4F_8, respectively. Inversely, the adoption of the CO_2+C_2H_3N mixture shows improved heat transfer performance, by around 17%. The results underline that the effects of adding a dopant to CO_2 can strongly influence the heat transfer characteristics of the newly defined working fluid, with non-negligible implications on the heat transfer area and the heat exchanger cost. If the same mean logarithmic temperature difference between the two sides of the recuperator (ΔT_{ML}) and the same amount of heat exchanged are assumed, the relative increment or reduction in the overall heat transfer coefficient corresponds to the same relative increment or reduction in heat transfer area.

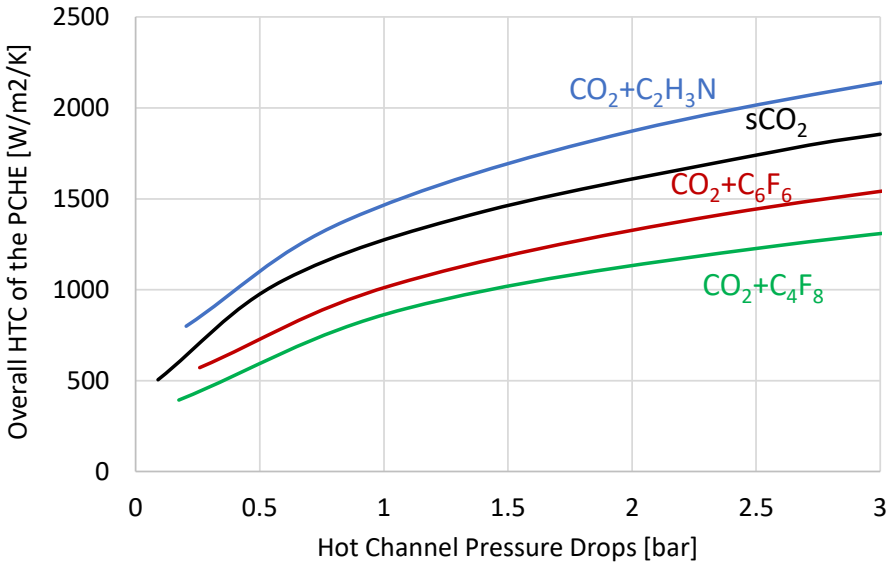

Figure 36. Dependency of the recuperator (PCHE) overall HTC on the pressure drop in the hot channel for the simple recuperative cycles working with different CO_2 mixtures and sCO_2

According to the cost correlation from literature for PCHE suitable for sCO_2 cycles of Weiland [110], the heat exchanger cost can be approximately proportional to UA with a scale factor of 0.7544, as reported in Equation (23):

$$C_{PCHE,CO_2} = const \cdot (UA)^{0.7544} \cdot f_T \tag{23}$$

Assuming that the cost of a heat exchanger is strictly related to its heat exchange area (and therefore its volume), the cost of the recuperator for a CO_2 mixture can be evaluated from the pure CO_2 case adopting the same scaling equation, with a correction factor $f_{U,PCHE,Mix}$, reported in Equation (24).

$$f_{U,PCHE,Mix} = \left(\frac{U_{CO_2}}{U_{Mix}}\right)^{0.7544} \quad (24)$$

The obtained fluid correction factors computed according to the results of Figure 36 for the PCHE costs are reported in Table 29. The cost function for PCHEs adopted in this work will thus have the form of Equation (25):

$$C_{PCHE,Mix} = f_{U,PCHE,Mix} \cdot C_{PCHE,CO_2} \quad (25)$$

Table 29. Fluid correction factors adopted to correct the literature costs function of the PCHE, on the basis of the PCHE cost for CO_2

	CO_2+C_6F_6	**CO_2+C_2H_3N**	**CO_2+C_4F_8**
CO_2 Molar fraction	84%	85%	73%
HTC variation compared to pure CO_2 (at constant ΔP)	-18%	+ 17%	-30%
Fluid Correction Factor for PCHE cost, $f_{U,PCHE,Mix}$	1.16	0.89	1.31

4.5.2 Heat transfer performances of PHE with CO_2-mixtures

The purpose of designing different S&T HXs as PHEs of different cycles is analogous to the one proposed for the recuperators: at first, the influence of different working fluids on the overall heat transfer coefficient of the HX is determined with the MATLAB model of this work, including a sensitivity analysis on the pressure drops on the tube side (i.e. the power cycle side). Then, some considerations about the costs of the heat exchangers are drawn.

The temperature and pressure range of each shell and tube PHE are reported in the reference literature work only for the tube side [109], considering the simple recuperative cycle layout for the various cycles simulated. The shell side is run with solar salts, presenting no influence of the pressure on its properties, being an ideal liquid. The results are reported at variable pressure drops both by assuming the value proposed in Table 28 of the tube length to shell diameter ratio and varying the tube diameter (with 16 baffles), and by assuming values in Table 28 for the tube diameter, varying the tube length to shell diameter ratio (i.e. varying the number of baffles). The underlying reason for this approach is to

understand whether it is more convenient to increase the tube side pressure losses by increasing the tube length or by decreasing the tube diameter.

Figure 37 reports the trends of the overall HTC for the various configurations of S&T PHE proposed, as function of the tube-side pressure drops. All the investigated CO_2 mixtures have higher heat transfer performances with respect to the pure sCO_2 in a shell and tubes PHE. From the results it is evident that, for the configurations studied in this work, increasing the tubes length, fixing their diameter, is a more advantageous approach to increase the HTC of these HXs, while limiting the increment of the pressure drop.

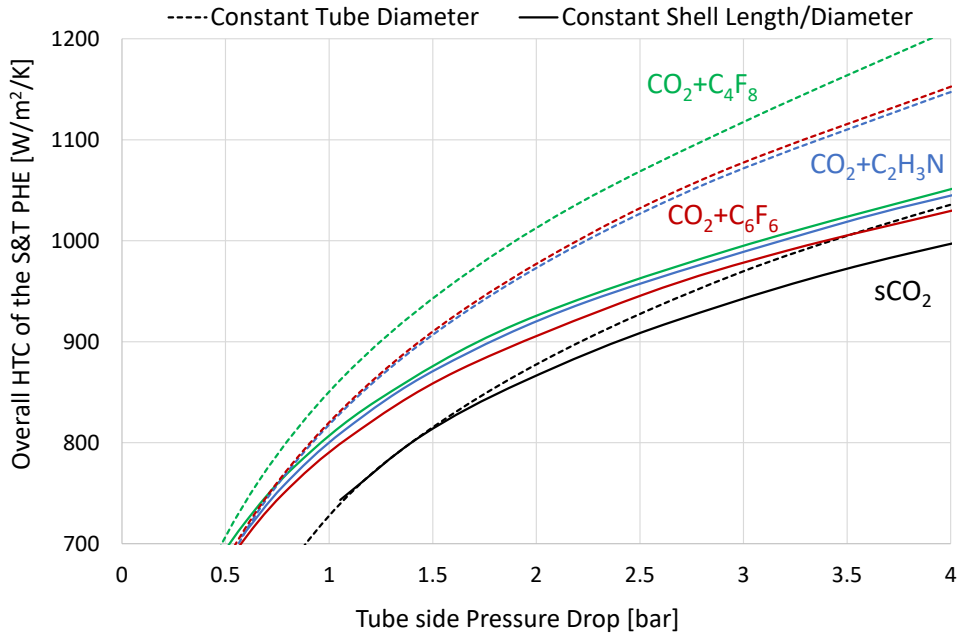

Figure 37. Dependency of the S&T PHE overall HTC on the pressure drop in the tube side for the simple recuperative cycles working with different CO_2 mixtures and sCO_2. HTC refers to the tube external area

The qualitative results of the comparative analysis on S&T PHE are different than the ones of the PCHE: for example, regarding the recuperator, the CO_2+C_4F_8 mixture has the lowest HTC at constant pressure drops, while, when the same mixture is adopted in the shell and tube PHE, it presents the highest HTC.

Comparing the results of the CO_2+C_4F_8 mixture with sCO_2, the most relevant contribution to the different heat exchange behavior is the density of the mixture (around 90% higher than the one of sCO_2), reducing the frictional pressure drop significantly, while still experiencing a slightly higher thermal conductivity. The CO_2+C_6F_6 mixture, on the other hand, presents thermal conductivity and viscosities in line with sCO_2, but a density 40% higher, while the CO_2+C_2H_3N mixture has the same density and a slightly lower viscosity than CO_2, but the higher thermal performances are given by a 20% increment in the thermal conductivity.

Finally, considering the results at variable tube length and constant tube diameter (that guarantee the highest HTC at constant pressure drops), the variation in overall HTC of the PHE for the tCO_2-mixtures power cycles with respect to the pure sCO_2 configuration is reported in Table 30. The table also reports the working fluid correction factor for the shell and tube cost ($f_{U,PHE,Mix}$), computed assuming a unitary scaling exponent of the cost with respect to the UA size parameter, as suggested by Carlson [111].

Table 30. Fluid correction factors adopted to correct the literature costs function of the PHE for the mixtures investigated, based on the CO_2 PHE cost

	CO_2+C_6F_6	**CO_2+C_2H_3N**	**CO_2+C_4F_8**
CO_2 Molar fraction	84%	85%	73%
HTC variation compared to pure CO_2 (at constant ΔP)	+12%	+12%	+17%
Fluid Correction Factor for PHE cost, $f_{U,PHE,Mix}$	0.894	0.894	0.857

Moreover, the generic form of the cost function of the PHE for CSP power cycles is reported in Equation (26): as done for the PCHE, it is assumed a cost function for pure sCO_2 with the same tube material and tube-side pressure drops, along with similar range of duty and UA.

$$C_{PHE,Mix} = f_{U,PHE,Mix} \cdot C_{PHE,CO_2}\left(f\left(\mathrm{UA}, \Delta P_{Tube}, Material\right)\right) \quad (26)$$

Nevertheless, no explicit cost correlations of shell and tubes PHE for sCO_2 cycles have been found in previous literature works in the form of Equation (26), differently from the PCHE, because no available correlation of S&T capital costs, to the best knowledge of the author, is able to cover the wide variability of input required (UA size parameter, tube pressure drops and HX materials).

In this case, the software Thermoflex v.29 [112] is adopted for the purpose, as it allows for a detailed design of sCO_2 shell and tubes PHE with solar salts and it provides the heat exchanger direct cost.

Two different sets of simulations have been run within Thermoflex, according to the characteristics of the S&T assumed in Table 28: one for PHE with heat duties above 100 MW_{th} and another one with heat duties between 10 MW_{th} and 100 MW_{th}. For each set of simulations, the tube side pressure drops are spanned in a wide range varying the tube length and tube diameter, assuming always solar salts on the shell side and pure sCO_2 at 254 bar as working fluid (with a maximum temperature of 550 °C and varying its inlet temperature from 300 °C and 420 °C).

The capital cost function for these HXs obtained by interpolating the Thermoflex results is reported in Appendix B.3.

4.5.3 Heat transfer performances of condensers with CO_2-mixtures

Analyses similar to the ones carried out for the PCHEs and the S&T PHEs are hypothetically possible also for the condensers (or the HRUs of sCO_2 cycles), simulating with the condenser MATLAB tool various HX designed for various mixtures and conditions.

Nevertheless, the interest for this comparison is more limited, since the capital cost of HRU is only a little fraction of the overall capital costs of the power cycle (around 5-10% [113]), mainly due to the low-cost materials adopted in the condenser tubes and the finned surfaces on the air side. Moreover, a significant fraction of the condenser cost is allocated to the fans, which costs depends on the fan manufacturers.

As for the cost correlations of the whole condenser (or HRU), the widely adopted and already mentioned literature model of Weiland [110] suggests scaling the capital costs proportionally to UA, with an exponent of 0.75: preliminary costs estimations within the SCARABEUS consortium tend to match this correlation.

With respect to sCO_2 cycles, the temperature difference of the CO_2-mixtures as working fluids across the condenser is more limited, given to the lower temperature increase across the compression step (the pump) when compared to the sCO_2 counterpart. Accordingly, an inherently higher surface area per unit of heat rejected is foreseeable in tCO_2-mixtures cycles if compared to sCO_2 cycles at constant air temperature difference, independently from the effects on the different HTC. Moreover, also the effects of the working fluid pressure drops increase the complexity of the comparison: the comparison must be carried out at constant pressure drops, but since the pressure drops experienced by a condensing mixture is modelled differently than the cooling of sCO_2, another degree of uncertainty must be considered.

Therefore, even if of difficult comparison, a single example of heat transfer performances assessing the sCO_2 and tCO_2-mixtures cycles is hereby shown, presented in literature together with the definition of the MATLAB model of the condenser [88]. The condensing process of the CO_2 mixture selected is the same one described in Figure 28 for the CO_2+C_6F_6 mixture, but a different tube is adopted. The advanced tube is proposed in Figure 38, where corrugated fins on the air side are introduced to enhance the air turbulence, increasing the air pressure drop by 12% at constant air face velocity and the external HTC of 20% at constant fan power. Moreover, internal microfins are added at the tube side, enhancing the HTC between 50% and 220% with respect to the smooth tube, increasing the pressure drops between 10% and 70%. The innovative tube is proposed by an industrial partner of the SCARABEUS project.

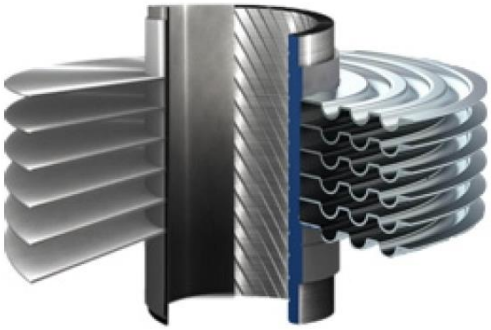

Figure 38. Advanced tube for the air-cooled condenser with internal microfins and external groovy fins, as proposed by a SCARABEUS partner [88]

The condensation of the mixture of Figure 28 is compared with the cooling of pure sCO_2 at 100 bar (selected as optimal cycle minimum pressure for this application at these conditions [53]), at same heat duty and temperature range, in order to compare two closest possible conditions, with a consequent different mass flow rate.

The results are presented in Table 31, showing a higher number of tubes and a lower tube length for the sCO_2 cooler to meet the same pressure drop. As the local working fluid velocity in case of pure sCO_2 is higher than the one of the mixture, a higher frictional pressure drop per unit length is computed. On the other hand, sCO_2 is characterized by an enhanced heat exchange performance thanks to its low viscosity that entails high local Reynolds and Nusselt numbers. The heat transfer performance of the pure CO_2 increases towards low temperatures, closer to the critical point, due to a marked increase of the thermal conductivity. The opposite trend is noted in the heat transfer performance of the mixture, which decreases during condensation. At almost the same mass flow in the single tube, the improved heat exchange capability and the higher frictional pressure drop in case of pure CO_2 entail a lower tube length to meet the same pressure drop.

Table 31. Comparison of heat transfer characteristics of a sCO_2 HRU and a representative condenser for tCO_2-mixture [88]

Input Parameter	Input / Output	CO_2+C_6F_6 mixture condenser	sCO_2 HRU
Heat duty [MW_{th}]	Input	236	
Working fluid temperature range [°C]	Input	From 114 to 51	
Air face velocity [m/s]	Input	3.23	
Working fluid pressure drop [bar]	Input	0.46	
Air ambient temperature [°C]	Input	36	
Working fluid	Input	CO_2+C_6F_6 (92% molar CO_2)	CO_2
Working fluid mass flow [kg/s]	Input	1200	1749
Working fluid pressure at inlet [bar]	Input	92	100
Air outlet temperature [°C]	Output	63.1	65.4
Number of tubes [-]	Output	2250	3055
Length of the tubes [m]	Output	104.2	70.2
Length of the pass [m]	Output	14.9	10.0
External HX area [m^2]	Output	417 300	381 700
Overall HTC [$W/m^2/K$]	Output	28.8	28.6

In conclusion, the heat exchange area is reduced for the sCO_2 configuration by 8% with respect to the mixture, although a slightly lower overall HTC is computed. The reason for this counterintuitive result lies in the average temperature difference between the cold and the hot flows, being higher in the case of sCO_2 HRU than in the condenser of the mixture, as larger temperature differences entail smaller HXs.

Figure 39 and Figure 40 depict the heat exchanged in the sCO_2 cooler and the deviation in hot and cold temperature difference between the sCO_2 case and the CO_2+C_6F_6 case, which generally is higher for the sCO_2 by up to 5 °C, depending on the cell position. The graphical results are shown for the solution of the HX problem according to the tube geometry of Figure 28.

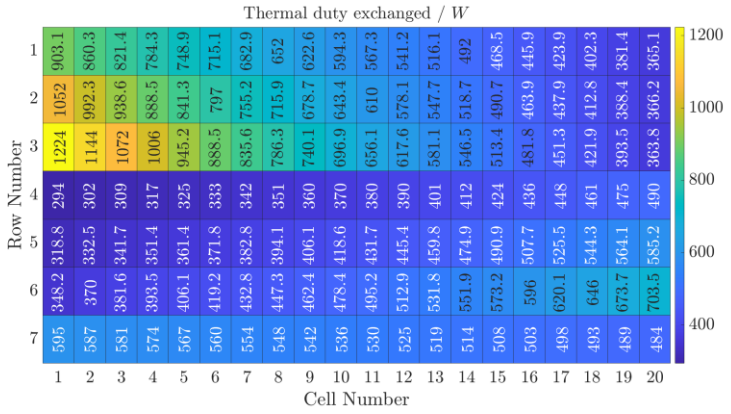

Figure 39. Heat exchanged [W] across the tube of the sCO_2 gas cooler of Table 31, with the tube geometry reported in Figure 28

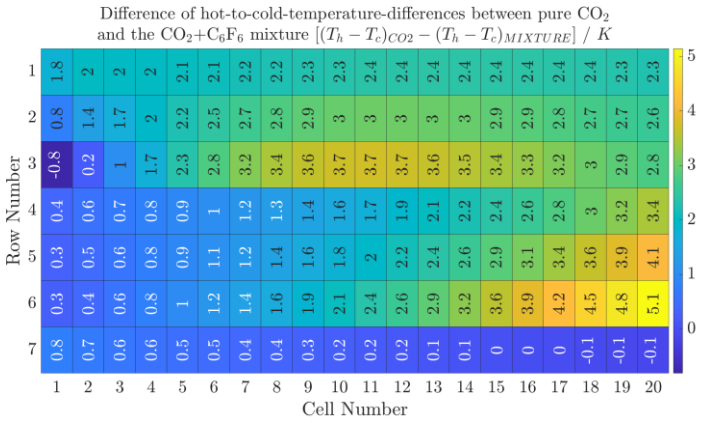

Figure 40. Increment in temperature difference between the working fluid and the air of the sCO_2 cooler with respect to the CO_2+C_6F_6 condenser of Table 31

As a consequence of this analysis, no capital cost correction factors are suggested for the condenser of tCO_2-mixture cycles, if computed starting from the cost of sCO_2 coolers and scaled with the UA size parameter. The advantage of dealing with sCO_2 coolers with respect to condensers of CO_2 mixtures can be in principle represented by dealing with a lower air mass flow rate (due to the higher air temperature difference): nevertheless, this factor is not included in the cost analysis of the HX, since it is more relevant from an energetic point of view (regarding the auxiliary electric consumption of the fans of the HX).

5. Modelling of the solar plant and its sub-systems

The components that influence the power production of a solar tower CSP plant are the solar field, the thermal receiver and the pumping system of the HTF. In addition, the TES and the eventual HTF-to-storage fluid HX must also be detailed to characterize the solar plant costs and its yearly operation.

Across this work these various components are rigorously designed adopting literature tools and models: their performances are also evaluated in off-design.

The methodology described in Figure 41 is adopted in this thesis to design the CSP plants: to start the modelling procedure, a first guess on the optimal solar multiple (SM) and power block size must be done. Then, in case an overall techno-economic optimization would return an optimal value of the SM different than the one initially assumed, the solar plant optimization will still be valid, but a different nominal electric power production will be expected.

Only tubular receivers will be considered in this work since, as proposed in Table 2, they have been already widely analyzed in literature for next generation of CSP plants. Accordingly, in addition to the SM and the power cycle characteristics, also the circuitation of the tubular receiver (number of flow paths of the HTF and number of panels per flow paths) and the tower height can be assumed from literature, since a detailed sensitivity analysis on these characteristics of the receiver is considered out of the scope for this work.

Finally, the diameter of the tubes adopted in the receiver is also a potential optimization parameter: the author of this work developed some case studies where this parameter was optimized [114] [115] and some other studies where the tube size was taken from literature [109].

In the design procedure of a CSP plant, and of any power plant in general, a target value on the electric power produced must be met, in this case by the power cycle. Therefore, after assuming the SM, a first guess value of both the optical efficiency and the thermal efficiency must be considered (based on literature results of similar works), along with a receiver diameter and height. With these guessed values and assuming a DNI representative of the location of interest, the designer can have a general idea of the solar field area. Moreover, the sun position at design conditions is always considered at the summer solstice and solar noon.

Afterwards, the map of the solar flux reflected to the receiver by the solar field can be computed with a numerical tool for solar fields design, and it is used

as input to the thermal model of the receiver: this will compute the convective, radiative and reflective thermal losses on the receiver surface.

After having assessed the conversion efficiency from the solar resource to the thermal power into the HTF on the basis of the first guess values of most parameters, an optimization procedure is run to maximize the solar-to-thermal efficiency with the goal to obtain an optimal configuration of solar field and receiver dimensions at design conditions.

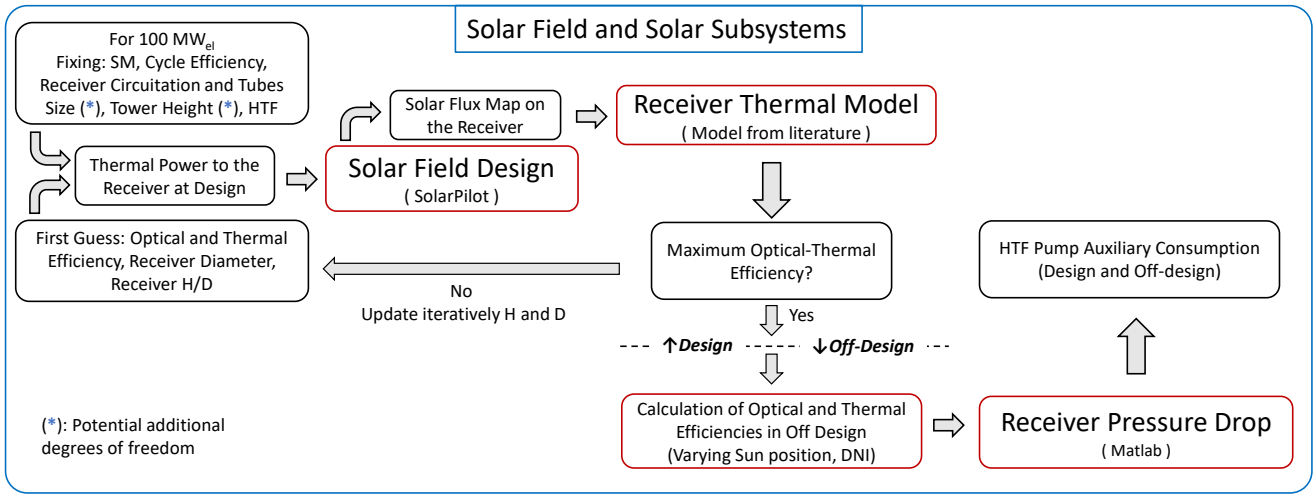

Figure 41. Overall methodology for the design and off-design of a central tower CSP plant

The tool for the solar field design adopted in this thesis is SolarPilot [116] [117], and the thermal model of the receiver is a tool developed within the Department of Energy of Politecnico di Milano by Giancarlo Gentile in Modelica [118]. The thermal model is also coupled to a hydraulic model that, with some assumptions tailored to the case studies of this work [109] [119], allows for an accurate assessment of the pressure drops of the HTF along the receiver tubes, for any condition of thermal power incident to the receiver.

The off-design analysis of the CSP plant allows for the calculation of the plant performances across each timespan in steady state conditions, with a temporal discretization depending on the weather data given as input. In this work, the DNI data are detailed on an hourly basis, taken from the database of SolarPilot. On this matter, the flowchart reported in Figure 42 can help in describing the off-design analysis carried out in this thesis.

The optical efficiency of the solar field is determined in SolarPilot univocally for each sun position, as it depend on the reciprocal position between the sun, the heliostats and the receiver, independently from the DNI. Then, fixing the sun position at the solar noon of the summer solstice, the receiver thermal efficiency is computed by linearly scaling the solar flux map on the receiver, computing the instantaneous power to the HTF. In fact, the approach is supported by evidence

from literature that shows a very limited dependency of the receiver thermal efficiency from the distribution of the solar flux on the receiver itself [30], demonstrating that the thermal efficiency can approximately only depend on the overall power hitting the receiver.

Finally, once the optical and thermal efficiency are computed in off-design conditions, the pressure drop of the HTF in the receiver can be computed by fixing the sun position (approaching the problem in an analogous way) and varying the DNI, estimating the electric consumption of the HTF pump.

The HTF mass flow rate is supposed to depend only on the overall power transferred across the receiver tubes, and it is not influenced by the flux distribution also while computing the HTF pressure drop.

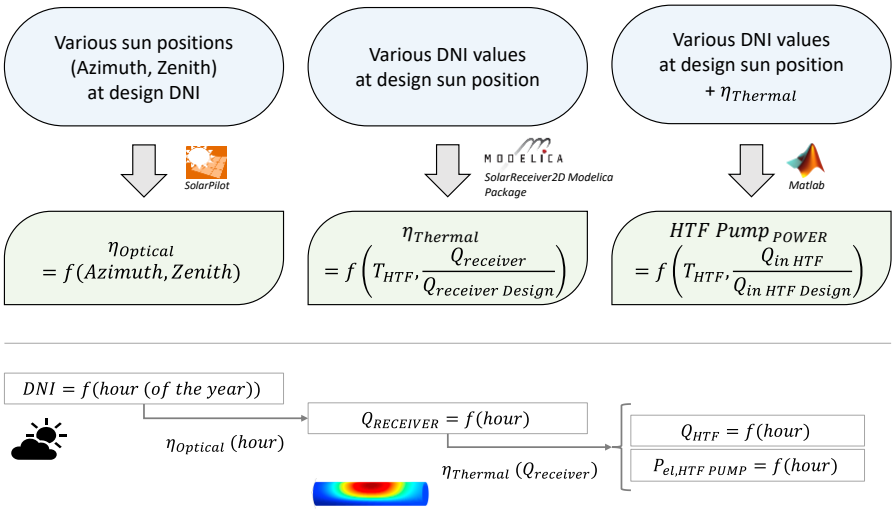

Figure 42. Yearly analysis of the CSP plant with hourly weather data

After computing the instantaneous power delivered to the HTF and the HTF pump electric consumption, the TES size must be determined according to a simplified TES operating strategy. According to this operating strategy, when the power block is running at full load and the hot tank of the TES is full, a partial defocusing of some heliostats is assumed, reducing the thermal input to the receiver. The TES size, optimized from a techno-economic point of view, is chosen to limit the equivalent defocusing hours of the plant without amplifying the tank dimensions over a certain limit.

In the following sub-chapters, each model adopted for the analysis of the various solar plant components is briefly introduced and described, underlining how it can be applied in CSP plants working with CO_2-based working fluids, eventually stressing the differences with respect to systems based on steam cycles.

5.1 Solar field modelling in SolarPilot

SolarPilot is a software developed by the National Renewable Energy Laboratory of the US DOE, extensively presented in a literature work by Wagner [117]. SolarPilot has the aim of quickly generate solar fields of CSP plants accounting for the position of each heliostat knowing the receiver geometry and the tower height, along with the DNI at design conditions, the location and the requested power hitting the receiver. It is an open-source software, it implements a ray-tracing approach that can provide an efficient estimation of the optical efficiency of all the heliostats across the solar field, placing them on the ground surface in the most effective way, minimizing the overall reflective area for a given thermal input to the receiver.

The optical losses included in the model are mainly: cosine losses, shadowing losses, blocking losses, attenuation losses, absorptive losses and spillage losses. In the software, the attenuation of the atmosphere is related to the distance between the heliostat and the receiver during a clear day (with no evident haziness), the absorptive loss is computed by defining the heliostat reflectivity coefficient while the cosine, shadowing and blocking losses are modelled with a ray tracing approach. The image intercept efficiency, also referred to as "spillage efficiency", quantifies the radiation correctly reflected by the heliostats that intercepts the receiver area, not missing the receiver structure. Spillage losses are commonly attributed to the heliostat surface quality and imprecisions in the tracking system. Moreover, the shape of the sun (limb-darkened sun) and other parameters assumed by default by the software are also assumed, summarized in Table 32.

Table 32. Main assumptions about the optical performance of the solar field

Parameter	Value
Attenuation efficiency	$-0.002845 \cdot r[km]^3 + 0.017 \cdot r[km]^2 - 0.1046 \cdot r[km] + 0.9932$
Heliostat layout positioning	Radial around the tower, staggered
Effective reflective heliostat surface	97%
Heliostat reflectivity	95%
Heliostat soiling efficiency	95%
Total reflected image error, σ_{tot}	3.07 mrad

While simulating the layout of the solar field in Solarpilot no thermal nor reflective losses are included on the receiver surface, effectively considering as output of the software the map of the concentrated solar flux hitting the receiver (as a matrix of values along the height and the circumferential direction of the receiver).

The optical performance of the solar fields in off-design are also computed with SolarPilot, by fixing the solar field and modifying the sun position.

5.2 Receiver thermal model and HTF pump system

In the characterization of the solar field optical efficiency the receiver is considered as a perfect cylinder, since the real distribution of the HTF between the flow paths and across the various panels and tubes is not relevant from the optical point of view.

Thermal models for tubular receivers are adopted to address two necessities: i) assessing univocally the flow field across the receiver (number of flow paths, panels per flow path, tubes per panels, tubes internal and external diameters, etc…) and the concentrated solar flux distributed across the tubes surface, ii) compute the thermal losses (convective, radiative and reflective) along all the receiver, usually with a finite-volume discretization.

The thermal model adopted in this work is developed by Gentile [118]: the model spans the various tubes across their circumferential (dimension "j") and axial (dimension "i") domain, discretizing with finite-volumes the tubes.

After the accurate discretization of the tube geometry on the basis of the assumptions made, the model is run to compute the reflective losses, the convective losses and the radiative losses on each finite volume. In particular, the radiative losses are modelled accounting for view factors from each of the finite-volume of the receiver tubes toward the external environment, according to the crossed strings method. Only a single tube is modelled for each panel, considered representative of all the other tubes of the panel.

The following considerations are reported to briefly describe the model of Gentile, while a more detailed description is presented in literature [118] [26].

The discretization of the tubes in finite volumes is proposed in Figure 43.

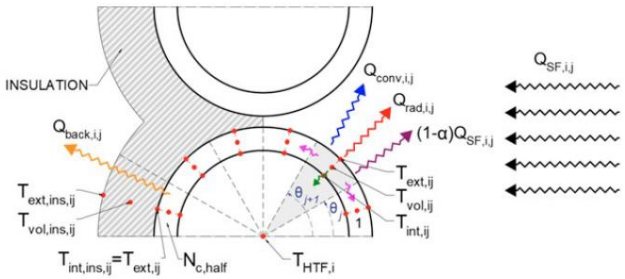

Figure 43. Discretization of the tube metal according to Gentile [118]

For each finite-volume, the heat absorbed by the tube (including the contribution of the reflective losses) can be computed as in Equation (27):

$$\dot{Q}_{in,ij} = q''_{SF,i} \cdot r_{ext} \cdot L_i \cdot (\sin(\theta_{j+1}) - \sin(\theta_j)) \cdot \alpha \quad \text{(for angles } \theta_j < \frac{\pi}{2}) \quad (27)$$

Where $\dot{Q}_{in,ij}$ is the heat absorbed by the tube, $q''_{SF,i}$ is the heat flux hitting the i-th element of the panel, r_{ext} is the tube external radius, L_i is the length of each control volume in the axial direction, and α is the tube coating absorptivity.

Then, the thermal power crossing the external wall of the tube in each i,j-th volume $\dot{Q}_{ext,i,j}$ is computed accounting for the radiative and convective losses as in Equation (28):

$$\dot{Q}_{ext,i,j} = \dot{Q}_{in,ij} - \dot{Q}_{Rad\ Loss,ij} - \dot{Q}_{Conv\ Loss,ij} \quad (28)$$

Where the radiative losses are calculated based on 2D view factors (obtained through the crossed strings method) and the convective losses are computed through Nusselt correlations mixing the effects of natural and forced convection.

Finally, the energy balance across the finite-volume of the tube is written and solved according to Equation (29):

$$m_{i,j} \cdot c_{metal} \frac{\partial T_{vol,i,j}}{\partial t} = \dot{Q}_{ext,i,j} + \dot{Q}_{int,i,j} + \dot{Q}_{n,i,j} + \dot{Q}_{p,i,j} \quad (29)$$

Where $\dot{Q}_{int,i,j}$ is the power that crosses the wall of the tube and is transferred to the HTF in each i,j-th volume, while $\dot{Q}_{n,i,j}$ and $\dot{Q}_{p,i,j}$ represent the amounts of thermal power exchanged with the next and the previous volumes of the tube wall in the circumferential direction, proposed in Figure 43.

As represented in Figure 41 and Figure 42 the receiver thermal model is adopted both to investigate the receiver performance while sizing the system and also to assess the off-design thermal efficiency of the given receiver under various conditions: to do so, the temperature difference of the HTF across the receiver is univocally determined considering a 15 °C temperature difference at the cold- and hot-ends of both the HTF-to-storage fluid HX and of the power cycle PHE.

5.2.1 Optimization of the receiver circuitation and receiver hydraulic model

As any receiver thermal model is by definition very sensitive to the assumed receiver circuitation (number of tubes, tubes dimensions, number of panels, etc…), a sensitivity analysis on the receiver circuitation is possible, finding an optimal condition that minimizes the overall losses.

In fact, in addition to the thermal model, a simplified optimization procedure can be carried out considering the hydraulic model of the receiver, used to compute the frictional and concentrated pressure drops of the HTF across the receiver.

The HTF pump allows the HTF circulation from ground level up to the top of the solar tower, where the receiver is placed. For direct storage systems, presented in Figure 3, the geodetic head provided by the pump is dissipated when the HTF enters the hot tank. In case of indirect storage systems, instead, the HTF flows in a closed loop between the receiver and the HTF-to-storage-fluid HX, where the HTF is cooled down: in this case the HTF pump head is only attributed to the compensation of the concentrated and distributed pressure losses within the receiver, since the distributed pressure drops in the piping and the pressure drop in the PHE or in the HTF to storage heat exchanger can be neglected (being one order of magnitude lower than the ones experienced across the receiver itself).

Focusing on the pressure drops in the receiver tubes, the frictional model assumes a receiver circuitation where each panel is connected to the subsequent one through a collector. A constraint on the maximum HTF velocity into the tubes of 6 m/s has been verified, to avoid erosion problems.

The pressure drops of the HTF are computed according to Equation (30) with a modelling procedure presented in literature [109] [119], as the sum of the geodetical term (considered only in case of direct storage) and of the receiver concentrated and distributed pressure losses, in accordance with the results of the receiver thermal model.

$$\Delta P_{HTF} = (\rho_{HTF} \cdot g \cdot h_{Tower})_{direct} + N_{panels} \cdot \left(\frac{f_{fric} \cdot L_{tube}}{2 \cdot D_{in,Tube}} \cdot \rho_{HTF} \cdot V_{HTF}^2 + \sum_i K_i \cdot \rho_{HTF} \cdot \frac{V_{HTF}^2}{2} \right) \quad (30)$$

In the proposed hydraulic model, the concentrated pressure drop coefficient K_i is dependent on the receiver circuitation and the types of concentrated pressure losses underwent by the HTF. In this work, a K_i of 0.6 and 0.5 at manifold inlet and outlet is considered, along with a K_i of 0.13 for each 90 ° bend, and other K_i values modelled according to literature [120] accounting for the various T-joints from the tubes to the manifold and from the manifolds to the tubes.

Finally, assuming a constant HTF electric pump efficiency $\eta_{HTF,elec}$ of 80%, the auxiliary electric consumption of the circulation pump is computed as in Equation (31), for each HTF mass flow rate $\dot{m}_{HTF}$, representing different values of thermal power absorbed by the HTF.

$$\dot{W}_{HTF\ Pump} = \frac{\dot{m}_{HTF} \cdot \Delta P_{HTF}}{\rho_{HTF} \cdot \eta_{HTF,elec}} \quad (31)$$

Once the thermal power transferred to the HTF is determined and the HTF pump auxiliary electric consumption computed at design conditions, the optimal trade-off between the two contributions can be found varying the tube dimensions and their arrangement.

In particular, the number of tubes per panel, the number of panels per flow path and the tubes outer diameter can be varied aiming at maximizing the fictitious thermal power ($\dot{Q}_{HTF,fictitious}$), obtained through Equation (32). The latter is the thermal power absorbed by the HTF at design conditions, to which it is subtracted the thermal power required by the power block to produce the electricity needed to run the HTF pump. For various combinations of tubes outer diameter, number of panels per flow path and number of tubes in parallel per panels, $\dot{Q}_{HTF,fictitious}$ can be determined assuming a distance between adjacent tubes of 2 mm [121]. Generally, the lower the HTF temperature difference across the receiver, the more is convenient to distribute the HTF across a wider tube passage area: this condition is normally achieved reducing the number of panels per flow path.

$$\begin{aligned} \dot{Q}_{HTF,fictitious} &= \dot{Q}_{IN,HTF,Design} - \frac{\dot{W}_{HTF\ Pump,Design}}{\eta_{cycle}} \\ &= \dot{Q}_{Solar\ Field} \cdot \eta_{Thermal} - \frac{\dot{W}_{HTF\ Pump,Design}}{\eta_{cycle}} \end{aligned} \tag{32}$$

The combination of tubes diameter and number of panels per flow path that maximises $\dot{Q}_{HTF,fictitious}$ can hence be considered an approximate optimal configuration of the overall receiver circuitation.

5.3 TES system

Four different storage fluids are considered in this work, selected as the least expensive for the solar plant specific condition among a larger pool presented in a literature work detailing different HTF and storage fluids for CSP [25].

For all the configurations characterized by a power cycle maximum temperature of 550 °C, state-of-the-art solar salts are selected, both for the direct and indirect storage configurations. In the solar fields designed for cycle maximum temperatures above 550 °C only indirect storage configurations are assessed, and the optimal storage fluid is selected according to the cold tank temperature, fixed 15 °C above the working fluid temperature entering in the PHE.

In particular, for each of the HTF temperature range considered, the selected storage fluid is the one that allows for the lower capital costs per unit of heat stored (MWh_{th}), according to the capital cost analysis presented for the TES in the next chapter. The factors that influence the analysis are both the specific cost of the fluid (on mass basis) and the costs of the TES tank, proportional to the tank volume and therefore to the specific volume of the storage fluid.

Accordingly, $NaCl+MgCl_2$ is adopted as storage fluid for cold tank temperatures higher than 460 °C: below this temperature this storage fluid cannot be used due to the proximity to the fluid melting point. For cold tank temperatures between 415 °C and 460 °C, $NaCl+KCl+MgCl_2$ is adopted as storage fluid, while for lower cold tank temperatures (i.e. below 415 °C) the fluid selected is $NaCl+KCl+ZnCl_2$.

All the considered storage fluids are listed in Table 33, along with their composition and costs, where the more expensive are the ones with a wider possible operating temperature range. On the other hand, increasing the temperature difference between the hot and cold tank has a beneficial impact on the storage fluid inventory, the HTF pump auxiliary consumption and the receiver thermal efficiency, with only a negative impact on the fluid specific costs on massic terms (for example, the specific cost of solar salts, relative to its mass, is six times higher than $NaCl+MgCl_2$).

Table 33. Characteristics of the storage fluids considered in this work [25]

Storage fluid	Molar composition	Melting point [°C]	Ideal maximum temperature [°C]	Cost [$/kg]
$NaNO_3+KNO_3$ (Solar Salts)	64% + 36%	223	601	0.80
$NaCl+MgCl_2$	58% + 42%	445	1465	0.12
$NaCl+KCl+MgCl_2$	30% + 20% + 50%	397	Above 700 °C	0.23
$NaCl+KCl+ZnCl_2$	13.8% + 41.9% + 44.3%	229	Above 700 °C	0.69

Once the storage fluid is selected, the TES tank must be properly sized. In this work it is assumed to study the TES tanks as proposed in literature by the NREL with many layers: i) an internal layer of dense refractory bricks in contact with the storage fluid, ii) a subsequent insulation layer with very low thermal conductivity, iii) a shell of either carbon steel or stainless steel or higher temperature alloys and, finally, iv) an external insulation fiber blanket [22] [122]. The cold tanks with storage fluids below 450 °C adopt carbon steel shells and the conventional insulations layers. For temperatures of the cold tank between 450 °C and 565 °C, SS304L is used for the shell, while above the conventional temperature levels of the state-of-the-art plants the second thermal layer of refractory bricks is introduced, with a thickness (and a volume) computed on a case specific basis, to maintain the internal temperature of the molten salts constant along the days. This

specific approach for the modelling of the TES is already evidenced in literature, along with its capital costs implications [25].

5.4 Energetic key performance parameters for CSP

The key performance parameters (KPI) selected for the thermodynamic analysis of the CSP plants are: the yearly optical efficiency, the yearly thermal efficiency, the electric cycle efficiency (computed including the electromechanical losses of the compressions and expansions), the gross yearly electric energy produced, the net yearly electric energy produced, the capacity factor of the power plant and the yearly solar to electric efficiency.

The yearly optical efficiency represents the annual energy collected by the solar field with respect to the annual direct normal irradiation, and it is computed according to Equation (33): it is expected to increase for smaller solar fields and tall solar towers, while it is expected to decrease with receiver of smaller dimensions.

$$\eta_{Optical,Yearly} = \frac{\sum_{h=1}^{8760} \dot{Q}_{h,Receiver}}{\sum_{h=1}^{8760} \dot{Q}_{h,Sun}} = \frac{A_{SF} \cdot \sum_{h=1}^{8760} \left(DNI_h \cdot \eta_{h,Optical}\right)}{\sum_{h=1}^{8760} DNI_h \cdot A_{SF}} \tag{33}$$

The yearly thermal efficiency is computed considering along the year the instantaneous power hitting the receiver (as an hourly average) and the power transferred to the HTF, as in Equation (34). It depends on the receiver size and the HTF minimum temperature, as discussed in Chapter 5.2.

$$\eta_{Thermal,Yearly} = \frac{\sum_{h=1}^{8760} \dot{Q}_{h,HTF}}{\sum_{h=1}^{8760} \dot{Q}_{h,Receiver}} = \frac{\sum_{h=1}^{8760} \dot{Q}_{h,Receiver} \cdot \eta_{h,Thermal}}{\sum_{h=1}^{8760} \dot{Q}_{h,Receiver}} \tag{34}$$

The electric cycle efficiency is computed as reported in Equation (35). It is computed starting from the mechanical power of the turbomachinery, including their electromechanical efficiencies.

$$\eta_{Cycle,Electric} = \frac{W_{Expansion} \cdot \eta_{el-mech} - \frac{W_{Compression}}{\eta_{el-mech}}}{\dot{Q}_{in,cycle}} \tag{35}$$

The gross yearly electric energy produced by the plant is computed according to Equation (36), while the net yearly electric energy is proposed as final thermodynamic KPI, expressed as in Equation (37), starting from the gross yearly

electric energy and including the auxiliary consumption of the air-cooled condenser and the HTF circulation pump.

$$EE_{gross,Yearly} = \sum_{h=1}^{8760} Q_{h,in,Cycle} \cdot \eta_{Cycle,Electric} \tag{36}$$

$$EE_{net,Yearly} = EE_{gross,Yearly} - \sum_{h=1}^{8760} (EE_{h,HTF\ Pump} + EE_{h,Air\ Condenser}) \tag{37}$$

Finally, as CSP is renowned within the many renewable energy technologies for being dispatchable, the capacity factor (CF) represents a crucial parameter to compare the energy produced by various power plants at constant nominal power, computed as in Equation (38).

$$CF = \frac{EE_{net,Yearly}}{\dot{Q}_{in,cycle} \cdot \eta_{Cycle,Electric} \cdot 8760\ h} \tag{38}$$

Similarly to the capacity factor, the yearly solar to electric efficiency is the parameter that correlates the yearly electric energy production with the available solar radiation along the year, proposed in Equation (39):

$$\eta_{sol-El,Yearly} = \frac{EE_{net,Yearly}}{\sum_{h=1}^{8760} DNI_h \cdot A_{SF}} \tag{39}$$

5.5 Economic analysis of CSP plants and CO_2-based cycles

The techno-economic performances of the innovative solar plants are described with synthetic parameters, such as the yearly electric energy produced ($EE_{net,Yearly}$), the specific capital costs of the overall plant and, after assuming an hourly profile of weather data along a representative year, the levelized cost of electricity (LCOE) of the solar plant for a given location.

The capital cost functions considered in this work for CSP plants are reported in Table 34: according to the literature, the higher uncertainties on these cost functions are usually related to the solar field and the receiver. For this reason,

conservative values on both costs are assumed, considering 140 \$/m^2 of aperture area for the solar field according to SAM (an NREL tool) [123] and a reference capital costs model from Kelly [124] for the receiver and the HTF subsystems, actualized according to the CEPCI index to 2020 and corrected considering a conversion factor of 1.13 \$/€, averaged on the 2020.

The solar tower cost is computed assuming a concrete tower structure with the cost model proposed by Turchi [125]. The TES costs are computed according to a recent work of Manzolini, mentioned in the previous chapter, detailing the characteristics of various storage systems applied to CSP plants [25], while the power block costs are generally assumed within the cost functions of Weiland [110], being specific for sCO_2 power cycles, except for the correction term applied to the recuperator and the PHE (as described in Chapter 4.5). Other uncertainties are also related to the cost of the HTF to storage medium heat exchanger: as recent studies of Guccione [104] [126] detailed this component, the author implemented analogous cost functions, even if they resulted in an almost negligible solar plant cost share (around 2%).

Table 34. Capital costs correlations for the CAPEX of the overall CSP plant

Component	Capital cost function	Reference and comments
Solar Plant and solar subsystems		
Heliostats	140 \$/m^2	SAM, 2020. Specific to heliostats area
Concrete solar tower	$C_{ref,tower} \cdot \frac{\exp(0.01133 \cdot H_{rec})}{\exp(0.01133 \cdot H_{rec,ref})}$	Turchi, 2013. Actualized to 2020, in \$
Receiver	$C_{ref,receiver} \cdot (D \cdot H)^{0.6} + f(Coating) + f(Tubes\ mass, material)$	Kelly, 2010. Actualized to 2020, in \$
HTF piping, HTF pump and HTF other costs	$C_{ref,piping} \cdot \left(\frac{Q_{des}}{Q_{des,Ref}}\right)^{0.7}$	Kelly, 2010. Actualized to 2020, in \$
TES	$Q_{tes} \cdot v_{HTF} \cdot C_{HTF} + C_{Hot\ Tank} + C_{Cold\ Tank} + C_{Other}$	Manzolini, 2021, in \$
Power Cycle		
Turbine	$0.1826 \cdot W_{turb}^{0.5561} \cdot f_T$	Weiland, 2019, in \$
Compressor/Pump	$1.23 \cdot W_{compr}^{0.3992}$	Weiland, 2019, in \$
Air condenser	$32.88 \cdot UA_{Cond}^{0.75}$	Weiland, 2019, in \$
Compressor/Pump motor	$0.2114 \cdot W_{compr}^{0.6227}$	Weiland, 2019, in \$
Turbine generator	$0.1089 \cdot W_{turb}^{0.5463}$	Weiland, 2019, in \$
Recuperator (PCHE)	$f_{U,PCHE,Mix} \cdot 49.45 \cdot (UA_{PCHE})^{0.7544} \cdot f_T$	Weiland, 2019. Corrected for fluid effects, in \$
PHE (S&T)	$f_{inst+eng} \cdot f_{U,PHE,Mix} \cdot UA \cdot 2.116 \cdot \Delta P_{Tube}{}^{-0.2705}$	Thermoflex v29, 2020. Corrected for fluid effects, in \$ (See Appendix B.3)

Regarding the calculation of the LCOE, it is assumed that the cycle operates always at full load, when thermal power is available from the solar plant, not

considering any dispatching strategy. The LCOE expression is proposed in Equation (40), and the other necessary assumptions to move from the capital cost estimation to the LCOE of the CSP plants are presented in Table 35, mainly taken from SAM.

$$LCOE\left[\frac{\$}{MWh_{el}}\right] = \frac{CAPEX + \sum_{t=0}^{Lifetime}\left((EE_{year}\cdot OPEX_{variab} + OPEX_{fix})\cdot\frac{(1+i)^t}{(1+d)^t}\right)}{\sum_{t=0}^{Lifetime}\left(\frac{EE_{year}}{(1+d)^t}\right)} \quad (40)$$

Table 35. Assumptions on the OPEX and the financial risk of the CSP plant [123]

Financial assumption	Value
Indirect + Contingency	20% of the CAPEX
Fixed OPEX	66 $/kW$_{el}$/year
Variable OPEX	3.5 $/MWh$_{el}$
Discount rate	8%
Inflation rate	1%
Plant lifetime	30 years

The objective of the economic analysis is to properly assess the differences between various solar plant configurations: while the working fluid selected and the power cycle plant layout mainly affect the cycle efficiency, hence the yearly energy produced, the effect of the working fluid on the overall capital cost breakdown is less evident, since the solar system cost is independent from the power cycle. Finally, as various solar fields will be considered for various cycle maximum temperatures (550 °C, 625 °C and 700 °C), the effects of the technology level related to the higher temperatures will be evidenced on the resulting LCOE. On this matter, although the LCOE is widely acknowledged not to be an appropriate index for an economic analysis of power plants that are supposed to operate on the free market (contrarily to the NPV or the IRR), it is nevertheless computed in this work. In fact, the focus of the methodology proposed in this thesis lies in the comparison between various plant configurations and conditions, not on the exact calculation of the economic profitability for a single case study.

6. Case study: Large scale CSP plant in Las Vegas

The methodology developed in the previous chapters is adopted to study the performances of some tCO_2-mixtures power cycles in a hypothetical solar power plant in Las Vegas (USA), a location with abundant solar radiation, that is often selected in literature for the modeling of CSP plants. The results will be scrutinized evidencing the effectiveness of the new technology with respect to a more conventional solution for CSP applications, considering the cycle efficiency, the energy produced and the cost effectiveness. The case study of this chapter is developed across a literature work belonging to the SCARABEUS project [93].

6.1 A sensitivity analysis on the CSP plant and power cycle design

A series of state-of-the-art and next-generation solar tower CSP plants adopting transcritical CO_2-based binary mixtures power cycles are analyzed. Three CO_2-based binary mixtures are selected and compared against sCO_2 considering: i) different cycle layouts, ii) different cycle maximum temperatures, iii) direct and indirect storage arrangements and iv) different HTF in the solar receiver. For each plant, the yearly electric energy yield and the LCOE are computed, optimized varying the SM and the TES capacity.

Since not all the combinations of working fluids and cycle maximum temperatures are technically feasible, due to the thermal stability limits of the working fluids (as reported in Chapter 2), the configurations proposed in this work are summarized in Table 36. Since the others CO_2 mixtures (as the ones with SO_2 or $TiCl_4$, for example) have been already investigated by other SCARABEUS partners, the purpose of this analysis is to explore innovative mixtures.

A sensitivity on the power cycle maximum temperature is carried out to understand the sensitivity of this parameter on the main techno-economic indicators, highlighting whether tCO_2-mixtures cycles employed in state-of-the-art plants can reach the level of attractiveness normally proposed in literature for sCO_2 cycles with maximum temperatures of 700 °C.

Table 36. Four cases proposed for the yearly analysis of the innovative CSP plant performances in Las Vegas

Cycle TIT	HTF	Storage Fluid	Storage Configuration	sCO_2 Cycles	CO_2+C_6F_6 Cycles	CO_2+C_4F_8 Cycles	CO_2+C_2H_3N Cycles
550 °C	Solar Salts	Solar Salts	Direct	✓	✓	✓	✓
550 °C	Sodium	Solar Salts	Indirect	✓	✓	✓	✓
625 °C	Sodium	Advanced Salts	Indirect	✓	✓	x	x
700 °C	Sodium	Advanced Salts	Indirect	✓	x	x	x

6.2 Solar plant optimization

In this chapter the four solar plants listed in Table 36 will be fully characterized, assuming a large-scale power plant size and evidencing the possible influence of the tCO_2-mixtures on the design of the various solar components.

Given the thermal stability of solar salts, only plants with direct storage and maximum power cycle temperature of 550 °C will adopt solar salts as HTF. For the other solar plants, using sodium as HTF, only the indirect storage configuration is considered, since the solution with direct storage adopting sodium is discarded due to a high specific cost per unit of mass and per unit of thermal energy stored [113].

In accordance with the HTF selection, different maximum allowable heat fluxes on the receiver must be considered: receivers working with solar salts are subjected to maximum allowable thermal fluxes of around 1 MW/m^2 [124], while receivers with sodium as HTF can theoretically handle maximum thermal inputs of 2 MW/m^2 [127], according to estimations from literature. Therefore, with similar thermal power delivered on the receiver, configurations of receivers with sodium as HTF are expected to have around half the area of the counterpart adopting solar salts, if the design of the receiver is carried out close to the maximum flux condition. For this reason, the receiver thermal efficiency can increase even if higher HTF average temperatures are foreseen, counterbalancing the higher convective and radiative losses.

For each solar field, the design receiver thermal input ($\dot{Q}_{in,rec}$) is obtained through Equation (41) considering a net power output (P_{net}) of 100 MW_{el}, a SM of 2.4 as in the Crescent Dunes plant [128] and net electric cycle efficiencies ($\eta_{Cycle,Electric}$) of 41%, 44% and 47% for the configuration with cycle maximum temperatures of 550 °C, 625 °C and 700 °C, respectively. First guesses on the thermal efficiency are also done: 85% is considered for the configuration with solar salts, while values of 88%, 86% and 84% are adopted for sodium-cooled

receivers with cycle maximum temperatures of 550 °C, 625 °C and 700 °C, respectively.

$$\dot{Q}_{in,rec} = \frac{P_{net} \cdot SM}{\eta_{Cycle,Electric} \cdot \eta_{th}} \tag{41}$$

Based on these first guesses on the receiver thermal input for each condition, the four solar fields are designed applying the procedure hereby described and mentioned briefly in Figure 41, where both the optical and the thermal efficiency are iteratively computed with the tools presented in this thesis. While designing the solar field in SolarPilot, image size priority with a maximum offset factor of 2 is adopted as heliostats aiming strategy [26].

The solar plant with solar salt as HTF is treated separately from the other three cases as it represents state-of-the-art molten salts solar towers (except for the HTF minimum temperature which is above 400 °C, instead of the typical value of 290 °C [124]). For this case, the tower height is set to 195 m as for the Crescent Dunes plant, and the receiver dimensions are chosen in order to have a maximum heat flux of 1 MW/m^2 with an aspect ratio (H/D) of 1.25 [124]. The resulting solar field characteristics and receiver dimensions are reported in Table 37. Both for the solar salts-cooled receiver and the sodium-cooled receiver with a working fluid maximum temperature of 550 °C, the heliostats dimensions (both height and width) were selected optimizing the optical efficiency at design conditions.

For the other three cases with sodium as HTF smaller heliostats and a higher tower height are assumed to reduce the cosine losses and to compensate for the reduction of the intercept factor and thus of the optical efficiency, caused by the smaller receiver dimensions. Afterwards, an iterative optimization procedure is applied to design each of the three solar fields with sodium-cooled receivers, as the one shown in Figure 41, and simultaneously determine the corresponding receiver dimensions necessary to deliver the desired receiver thermal input, as proposed in Equation (41). In detail, the receiver diameter and height are varied (with a 0.1 m step in diameter) fixing the H/D aspect ratio to 1.25 (similarly to Crescent Dunes). After this first iteration loop, the receiver area was fixed to the condition with maximum optical-thermal efficiency in design conditions. Finally, a second iteration loop is added, at constant receiver area varying the receiver aspect ratio to find its optimal value according to the same criterion. The characteristics of the optimal solar field and receiver obtained for each case are reported in Table 37. The latter shows how, when sodium is adopted HTF, the optimal receiver aspect ratio computed according to this procedure is 1.1, while the optimal peak heat flux results about 1.7 MW/m^2 for all the cases, thus below the value 2 MW/m^2 considered as typical limit for sodium-cooled receivers [129]. This is consistent with the results obtained by Asselineau [130], who showed that

the optimal maximum flux for sodium receivers is not necessarily 2 MW/m^2, as this condition significantly penalizes the optical efficiency.

Table 37. Characteristics of the different solar fields designed: geometrical data and optical performances

	Solar Fields Design Assumptions			
Location	Las Vegas			
Geographical Coordinates	N: 36.08° W: 115.17°			
Direct Normal Irradiation at design [W/m^2]	950			
Sun Location at design point	Solar Noon, Summer Solstice Solar Altitude: 77.4°			
Denomination of the Solar Field	**Direct 550 °C**	**Indirect 550 °C**	**Indirect 625 °C**	**Indirect 700 °C**
HTF temperature range [°C]	421-565	436-580	488-655	540-730
Working fluid maximum temperature [°C]	550	550	625	700
TES Configuration	Direct	Indirect	Indirect	Indirect
HTF	Solar Salts	Sodium	Sodium	Sodium
Storage Fluid	Solar Salts	Solar Salts	Advanced Salts	Advanced Salts
Tower height [m]	195	235	235	235
Heliostat size [m x m]	8 x 10	5 x 7	5 x 7	5 x 7
	Design Results			
Receiver Height [m]	21.0	15.4	15.1	15.0
Receiver Diameter [m]	16.8	14.0	13.7	13.7
Solar field area [m^2]	1 246 240	1 197 315	1 125 950	1 097 460
Number of heliostats	15 578	34 209	32 170	31 356
Nominal optical efficiency [%]	61.78	61.82	62.35	62.82
Maximum solar flux on the receiver [MW$_{th}$/m^2]	0.972	1.719	1.752	1.719
Overall power on the receiver [MW$_{th}$]	709.5	682.1	646.9	635.3

As a result, the difference in optical efficiency between the various solar plants is limited: sodium-cooled receivers benefit from an increment in tower height with respect to the solar salts-cooled receiver, the cosine effects are reduced, counterbalancing the spillage losses. Moreover, the progressive reduction in the overall thermal power to the receiver for the sodium-cooled receivers and the subsequent reduction in solar field dimension also entails an increment in optical efficiency. The planar view of the solar fields and the solar flux on the receiver at design conditions are reported in Appendix C.1, along with the optical performance maps of each solar field.

6.3 Receiver design and performances

The number of panels for each flow path of the HTF of the four receivers investigated in this case study was taken from literature: the receiver with solar salts as HTF adopted the characteristics of crescent dunes plant, while for the receivers with sodium a reference condition from literature was assumed [24]. The

tubes diameter and thickness are assumed between the standard pipe sizes [131] and the number of tubes per panels are computed ensuring a spacing between the tubes of 2 mm [121]. As a consequence, the receivers main characteristics and operating conditions are reported in Table 38. Among those, the HTF temperature range is selected considering a 15 °C temperature difference at the cold- and hot-ends of both the HTF-to-storage fluid HX and of the power cycle PHE, assuming the power cycle working with the CO_2+C_6F_6 mixture in simple recuperative configuration as reference case for the innovative technology adopting CO_2-based cycles.

Table 38. Assumed characteristics and design performances of the receivers of the solar plants investigated

	Assumptions on the receiver characteristics			
Configuration and HTF	Direct 550 °C, Solar Salts	Indirect 550 °C, Sodium	Indirect 625 °C, Sodium	Indirect 700 °C, Sodium
HTF temperature range [°C]	421-565	436-580	488-655	540-730
Wind speed [m/s]	5.2	5.8	5.8	5.8
Tube material	Haynes 230			
Tube internal diameter [mm]	49.6			
Tube thickness [mm]	1.65			
Tube spacing [mm]	2			
Tube absorptivity [%]	94			
Tube emissivity [%]	87			
Number of panels per flow path	7	4	4	4
Number of flow paths	2	2	2	2
	Resulting characteristics of the receiver and design performances			
Number of tubes per panel [-]	68	100	98	98
Overall number of tubes [-]	952	800	784	784
Thermal efficiency [%]	85.9	88.4	87.1	85.8
Specific thermal losses [$kW_{th}/m^2_{receiver}$]	90.2	116.8	128.5	139.7
Thermal power to the HTF [MW_{th}]	609.5	603.0	563.4	545.1
HTF mass flow rate [kg/s]	2768	3313	2687	2292

The wind speed on the tower is assumed as function of the receiver altitude as a yearly average value for the location [132]. In addition, the receiver thermal efficiencies are evaluated for different values of working fluid temperature at the inlet of the PHE at design conditions, with the same assumptions of the temperature difference at cold end of the HXs, developing the relationships for the thermal efficiency as function of the thermal input to the receiver and the HTF temperature range, as suggested in Figure 42. The resulting thermal efficiency maps, which will be adopted for the plant yearly analysis, are reported in Figure 44. The figure shows how the thermal efficiency strongly depends on the working fluid temperature at the inlet of the PHE when sodium is adopted as HTF. Moreover, the use of sodium is beneficial to the thermal efficiency for all configurations, when compared to solar salts, even at much higher temperatures, due to the significant reduction in the receiver area. Accordingly, the indirect

configuration with sodium as HTF and molten salts as storage fluid (Figure 44 (b), (c), (d)) presents evident advantages in terms of thermal efficiency with respect to the direct TES configuration (Figure 44 (a)).

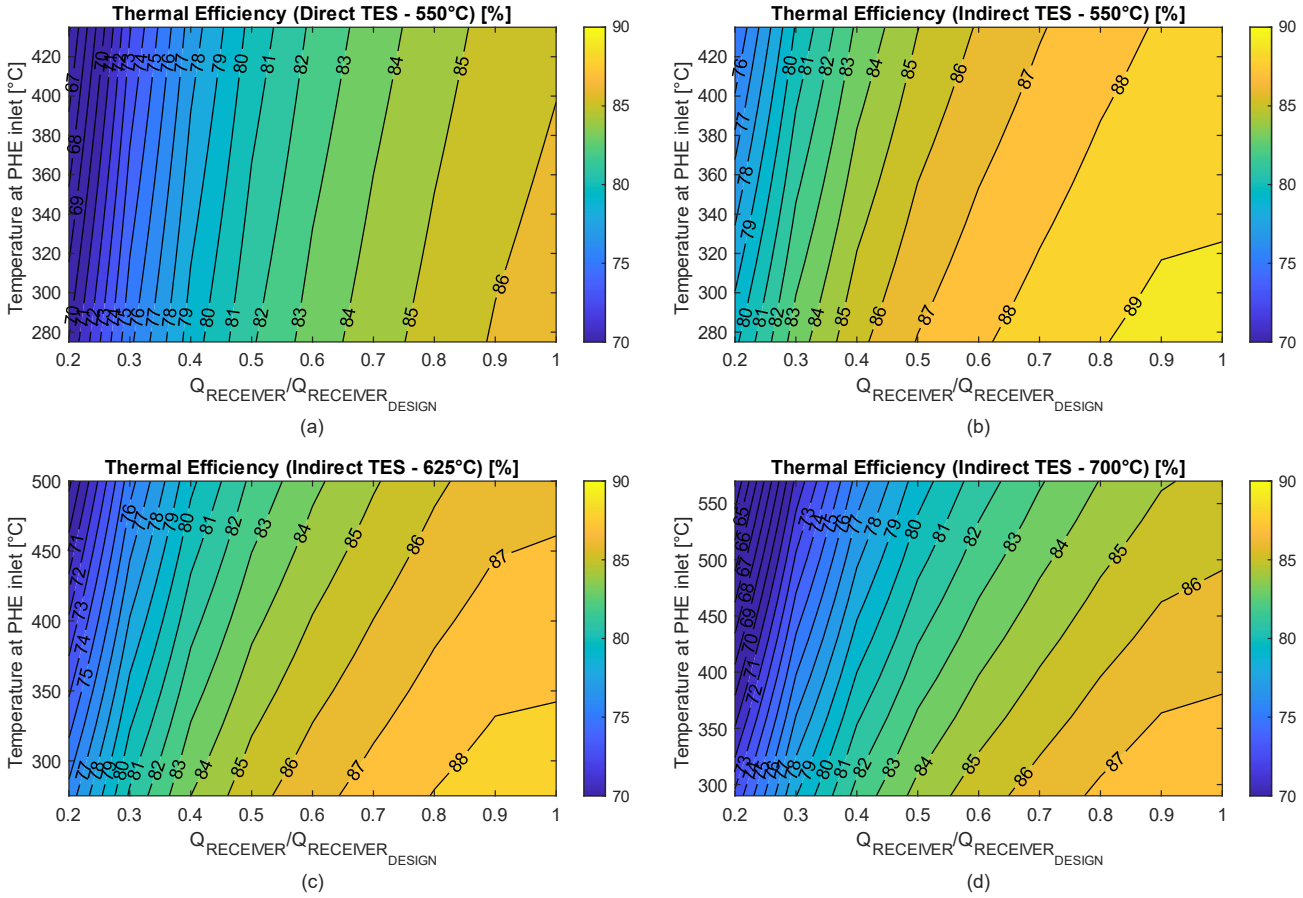

Figure 44.Thermal efficiency maps for the four receivers considered in this work: direct 550 °C (a), indirect 550 °C (b), indirect 625 °C (c), indirect 700 °C (d). The denomination refers to the ones proposed in Table 37

6.4 HTF pump consumption

The maps reported in Figure 45 quantify the electric power consumed by the HTF pump as function of the thermal power to the receiver and the temperature of the working fluid at the inlet of the PHE at design conditions (univocally determined for each power cycle – solar plant combination).

In accordance to Equation (30), the calculation of the computed HTF pump consumption for the direct storage configuration is significantly higher than the indirect configurations (due to the influence of the geodetical term), with the highest relative difference in off design conditions where the power incident on

the receiver is lower than the design value due to a reduction in HTF mass flow rate.

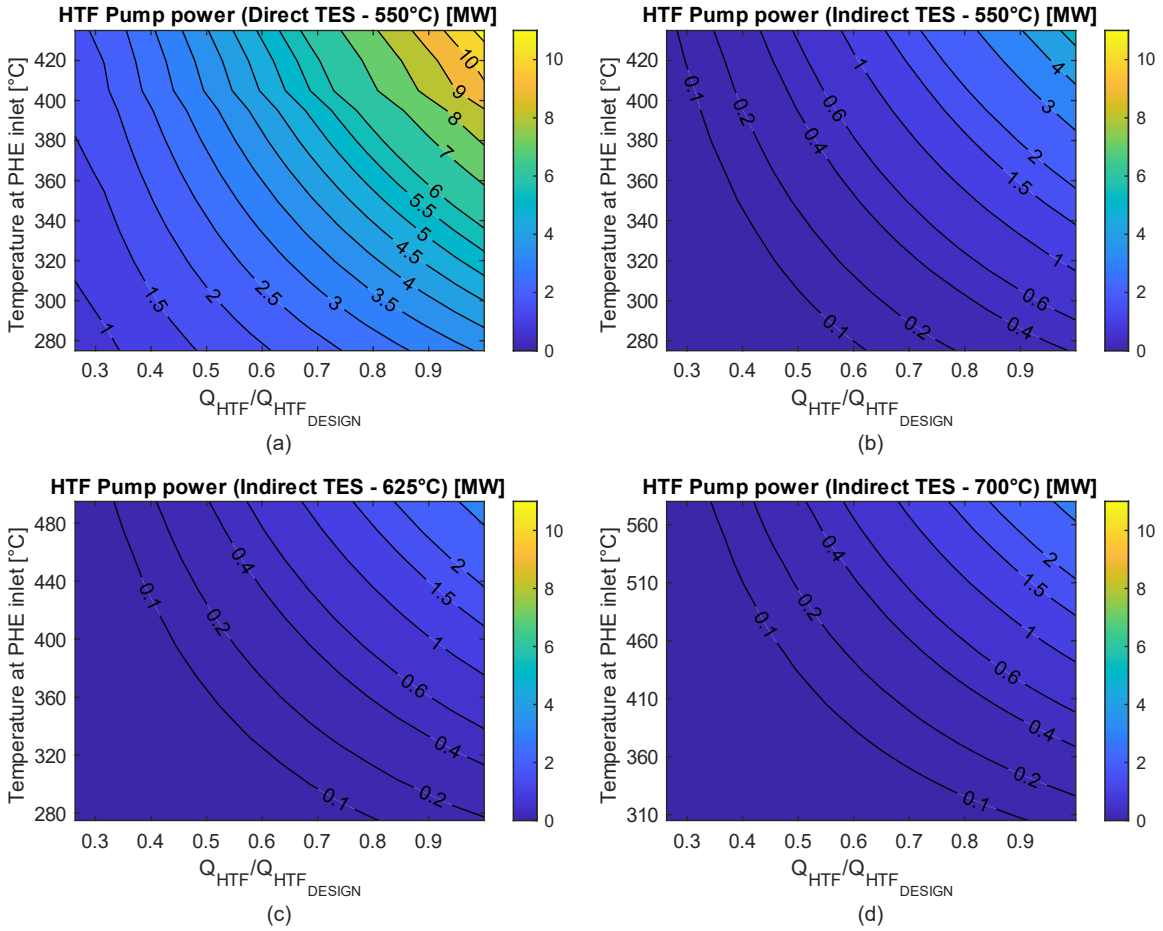

Figure 45. HTF pump auxiliary consumption maps for the four solar fields considered in this work, expressed in MW_{el}: direct 550 °C (a), indirect 550 °C (b), indirect 625 °C (c), indirect 700 °C (d). The denomination of the four solar plants refers to the ones proposed in Table 37

According to the results presented in terms of solar field optical efficiency and receiver thermal efficiency, the considerations on the solar field area and accounting for the drastic reduction of the auxiliary consumption of the HTF circulation pump, the indirect storage configuration appears more promising than the direct one for any HTF temperature range across the receiver.

From an energetic point of view, the drop in optical efficiency of the solar plants with indirect storages can be balanced increasing the solar tower height, while the thermal efficiency computed can increase by 2.5% at constant HTF temperature range, so that indirect storage solutions with cycle maximum temperatures around 700 °C present comparable thermal efficiencies to direct storage solutions with cycle maximum temperatures of 550 °C. Finally, the HTF pump consumption can be reduced by a factor from 5 to 10, depending on the thermal input to the receiver. As a matter of fact, the HTF pump auxiliary consumption for a direct storage system based on solar salts in Figure 45 (a) is

considerably high for any value of working fluid temperature at PHE inlet. In this particular case, with a reference plant of around 100MW_{el}, the HTF pump consumes up to 10 MW_{el} at design conditions, for a recompressed sCO_2 cycle with high PHE inlet temperature. Even if this peak electric consumption is experienced for a minor fraction of operating hours, due to the effects of high solar multiple and DNI lower than the design value, the adoption of an indirect storage is a determining factor in cutting this significant source of parasitic electric consumption.

6.5 Power cycle and TES coupling

The analysis proposed in this case study includes power cycle simulations for the four working fluids listed in Table 36. Each one of them is considered in four plant layouts, including the simple recuperative, the recompressed, the precompressed and the cascade layout (shown in Figure 16): the simple recuperative layout is selected as a reference, the precompressed and recompressed are studied in order to increase the performance of the simple layout, while the cascade is studied to emphasize the capabilities of tCO_2-mixtures cycles to efficiently run in conditions where a large temperature difference across the hot source is imposed. For each combination of mixture, cycle layout and cycle maximum temperature, a sensitivity analysis on the mixture molar fraction is performed, with the goal of maximizing the cycle efficiency.

For representation purposes, the trends of the simple recuperative cycle efficiencies as function of dopant fraction for each mixture are plotted in Figure 46, assuming a cycle maximum temperature of 550 °C.

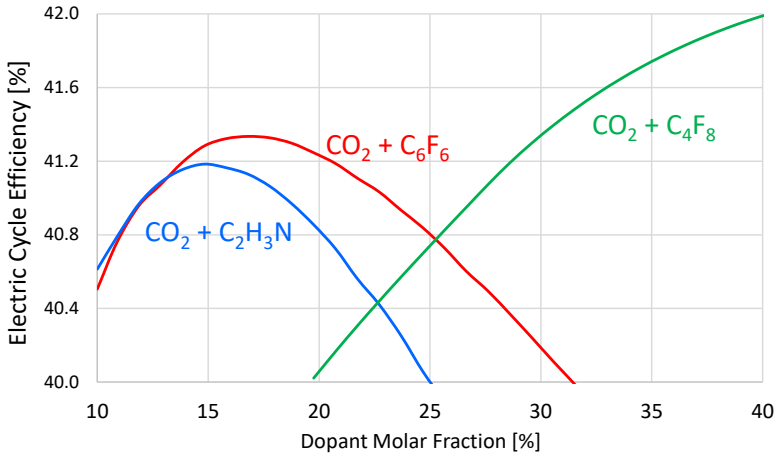

Figure 46. Analysis on the mixture composition on the electric cycle efficiency of the simple recuperative cycles with a TIT of 550 °C

For the precompressed layout the turbine outlet pressure is included as additional optimization variable, while, for the cascade layout, the splitter mass ratio is set to have both the cold and hot end temperature difference in the HT recuperator equal to the minimum allowed temperature difference (i.e. 5 °C).

The optimized dopant fractions for each cycle layout and mixture, together with the temperature at the inlet of the primary heat exchanger, are presented in Table 39 with the electric cycle efficiency, again assuming the conditions at maximum temperature of 550 °C.

Table 39. Cycle conditions considering for the analyzed fluids as function of the plant layout, at cycle maximum temperatures of 550 °C

	Working fluid	Power block layout			
		Simple Recuperative	Precompressed	Recompressed	Cascade
Dopant molar fraction [%]	CO_2+C_6F_6	16	15	-	16
	CO_2+C_4F_8	27	27	27	27
	CO_2+C_2H_3N	15	13	-	15
Cycle Electric Efficiency [%]	CO_2+C_6F_6	41.3	42.2	-	39.2
	CO_2+C_4F_8	40.9	42.0	43.4	38.8
	CO_2+C_2H_3N	41.2	41.9	-	39.2
	Pure CO_2	37.4	40.0	41.7	35.5
Working fluid Temperature at PHE inlet [°C]	CO_2+C_6F_6	406	400	-	293
	CO_2+C_4F_8	408	405	425	296
	CO_2+C_2H_3N	364	361	-	293
	Pure CO_2	384	409	418	293

For C_6F_6 and for C_2H_3N the recompressed layout is not considered because it is not possible to reach single-phase conditions at the inlet of the compressor (point #10 in Figure 16), due to the extended range of the VLE region for any composition of interest (referring, for example, to Figure 10 and Figure 15). On the other hand, for the CO_2+C_4F_8 mixture the optimal molar composition is limited to a maximum value of 27% for C_4F_8 in all the cycle architectures, in order to have a good cycle efficiency without reducing excessively the presence of CO_2 (especially on mass basis) in the working fluid.

A second relevant cycle parameter is the working fluid temperature at the PHE inlet. This parameter strongly influences the achievable cycle efficiency, the receiver thermal efficiency and the cost of the storage section, as the higher the temperature difference of the storage fluid across the PHE, the lower the HTF mass flow rate in the receiver, with small TES volume and lower costs at constant thermal input. Under this perspective, the CO_2 mixture with C_2H_3N is significantly more performant than the other working fluids.

The air-cooled condenser fan consumption is assumed equal to 0.85% of the heat rejected at the condenser at design conditions (at an ambient temperature of

36 °C). Along the year the power block is always operated at full-load, if thermal power is available, and with a constant cycle minimum temperature, considering as the only off-design effect the impact of the ambient temperature on the air condenser fan rotational speed [114]. The fan consumption is computed as function of the mass flow rate of the air, as already proposed in literature, for any ambient temperature [133] [134]: the simplified approach can help in comparing performances of different power cycles independently from the study of their off-design.

Since both the receiver thermal efficiency and the TES dimension are affected by the coupling between the solar plant and the power block layout, the optimal techno-economic configuration will inevitably be influenced by these factors, as lower TES specific costs and lower cycle efficiencies are two contrasting effects. In Figure 47 it is qualitatively summarized the impact of the temperature difference across the PHE on the system performance and cost.

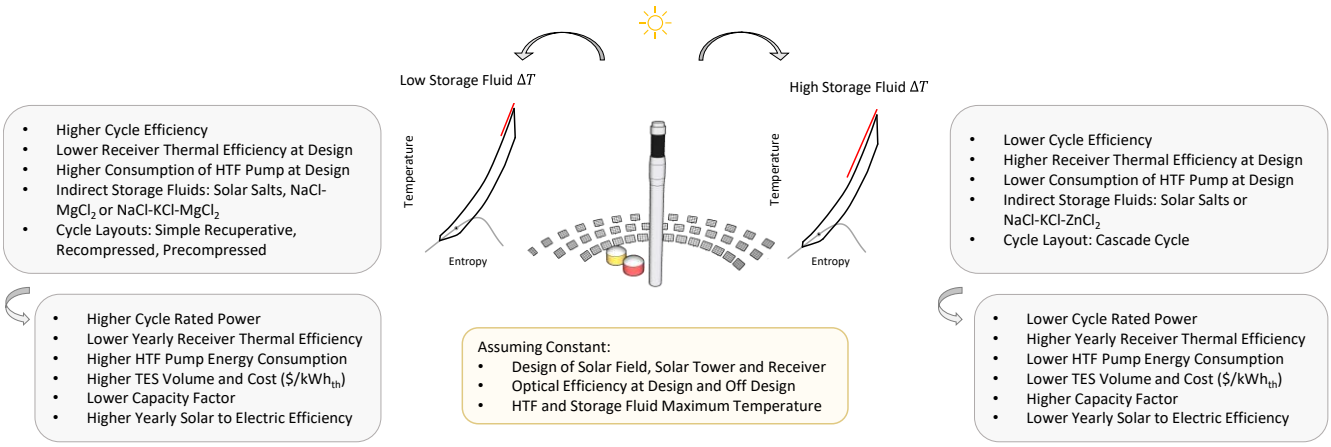

Figure 47. Differences between a high heat recovery and a low heat recovery power cycle for CSP configurations working with CO_2-based fluid

The objective of the economic analysis is to properly assess the differences between various plant configurations: while the working fluid selection largely affects the cycle efficiency, hence the yearly energy produced ($EE_{net,Yearly}$), the effect of the working fluid on the overall CAPEX breakdown is less evident, since the solar system costs are independently from the power block layout and the TES. On the other hand, different power cycle layouts using the same working fluids will present different capital costs: for example, the cascade cycle is a simple layout recovering heat from the hot source across a wide temperature range. For these reasons, the lower values of cycle efficiencies would entail a lower yearly energy produced, but at the same time this effect is well balanced by the lower capital cost of both the TES and the power block. The recompression cycle, instead, is expected to produce more electric energy yearly, with

significantly higher TES costs, due to the lower HTF temperature difference, and high power block costs, due to addition of power block components.

Finally, as the four different solar fields are considered for three cycle maximum temperatures (550 °C, 625 °C and 700 °C), the effects of increasing the technology level related to the higher temperatures will be evidenced on the resulting LCOE.

The trade-off between the various effects related to costs (hence complexity) of the solar plants and the actual yearly electricity yield is the main outcome of the techno-economic analysis carried out, which is proposed in the following chapter.

6.6 Yearly thermodynamic analysis of the plants at full load

In this chapter the different combinations of solar fields, power cycles and TES systems explored are described in terms of annual electricity yield for each configuration, along with the main technical and economic key performance indicators described in Chapter 5.4. As already mentioned, the calculations are carried out considering Las Vegas (DNI_y =2672 kWh/m^2/year) as location and using hourly DNI data from SolarPilot. Even if in the design procedure the solar multiple was fixed at 2.4, its optimal value is not known in advance: for this reason, a sensitivity analysis on both the solar multiple and the TES size is carried out for each configuration proposed, with the aim of minimizing the LCOE.

In addition, as each configuration has a specific receiver thermal efficiency (determined in Figure 44), cycle efficiency, and auxiliary consumptions (computed as reported in Figure 45), even by fixing the solar field the various solutions will present different optimal cycle nominal electric powers, lower than 100 MW_{el} if the optimal solar multiple is higher than the reference value of 2.4.

The overall yearly analysis proposed is evaluated as discussed in Figure 42.

The resulting thermodynamic performances of the optimal configuration of power cycles investigated in this work are reported in the four tables below. The mixture CO_2+C_6F_6 is not explored for maximum temperatures of 700 °C and both the CO_2+C_4F_8 and CO_2+C_2H_3N mixtures are only proposed at 550 °C due to the thermal stability limits, referring to Table 36.

As presented in the next chapter, all the solar plants report optimal SM equal to 2.8 and an optimal TES size of 12 equivalent hours, since this is the condition that minimizes the LCOE for all the configurations studied.

Table 40. Characterization of the optimal cycle and yearly energy analysis of the various configurations of CSP plants adopting the direct 550 °C solar field

Power Cycle 550 °C Direct Storage		**Power [MW_{el}]**	η_{Cycle}	CF	$EE_{gross,\ Yearly}$ **[GWh_{el}]**	$EE_{Aux,\ Yearly}$ **[GWh_{el}]**	$EE_{net,\ Yearly}$ **[GWh_{el}]**	$\eta_{Thermal,\ Yearly}$	$\eta_{sol-El,\ Yearly}$
sCO_2	Simple	81.4	37.4%	69.7%	521	24	497	83.8%	15.4%
	Recompressed	90.4	41.7%	69.5%	578	28	550	83.5%	17.0%
	Precompressed	86.8	40.0%	69.5%	555	27	528	83.6%	16.4%
	Cascade	77.5	35.5%	71.0%	497	15	482	84.4%	14.9%
CO_2 + C_6F_6	Simple	89.7	41.3%	69.6%	574	27	547	83.6%	16.9%
	Recompressed	-	-	-	-	-	-	-	-
	Precompressed	91.7	42.2%	69.8%	586	26	561	83.7%	17.4%
	Cascade	85.6	39.2%	71.1%	549	15	533	84.4%	16.5%
CO_2 + C_4F_8	Simple	88.8	40.9%	69.5%	568	27	541	83.6%	16.8%
	Recompressed	94.2	43.4%	69.5%	602	29	573	83.5%	17.8%
	Precompressed	91.3	42.0%	69.7%	584	26	558	83.6%	17.3%
	Cascade	84.7	38.8%	71.1%	543	15	528	84.3%	16.3%
CO_2 + C_2H_3N	Simple	89.6	41.2%	70.2%	573	22	551	83.9%	17.1%
	Recompressed	-	-	-	-	-	-	-	-
	Precompressed	91.2	41.9%	70.3%	584	22	562	83.9%	17.4%
	Cascade	85.7	39.2%	71.1%	550	16	534	84.4%	16.5%

Table 41. Characterization of the optimal cycle and yearly energy analysis of the various configurations of CSP plants adopting the indirect 550 °C solar field

Power Cycle 550 °C Indirect Storage		**Power [MW_{el}]**	η_{Cycle}	CF	$EE_{gross,\ Yearly}$ **[GWh_{el}]**	$EE_{Aux,\ Yearly}$ **[GWh_{el}]**	$EE_{net,\ Yearly}$ **[GWh_{el}]**	$\eta_{Thermal,\ Yearly}$	$\eta_{sol-El,\ Yearly}$
sCO_2	Simple	80.5	37.4%	70.9%	509	10	500	87.2%	16.1%
	Recompressed	89.3	41.7%	70.6%	565	12	553	86.8%	17.8%
	Precompressed	85.8	40.0%	70.7%	543	11	531	86.9%	17.1%
	Cascade	76.9	35.5%	71.5%	488	6	482	88.0%	15.5%
CO_2 + C_6F_6	Simple	88.7	41.3%	70.7%	561	12	549	86.9%	17.7%
	Recompressed	-	-	-	-	-	-	-	-
	Precompressed	90.6	42.2%	70.8%	574	11	562	87.0%	18.1%
	Cascade	84.9	39.2%	71.6%	538	6	532	88.0%	17.2%
CO_2 + C_4F_8	Simple	87.8	40.9%	70.7%	555	12	544	86.9%	17.5%
	Recompressed	93.0	43.4%	70.6%	588	13	575	86.7%	18.5%
	Precompressed	90.2	42.0%	70.8%	571	11	560	87.0%	18.0%
	Cascade	84.0	38.8%	71.6%	533	6	527	88.0%	17.0%
CO_2 + C_2H_3N	Simple	88.7	41.2%	71.1%	562	9	552	87.3%	17.8%
	Recompressed	-	-	-	-	-	-	-	-
	Precompressed	90.3	41.9%	71.2%	572	9	563	87.4%	18.1%
	Cascade	85.0	39.2%	71.5%	539	7	533	88.0%	17.2%

Table 42. Characterization of the optimal cycle and yearly energy analysis of the various configurations of CSP plants adopting the indirect 625 °C solar field

Power Cycle 625 °C Indirect Storage		**Power [MW_{el}]**	η_{Cycle}	CF	$EE_{gross,\ Yearly}$ **[GWh_{el}]**	$EE_{Aux,\ Yearly}$ **[GWh_{el}]**	$EE_{net,\ Yearly}$ **[GWh_{el}]**	$\eta_{Thermal,\ Yearly}$	$\eta_{sol-El,\ Yearly}$
sCO_2	Simple	80.1	40.6%	71.0%	509	8	498	85.4%	17.5%
	Recompressed	88.8	45.2%	70.8%	560	9	551	84.9%	19.4%
	Precompressed	85.3	43.3%	70.8%	538	9	530	85.1%	18.6%
	Cascade	76.2	38.0%	71.6%	483	5	478	87.1%	16.8%
CO_2 + C_6F_6	Simple	87.3	44.4%	70.8%	550	9	541	85.1%	19.0%
	Recompressed	-	-	-	-	-	-	-	-
	Precompressed	90.0	45.7%	70.9%	568	9	559	85.1%	19.6%
	Cascade	84.6	42.5%	71.5%	535	6	530	86.5%	18.6%

Table 43. Characterization of the optimal cycle and yearly energy analysis of the various configurations of CSP plants adopting the indirect 700 °C solar field

Power Cycle 700 °C Indirect Storage		**Power [MW_{el}]**	η_{Cycle}	CF	$EE_{gross,\ Yearly}$ **[GWh_{el}]**	$EE_{Aux,\ Yearly}$ **[GWh_{el}]**	$EE_{net,\ Yearly}$ **[GWh_{el}]**	$\eta_{Thermal,\ Yearly}$	$\eta_{sol-El,\ Yearly}$
sCO_2	Simple	86.5	43.7%	70.7%	543	7	536	83.6%	18.4%
	Recompressed	94.4	47.9%	70.5%	592	8	584	83.1%	20.0%
	Precompressed	91.0	45.9%	70.8%	571	7	564	83.6%	19.3%
	Cascade	83.5	41.7%	71.2%	526	5	521	84.9%	17.8%

According to the results, it is evident that in any optimal configuration the capacity factor is always around 70%. This outcome is very encouraging since it demonstrates that all the proposed solar tower CSP plants can achieve a power production profile close to a baseload plant, particularly in the summer season.

Regarding the power cycle electric efficiencies, the results evidence significant increments in cycle efficiency for the CO_2 based mixtures with respect to sCO_2 cycle (higher than 3% in absolute value, as an average) for the two simpler power cycle adopting the simple recuperative plant layout and the cascade layout. Cycle efficiency increments with respect to sCO_2 are also evidenced for CO_2 mixture transcritical cycles adopting the precompression and recompression layout, but are more limited, below 2% in absolute value. The resulting cycle performances, then, prove the good characteristics of simpler plant layouts for CSP applications, especially when CO_2 mixtures are adopted. As a matter of fact, the two simpler layouts are characterized by a single compression step across the whole power cycle, that for transcritical cycles occurs in the liquid region. This key characteristic is a significant technological advantage that can favor the innovative transcritical cycles based on tCO_2-mixtures, on the basis of a simpler design process of the components and on the operation of the power cycle.

The auxiliary yearly energy consumption is relevant for the direct storage configuration in Table 40: a comparison between the two configurations at 550 °C of cycle maximum temperature adopting a direct and an indirect storage system

(in Table 41) can evidence that as an average around 12 GWh_{el} (up to 15 GWh_{el}) are saved yearly in HTF pump consumption, a difference already marked in Figure 45. This energy saved can represent between 2% and 3% of the overall yearly energy produced by the CSP plant and it is only ascribed to the different storage configuration.

Regarding the yearly thermal efficiencies, comparing the same cycle configuration and working fluid at 550 °C maximum temperature with the direct and the indirect storage, variations in yearly thermal efficiencies can easily reach 3%. Combining the energy saving of the HTF pump and the increment in thermal efficiency of the receiver, this work emphasizes the potentiality of the indirect storage configuration as a possible solution to increase the yearly energy yield of conventional CSP plants. Finally, the yearly values of solar to electric efficiencies varies between 15% and 20%, mainly depending on the maximum temperature levels, as higher cycle maximum temperatures entail higher cycle efficiencies and therefore higher solar to electric efficiencies.

From the point of view of the net yearly energy produced, the innovative CO_2 based mixtures present non-negligible advantages with respect to sCO_2 cycles, as all power cycle layouts with all the proposed mixtures in this work are able to produce more energy than the sCO_2 counterpart in these CSP plants. It is crucial to underline that these conclusions are presented fixing the solar field, the receiver and the solar tower between different working fluids, but the optimal power cycle size (its nominal power) results different for each configuration, and this directly influences the yearly energy production.

6.7 Yearly economic analysis of the plants at full load

For the different configurations of solar plants considered in this work, and proposed in the previous chapter, this chapter shows their economic analysis.

The results of the sensitivity analysis of the solar multiple and the TES size on the LCOE and the capacity factor are presented in Figure 48, only for two configurations of cycles at 550 °C maximum temperature and indirect storage system: the recompression sCO_2 cycle (since it is the most studied layout in CSP plants) and the simple recuperative cycle with the CO_2+C_6F_6 mixture (one of the most studied mixture in this thesis). These results are representative of all the calculations carried out within this work, as the other configurations present different absolute values of LCOE but identical trends. As mentioned and clearly noticeable in the LCOE maps, the condition characterized by a solar multiple of 2.8 and 12 equivalent hours of storage capacity is the optimal and always presents capacity factors around 70%, for this case study. Nevertheless, the results show that profitable configurations are achievable also for a range of capacity factors from 60% (SM of 2.4, 8 h of TES) to 74% (SM of 3, 14h of TES).

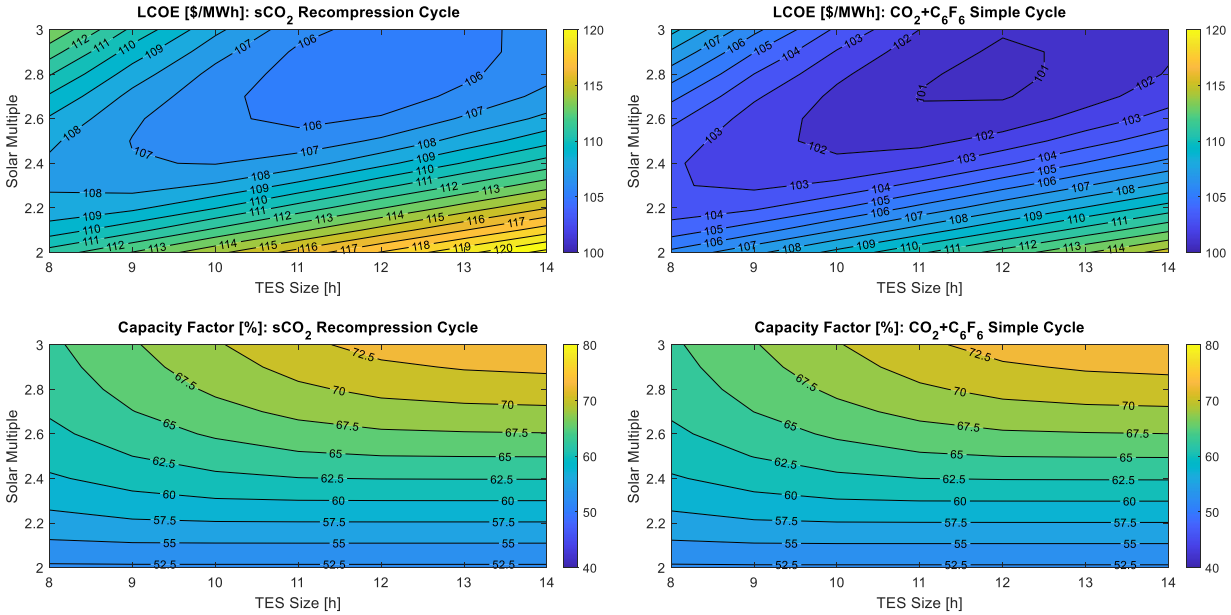

Figure 48. LCOE and CF maps of the CSP plants with indirect storage and 550 °C of cycle maximum temperature: sCO_2 recompression cycle (left) and CO_2+C_6F_6 simple recuperative cycle (right)

In Appendix C.2 is presented the capital cost breakdown of the many solar plants considered, along with the LCOE of each case. The capital cost of the power cycle is reported both in specific terms and absolute terms, and it is shown to underline the dependence of the power block costs on: i) the working fluid adopted (to stress the implications of different cost functions of the main heat exchangers, according to the analysis of Chapter 4.5), ii) the cycle maximum temperature and iii) the power cycle layout. The large variability in the TES capital costs stresses the implications of choosing a different power cycle layout on the overall capital costs of the CSP plant: for example, a cost saving in the order of 7% of the overall capital cost can be achieved in case the cascade power cycle is adopted with respect to the recompression cycle. The final total cost for each configuration is also reported in Appendix C.2, including the indirect and contingency additional fraction of the costs: the resulting capital cost specific to the nominal power production capacity is between 5500 and 6300 $\$/kW_{el}$, depending on the configuration adopted, a range coherent with values of real power plants with storage capacities in the same range [21]. This result can be compared to other renewable energy technologies, such as PV or wind power, only considering the two inherently advantageous characteristics that CSP proposes with respect to other renewables: the higher capacity factor (around 70% in this work), and the dispatchability of the energy produced.

Finally, the LCOE for each configuration is proposed: it is usually considered the key economic indicator for power production technologies, even if its value is

normally strongly dependent on the solar resources of the location, the size of the power plant and the cost functions adopted. LCOE in the order of 105 $/MWh_{el}$ can be achieved in case sCO_2 power cycles are adopted at 550 °C of maximum temperature, while it can easily drop below 100 $/MWh_{el}$ if the maximum temperature of the system is moved up to 700 °C. In case CO_2-based mixtures are adopted in transcritical power cycles, the LCOE of the CSP plants is expected to drop with respect to the sCO_2 case by around 5% for the CO_2+C_6F_6 mixture, 4% for the CO_2+C_4F_8 mixture and up to 10% for the CO_2+C_2H_3N mixture. As a matter of fact, the CO_2+C_2H_3N mixture takes the highest advantages from the lower capital cost of the TES systems (given the lower temperature of heat introduction in the power cycles) and the lower capital cost for the main heat exchanger of the power cycles, as reported in Table 29 and Table 30, while still presenting a good cycle efficiency.

In addition, the selection of the two complex cycle layouts (the recompression and precompression layout) is not supported by the LCOE as an economic indicator, as the simple recuperative cycle and the cascade cycle presents low LCOE, mainly due to the lower costs of the power block and the TES, which compensate a lower energy production. Simpler plant layouts and can be therefore preferred due to their inherent lower complexity of the power block itself. The LCOE of the various optimized configurations are reported also in Figure 49.

All the suggested working fluids are able to reach LCOEs below 100 $/MWh_{el}$ considering a location with a yearly DNI of 2672 kWh/m^2/year: nevertheless, different maximum temperatures (and therefore technological levels) are necessary for this target. The power cycles based on sCO_2 requires cycle maximum temperatures around 700 °C, while the innovative CO_2 based mixtures adopted in transcritical cycles can run in the state-of-the-art CSP plants at maximum temperatures around 550 °C.

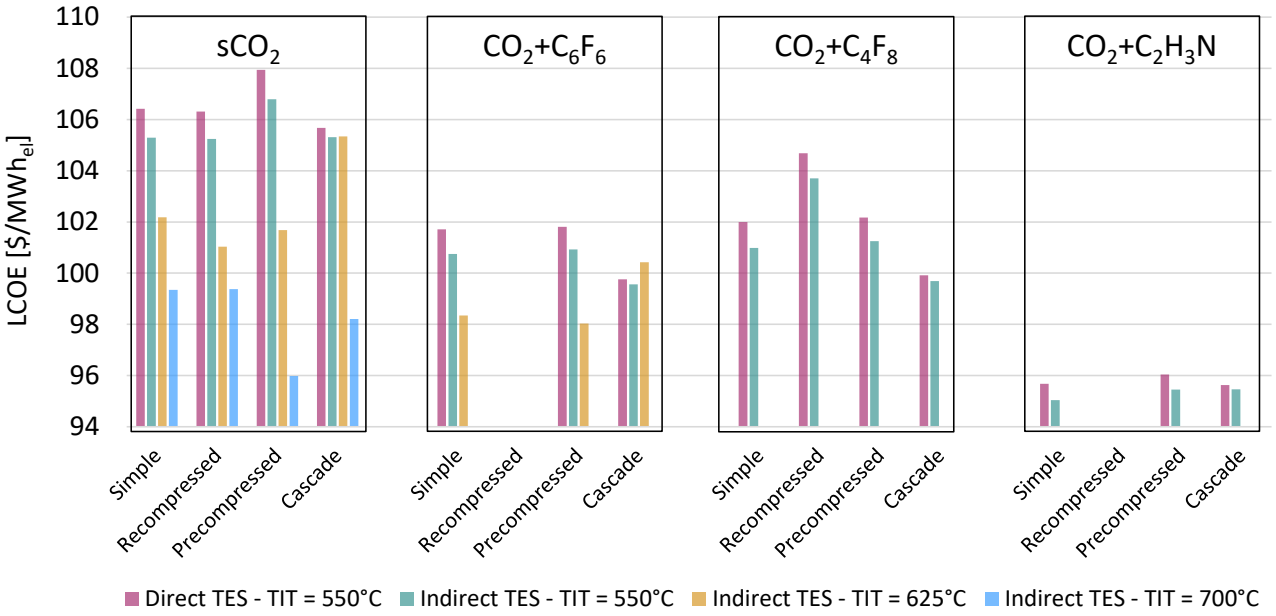

Figure 49. LCOE of the various configurations of CSP plants studied in this work

6.8 Remarks on the design and off-design of the solar plant with tCO$_2$-mixtures power cycles

A techno-economic evaluation of various CSP plants adopting four different power block layouts and four working fluids is shown in this chapter. According to literature studies, sCO$_2$ as working fluid has been widely adopted as a reference fluid for power cycles working at 700 °C, especially for CSP applications: nevertheless, the current state-of-the-art of CSP plants considers power cycle maximum temperatures at a level around 550 °C.

From a thermodynamic perspective, the traditional range of cycle minimum temperatures for CSP applications (around 50 °C) are representative of conditions far from the critical point of the pure CO$_2$, penalizing the compression work and the cycle efficiency of the respective sCO$_2$ cycle. For these reasons, transcritical cycles adopting CO$_2$ based mixtures can be a solution to overcome the limit of pure sCO$_2$ cycles for CSP applications.

The results evidenced the promising techno-economic performances of the innovative mixtures as working fluids in CSP plants, always superior to the respective sCO$_2$ configuration at constant cycle maximum temperature, especially in case of indirect storage configurations when sodium is considered as HTF. The simpler power block layouts, characterized by a slightly lower nominal efficiency, have been proved to be highly competitive from an economic point of view with

respect to the recompression and the precompression layouts, more investigated in literature for their higher nominal efficiency in CSP applications.

In particular, the mixture CO_2+C_6F_6 can allow for a net cycle electric efficiency higher than 42% when coupled with conventional CSP plant exploiting solar salts (at 550 °C of cycle maximum temperature) and it presents overall yearly solar to electric efficiencies higher than 17%, with LCOE around 100 $/MWh$_{el}$ (a 5% reduction with respect to the solution based on sCO_2 cycles). In these cases, the simulations are run considering the cycle always at full load, with little influence of the ambient temperature on the cycle performances. The most cost-effective solution, instead, is the one adopting the CO_2+C_2H_3N mixture, mainly due to the lower cost related to the power block components and a TES reduced in dimensions, while still holding a good cycle efficiency. As a matter of fact, this solution can theoretically reach LCOE in the range of 95 $/MWh$_{el}$, 10% lower than the s$CO_2$ cycle at same temperature levels, but higher uncertainties on the fluids thermal stability are to be included. For the highest temperature levels, with cycle maximum temperatures of 700 °C, the precompressed sCO_2 cycle is suggested as best available option with LCOE around 96 $/MWh$_{el}$.

7. Off design of tCO_2-mixtures power cycles for high temperature applications

The off-design performances of tCO_2-mixture power cycles are investigated as final step of the analysis carried out in this work, assuming the characteristics of the cycle suitable for a CSP application, assumed as a representative condition of a high temperature heat source.

During the operation along the year of an air-cooled cycle, the plant operator must account for both a variation of the ambient temperature and a variation of the electric power requested by the grid, eventually shutting down the power cycle in the periods of low (or even null) electricity prices.

In this chapter it is proposed a methodology to evaluate the off-design performances of a simple recuperative cycle with tCO_2-mixtures, at variable load and variable ambient conditions: the choice of the power block layout is done for sake of simplicity and due to the already good techno-economic performances of the simple recuperative cycle for many CO_2-mixtures (according to the results of the previous chapter, for example). Nevertheless, the methodology proposed can be adopted with minor modifications for any other cycle layout.

7.1 Literature review on off-design of cycles for CSP

The modelling of the off-design performances of solarized power cycles is a topic widely studied in literature for steam Rankine cycles as much as for sCO_2 power cycles: Thermoflex is usually exploited for the analysis of steam cycles, while in-house models are developed for the study of sCO_2 cycles. The research on this topic must focus on the study of the cycle performances due to: i) a lower electric load required, and ii) a variation of the ambient temperature.

Regarding steam cycles in large scale state-of-the-art CSP plants with solar salts, net cycle efficiencies can be expected in a range around 39% to 40% for an ambient temperature of 30 °C, strongly penalized by the air condenser auxiliary consumption [2]. Moreover, the cycle efficiency can be penalized by up to 1.5% when the ambient temperature moves from 30 °C to 40 °C and can increase only by 0.8% with an ambient temperature of 20 °C.

Fast transients (both for ramp-up and ramp-down) and start-ups are not favored in steam cycles, penalizing the overall performances. In fact, for renewable energy applications as CSP, a fast regulation of the load might affect the overall competitiveness of the system, especially while competing with electric storage with batteries.

Numerous literature studies underlined the necessity for CSP to effectively be tuned to the residual electric load: for example, a literature work by Hamilton [135] proposed an analysis of the off-design control strategies of a large-scale steam Rankine cycle under different boundary conditions, when applied to a CSP plant located in California. In a follow-up work the authors evidenced that revenues are maximized when start-ups of both the solar plant and the power cycle are minimized along the year [136].

Moreover, in a work of Wagner [137] the economic impact of the startup of a conventional Rankine was identified for a 150 MW_{el} CSP plant at around 10 thousand dollars, with a minimum start-up time of 30 minutes: accordingly, the authors proposed a dispatchability optimization model that, minimizing the continuous start-ups and shut downs forecasted following the residual load curve, would increase the annual net revenues by 8.5% by accounting for the operational cost and the limited deterioration of the plant equipment over the years.

As a matter of fact, at constant solar plant characteristics and power block size, a cycle operation that allows for part load conditions (even below 50% of the thermal input at design), would inevitably and drastically cut the yearly cycle start-ups and shut-downs potentially foreseeable with respect to a baseload plant.

Other studies focused on the integration of CSP with PV to cost-effectively increase the dispatchability of the plants (running the CSP section mostly to balance the intermittency of PV): in a work of Pilotti [138] on the comparison between PV with battery storage and PV+CSP, the authors highlighted that PV+CSP can be a suitable solution in case 70% of the annual load request must be satisfied. Regarding the steam cycle performance at part load, the same work proposed for various plant sizes, various ambient temperatures and part load conditions the trend of the cycle efficiency computed in Thermoflex v29 [112], pointing out a higher cycle efficiency penalization at part load for small scale power plants.

In addition to steam cycles for CSP applications, many literature works emphasized the performances of sCO_2 in off-design. In a work by White [139], the main control strategies reported in literature for the simple recuperated and recompression cycles are summarized. Working fluid inventory control is widely accepted as the main load control method since it achieves the highest cycle efficiency at reduced loads. The working fluid is bled from the high-pressure section of the system and stored in an inventory tank: it can be reinjected back to the low-pressure side of the cycle when higher loads are demanded. On this regard, a comprehensive steady-state and transient analysis of the inventory control system referring to a 50 kW_{el} sCO_2 test facility has been recently presented by Marchionni [140]. Moisseytsev [141] proposed a control strategy for

a recompression sCO_2 cycle for 100% to 0% electric load, ensuing the cycle operation by (i) bypassing the turbine for load between 90 and 100% of the nominal value, (ii) controlling the inventory between 90% and 50% of the load and (iii) throttling the turbine for part-load operation below 50%.

Furthermore, several authors studied the integration of the sCO_2 cycle in off-design with the solar subsystem: for example, Yang [142] studied the off-design performance of a 50 MW_{el} simple recuperated cycle integrated in a CSP plant. The authors fixed the TIT, compressor inlet temperature and compressor inlet pressure to the design values, concluding that the HTF outlet temperature varies at part-load, affecting the receiver thermal efficiency. In addition, a work of Alfani presented the operation of a CSP plant employing sodium as HTF and a recompression sCO_2 cycle under different inventory control schemes [143]. It was observed that a reduction in the compressor inlet pressure benefits the system efficiency at part-load with respect to a constant inlet pressure, and that fixing the TIT introduces an upsurge in the HTF temperature at PHE outlet, which may be detrimental for TES performance due to a progressive temperature increase of the cold storage tank. The authors also showed that adjusting the cycle minimum pressure to fix the HTF temperature range results in a large penalization of the cycle efficiency at low thermal load.

Further studies by Neises focus on the off-design of a 50 MW_{el} recompression sCO_2 cycle under the hypothesis of constant HTF outlet temperature [144]. This approach, compared to the control strategy of the previous studies (constant TIT), reduces several thermo-mechanical problems due to the fluctuation of temperatures in the receiver and TES and, more importantly, it avoids the decrease of the effective capacity of the TES due to a higher HTF cold temperature. It is concluded that at a higher ambient temperature than the one at design conditions, this strategy cannot achieve the target HTF outlet temperature without increasing cycle maximum pressure over its design value, resulting in a drop of net power output.

According to the brief literature review proposed, in this work the variable inventory configuration is adopted as a valid system to regulate the cycle minimum pressure, and the simulations are run at constant HTF temperature difference, not to penalize the exploitation of the hot source.

7.2 Plant layout and boundary conditions of tCO_2-mixtures cycles in off-design

The simple recuperative power block layout analyzed in off-design conditions is proposed in Figure 50. The proposed configuration consists of a variable speed

pump driven by an electric motor, a recuperator that cools down the flow at the outlet of the turbine, a primary heat exchanger where the working fluid is heated up to the cycle maximum temperature by cooling down the HTF, an axial turbine with a direct-drive generator and a air-cooled condenser that rejects heat to the environment cooling down and condensing the working fluid to the minimum cycle temperature. A hotwell is present between the pump and the condenser to accommodate the working fluid at the condenser outlet and to define the thermodynamic conditions of the fluid across the pump: the component is not present in sCO_2 cycles, but it is necessary to keep separated the two phases of the transcritical cycle after the condensation. The power block layout is completed by a variable-volume working fluid storage vessel, containing the working fluid at nominal composition in liquid phase, at an intermediate pressure between the cycle maximum and minimum pressure.

Only steady-state conditions are considered, as dynamic simulations are beyond the scope of this work because they require different numerical tools accounting for the thermal and mechanical inertias of the components.

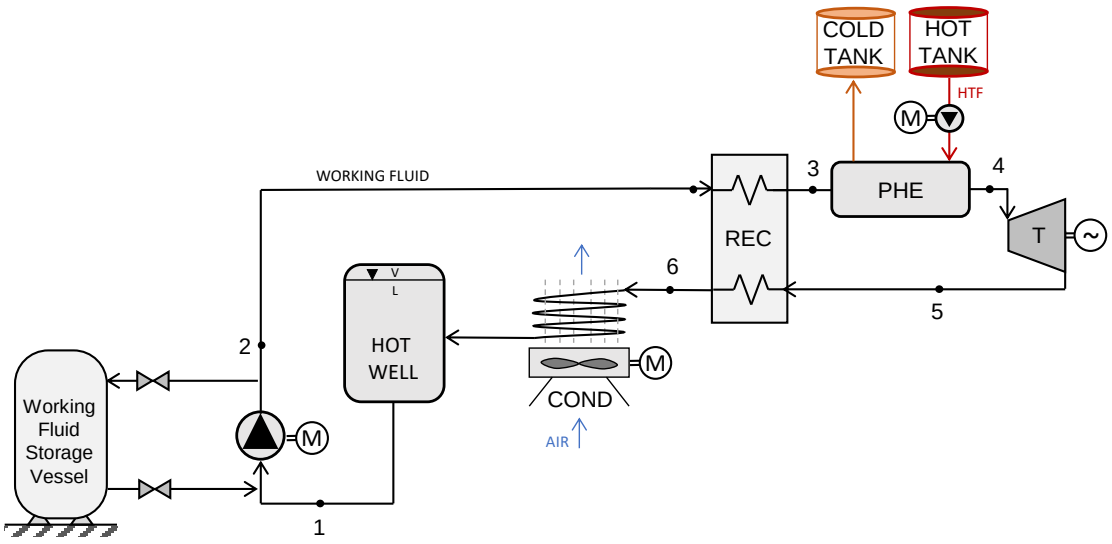

Figure 50. Plant layout of the simple recuperative tCO_2-mixture cycle for CSP

In order to set up the MATLAB model that manages the separate codes for the off-design of each single cycle component, various control options, control variables and independent variables must be defined. Specifically, the control variable can be univocally determined by the control options, for any reasonable value assumed by the independent variables.

Table 44 lists the control options and variables, along with the two independent variables, which are the thermal input to the power cycle that is related to the mass flow rate of the HTF (by varying the HTF pump rotational speed), and the ambient temperature, that can assume any value.

According to the control philosophy, the heat rejection from the power cycle is regulated with the air-cooled condenser, eventually working in off-design conditions with the EC axial fans. Any variation of the inventory of the power cycle is obtained through a careful management of the working fluid storage vessel, that can introduce or remove working fluid from the loop. The mass flow rate of the working fluid itself is regulated with the variation of the pump rotational speed, that is assumed not to influence the compression ratio across the pump.

Finally, the working fluid storage vessel is regulated always to have a negligible vapor fraction in the hotwell. This last condition is crucial while handling mixtures as working fluids for transcritical cycles. While in power cycles working with pure fluids (e.g., steam Rankine cycles) the hotwell can experience a variable free surface level during off-design conditions, this cannot be a viable solution when mixtures are adopted as working fluids, as the vapor and liquid phases compositions in the hotwell are different. For this reason, a variation of the hotwell free surface level would inevitably cause a change of the liquid phase composition, that, circulated by the pump, would cause a variation of the working fluid composition in the power cycle.

Table 44. Independent and control variables of the power plant while operating in off-design

Control Option	Control Variable		Independent Variable
Rotational speed of the condenser fans	Working fluid conditions at pump inlet		HTF pump rotational speed (HTF mass flow rate)
Conditions of the working fluid storage vessel	Hotwell level		Ambient temperature
Rotational speed of the cycle pump	Working fluid mass flow rate		/

After defining the independent variables for the cycle off-design and its control philosophy, some boundary conditions must be included to consider the thermo-mechanical limits of the cycle components, proposed in Table 45.

According to these limitations, the cycle maximum pressure must always be lower than its value at design conditions (due to the mechanical limits of the materials) and higher than the cricondenbar of the mixture, in order to avoid VLE conditions in the high-pressure side of the PCHE and to limit the size of the inventory of the working fluid (since large inventory vessels would be necessary to reach very low cycle minimum pressures).

As the cycle minimum pressure and temperature are univocally determined by the phase behavior of the mixture at bubble conditions, differently than sCO_2 cycles, no conditions at cycle minimum temperature above the design value are considered: that would lead to a maximum pressure above the mentioned upper bound.

Due to the coupling between the power cycle and the solar plant, the temperature of the hot tank of the TES is fixed at all conditions, representing the

maximum temperature of the hot source of the power cycle. Given the non-perfect counter-current arrangement of the S&T HX, the minimum temperature difference (pinch) both at the hot-end and the cold-end of the PHE is fixed at 4 °C: accordingly, a limit on the maximum temperature of the cycle (TIT) and the maximum temperature of the working fluid at the inlet of the PHE (T_3) is introduced.

If the limit on the cold-end minimum pinch cannot be satisfied, at very low thermal load into the power cycle, the model includes the possibility to increase the outlet temperature of the HTF across the PHE: nevertheless, if this condition occurs for a large fraction of the yearly operating hours it may indicate an inappropriate design of the PHE, as that leads to an increment of the cold tank temperature, varying the operating conditions of the receiver and badly affecting its thermal efficiency and the pressure drops of the HTF.

Finally, regarding the flexibility of the heat rejection unit, the EC fans of the air-condenser are supposed to deliver a variable volumetric flow rate, from a minimum value of 30% to a maximum of 130% of the design air volumetric flow rate.

Table 45. Boundary conditions of the power block operating in off-design

Off-Design boundary conditions
$P_{Cricondenbar} < P_{in,turb} < P_{in,Turb,Design}$
$P_{bubble}(T_{min,min}) < P_{min} < P_{bubble}(T_{max,min})$
$T_{min,cycle} \leq T_{min,cycle,Design}$
$TIT < (T_{hot,tank} - 4°C)$
$T_{hot,tank} = T_{hot,tank,Design}$
$T_{out,HTF} = T_{out,HTF,Design}$ if: $(T_{out,HTF} - T_3) > 4°C$
$(T_{out,HTF} - T_3) = 4°C$ if: $T_3 > (T_{out,HTF,Design} - 4°C)$
$Minimum\ internal\ temperature\ approach\ (MITA)_{PCHE} > 3°C$
$30\% \cdot \dot{V}_{air,design} \leq \dot{V}_{air} \leq 130\% \cdot \dot{V}_{air,design}$
Hotwell Negligible Vapor Fraction $(\frac{V}{L} \to 0)$

In conclusion, the control philosophy in off-design conditions of the power plant is defined including a variation of turbine inlet temperature: the solution is specifically tailored to CSP applications, where the main objective is to fix the temperature level across the HTF, resulting inevitably in variable temperature levels of the working fluid in off-design conditions.

7.3 Methodology for the analysis of the cycle in off-design

The overall outlook of the methodology adopted to solve the cycle in off-design conditions is illustrated in Figure 51. The off-design simulations necessitate of the definition of both the thermal input to the power cycle (proportional to the mass flow rate of HTF) and the condition of the cycle minimum pressure and temperature. Then, the iterative procedure starts guessing a value of the cycle maximum temperature (T_4), the pressure at turbine inlet (P_4), the working fluid temperature at PHE inlet (T_3) and the cycle mass flow rate. Running the code of the PHE in off-design, the procedure updates each of these four variables according to the methodology proposed in the figure and detailed in the next chapter, considering the operation of the turbine in sliding pressure determined by the turbine map.

When the off-design sub-routine of the PHE is solved, the turbine and pump isentropic efficiencies are estimated from the respective turbomachinery maps, and the turbine outlet temperature (T_5) and pump outlet temperature (T_2) are directly computed. Finally, the recuperator model is run in off-design (as shown in Figure 31) to reach convergency on the temperature at PHE inlet (T_3). In case the recuperator off-design model does not provide the same results on T_3, then the value initially assumed of T_3 is updated, and the overall process is iteratively reproposed up to convergency on T_3.

Once the convergency is reached, the cycle is univocally solved. A comparison between the MATLAB solution and the calculation of ASPEN Plus is carried out in the end, to verify convergency on the last variable T_6. The iterative procedure is then repeated for different input values of HTF mass flow rate and cycle minimum temperature and pressure.

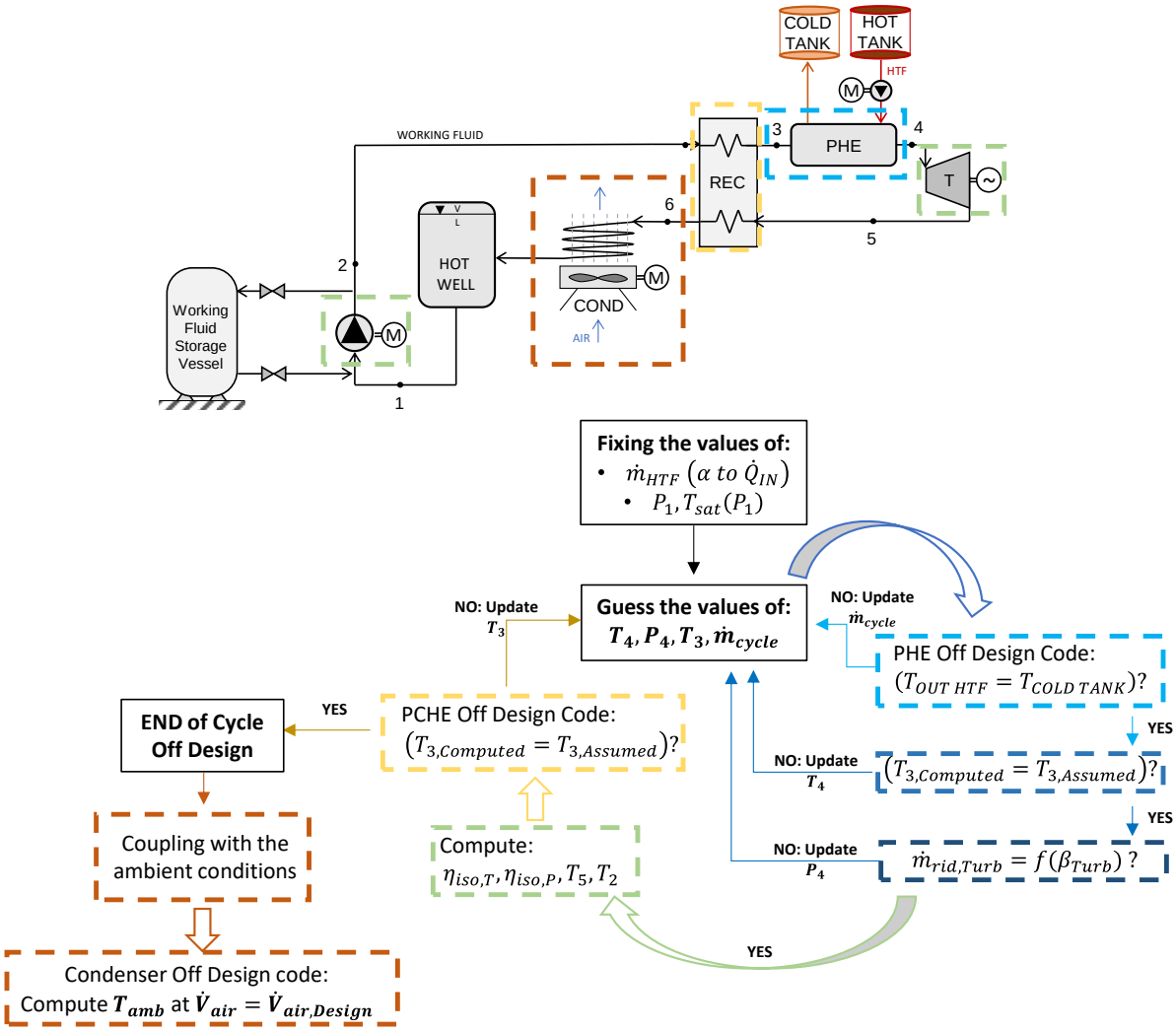

Figure 51. Methodology adopted for the analysis of the power block in off-design

Since the independent variables of the system are the HTF mass flow rate and the ambient temperature, a specific value of ambient temperature is associated with each cycle solution through the off-design model of the air-condenser at constant fan speed, fixed at design value. In fact, during the off-design operation, the proposed control philosophy of the air-cooled condenser is to run the fans at design rotational speed, without any penalization of the hydraulic efficiency, always delivering the same air volumetric flow rate.

According to this approach, it is possible to define the power cycle conditions in off-design at a given thermal input (i.e. HTF mass flow rate) and ambient temperature, which is the ultimate objective of the overall routine, as summarized in Table 44.

Finally, once all cycle off-design simulations are associated with an ambient temperature at constant air flow rate, the ambient temperature range is extended by assuming all possible values of fan rotational speed, down to 30% of the nominal value and up to 130% of the nominal value. In these cases, a new value

of ambient temperature is computed at different air face velocities with the off-design code of the condenser (shown in Figure 26), keeping constant the solutions of the cycle reached in sliding pressure on the working fluid side (mass flow rate, temperature and pressure at both inlet and outlet of the condenser).

7.3.1 Cycle control in off-design and turbomachinery maps

In addition to the off-design methodology followed to assess the HXs performances, the off-design behavior of the turbomachinery adopted in the power cycle must be carefully evaluated, in particular for the turbine. As mentioned, in this work accurate in-house design and performance models for turbines and pumps are not developed, as within the consortium of the SCARABEUS project other partners worked on this topic: City University of London characterized the multi-stage axial turbines both with 1-D mean lines models and with CFD, while some proprietary data on the pump characteristics is taken from industrial partners of the project.

Depending on the turbine maps, for any given value of reduced mass flow rate at turbine inlet, referring to Equation (42), a turbine pressure ratio is indicated to achieve the maximum efficiency. Additionally, the information of the turbine efficiency is presented only as function of the pressure ratio (and therefore of the reduced mass flow rate at the turbine inlet) and independently to the actual values of the mass flow rate, the turbine inlet temperature and pressure.

$$\dot{m}_{Red,In\ Turb} = \frac{\dot{m}_{In\ Turb}\sqrt{\gamma R T_{In\ Turb}}}{D^2 P_{In\ Turb}} \tag{42}$$

A qualitative representation of the turbine map necessary for the off-design model of the cycles in this work is proposed in Figure 53, on the right.

The dimensionless turbine map ideally required is not per se restricted to any specific control technique of the power cycle, as its validity holds even for stand-alone turbines: nevertheless, in this work the control philosophy normally referred to as “sliding pressure” is adopted for the plant off-design.

By operating the cycle in sliding pressure, the turbine control valves are left in wide open position thus minimizing the throttling losses. The plant operator does not actively control the pressure at turbine inlet, which is instead freely varied as consequence of the plant thermal input and the cycle minimum temperature. In particular, at constant cycle minimum temperature, and therefore at constant minimum pressure, a reduction of the thermal input corresponds a reduction of the working fluid mass flow rate and thus of the maximum pressure, due to the

relation dictated by turbine operating curve. On the other hand, at constant thermal input, a reduction of the cycle minimum temperature, and hence a reduction in cycle minimum pressure, corresponds to a reduction of the working fluid mass flow rate and maximum pressure. Thus, no linear dependence occurs between the reduced mass flow rate and the mass flow rate flowing in the cycle, due to the variation of the maximum pressure of the cycle.

The implementation of the sliding pressure control technique in the MATLAB off-design tool is shown in Figure 52: the flowchart focuses on the strict connection between the off-design of the PHE and the turbine, since the two models are solved simultaneously (as evidenced in Figure 51).

In the sliding pressure model, the cycle thermal input and the temperature at PHE inlet (T_3) are given as inputs, while convergency is reached on the cycle mass flow rate, the cycle maximum pressure and the turbine inlet temperature, enforcing the energy balance and constitutive equation across the PHE in accordance with the turbine map.

Finally, also the off-design of the pump of the power cycles is a necessary input to the overall off-design model of the cycle, represented qualitatively in Figure 53, on the left.

The pump is assumed to be extremely flexible in its operational range, safely managing any compression ratio without any impact on its cycle efficiency. The single degree of freedom assumed is its rotational speed, actively influencing the mass flow rate of the cycle.

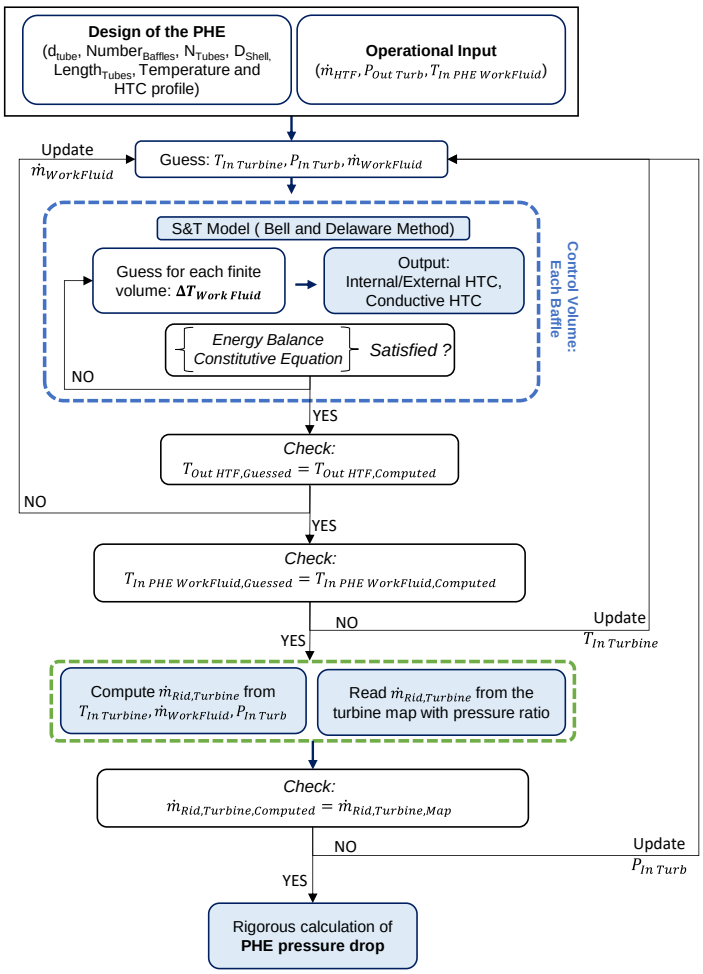

Figure 52. Methodology for the modeling of the system "PHE + Turbine" while operating the power cycle in sliding pressure

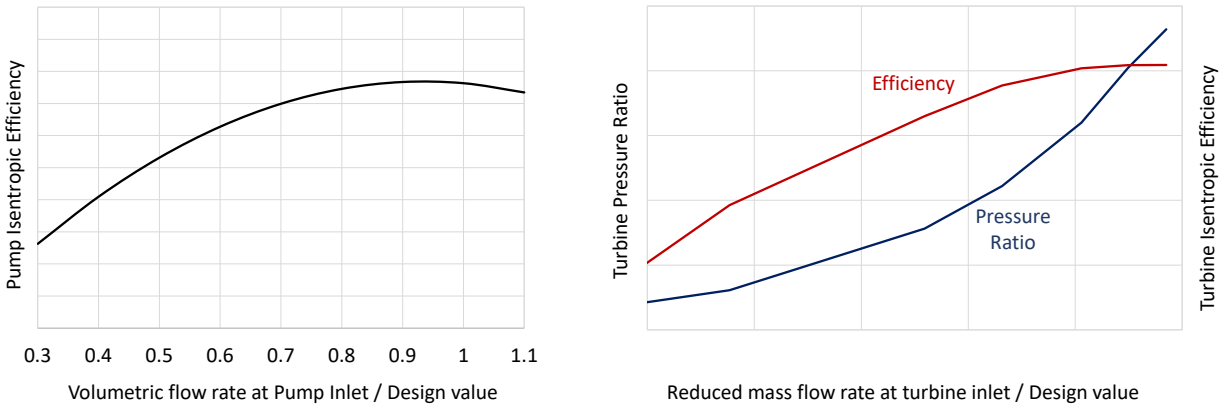

Figure 53. Qualitative representation of the map of the turbine (right) and the pump (left) adopted in this work for the cycle off-design analysis

7.3.2 Power cycle coupling with the ambient conditions

Once the off-design analysis of the power cycle is correctly computed for each combination of thermal input and cycle minimum temperature (referring to Figure 51), the cycle mass flow rate, the temperatures and pressures across the various cycle components are univocally defined.

In this case, the inlet and outlet mass flow rate, temperatures and pressures across the condenser are known, and the off-design model of the condenser, described in Figure 26, can be directly run for all cycle off-design conditions.

The goal of the MATLAB model is to determine, for each ambient temperature and power cycle condition, the air face velocity on the tube (directly proportional of the volumetric flow rate developed by the fans) that allows to completely exchange the necessary heat into the environment.

The qualitative results reported in Figure 54 can help in understanding the control philosophy of the air condenser, which is simulated for a wide range of ambient temperatures and air volumetric flow rate from 30% to 130% of the design value (as reported in Table 45).

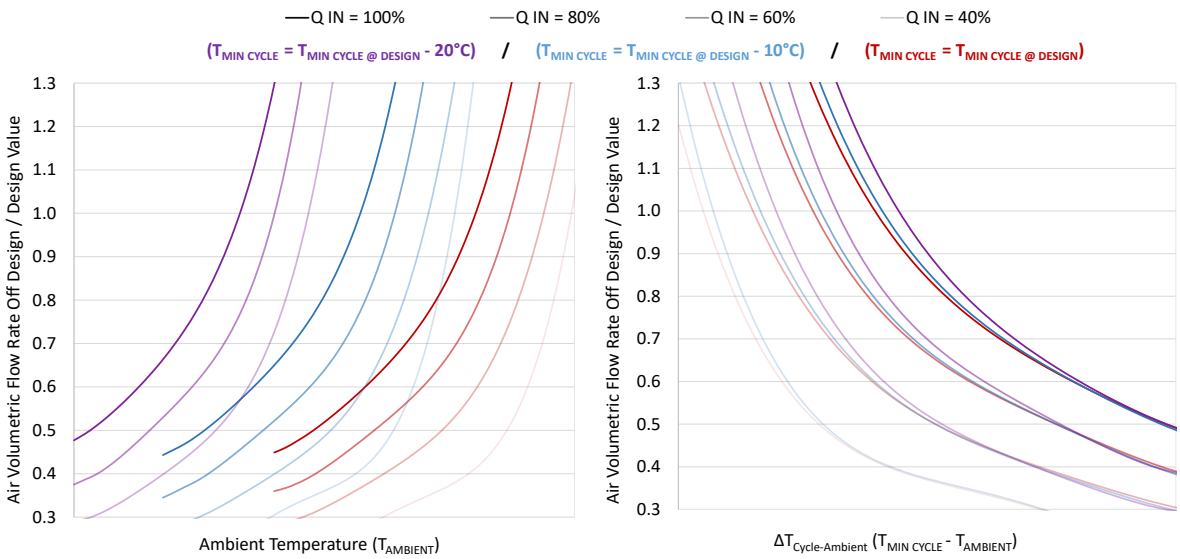

Figure 54. Qualitative trend of the coupling between the cycle in off-design and the air condenser fans

Focusing on the difference between the cycle minimum temperature and the ambient temperature (called $\Delta T_{Cycle-Ambient}$ in Figure 54), it is possible to define, at nominal air flow rate, the relationship between $\Delta T_{Cycle-Ambient}$ at design and any other off-design conditions as in Equation (43) by simply accounting for the rejected heat.

This simple but effective approach can help in defining the actual coupling between the off-design conditions of the cycle and the ambient temperature,

presented in Figure 51, which is one of the main scopes of the cycle off-design analysis.

$$\Delta T_{Cycle-Ambient} = \Delta T_{Cycle-Ambient,Design} \cdot \frac{\dot{Q}_{rejected}}{\dot{Q}_{rejected,Design}} \quad (43)$$
$$(while\ considering\ \dot{V}_{air} = \dot{V}_{air,Design})$$

Accordingly, the approach proposed in this work for the control of the air-condenser fans is to run them always at constant speed in design conditions, modifying the power cycle conditions running it in sliding pressure.

Unfortunately, this approach leads to a limited range in allowable ambient temperature at constant thermal input, qualitatively depicted in Figure 54: when the plant operator has to extend the operating range in terms of ambient temperatures, the air-cooled condenser fan velocity can be reduced down to 30% of the nominal value (extending the lower bound of the operating conditions, fixing the cycle in the configuration at the lowest cycle minimum temperature), or increased up to 130% (extending the higher bound of the ambient temperature range, operating the cycle at the maximum value of cycle minimum temperature.

8 Case study: Off-design of a simple recuperative cycle working with the CO_2+C_6F_6 mixture

The second case study shown in this work is centered around the performance of the simple recuperative transcritical cycle working with the CO_2+C_6F_6 mixture, underlining the performance in off-design and at part load conditions. The case study of this chapter is available in a literature work part of the SCARABEUS project [145].

In the following sub-chapters the design of each cycle component will be proposed, assuming a cycle gross power output of 100 MW coupled with a state-of-the-art CSP plant at cycle maximum temperature of 550°C, in order to completely detail within this thesis the analysis of the innovative solar plants. Then, the off-design performances of the cycle are computed, including the cycle analysis in sliding pressure and by modifying the rotational speed of the condenser fans, according to the methodology of Chapter 7, for a wide range of thermal input.

In this analysis the mixture is modelled with the PC-SAFT EoS and the molar composition of the working fluid is 87% of CO_2, a value set to reach the maximum efficiency for this plant layout under these conditions [37].

8.1 Thermodynamic conditions of the power cycle at design

The simple recuperative cycle characteristics are computed at design conditions in ASPEN Plus, adopting the cycle assumptions of Table 46. The resulting thermodynamic conditions at the inlet and outlet of each cycle component are also listed in Table 47.

The nominal value of the ambient temperature is assumed at 36 °C, representative of the average temperature during daytime in summer for a location with high solar resources.

Table 46. Characteristics of the simple recuperative transcritical CO_2+C_6F_6 power cycle at design conditions

Variable	Value at design conditions	Notes
Cycle minimum temperature [°C]	51	For air-cooled heat rejection in hot environments
Cycle maximum temperature [°C]	550	For state-of-the-art CSP
Turbine inlet pressure [bar]	252	Computed to meet ΔP requirements
Pump inlet pressure [bar]	84.5	At bubble conditions
Recuperator MITA [°C]	5	According to literature [113]
Turbine isentropic efficiency [%]	92.08	According to the maps of Figure 78
Pump isentropic efficiency [%]	88	According to the maps by industrial partners
Primary HX pressure drops [bar]	2	According to the analysis in Figure 37
Condenser pressure drops [bar]	1	Assumed
PCHE pressure drops (LP) [bar]	1	Assumed
PCHE pressure drops (HP) [bar]	0.3	Computed by the model
Motor and generator efficiency [%]	99	Assumed
HTF inlet / outlet temperature [°C]	420 / 565	Assuming a pinch at cold end of the PHE
Ambient temperature [°C]	36	Assumed

Table 47. Thermodynamic conditions of the tCO_2+C_6F_6 cycle at design

Thermodynamic condition	Temperature [°C]	Pressure [bar]	Enthalpy [kJ/kg]	Entropy [kJ/kg/K]	Density [kg/m^3]	Molar vapor quality
1	51.0	84.5	0	0	935.6	0
2	67.9	254.3	19.8	0.007	1000.2	0
3	401.3	254.0	530.6	1.080	279.3	1
4	550.0	252.0	727.0	1.344	217.0	1
5	455.9	86.5	624.0	1.356	89.5	1
6	81.2	85.5	113.2	0.336	338.4	0.69

The cycle is also depicted in design conditions in the T-s and P-T diagrams of Figure 55: from the figure it is possible to appreciate the cycle highly recuperative capacity and the limited temperature difference of the hot source, typical of highly efficient solarized power cycles. The mechanical and thermal power balance at design condition is described in Table 48: by including the condenser auxiliary consumption and the electromechanical losses the power cycle has a net electric efficiency of 41.4%. The value is not low for a state-of-the-art CSP solar plant, but the focus of this analysis is to understand how the variation in thermal load and ambient temperature can influence the cycle efficiency, down to low cycle minimum temperature, below the level conventionally explored with sCO_2 cycles.

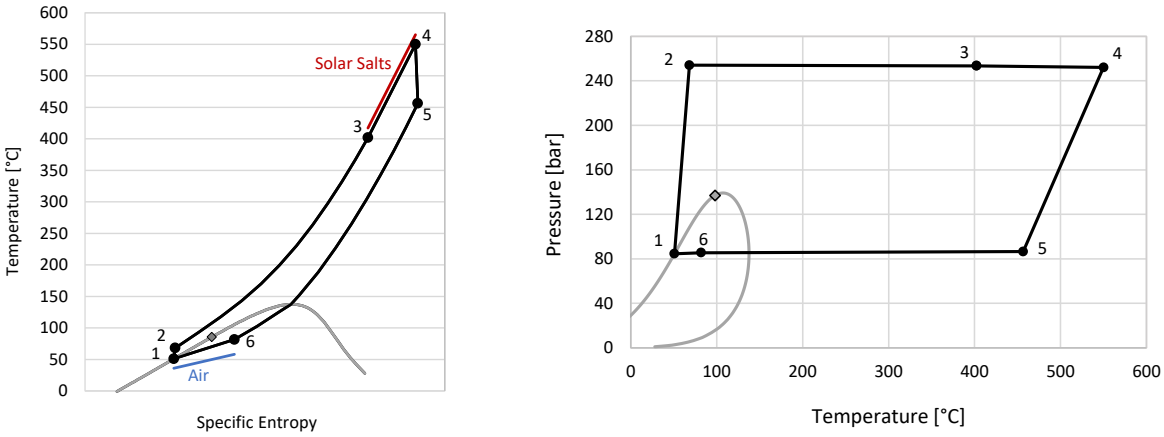

(a) (b)

Figure 55. Cycle at design conditions in the T-s (a) and the P-T diagram (b)

Table 48. Thermal and mechanical power balance of the cycle at design conditions

Variable	Value at design conditions
Working fluid flow rate [kg/s]	1202.3
Gross specific work [kJ/kg]	83.2
Pump mechanical power [MW]	23.9
Turbine mechanical power [MW]	123.9
Recuperator heat duty [MW_{th}]	614.0
PHE heat duty [MW_{th}]	236.1
Condenser heat duty [MWth]	136.1
UA_{PCHE}/PHE heat duty [1/K]	0.15
Gross cycle efficiency [%]	42.36
Electromechanical losses, condenser consumption [MW_{el}]	2.2
Net electric cycle efficiency [%]	41.42

The next subchapters will describe the sizing of the HXs of the cycle. The design and off-design characteristics of the turbine (computed by a partner of the SCARABEUS project, not directly involved in this thesis) are detailed in Appendix D.1 and not shown in this chapter for sake of brevity.
The map of the pump, with the form proposed in Figure 53, is provided by an industrial partner of the SCARABEUS consortium: it is not provided in this work due to an NDA with the manufacturer.

8.2 Sizing of the power cycle components

8.2.1 Sizing of the recuperator

The design conditions at the inlet and outlet of the recuperator of the power cycle are proposed in Table 47, while the respective T-Q diagram is shown in Figure 56: in the considered mixture as working fluid the minimum internal temperature difference of the countercurrent heat exchanger (set at 5 °C) is located where the flow in the low-pressure side (hot side) starts condensing, at around 25% of the heat exchanged, as visible in the T-Q diagram.

The high-pressure side, on the other hand, being at a high reduced pressure (around 2, as underlined in Figure 55 (b)), does not show large specific heat capacity variations while moving from the supercritical region to the liquid region.

The final design of the PCHE recuperator to meet the required pressure drop of 1 bar on the low-pressure side features a mass velocity of 500 kg/s/m^2 in the channels and a consequent cold side pressure drop of 0.3 bar. The overall results of the PCHE model are proposed in Table 49.

Table 49. Geometrical and operational characteristics of the recuperator (PCHE) of the cycle analyzed

Parameter	Value
Channel length [m]	4.42
Number of channels	1 530 430
Hot side pressure drop [bar]	1.0
Cold side pressure drop [bar]	0.3
Mass velocity [kg/s/m^2]	500
Fluid velocity, hot side [m/s]	From 2.3 to 5.5
Fluid velocity, cold side [m/s]	From 0.5 to 1.8
Average overall HTC [W/m^2/K]	1032

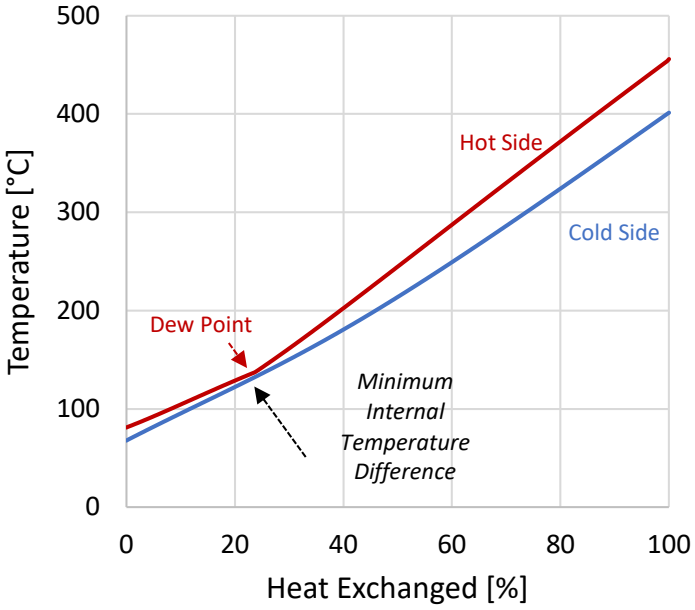

Figure 56.T-Q diagram of the recuperator of the cycle at design conditions

A particular focus is dedicated to the in-channel axial distribution of the convective heat transfer coefficients (proposed in Figure 57) and to the pressure drops per unit length on both channels (shown in Figure 58). The convective HTC presents no discontinuities along the cold channel while, for the hot channel, a drastic discontinuity (+10%) is noticeable when the flow moves from the vapor conditions (modelled with the Gnielinski correlation) to the VLE conditions (computed according to the Cavallini model for two-phase mixtures). At the same time, the high-pressure and high-density working fluid on the cold side presents a velocity significantly lower than the low-pressure side, as reported in Table 49, entailing a lower pressure drop per unit length, with a linear trend along the channel. Similarly to the heat transfer coefficients, the hot-side channel experiences a discontinuity on the pressure drop per unit length, moving from the vapor region (adopting the Darcy-Weisbach equation and computing the friction factor with the Chen correlation) to the VLE (modelled with the Del Col model).

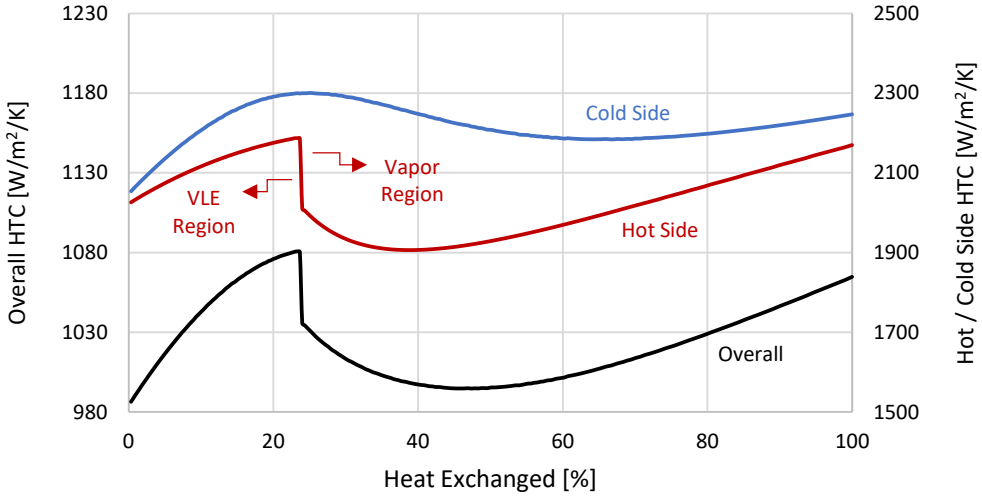

Figure 57. HTC of the PCHE along the channel, referring to the design of Table 49

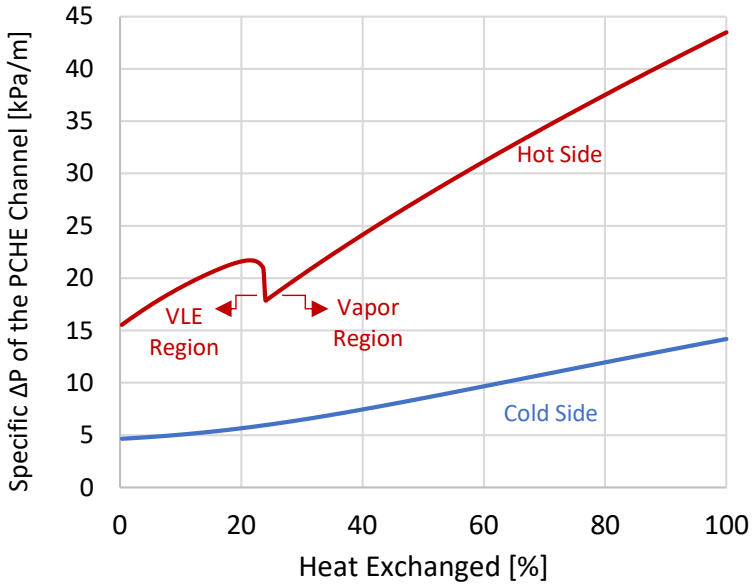

Figure 58. Pressure drop per unit of length of the PCHE along the channel, referring to the design of Table 49

8.2.2 Sizing of the PHE

The designed S&T PHE of the power cycle adopts conventional solar salts on the shell side cooled down from 565 °C to 420 °C at nominal conditions, as

reported in Table 46. The heat exchanger is sized for a tube (working fluid side) pressure drop of 2 bar, according to the methodology shown in Figure 33. The resulting characteristics of the PHE are listed in Table 50, evidencing an average value of the overall HTC of 869 W/m^2/K referred to the overall tube external area. With respect to the recuperator, where the contribution of the conductive resistance to the overall HTC is negligible, for the S&T PHE the relative contribution of the conduction along the tube thickness is significant. The trends in Figure 59 are proposed to evidence the linear and almost constant value of the HTC across the PHE.

Table 50. Geometrical and operational characteristics of the S&T PHE of the cycle analyzed

Parameter	Value
Tube length [m]	27.2
Number of tubes	11’514
Tubes external area [m^2]	16’740
Number of baffles	16
Shell diameter [m]	3.20
Tube side pressure drop [bar]	2.0
Shell side pressure drop [bar]	0.3
Working fluid velocity, tube side [m/s]	From 4.8 to 6
Working fluid mass velocity [kg/s/m^2]	1392
Average overall HTC [W/m^2/K]	869

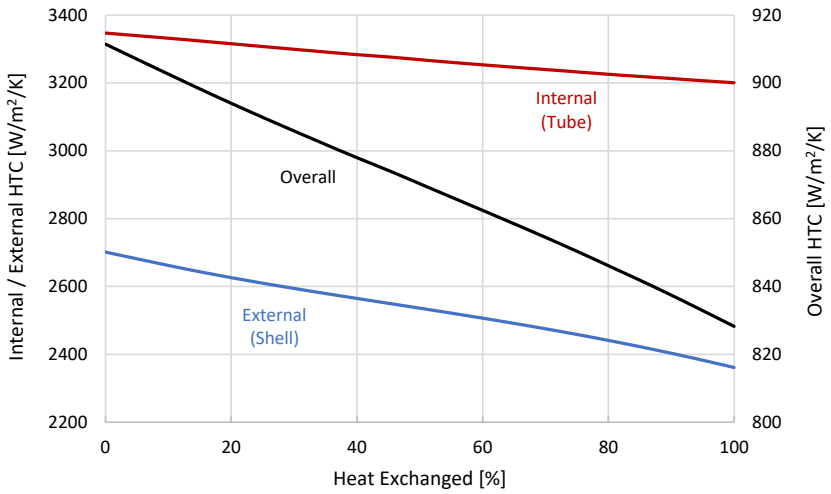

Figure 59. HTC trends along the S&T PHE (hot end at 0% thermal power exchanged), referring to the design of Table 50

8.2.3 Sizing of the air-cooled condenser

The two most crucial parameters for the design of a condenser are the ambient temperature and the air face velocity on the tubes. These two aspects can be potentially investigated in future works with the scope of carry out a detailed optimization procedure and describing the most suitable design condition depending also on off-design aspects. In this work, the ambient temperature is fixed at design at 36 °C and the air face velocity is subsequently fixed at a 2.6 m/s, a value that guarantees a target electric consumption of the fan around 0.8 MW_{el} at design conditions (a low parasitic consumption for the power cycle, around 0.6% of the rejected heat). The methodology adopted for the design of the condenser is reported in Figure 25.

The condenser sizing is carried out considering the inlet and outlet conditions of the working fluid reported in Table 47, aiming at a target value of the working fluid pressure drop of 1 bar. The model provides the number of tubes and their length, along with the air side pressure drop and outlet temperature. The results of the condenser design are given in Table 51: the computed temperature difference on the air side is 23 °C, a value higher than typical air-cooled condensers of steam cycles, thanks to the non-isothermal heat rejection from the power cycle analyzed.

Table 51. Geometrical and operational characteristics of the air-cooled condenser of the cycle considered

Parameter	Value
Number of Tubes	2795
Tube overall length / Pass length [m]	74.6 / 10.7
External condenser area (air side) [m^2]	370’924
Ambient temperature [°C]	36
Air velocity on the tube [m/s]	2.6
Air temperature difference [°C]	23.0
Air mass flow rate [kg/s]	5892
Minimum Internal Temperature Difference [°C]	12.0
Working fluid pressure drop [bar]	1
Working fluid velocity [m/s]	From 3.7 to 1.4
Working fluid mass velocity [kg/s/m^2]	1271
Air side pressure drop [Pa]	72
Overall HTC [W/m^2/K]	24.9
Electric Fan Consumption [MW_{el}]	0.80

The heatmaps in Figure 60 depict the temperature distribution on both the air and the working fluid side of the air-cooled condenser at design condition along each finite volume of the 7 passes tube, assuming the tube geometry in Figure 25.

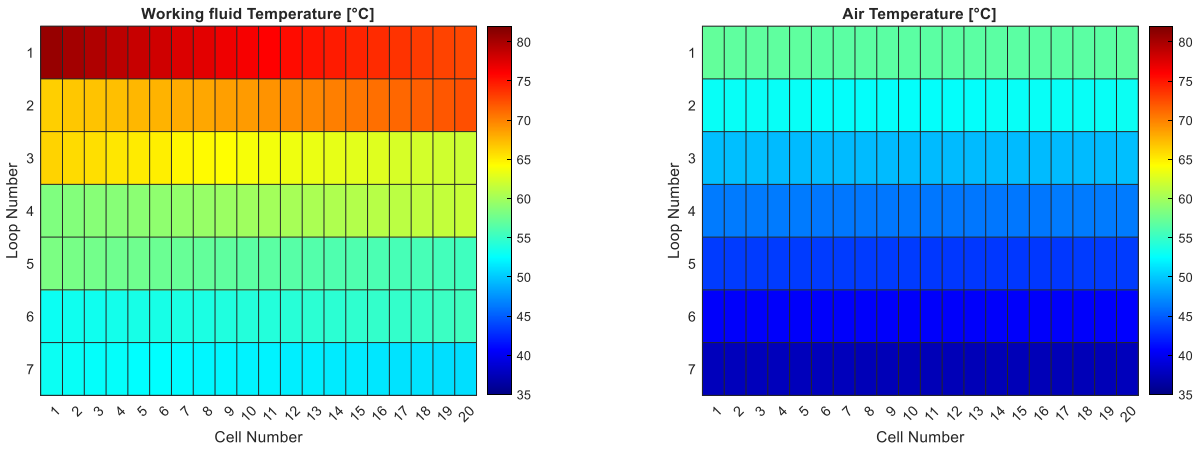

(a) (b)

Figure 60. Temperature distribution across the tube of the air condenser: working fluid side (a), air side (b)

8.3 Cycle off-design: Results at given cycle minimum temperature and variable thermal input

A first set of results of the off-design MATLAB tool is reported in Figure 61, not detailing the coupling between the cycle and the ambient condition, according to the methodology discussed in Figure 51. The results are presented as function of the cycle minimum temperature and the thermal input, considering a thermal input ranging from the 100% down to 40% of the nominal value and a cycle minimum temperature from 51 °C (the design value) to 31 °C (a minimum temperature not achievable with sCO_2 cycles).

The results evidence almost linear trends of the mass flow rate, pressures and temperatures involved, with an inversion of some trends only where the limit of cold end pinch point at the PHE is met (i.e. where the working fluid temperature at PHE inlet is higher than 416 °C) and the HTF temperature at PHE outlet increases. When this condition is met the cold end temperature difference of the PHE is fixed at the minimum value (4 °C) and cannot be furtherly reduced (a condition underlined in Table 45): the only solution to control the mean logarithmic temperature difference across the PHE is to increase the TIT.

The simulations at cycle minimum temperature of 31 °C, instead, are not presented below 50% of the design thermal input because the minimum value of maximum pressure is met.

From the results of the turbine pressure ratio, the lower the cycle minimum temperature the higher the pressure ratio: this aspect would imply a higher

reduced mass flow rate at the turbine inlet and therefore a higher isentropic efficiency of the turbine, according to the turbine map of Figure 78. It is therefore suggested to design the transcritical cycle at the highest cycle minimum pressure, as done in this work.

Analyzing the nominal minimum temperature case (51 °C), it is possible to notice that the cycle efficiency reduction with the decrease of the thermal input is initially contained with respect to the design value, at around 0.7 percentage points at 70% thermal input. This is possible thanks to the increased effectiveness of the recuperator: in fact, its heat transfer area results oversized, when the working fluid mass flow rate reduces (Figure 61, top right).

The enhanced internal heat recovery increases the working fluid temperature at the PHE inlet (Figure 61, top center) with a positive effect on the cycle thermodynamic efficiency. As the load is further reduced, the reduction of the cycle pressure ratio (Figure 61, bottom center) counterbalances more and more this effect, eventually causing a marked decrease in the gross cycle efficiency, also caused by the low values of turbine and pump isentropic efficiencies.

As the calculation of the PHE HTC is computationally expensive, Appendix D.2 details a possible approach to model it without solving the HX for each finite-volume: the approach in the appendix can be adopted in future analyses in case simplified models for the HX will be of interest.

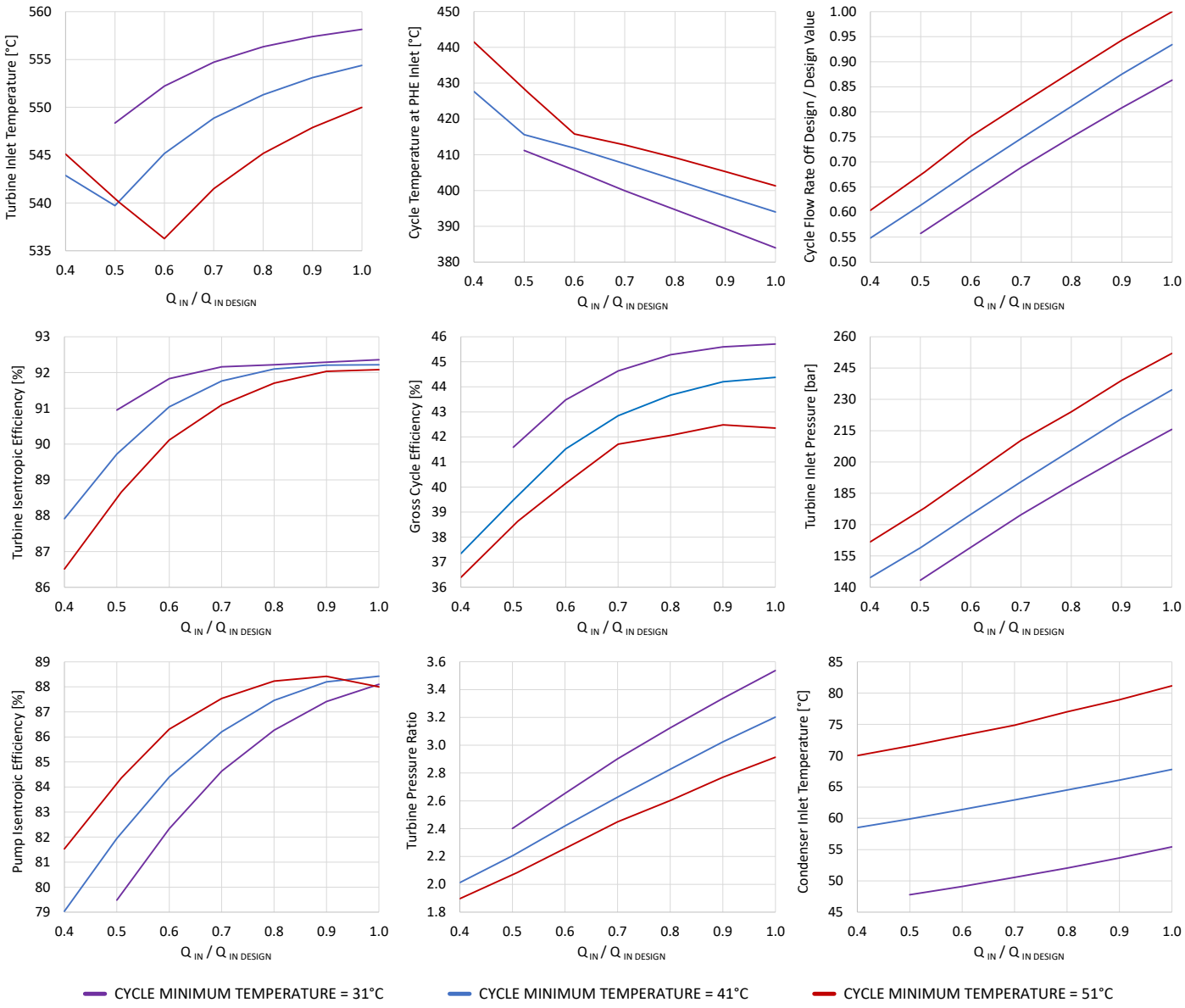

Figure 61. Off-design results of the power cycle at given cycle minimum temperature and variable thermal input

8.4 Cycle off-design: Results at variable thermal input and ambient temperature

The analysis of the off-design performance of the cycle coupled with the ambient conditions is studied and presented in this work with two approaches: at first by keeping the nominal rotational speed of the air condenser at design value

and operating the cycle in sliding pressure, then fixing the thermodynamic conditions of the cycle and its mass flow rate, while varying the rotational speed of the condenser fans. The whole methodology followed in this case study has been already discussed both in the flowchart of Figure 51 and in Figure 54.

8.4.1 Condenser fan at design rotational speed

Taking the conditions of the power cycle in off-design of Figure 61 as an input to the calculations, the off-design model of the condenser (referring to Figure 26) can compute for each cycle condition the air face velocity (i.e. the volumetric flow rate of the air) necessary to satisfy the heat exchange problem, given an ambient temperature.

The results are presented in Figure 62 for a wide range of cycle thermal input and the three analyzed cycle minimum temperatures (51 °C, 41 °C and 31 °C). In the figure it is also evidenced the control strategy chosen to regulate the air-cooled condenser and its effect on the off-design behavior of the plant at a thermal load equal to 80% of the design value. For that specific condition, the air-cooled condenser is not controlled (keeping fixed the fan velocity) in an ambient temperature range from 18 °C to 39 °C, and thus the power cycle minimum temperature varies in a range between 31 °C and 51 °C, respectively, operating the power cycle in sliding pressure. When the ambient temperature is higher than 39 °C, it is not possible anymore to achieve a cycle minimum temperature lower or equal to 51 °C with the nominal volumetric flow rate of the cooling air, and the fan rotational speed should increase. The rotational speed limit of 130% of the design value is reached at an ambient temperature around 42 °C with a cycle minimum temperature of 51 °C: above this ambient temperature it is no more possible to run the plant at 80% of the thermal load, according to these condenser maps. On the other hand, for ambient temperatures below 18 °C the fan speed is reduced to avoid reducing the cycle minimum temperature below 31 °C. This solution is feasible down to 30% of the nominal value of the fan rotational speed, corresponding to an ambient temperature below 0 °C. Below the minimum value of rotational speed, a hypothetical possibility to run the plant at 80% of the thermal load relies in shutting down some of the fans of the air-cooled condenser and cooling some tube banks just by means of natural convection with the environment. Nevertheless, this solution has not been explored in this work as the uneven cooling of the tube banks could lead to an unbalanced flow distribution and issues related to the working fluid composition at the condenser outlet. Ultimately, to overcome the limitations of the upper and lower limits in ambient temperature dictated by the rotational speed operational range of the condenser, it is always possible to modify the thermal input into the cycle.

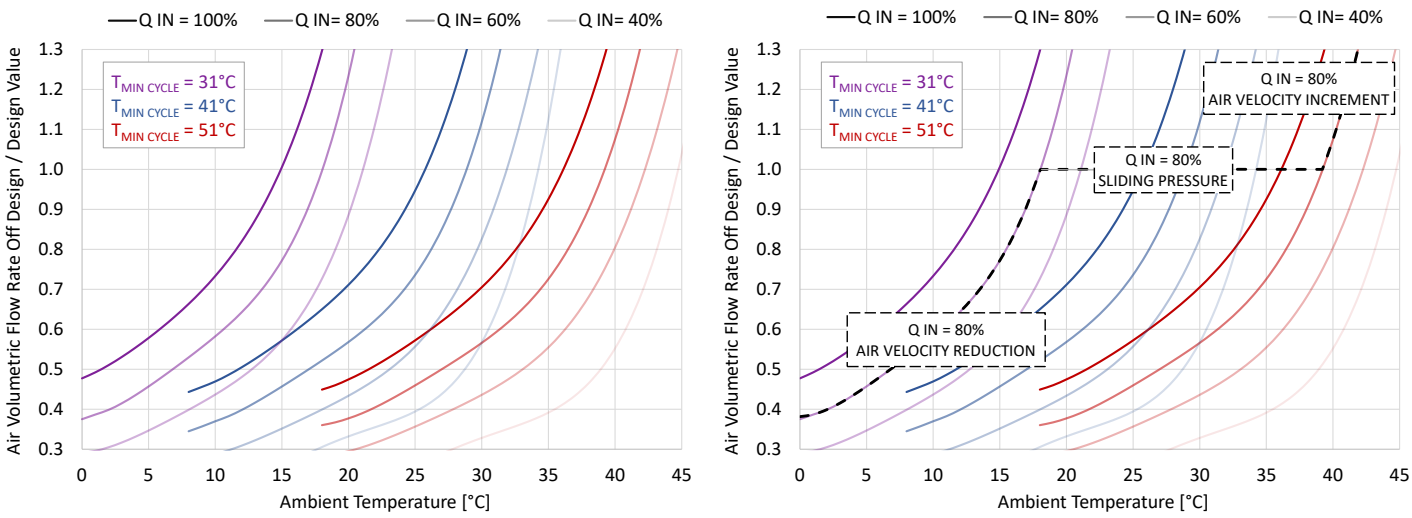

Figure 62. Air volumetric flow rate across the condenser varying the ambient temperature, the thermal input and the minimum temperature of the cycle. Fan control philosophy for a thermal input of 80% the nominal value, on the right

The trend of the temperature difference between the cycle minimum temperature and the ambient condition is also reproposed in Figure 63, adopting the methodology described in Chapter 7.3.2, allowing for a coupling between the ambient temperature and the cycle conditions for any off-design simulations, according to Equation (43).

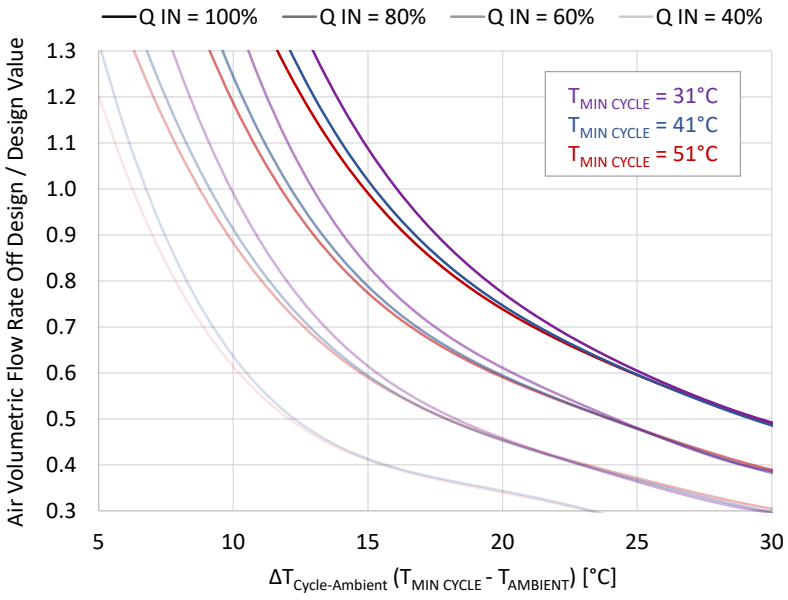

Figure 63. Air volumetric flow rate across the condenser as function of the temperature difference between the cycle minimum temperature and the ambient

Considering these results, it is possible to run the cycle in sliding pressure from ambient temperatures of 24 °C to 36 °C for any thermal input: at ambient temperatures of 40 °C and higher, full load solutions can be achieved only at the maximum cycle minimum temperature (of 51 °C), increasing the fan speed of the air condenser. At the same time, for ambient temperatures below 20 °C it is possible to run the cycle only at the minimum value of cycle minimum temperature (31 °C) and decreasing the velocity of the condenser fans.

The trend of some of the thermodynamic variables and parameters of the cycle in off-design conditions and fixed fan rotational speed are evidenced in Figure 64, and a complete characterization of all the variables are reported in Appendix D.3.

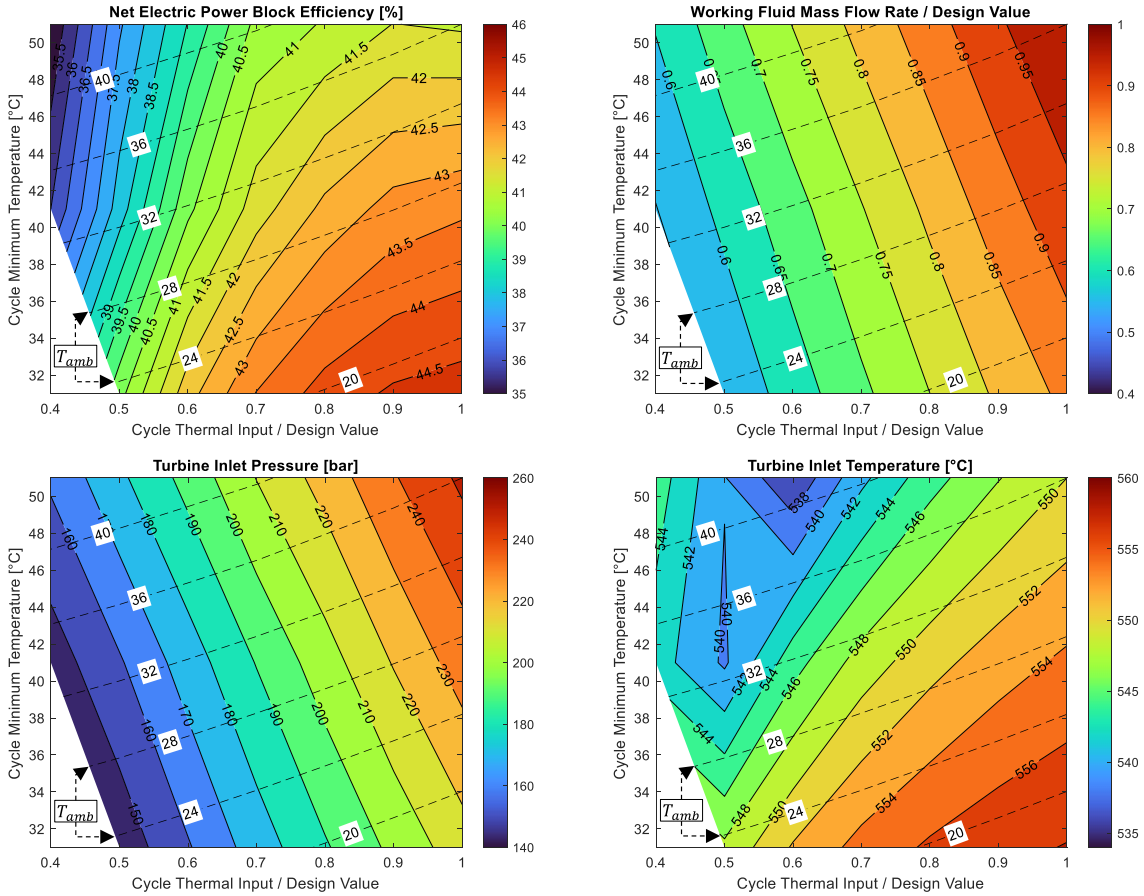

Figure 64. Off-design characteristics of the cycle investigated operating in sliding pressure, at design speed of the air-cooled condenser fans

Most of the trends are linear in terms both of ambient temperature and cycle thermal input, like the working fluid temperature at PHE inlet, the cycle maximum pressure and turbine pressure ratio, the working fluid mass flow rate, both the turbine and pump efficiencies. The cycle efficiency, instead, shows larger gradients with respect to the ambient temperature at high thermal load, and the turbine inlet temperature is characterized by an inversion of trend for off-design conditions of the HTF temperature at the PHE outlet, according to the limits of Table 45. The net electric power block efficiency (computed from the gross cycle

efficiency, adding the electromechanical losses and the auxiliary consumption of the air condenser) evidences a strong variability in off-design, moving from a maximum value of 44.5% at low ambient temperatures and high load, down to 37% at low load and more adverse ambient conditions.

8.4.2 Condenser fan at variable speed

When the ambient temperature is lower than 20 °C or slightly higher than the design value it is possible to modify the rotational speed of the condenser fan to reject the necessary heat into the environment at fixed cycle conditions, as presented in Figure 62. Under this assumption, the resulting net electric power block efficiency is computed starting from the one of the cycle (including the electromechanical losses of the turbomachinery) and considering the electric consumption of the air-condenser fans, modelled in any conditions according to the air-side pressure drop calculation depicted in Figure 27. The resulting trend of the net power block cycle efficiency is depicted in Figure 65, with both the thermal input and the ambient temperature selected as independent variables.

By changing the rotational speed of the condenser fans the range of admissible ambient temperatures expands down to 0 °C at full load, and 8 °C at 50% thermal load. On the other hand, much smaller gains of the maximum admissible ambient temperature are possible by increasing the fan speed to the maximum value, of only 3 °C.

The results show a strong and very encouraging dependency of the cycle efficiency on the ambient temperature, suggesting to fix the power cycle design conditions at both a high ambient temperature and a high cycle minimum temperature: the conversion efficiency of the cycle at design, in fact, can be reached at a 55% thermal load with an ambient temperature of 20 °C, only 16 °C lower than the value at design.

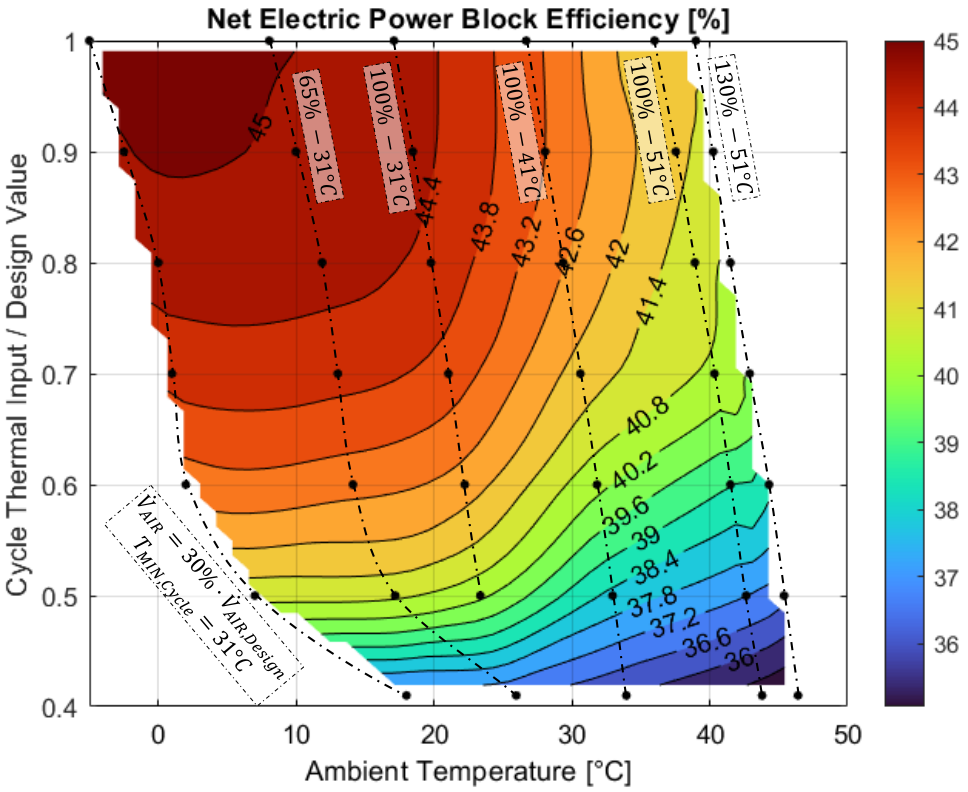

Figure 65. Net electric power block efficiency of the power cycle in off-design as function of the ambient conditions and the thermal input

8.5 Cycle off-design: conclusive remarks

The calculations of Chapter 8 describe a case study on the performance in off-design conditions of a transcritical simple recuperative cycle working with CO_2-based mixtures as working fluid. The mixture adopted, CO_2+C_6F_6, is identified in this work as very promising from a techno-economic point of view for state-of-the-art CSP plants with solar salts as HTF.

The results indicates that the high net electric cycle efficiency computed in nominal conditions are still possible down to 80% of the thermal input (between 42% and 45%, depending on the ambient temperature), while acceptable levels of efficiency can be still reached down to 50%-60% of the thermal input, corresponding to around 45-55% of the electric output, proving the capability of the CSP plant to efficiently follow a residual load curve, working in partial load.

Moreover, reducing to the minimum the fan speed of the condenser can allow for operation with ambient temperatures from 20 to 25 °C lower than the value

computed assuming the power cycle running in sliding pressure, extending the ambient temperature operating range to any season.

On the other hand, running the condenser at its maximum power results in a small gain in allowable ambient temperature. Accordingly, the choice of the cycle designer in selecting a high cycle minimum temperature and a high ambient temperature at design conditions has been effectively proven and confirmed as a good design practice.

Comparing the net electric cycle performances with simulations of steam cycles from literature for the same application, it is clearly noticeable an increment of around 3.5% to 4% (in absolute terms, which is about 9% in relative terms) of net electric cycle efficiency at full load, for any ambient temperature, and 2.5% to 3% (about 7% in relative terms) at 60% thermal input. The positive results prove the good performances of simple recuperative transcritical power cycles working with CO_2-mixtures, both from a design point of view and especially from an off-design perspective, collecting useful information for future annual analyses on the CSP plant profitability when adopting these solutions for the power cycle.

9. Conclusions and future developments

9.1 Conclusions

This thesis proposes a methodology to evaluate the performances of innovative mixtures based on CO_2 to be used as working fluids in closed transcritical cycles.

The selection of the dopant for the mixture must be considered a delicate subject of research, where many characteristics must be evaluated for each dopant, such as its thermal stability, toxicity, compatibility with the materials and the availability on the market, among the many, not neglecting the resulting thermal efficiency of the overall cycle.

Mixtures cannot be considered easy working fluids to be modelled from a thermodynamic point of view: accordingly, any equations of state (from the simplest to the most complex ones) should be optimized at least on experimental VLE data, and subsequently evaluated based on their accuracy on other categories of experimental data.

Accordingly, this work focuses on some innovative CO_2-mixtures to be efficiently exploited as working fluid, contributing to the development of this research field and increasing the existing knowledge on it.

In particular, the CO_2+C_6F_6 and the CO_2+SO_2 mixtures are considered between the most promising, mainly due to their thermal stability experimentally evaluated at least up to 600 °C.

With the help of the selected EoS tailored to each mixture it is possible to run power cycle simulations: the higher efficiency of the innovative power cycles with respect to technical solutions already available in literature are evidenced, always considering high cycle minimum temperatures, compatible with air-cooled HRU. For example, for power cycles at maximum temperature of 700 °C, the recompressed power cycle adopting CO_2+SO_2 presents efficiencies more than 2% higher than the sCO_2 cycle (4% in relative terms), while, for maximum temperatures of 550 °C, the simple cycle with the CO_2+C_6F_6 mixture presents efficiencies at least 2% higher (5% in relative terms) than conventional steam Rankine cycles. It has also been found that both the mixture composition and the power block layout highly influence the cycle performances, and each mixture can have a different optimal power block layout, mainly depending on the extension of the VLE region.

After introducing the thermodynamic modeling of the power cycles, numerical tools developed as in-house codes are presented to characterize the design and the off-design of all the heat exchangers across the cycles. For each of them the geometrical domain is analyzed with a 1-D finite volume approach, where the energy balance and the constitutive equation are solved simultaneously up to convergency. The approach led to an off-design characterization of the cycle behavior where any condition is numerically directly solved along the whole geometrical domain.

An additional contribution of this work to the literature regarding the development of detailed models for heat exchangers is the inclusion of suitable correlations for HTC of mixtures for two-phase conditions in the numerical models. This led to one of the first model in the open literature for the design and off-design of a crossflow air-cooled condenser with multi-pass finned tubes, particularly suitable for power cycles.

Moreover, selecting from literature transport properties models for mixtures, it has been evidenced a methodology to evaluate the heat transfer characteristics of the new working fluids in HX comparing the convective heat transfer coefficients with the values obtained for sCO_2 cycles. The methodology proposed can have an impact on the manufacturing of the components and even on the estimation of their capital cost.

Finally, two large case studies have been proposed focusing on large scale power plants for CSP applications (at around $100MW_{el}$). They are considered of interest since large scale plants can exploit economies of scale to reduce the overall capital costs of the plant and they can also benefit from higher efficiencies of the power cycles.

Many configurations of solar plants are designed and investigated in this work, proposing a sensitivity analysis on both the cycle maximum temperature and the storage configurations. The results evidenced that indirect storage configurations can lead to a more effective solar to electric power conversion, reducing the costs of the systems. Assuming Las Vegas as location for the CSP plant, the good economic performances of the innovative power cycles are highlighted, allowing for a limited reduction of LCOE with respect to sCO_2 cycles (resulting in values below the 100 $\$/MWh_{el}$ threshold), while at the same time increasing the competitiveness of CSP plants at maximum temperature of 550 °C.

In order to meet the need from the electric grid of increasingly efficient and fast power conversion systems, the off-design of the simple recuperative transcritical cycle working with CO_2+C_6F_6 is proposed, focusing on a configuration for state-of-the-art CSP applications. Starting from a net electric efficiency of 41.4% computed at design conditions, the off-design and part-load simulations reported stressed the large possible increment in cycle efficiency when the ambient temperature is reduced and the cycle operates in sliding pressure (reaching efficiencies up to 45% at ambient temperatures around 10 °C),

while still good efficiencies are possible at 50% electric output for ambient temperatures below 20 °C. The results, compared to conventional steam Rankine cycles adopted in the same CSP plant, evidenced increments in net cycle efficiencies around 3% in absolute terms, while at the same time leading to an enormous simplification of the power block layout and large improvements in the reactiveness of the plant to fast modulations of the electric output.

9.2 Future developments and suggestions for further studies

As this thesis highlights the use of tCO_2-mixture power cycles for concentrated solar power, the potentialities of the innovative cycles in other applications can still be extensively studied. Given the characteristics of the hot and cold source, interesting applications for these cycles can be nuclear power, indirectly fired plants (such as biomass plants) or waste heat recovery plants, among the many. Numerical tools can be developed in the future to explore the possible adoption of the power cycles proposed in this thesis for these other high temperature applications.

Moreover, moving to power cycles with maximum temperatures lower than the ones typical of CSP (in the range 350-450 °C), great potentialities are foreseeable thanks to the adoption of innovative mixtures with a less strict thermal stability requirements, not investigated in this work. In fact, focusing on less ambitious maximum temperatures can lead to an easier and faster TRL leveling up of the innovative tCO_2-mixture power cycles, as commonly available, non-reactive and non-toxic dopants can be considered.

Some additional analyses are carried out by the author of this thesis, that can potentially point at future paths in the research of tCO_2-mixture power cycles:

- The coupling of the innovative power cycles with waste heat recovery systems (WHR) can be considered of interest, assuming hot source temperatures around 300-500 °C.
  At this temperature level the direct competitors for heat recovery systems are conventional ORC: a literature work of Astolfi [48] proposed a comparison between sCO_2 cycles and ORC for this application, depending on the flue gases temperature and the possible cooling rate of the hot source. Given the compression in liquid phase and the limited temperature difference between the maximum and minimum temperatures of the cycle, it is foreseeable that tCO_2-

mixture power cycles can overcome the performance of sCO_2 cycles, offering a better alternative to ORC systems for WHR.
For example, the performances of the mixtures CO_2+C_2H_3N and CO_2+C_2Cl_4 were briefly analyzed in a literature work discussing the recovery of waste heat between 450 and 120 °C [146]. Analogously, the CO_2+C_6F_6 mixture was considered as working fluid for a heat recovery bottom cycle of a small-scale gas turbine, evidencing the good performances when compared to sCO_2 cycles at the same conditions [147].

- The effective exploitation of CO_2-based power cycles for the recovery of a large amount of thermal power at the cycle HRU, in order to directly use the low temperature heat. The rejected heat from the cycles can be in the temperature range between 45 and over 120 °C, depending on the cycle conditions.
  Focusing on the direct use of thermal power in a district heating network, a literature study by the author of this work evidenced the good performance of tCO_2 mixtures power cycles as bottom systems [147], recovering heat from flue gases and producing useful thermal power for district heating through the rejected heat from the condenser.
  Under this perspective, the higher the cycle minimum temperature the more valuable the heat recovered from the condenser for a direct use, suggesting a beneficial effect in thermodynamic efficiency of tCO_2 mixtures cycles with respect to sCO_2 cycles, given by the drop of cycle efficiency of sCO_2 cycles at cycle minimum temperatures higher than 45-50 °C.

- The coupling between tCO_2 mixtures power cycles and thermal seawater desalination systems. This topic is covered by the author of this thesis while working within the consortium of the EU H2020 project DESOLINATION. Approaching the rejected heat from the power cycle with the same perspective as its direct use in a district heating network, it can be also used to feed a thermal desalination plant. The conventional technology for this purpose is the multi effect distillation (MED), while an innovative technology based on the concept of forward osmosis is investigated in the DESOLINATION project [148]. The two technologies can reach specific thermal energy consumption in a range between 80 and 180 kWh_{th}/m^3 of fresh water produced: while the coupling between tCO_2 mixtures cycles for CSP and a MED plant has been already investigated by the author [115], future works will detail the performance of the coupling between a solar plant with CO_2-based cycles a forward osmosis desalination plant.

References

[1] S. T. Huber and K. Steininger, “Critical sustainability issues in the production of wind and solar electricity generation as well as storage facilities and possible solutions,” *J Clean Prod*, vol. 339, p. 130720, Mar. 2022, doi: 10.1016/J.JCLEPRO.2022.130720.

[2] D. Belverato, E. Martelli, M. Binotti, L. Pilotti, and A. Giaconia, “Part-Load of Steam Rankine Cycles for Solar Salts-Based Concentrating Solar Power Plants,” in *Proceedings of the ASME Turbo Expo*, American Society of Mechanical Engineers Digital Collection, Oct. 2022. doi: 10.1115/GT2022-79378.

[3] S. El Marazgioui and A. El Fadar, “Impact of cooling tower technology on performance and cost-effectiveness of CSP plants,” *Energy Convers Manag*, vol. 258, p. 115448, Apr. 2022, doi: 10.1016/J.ENCONMAN.2022.115448.

[4] M. T. White, G. Bianchi, L. Chai, S. A. Tassou, and A. I. Sayma, “Review of supercritical CO2 technologies and systems for power generation,” *Appl Therm Eng*, vol. 185, Feb. 2021, doi: 10.1016/J.APPLTHERMALENG.2020.116447.

[5] G. Manente and F. M. Fortuna, “Supercritical CO2 power cycles for waste heat recovery: A systematic comparison between traditional and novel layouts with dual expansion,” *Energy Convers Manag*, vol. 197, no. July, p. 111777, 2019, doi: 10.1016/j.enconman.2019.111777.

[6] S. A. Wright, C. S. Davidson, and W. O. Scammell, “Thermo-Economic Analysis of Four sCO2 Waste Heat Recovery Power Systems,” *The 5th International Symposium - Supercritical CO2 Power Cycles*, pp. 1–16, 2016.

[7] D. Alfani, M. Astolfi, M. Binotti, and P. Silva, “Part-Load Strategy Definition and Preliminary Annual Simulation for Small Size sCO2-Based Pulverized Coal Power Plant,” *J Eng Gas Turbine Power*, vol. 143, no. 9, Sep. 2021, doi: 10.1115/1.4051003/1108261.

[8] V. Dostal, M. J. Driscoll, and P. Hejzlar, “A Supercritical Carbon Dioxide Cycle for Next Generation Nuclear Reactors,” *Technical Report MIT-ANP-TR-100*, pp. 1–317, 2004, doi: MIT-ANP-TR-100.

[9] P. Wu *et al.*, “A review of research and development of supercritical carbon dioxide Brayton cycle technology in nuclear engineering applications,” *Nuclear Engineering and Design*, vol. 368, Nov. 2020, doi: 10.1016/J.NUCENGDES.2020.110767.

[10] S. Khatoon and M. H. Kim, “Potential improvement and comparative assessment of supercritical Brayton cycles for arid climate,” *Energy Convers Manag*, vol. 200, no. June, p. 112082, 2019, doi: 10.1016/j.enconman.2019.112082.

[11] G. G. Simeoni *et al.*, “The Widom line as the crossover between liquid-like and gas-like behaviour in supercritical fluids,” *Nature Physics 2010 6:7*, vol. 6, no. 7, pp. 503–507, Jun. 2010, doi: 10.1038/nphys1683.

[12] R. Span and W. Wagner, “A New Equation of State for Carbon Dioxide Covering the Fluid Region from the Triple-Point Temperature to 1100 K at Pressures up to 800 MPa,” *J Phys Chem Ref Data*, vol. 25, no. 6, pp. 1509–1596, Nov. 1996, doi: 10.1063/1.555991.

[13] R. Cao, Q. Deng, Z. Li, J. Li, and T. Gao, “Design strategy for inlet conditions of supercritical CO2 centrifugal compressors,” *Journal of Supercritical Fluids*, vol. 196, May 2023, doi: 10.1016/J.SUPFLU.2023.105879.

[14] A. Romei, P. Gaetani, A. Giostri, and G. Persico, “The Role of Turbomachinery Performance in the Optimization of Supercritical Carbon Dioxide Power Systems,” 2020, doi: 10.1115/1.4046182.

[15] F. Crespi, G. Gavagnin, D. Sánchez, and G. S. Martínez, “Supercritical carbon dioxide cycles for power generation: A review,” *Appl Energy*, vol. 195, pp. 152–183, Jun. 2017, doi: 10.1016/j.apenergy.2017.02.048.

[16] A. de la Calle, A. Bayon, and Y. C. Soo Too, “Impact of ambient temperature on supercritical CO2 recompression Brayton cycle in arid locations: Finding the optimal design conditions,” *Energy*, vol. 153, pp. 1016–1027, Jun. 2018, doi: 10.1016/J.ENERGY.2018.04.019.

[17] “IEA Report on CSP - 2021.” https://www.iea.org/reports/concentrated-solar-power-csp (accessed Jul. 18, 2022).

[18] “CSPDATA.” https://cspdata.com/

[19] D. Feldman, M. Bolinger, and P. Schwabe, “Current and Future Costs of Renewable Energy Project Finance Across Technologies,” 2020, Accessed: Jul. 18, 2022. [Online]. Available: www.nrel.gov/publications.

[20] P. et al Viebahn, “Power Tower Technology Roadmap and cost reduction plan.,” *Energy Policy*, vol. 14, no. September, pp. 5–7, Apr. 2011, doi: 10.2172/1011644.

[21] C. S. Turchi *et al.*, “CSP Systems Analysis - Final Project Report,” 2019. Accessed: Jul. 20, 2022. [Online]. Available: www.nrel.gov/publications.

[22] M. Mehos *et al.*, “Concentrating Solar Power Gen3 Demonstration Roadmap,” *Nrel/Tp-5500-67464*, no. January, pp. 1–140, 2017, doi: 10.2172/1338899.

[23] I. Arias, J. Cardemil, E. Zarza, L. Valenzuela, and R. Escobar, “Latest developments, assessments and research trends for next generation of concentrated solar power plants using liquid heat transfer fluids,” *Renewable and Sustainable Energy Reviews*, vol. 168, p. 112844, Oct. 2022, doi: 10.1016/J.RSER.2022.112844.

[24] S. Polimeni, M. Binotti, L. Moretti, and G. Manzolini, “Comparison of sodium and KCl-MgCl2 as heat transfer fluids in CSP solar tower with sCO2 power cycles,” *Solar Energy*, vol. 162, pp. 510–524, Mar. 2018, doi: 10.1016/j.solener.2018.01.046.

[25] G. Manzolini, G. Lucca, M. Binotti, and G. Lozza, “A two-step procedure for the selection of innovative high temperature heat transfer fluids in solar tower power plants,” *Renew Energy*, vol. 177, pp. 807–822, Nov. 2021, doi: 10.1016/J.RENENE.2021.05.153.

[26] G. Gentile, G. Picotti, M. Binotti, M. E. Cholette, and G. Manzolini, “Dynamic thermal analysis and creep-fatigue lifetime assessment of solar tower external receivers,” *Solar Energy*, vol. 247, pp. 408–431, Nov. 2022, doi: 10.1016/J.SOLENER.2022.10.010.

[27] Y. Liu, Y. Wang, and D. Huang, “Supercritical CO2 Brayton cycle: A state-of-the-art review,” *Energy*, vol. 189, Dec. 2019, doi: 10.1016/J.ENERGY.2019.115900.

[28] F. Crespi, D. Sánchez, J. M. Rodríguez, and G. Gavagnin, “A thermo-economic methodology to select sCO2 power cycles for CSP applications,” *Renew Energy*, vol. 147, pp. 2905–2912, Mar. 2020, doi: 10.1016/j.renene.2018.08.023.

[29] F. Crespi, D. Sánchez, G. S. Martínez, T. Sánchez-Lencero, and F. Jiménez-Espadafor, “Potential of Supercritical Carbon Dioxide Power Cycles to Reduce the Levelised Cost of Electricity of Contemporary Concentrated Solar Power Plants,” *Applied Sciences 2020, Vol. 10, Page 5049*, vol. 10, no. 15, p. 5049, Jul. 2020, doi: 10.3390/APP10155049.

[30] M. Binotti, M. Astolfi, S. Campanari, G. Manzolini, and P. Silva, “Preliminary assessment of sCO2 cycles for power generation in CSP solar tower plants,” *Appl Energy*, vol. 204, pp. 1007–1017, Oct. 2017, doi: 10.1016/J.APENERGY.2017.05.121.

[31] J. Q. Guo, M. J. Li, J. L. Xu, J. J. Yan, and K. Wang, “Thermodynamic performance analysis of different supercritical Brayton cycles using CO2-based binary mixtures in the molten salt solar power tower systems,” *Energy*, vol. 173, pp. 785–798, 2019, doi: 10.1016/j.energy.2019.02.008.

[32] W. S. Jeong, J. I. Lee, and Y. H. Jeong, “Potential improvements of supercritical recompression CO2Brayton cycle by mixing other gases for power conversion system of a SFR,” *Nuclear Engineering and Design*, vol. 241, no. 6, pp. 2128–2137, 2011, doi: 10.1016/j.nucengdes.2011.03.043.

[33] P. Tafur-Escanta, I. López-Paniagua, and J. Muñoz-Antón, “Thermodynamics analysis of the supercritical CO2 binary mixtures for Brayton power cycles,” *Energy*, vol. 270, May 2023, doi: 10.1016/J.ENERGY.2023.126838.

[34] N. Zheng, Z. Li, J. Fang, and J. Wei, “Supercritical CO2 mixture Brayton cycle with floating critical points for concentrating solar power application: Concept and thermodynamic analysis,” *Energy Convers Manag*, vol. 284, May 2023, doi: 10.1016/J.ENCONMAN.2023.116989.

[35] X. Liu, Z. Xu, Y. Xie, and H. Yang, “CO2-based mixture working fluids used for the dry-cooling supercritical Brayton cycle: Thermodynamic evaluation,” *Appl Therm Eng*, vol. 162, no. 17923, p. 114226, Nov. 2019, doi: 10.1016/j.applthermaleng.2019.114226.

[36] N. Ma, F. Meng, W. Hong, H. Li, and X. Niu, “Thermodynamic assessment of the dry-cooling supercritical Brayton cycle in a direct-heated solar power tower plant enabled by CO2-propane mixture,” *Renew Energy*, vol. 203, pp. 649–663, Feb. 2023, doi: 10.1016/J.RENENE.2022.12.084.

[37] G. Di Marcoberardino, E. Morosini, and G. Manzolini, “Preliminary investigation of the influence of equations of state on the performance of CO2 + C6F6 as innovative working fluid in transcritical cycles,” *Energy*, vol. 238, p. 121815, Jan. 2022, doi: 10.1016/J.ENERGY.2021.121815.

[38] NIST - National Institute of Standards and Technology, “REFPROP - Reference Fluid Thermodynamic and Transport Properties.”

[39] D. Y. Peng and D. B. Robinson, “A New Two-Constant Equation of State,” *Industrial and Engineering Chemistry Fundamentals*, vol. 15, no. 1, pp. 59–64, 1976, doi: 10.1021/i160057a011.

[40] M. E. Siddiqui, E. Almatrafi, A. Bamasag, and U. Saeed, “Adoption of CO2-based binary mixture to operate transcritical Rankine cycle in warm regions,” *Renew Energy*, vol. 199, pp. 1372–1380, Nov. 2022, doi: 10.1016/J.RENENE.2022.09.095.

[41] G. Shu, Z. Yu, H. Tian, P. Liu, and Z. Xu, “Potential of the transcritical Rankine cycle using CO2-based binary zeotropic mixtures for engine’s waste heat recovery,” *Energy Convers Manag*, vol. 174, pp. 668–685, Oct. 2018, doi: 10.1016/J.ENCONMAN.2018.08.069.

[42] C. Wu, S. sen Wang, X. Jiang, and J. Li, “Thermodynamic analysis and performance optimization of transcritical power cycles using CO2-based binary zeotropic mixtures as working fluids for geothermal power plants,” *Appl Therm Eng*, vol. 115, pp. 292–304, Mar. 2017, doi: 10.1016/J.APPLTHERMALENG.2016.12.077.

[43] L. Feng, D. Zheng, J. Chen, X. Dai, and L. Shi, “Exploration and Analysis of CO2 + Hydrocarbons Mixtures as Working Fluids for Trans-critical ORC,” *Energy Procedia*, vol. 129, pp. 145–151, 2017, doi: 10.1016/J.EGYPRO.2017.09.191.

[44] M. E. Siddiqui, “Thermodynamic Performance Improvement of Recompression Brayton Cycle Utilizing CO2-C7H8 Binary Mixture,” *Mechanics*, vol. 27, no. 3, pp. 259–264, Jun. 2021, doi: 10.5755/J02.MECH.28126.

[45] S. Lasala, C. Invernizzi, P. Iora, P. Chiesa, and E. Macchi, “Thermal Stability Analysis of Perfluorohexane,” in *Energy Procedia*, Elsevier Ltd, Aug. 2015, pp. 1575–1582. doi: 10.1016/j.egypro.2015.07.358.

[46] D. M. Lemal, “Perspective on Fluorocarbon Chemistry,” *Journal of Organic Chemistry*, vol. 69, no. 1, pp. 1–11, Jan. 2004, doi: 10.1021/JO0302556/ASSET/IMAGES/LARGE/JO0302556F26.JPEG.

[47] W. L. Fielder, “Thermal Decomposition of Some Linear Perfluoroalkanes in an Inconel Tube.” 1961.

[48] M. Astolfi, D. Alfani, S. Lasala, and E. Macchi, “Comparison between ORC and CO2 power systems for the exploitation of low-medium

temperature heat sources," *Energy*, vol. 161, pp. 1250–1261, Oct. 2018, doi: 10.1016/J.ENERGY.2018.07.099.

[49] S. Gallarini, A. Spinelli, L. Lietti, and A. Guardone, "Thermal stability of linear siloxanes and their mixtures," *Energy*, vol. 278, p. 127687, Sep. 2023, doi: 10.1016/J.ENERGY.2023.127687.

[50] S. A. Gornati, D. Di Bona, and P. Chiesa, "New experimental VLE data for the binary mixture of carbon dioxide + perfluorohexane (CO2 + C6F14) from 273 K to 333 K," *Fluid Phase Equilib*, vol. 498, pp. 94–103, Oct. 2019, doi: 10.1016/j.fluid.2019.06.024.

[51] "Scarabeus H2020 Project." https://www.scarabeusproject.eu/ (accessed Oct. 01, 2021).

[52] G. Manzolini, M. Binotti, D. Bonalumi, C. Invernizzi, and P. Iora, "CO2 mixtures as innovative working fluid in power cycles applied to solar plants. Techno-economic assessment," *Solar Energy*, vol. 181, pp. 530–544, Mar. 2019, doi: 10.1016/j.solener.2019.01.015.

[53] M. Binotti, C. M. Invernizzi, P. Iora, and G. Manzolini, "Dinitrogen tetroxide and carbon dioxide mixtures as working fluids in solar tower plants," *Solar Energy*, vol. 181, pp. 203–213, Mar. 2019, doi: 10.1016/J.SOLENER.2019.01.079.

[54] D. Bonalumi, S. Lasala, and E. Macchi, "CO2-TiCl4 working fluid for high-temperature heat source power cycles and solar application," *Renew Energy*, vol. 147, pp. 2842–2854, Mar. 2020, doi: 10.1016/j.renene.2018.10.018.

[55] F. Crespi *et al.*, "Thermal efficiency gains enabled by using CO2 mixtures in supercritical power cycles," *Energy*, vol. 238, Jan. 2022, doi: 10.1016/J.ENERGY.2021.121899.

[56] E. Morosini, D. Di Bona, G. Di Marcoberardino, and G. Manzolini, "Characterization of the Andrew's curve for the selected most promising fluid - Deliverable 2.2 of the SCARABEUS project," 2021.

[57] G. Di Marcoberardino *et al.*, "Experimental characterisation of CO2 + C6F6 mixture: Thermal stability and vapour liquid equilibrium test for its application in transcritical power cycle," *Appl Therm Eng*, vol. 212, Jul. 2022, doi: 10.1016/J.APPLTHERMALENG.2022.118520.

[58] National Fire Protection Association, *NFPA 704 - Standard System for the Identification of the Hazards of Materials for Emergency Response*. 2007.

[59] W. Liu *et al.*, "Performance analysis of organic Rankine cycle power generation system for intercooled cycle gas turbine," *Research Article Advances in Mechanical Engineering*, vol. 10, no. 8, p. 2018, 2018, doi: 10.1177/1687814018794074.

[60] J. M. Antonucci and L. A. Wall, "High-Temperature Reactions of Hexafluorobenzene," *JOURNAL OF RESEARCH of the Notional Bureau of Standards - A. Physics and Chemistry*, vol. 70A, no. 6, 1966.

[61] L. R. Dinanno, F. A. Dibella, and M. D. Koplow, "An RC-1 Organic Rankine Bottoming Cycle for an Adiabatic Diesel Engine," 1983.

[62] L. Mignion, J. Magat, O. Schakman, E. Marbaix, B. Gallez, and B. F. Jordan, “Hexafluorobenzene in comparison with perfluoro-15-crown-5-ether for repeated monitoring of oxygenation using 19F MRI in a mouse model,” *Magn Reson Med*, vol. 69, no. 1, pp. 248–254, 2013, doi: 10.1002/MRM.24245.

[63] AspenTech, “Aspen Plus | Leading Process Simulation Software | AspenTech.” https://www.aspentech.com/en/products/engineering/aspen-plus

[64] A. M. A. Dias *et al.*, “Vapor - Liquid equilibrium of carbon dioxide - Perfluoroalkane mixtures: Experimental data and SAFT modeling,” *Ind Eng Chem Res*, vol. 45, no. 7, pp. 2341–2350, Mar. 2006, doi: 10.1021/ie051017z.

[65] “Desolination H2020 Project.” https://desolination.eu/ (accessed Oct. 25, 2022).

[66] A. Yasuhara, “Thermal decomposition of tetrachloroethylene,” *Chemosphere*, vol. 26, no. 8, pp. 1507–1512, 1993, doi: 10.1016/0045-6535(93)90218-T.

[67] L. D. Trowbridge, “Potential Hazards Relating to Pyrolysis of c-C4F8O, n-C4F10 and c-C4F8 in Selected Gaseous Diffusion Plant Operations,” Mar. 2000. Accessed: Jul. 18, 2022. [Online]. Available: https://digital.library.unt.edu/ark:/67531/metadc738055/m2/1/high_res_d/814073.pdf

[68] S. C. Moldoveanu, “Pyrolysis of Various Derivatives of Carboxylic Acids,” in *Techniques and Instrumentation in Analytical Chemistry*, Elsevier, 2010, pp. 579–627. doi: 10.1016/S0167-9244(09)02819-4.

[69] Y. Li, X. Zhang, S. Tian, S. Xiao, Y. Li, and D. Chen, “Insight into the decomposition mechanism of C6F12O-CO2 gas mixture,” *Chemical Engineering Journal*, vol. 360, pp. 929–940, Mar. 2019, doi: 10.1016/J.CEJ.2018.10.167.

[70] A. Kordikowski, A. P. Schenk, R. M. Van Nielen, and C. J. Peters, “Volume expansions and vapor-liquid equilibria of binary mixtures of a variety of polar solvents and certain near-critical solvents,” *J Supercrit Fluids*, vol. 8, no. 3, pp. 205–216, Sep. 1995, doi: 10.1016/0896-8446(95)90033-0.

[71] H. S. Byun, B. M. Hasch, and M. A. McHugh, “Phase behavior and modeling of the systems CO2-acetonitrile and CO2-acrylic acid,” *Fluid Phase Equilib*, vol. 115, no. 1–2, pp. 179–192, Feb. 1996, doi: 10.1016/0378-3812(95)02830-7.

[72] M. L. Corazza, L. C. Filho, O. A. C. Antunes, and C. Dariva, “High pressure phase equilibria of the related substances in the limonene oxidation in supercritical CO2,” *J Chem Eng Data*, vol. 48, no. 2, pp. 354–358, Mar. 2003, doi: 10.1021/JE020150K.

[73] M. J. Lazzaroni, D. Bush, J. S. Brown, and C. A. Eckert, “High-pressure vapor-liquid equilbria of some carbon dioxide + organic binary systems,” *J*

Chem Eng Data, vol. 50, no. 1, pp. 60–65, Jan. 2005, doi: 10.1021/JE0498560.

[74] C. Coquelet, A. Valtz, and P. Arpentinier, "Thermodynamic Study of binary and ternary systems containing CO2 + impurities in the context of CO2 transportation," *Elsevier B.V.*, 2014, doi: 10.1016/j.fluid2014.08.03.

[75] B. Gimeno, M. Artal, I. Velasco, J. Fernández, and S. T. Blanco, "Influence of SO2 on CO2 Transport by Pipeline for Carbon Capture and Storage Technology: Evaluation of CO2/SO2 co-capture," *Energy and Fuels*, vol. 32, no. 8, pp. 8641–8657, 2018, doi: 10.1021/acs.energyfuels.8b01666.

[76] M. Nazeri, A. Chapoy, A. Valtz, C. Coquelet, and B. Tohidi, "New experimental density data and derived thermophysical properties of carbon dioxide – Sulphur dioxide binary mixture (CO2 - SO2) in gas, liquid and supercritical phases from 273 K to 353 K and at pressures up to 42 MPa," *Fluid Phase Equilib*, vol. 454, pp. 64–77, 2017, doi: 10.1016/j.fluid.2017.09.014.

[77] R. *et al.*, "TREND. Thermodynamic Reference and Engineering Data 5.0." Ruhr-Universität Bochum, 2020.

[78] T. Neumann, "Development of New Helmholtz Models for Binary Mixture Relevant for CCS."

[79] O. Kunz and W. Wagner, "The GERG-2008 wide-range equation of state for natural gases and other mixtures: An expansion of GERG-2004," *J Chem Eng Data*, vol. 57, no. 11, pp. 3032–3091, Nov. 2012, doi: 10.1021/je300655b.

[80] J. F. ; Boston and P. M. Mathias, "Phase Equilibria in a Third-Generation Process Simulator," in *2nd International Conference of Phase Equlibria and Fluid Properties in the Chemical Industry*, Berlin, Germany, 1980.

[81] T. Holderbaum and J. Gmehling, "PSRK: A Group Contribution Equation of State Based on UNIFAC," *Fluid Phase Equilib*, vol. 70, no. 2, pp. 251–265, 1991, doi: https://doi.org/10.1016/0378-3812(91)85038-V.

[82] B. I. Lee and M. G. Kesler, "A generalized thermodynamic correlation based on three-parameter corresponding states," *AIChE Journal*, vol. 21, no. 3, pp. 510–527, 1975, doi: 10.1002/aic.690210313.

[83] U. Plöcker, H. Knapp, and J. Prausnitz, "Calculation of High-Pressure Vapor-Liquid Equilibria from a Corresponding-States Correlation with Emphasis on Asymmetric Mixtures," *Industrial and Engineering Chemistry Process Design and Development*, vol. 17, no. 3, pp. 324–332, 1978, doi: 10.1021/i260067a020.

[84] J. Gross and G. Sadowski, "Perturbed-chain SAFT: An equation of state based on a perturbation theory for chain molecules," *Ind Eng Chem Res*, vol. 40, no. 4, pp. 1244–1260, Feb. 2001, doi: 10.1021/ie0003887.

[85] J. F. Ely and H. J. M. Hanley, "Prediction of Transport Properties. 1. Viscosity of Fluids and 673 Mixtures," *Industrial and Engineering Chemistry Fundamentals*, vol. 20, pp. 323–332, 1981.

[86] M. Nazeri, A. Chapoy, R. Burgass, and B. Tohidi, "Viscosity of CO2-rich mixtures from 243 K to 423 K at pressures up to 155 MPa: New

experimental viscosity data and modelling," *J Chem Thermodyn*, vol. 118, pp. 100–114, Mar. 2018, doi: 10.1016/J.JCT.2017.11.005.

[87] S. E. Quiñones-Cisneros, C. K. Zéberg-Mikkelsen, and E. H. Stenby, "One parameter friction theory models for viscosity," *Fluid Phase Equilib*, vol. 178, no. 1–2, pp. 1–16, Mar. 2001, doi: 10.1016/S0378-3812(00)00474-X.

[88] V. Illyés *et al.*, "Design of an Air-Cooled Condenser for CO2-Based Mixtures: Model Development, Validation and Heat Exchange Gain with Internal Microfins," *Proceedings of ASME Turbo Expo 2022: Turbomachinery Technical Conference and Exposition*, vol. Volume 9, Oct. 2022, doi: 10.1115/GT2022-82438.

[89] E. Morosini, A. Ayub, G. di Marcoberardino, C. M. Invernizzi, P. Iora, and G. Manzolini, "Adoption of the CO2 + SO2 mixture as working fluid for transcritical cycles: A thermodynamic assessment with optimized equation of state," *Energy Convers Manag*, vol. 255, Mar. 2022, doi: 10.1016/J.ENCONMAN.2022.115263.

[90] D. Alfani, M. Binotti, E. Macchi, P. Silva, and M. Astolfi, "sCO2 power plants for waste heat recovery: design optimization and part-load operation strategies," *Appl Therm Eng*, vol. 195, p. 117013, Aug. 2021, doi: 10.1016/J.APPLTHERMALENG.2021.117013.

[91] P. Rodríguez-deArriba, F. Crespi, D. Sánchez, A. Muñoz, and T. Sánchez, "The potential of transcritical cycles based on CO2 mixtures: An exergy-based analysis," *Renew Energy*, vol. 199, pp. 1606–1628, Nov. 2022, doi: 10.1016/J.RENENE.2022.09.041.

[92] F. Crespi, G. S. Martínez, P. R. De Arriba, D. Sánchez, and F. Jiménez-Espadafor, "Influence of Working Fluid Composition on the Optimum Characteristics of Blended Supercritical Carbon Dioxide Cycles," *Proceedings of the ASME Turbo Expo*, vol. 10, Sep. 2021, doi: 10.1115/GT2021-60293.

[93] E. Morosini, E. Villa, G. Quadrio, M. Binotti, and G. Manzolini, "Solar tower CSP plants with transcritical cycles based on CO2 mixtures: A sensitivity on storage and power block layouts," *Solar Energy*, vol. 262, Sep. 2023, doi: 10.1016/J.SOLENER.2023.05.054.

[94] V. Gnielinski, "New Equations for Heat and Mass Transfer in Turbulent Pipe and Channel Flow," *International Journal of Chemical Enginnering*, vol. 16, no. 2, pp. 359–368, 1976.

[95] A. Cavallini *et al.*, "Condensation in Horizontal Smooth Tubes: A New Heat Transfer Model for Heat Exchanger Design," *Heat Transfer Engineering*, vol. 27, no. 8, pp. 31–38, Sep. 2006, doi: 10.1080/01457630600793970.

[96] K. J. Bell and M. Ghali, "An approximate generalized design method for multicomponent/ partial condensers," *AICHE Symp. Ser*, vol. 69, pp. 72–79, 1973.

[97] D. Del Col, A. Bisetto, M. Bortolato, D. Torresin, and L. Rossetto, "Experiments and updated model for two phase frictional pressure drop

inside minichannels," *Int J Heat Mass Transf*, vol. 67, pp. 326–337, Dec. 2013, doi: 10.1016/J.IJHEATMASSTRANSFER.2013.07.093.

[98] A. Cavallini, D. Del Col, M. Matkovic, and L. Rossetto, "Frictional pressure drop during vapour–liquid flow in minichannels: Modelling and experimental evaluation," *Int J Heat Fluid Flow*, vol. 30, no. 1, pp. 131–139, Feb. 2009, doi: 10.1016/J.IJHEATFLUIDFLOW.2008.09.003.

[99] E. D. Grimison, "Correlation and Utilization of New Data on Flow Resistance and Heat Transfer for Cross Flow of Gases Over Tube Banks," *J Fluids Eng*, vol. 59, no. 7, pp. 583–594, Oct. 1937, doi: 10.1115/1.4020557.

[100] S. Marković, B. Jaćimović, S. Genić, M. Mihailović, U. Milovančević, and M. Otović, "Air side pressure drop in plate finned tube heat exchangers," *International Journal of Refrigeration*, vol. 99, pp. 24–29, Mar. 2019, doi: 10.1016/J.IJREFRIG.2018.11.038.

[101] K. K. Robinson and D. E. Briggs, "Pressure drop of air flowing across triangular pitch banks of finned tubes," *Chem. Eng. Prog. Symp.*, vol. 62, no. 64, pp. 177–184, 1966.

[102] H. A. Navarro and L. C. Cabezas-Gómez, "Effectiveness-NTU computation with a mathematical model for cross-flow heat exchangers," *Brazilian Journal of Chemical Engineering*, vol. 24, no. 4, pp. 509–521, 2007, doi: 10.1590/S0104-66322007000400005.

[103] D. Alfani, M. Astolfi, M. Binotti, S. Campanari, F. Casella, and P. Silva, "Multi Objective Optimization of Flexible Supercritical CO2 Coal-Fired Power Plants," in *Proceedings of the ASME Turbo Expo*, American Society of Mechanical Engineers Digital Collection, Nov. 2019. doi: 10.1115/GT2019-91789.

[104] S. Guccione, A. Fontalvo, R. Guedez, J. Pye, L. Savoldi, and R. Zanino, "Techno-economic optimisation of a sodium–chloride salt heat exchanger for concentrating solar power applications," *Solar Energy*, vol. 239, pp. 252–267, Jun. 2022, doi: 10.1016/J.SOLENER.2022.04.052.

[105] P. A. González-Gómez, J. Gómez-Hernández, C. Ruiz, and D. Santana, "Can solar tower plants withstand the operational flexibility of combined cycle plants?," *Appl Energy*, vol. 314, May 2022, doi: 10.1016/J.APENERGY.2022.118951.

[106] S. Fettaka, J. Thibault, and Y. Gupta, "Design of shell-and-tube heat exchangers using multiobjective optimization," *Int J Heat Mass Transf*, vol. 60, no. 1, pp. 343–354, May 2013, doi: 10.1016/J.IJHEATMASSTRANSFER.2012.12.047.

[107] S. Kakaç, H. Liu, and A. Pramuanjaroenkij, *Heat Exchangers : Selection, Rating, and Thermal Design*. CRC Press, 2020. doi: 10.1201/9780429469862.

[108] D. Walraven, "Optimization of the Energy Conversion Starting from Low-Temperature Heat: Application to Geothermal Binary Cycles," KU Leuven - Arenberg doctoral school, 2014.

[109] E. Morosini, E. Villa, G. Quadrio, M. Binotti, and G. Manzolini, “Solar tower CSP plants with transcritical cycles based on CO2 mixtures: a sensitivity on storage and power block layouts,” *Solar Energy*, vol. 260 C, 2023, doi: 10.1016/j.solener.2023.05.054.

[110] N. T. Weiland, B. W. Lance, and S. R. Pidaparti, “SCO2 power cycle component cost correlations from DOE data spanning multiple scales and applications,” in *Proceedings of the ASME Turbo Expo*, American Society of Mechanical Engineers (ASME), 2019. doi: 10.1115/GT2019-90493.

[111] M. D. Carlson, B. M. Middleton, and C. K. Ho, “Techno-Economic Comparison of Solar-Driven sCO2 Brayton Cycles Using Component Cost Models Baselined With Vendor Data and Estimates,” *Proceedings of the ASME 2017 Power and Energy Conference*, pp. 1–7, 2017, doi: 10.1115/ES2017-3590.

[112] “THERMOFLEX v29 - Heat Balance Software.”

[113] G. Manzolini *et al.*, “Adoption of CO2 blended with C6F6 as working fluid in CSP plants,” in *AIP Conference Proceedings*, AIP Publishing LLCAIP Publishing, May 2022, p. 090005. doi: 10.1063/5.0086520.

[114] E. Morosini, G. Gentile, M. Binotti, and G. Manzolini, “Techno-economic assessment of small-scale solar tower plants with modular billboard receivers and innovative power cycles,” in *Journal of Physics: Conference Series*, IOP Publishing, Dec. 2022, p. 012109. doi: 10.1088/1742-6596/2385/1/012109.

[115] M. Doninelli *et al.*, “Thermal desalination from rejected heat of power cycles working with CO2-based working fluids in CSP application: a focus on the MED technology,” *Sustainable Energy Technologies and Assessments*, no. Special Issue of the SDEWES 2022 Conference (Under Review), 2023.

[116] NREL, “SolarPILOT - Solar Power tower Integrated Layout and Optimization Tool.” [Online]. Available: https://www.nrel.gov/csp/solarpilot.html

[117] M. J. Wagner and T. Wendelin, “SolarPILOT: A power tower solar field layout and characterization tool,” *Solar Energy*, vol. 171, pp. 185–196, Sep. 2018, doi: 10.1016/J.SOLENER.2018.06.063.

[118] G. Gentile, G. Picotti, F. Casella, M. Binotti, M. E. Cholette, and G. Manzolini, “SolarReceiver2D: a Modelica Package for Dynamic Thermal Modelling of Central Receiver Systems,” *IFAC-PapersOnLine*, vol. 55, no. 20, pp. 259–264, Jan. 2022, doi: 10.1016/J.IFACOL.2022.09.105.

[119] G. Quadrio and E. Villa, “CO2 mixtures: cycle selection and plant optimization for CSP applications,” M.Sc Thesis - Politecnico di Milano, 2021.

[120] I. E. Idelchik, A. S. Ginevskiy, A. V Kolesnikov, G. R. Malyavskaya, and N. K. Shveyeva, *Handbook of Hydraulic Resistance, 4th Edition* . Begell House, 2008.

[121] A. Montoya, M. R. Rodríguez-Sánchez, J. López-Puente, and D. Santana, “Numerical model of solar external receiver tubes: Influence of mechanical

boundary conditions and temperature variation in thermoelastic stresses," *Solar Energy*, vol. 174, pp. 912–922, Nov. 2018, doi: 10.1016/J.SOLENER.2018.09.068.

[122] M. Jonemann, "Advanced Thermal Storage System with Novel Molten Salt," 2013. Accessed: Oct. 01, 2020. [Online]. Available: http://www.osti.gov/bridge

[123] NREL, "System Advisory Model," 2020.

[124] B. Kelly, M. Izygon, and L. Vant-Hull, "Advanced Thermal Energy Storage for Central Receivers with supercritical coolants," *SolarPaces Conference*, 2010, doi: 10.2172/981926.

[125] C. S. Turchi and G. A. Heath, "Molten Salt Power Tower Cost Model for the System Advisor Model (SAM)," Feb. 2013.

[126] S. Guccione, "Design and Optimization of a Sodium Molten Salt Heat Exchanger for Concentrating Solar Power Applications," Politecnico di Torino, KTH Royal Institute of Technology, 2020.

[127] T. Conroy, M. N. Collins, and R. Grimes, "A review of steady-state thermal and mechanical modelling on tubular solar receivers," *Renewable and Sustainable Energy Reviews*, vol. 119, p. 109591, Mar. 2020, doi: 10.1016/J.RSER.2019.109591.

[128] Solar Reserve, "Crescent Dunes Solar Energy Plant," 2014. http://website.eventpower.com/paperclip/exhibitor_docs/15AE/SolarReserve_311.pdf (accessed Jan. 24, 2023).

[129] T. Conroy, M. N. Collins, J. Fisher, and R. Grimes, "Levelized cost of electricity evaluation of liquid sodium receiver designs through a thermal performance, mechanical reliability, and pressure drop analysis," *Solar Energy*, vol. 166, pp. 472–485, May 2018, doi: 10.1016/J.SOLENER.2018.03.003.

[130] C. A. Asselineau, J. Pye, and J. Coventry, "Exploring efficiency limits for molten-salt and sodium external cylindrical receivers for third-generation concentrating solar power," *Solar Energy*, vol. 240, pp. 354–375, Jul. 2022, doi: 10.1016/J.SOLENER.2022.05.001.

[131] Steel Tubes, "Dimensions and weights of seamless tubes according to standard ASME B36.10M - Steel tube." https://www.steeltube.sk/sizes/dimensions-and-weights-of-seamless-tubes-according-to-standard-asme-b36-10m/ (accessed Jan. 24, 2023).

[132] "Global Wind Atlas." https://globalwindatlas.info/ (accessed Jul. 20, 2022).

[133] D. Alfani, M. Astolfi, M. Binotti, P. Silva, and E. Macchi, "Off-design Performance of CSP Plant Based on Supercritical CO2 Cycles," *AIP Conf Proc*, vol. 2303, Dec. 2020, doi: 10.1063/5.0029801.

[134] E. Morosini, M. Binotti, G. Di Marcoberardino, C. Invernizzi, P. Iora, and G. Manzolini, "Adoption of CO2 Mixtures as Working Fluid for CSP Cycles with Linear Collectors and Molten Salts as HTF," in *SolarPaces Conference 2021*, American Institute of Physics Inc., 2023.

[135] W. T. Hamilton, A. M. Newman, M. J. Wagner, and R. J. Braun, "Off-design performance of molten salt-driven Rankine cycles and its impact on

the optimal dispatch of concentrating solar power systems," *Energy Convers Manag*, vol. 220, p. 113025, Sep. 2020, doi: 10.1016/J.ENCONMAN.2020.113025.

[136] M. J. Wagner, A. M. Newman, W. T. Hamilton, and R. J. Braun, "Optimized dispatch in a first-principles concentrating solar power production model," *Appl Energy*, vol. 203, pp. 959–971, Oct. 2017, doi: 10.1016/J.APENERGY.2017.06.072.

[137] M. J. Wagner, W. T. Hamilton, A. Newman, J. Dent, C. Diep, and R. Braun, "Optimizing dispatch for a concentrated solar power tower," *Solar Energy*, vol. 174, pp. 1198–1211, Nov. 2018, doi: 10.1016/J.SOLENER.2018.06.093.

[138] L. Pilotti, M. Colombari, A. F. Castelli, M. Binotti, A. Giaconia, and E. Martelli, "Simultaneous design and operational optimization of hybrid CSP-PV plants," *Appl Energy*, vol. 331, Feb. 2023, doi: 10.1016/J.APENERGY.2022.120369.

[139] M. T. White, G. Bianchi, L. Chai, S. A. Tassou, and A. I. Sayma, "Review of supercritical CO2 technologies and systems for power generation," *Appl Therm Eng*, vol. 185, pp. 0–3, 2021, doi: 10.1016/j.applthermaleng.2020.116447.

[140] M. Marchionni, M. Usman, L. Chai, and S. A. Tassou, "Inventory control assessment for small scale sCO2 heat to power conversion systems," *Energy*, vol. 267, Mar. 2023, doi: 10.1016/J.ENERGY.2022.126537.

[141] A. Moisseytsev and J. J. Sienicki, "Recent developments in s-CO2 cycle dynamic modeling and analysis at ANL," in *The 4th International Symposium–Supercritical CO2 Power Cycles*, Pittsburgh, Pennsylvania, 2014.

[142] J. Yang, Z. Yang, and Y. Duan, "Off-design performance of a supercritical CO2 Brayton cycle integrated with a solar power tower system," *Energy*, vol. 201, Jun. 2020, doi: 10.1016/J.ENERGY.2020.117676.

[143] D. Alfani, M. Astolfi, M. Binotti, P. Silva, and E. Macchi, "Off-design performance of CSP plant based on supercritical CO2 cycles," *AIP Conf Proc*, vol. 2303, no. 1, p. 130001, Dec. 2020, doi: 10.1063/5.0029801.

[144] T. Neises, "Steady-state off-design modeling of the supercritical carbon dioxide recompression cycle for concentrating solar power applications with two-tank sensible-heat storage," *Solar Energy*, vol. 212, pp. 19–33, Dec. 2020, doi: 10.1016/J.SOLENER.2020.10.041.

[145] E. Morosini *et al.*, "Off-design of a transcritical cycle working with the CO2+C6F6 mixture in a CSP environment: analysis at part load and variable ambient temperature," *Applied Thermal Engineering (Submitted)*, 2023.

[146] E. Morosini, M. Doninelli, D. Alfani, M. Astolfi, G. Di Marcoberardino, and G. Manzolini, "Analysis of the potential of CO2 based mixtures to improve the efficiency of cogenerative waste heat recovery power plants," in *The 5th European sCO2 Conference for Energy Systems*, Prague, 2023. doi: 10.17185/duepublico/77287.

[147] M. Baiguini *et al.*, “Potential of trigenerative waste heat recovery CO2-mixture transcritical power plants for increasing the sustainability of district heating and cooling networks,” in *Proceedings of the 7th International Seminar of ORC Power Systems*, Sevilla, 2023.

[148] R. Colciaghi, R. Simonetti, L. Molinaroli, M. Binotti, and G. Manzolini, “Potentialities of thermal responsive polymer in forward osmosis (FO) process for water desalination,” *Desalination*, vol. 519, Jan. 2022, doi: 10.1016/J.DESAL.2021.115311.

[149] G. Di Marcoberardino *et al.*, “Experimental and analytical procedure for the characterization of innovative working fluids for power plants applications,” *Appl Therm Eng*, vol. 178, 2020, doi: 10.1016/j.applthermaleng.2020.115513.

[150] Y. FU, A. VALTZ, S. AHAMADA, H. HU, and C. COQUELET, “Density data for carbon dioxide (CO2) +trans-1,3,3,3-tetrafluoroprop-1-ene (R-1234ze(E)) mixture at temperatures from 283.32 to 353.02K and pressures up to 10MPa,” *International Journal of Refrigeration*, vol. 120, pp. 430–444, Dec. 2020, doi: 10.1016/J.IJREFRIG.2020.06.006.

[151] C. Coquelet, A. Valtz, P. Théveneau, C. Coquelet, A. Valtz, and P. Théveneau, “Experimental Determination of Thermophysical Properties of Working Fluids for ORC Applications,” in *Organic Rankine Cycles for Waste Heat Recovery - Analysis and Applications*, IntechOpen, 2019. doi: 10.5772/INTECHOPEN.87113.

[152] E. Neyrolles, A. Valtz, C. Coquelet, and A. Chapoy, “On the phase behaviour of the CO2 + N2O4 system at low temperatures,” *Chem Eng Sci*, vol. 258, p. 117726, Aug. 2022, doi: 10.1016/J.CES.2022.117726.

[153] S. Salma, F. Crespi, and M. White, “Axial turbine flow path design for concentrated solar power plants operating with CO2 blends,” *Applied Thermal Engineering (Submitted)*.

[154] S. I. Salah, M. T. White, and A. I. Sayma, “A comparison of axial turbine loss models for air, sCO2 and ORC turbines across a range of scales,” *International Journal of Thermofluids*, vol. 15, Aug. 2022, doi: 10.1016/J.IJFT.2022.100156.

[155] R. H. Aungier, *Turbine Aerodynamics: Axial-Flow and Radial-Flow Turbine Design and Analysis*. ASME Press, 2006. doi: 10.1115/1.802418.

[156] A. S. Abdeldayem, M. T. White, A. Paggini, M. Ruggiero, and A. I. Sayma, “Integrated Aerodynamic and Structural Blade Shape Optimization of Axial Turbines Operating With Supercritical Carbon Dioxide Blended With Dopants,” *J Eng Gas Turbine Power*, vol. 144, no. 10, Oct. 2022, doi: 10.1115/1.4055232/1145514.

Nomenclature

Acronyms

CAPEX: Capital Cost
CF: Capacity Factor of a Power Plant
CFD: Computational Fluid Dynamics
CSP: Concentrated Solar Power
DNI: Direct Normal Irradiation
EoS: Equation of State
HTC: Heat transfer coefficient of the heat exchanger
HTF: Heat Transfer Fluid
HP: High Pressure side
HRU: Heat Rejection Unit
HX: Heat Exchanger
LCOE: Levelized Cost of Electricity
LC: Lethal Concentration
LP: Low Pressure side
LUT: Look-up Table
MITA: Minimum Internal Temperature Approach of an HX
NFPA: National Fire Protection Association
ORC: Organic Rankine Cycle
PC-SAFT: Perturbed Chain Statistical Associating Fluid Theory EoS
PCHE: Printed Circuit Heat Exchanger
PHE: Primary Heat Exchanger
PR: Peng Robinson EoS
PV: Photovoltaics
sCO_2: Supercritical Carbon Dioxide
S&T: Shell and Tubes Heat Exchanger
SM: Solar Multiple
TES: Thermal Energy Storage
TIT: Turbine Inlet temperature
TUW: Technische Universität of Wien
UNIBS: Università degli studi di Brescia
VLE: Vapor Liquid Equilibrium of a mixture

Symbols

A: Heat Exchange Area of the Heat Exchanger [m^2]
AR: Area ratio between the external and internal surface of the tube
CR: Heat Capacity Ratio
C_P: Specific Heat Capacity [kJ/kg/K]

k_{ij}: Binary interaction coefficient of a mixture specific to an EoS
EE: Electric energy [MWh_{el}]
$\dot{m}_{HTF}$: Mass flow rate of the HTF [kg/s]
$\dot{m}_{Work\ Fluid}$: Mass flow rate of the working fluid [kg/s]
$\dot{m}_{Rid}$: Reduced mass flow rate at turbine inlet
$\dot{W}_{Pump,mech}$: Mechanical power absorbed by the pump of the cycle [MW]
$\dot{W}_{Turbine,mech}$: Mechanical power produced by the turbine of the cycle [MW]
$\dot{W}_{El\ Mech,Losses}$: Electro-mechanical losses of the turbine and pump [MW]
$\dot{W}_{Condenser,AUX}$: Electric power consumed by the condenser air fans [MW_{el}]
η: Efficiency
η_{Gross} : Cycle mechanical efficiency
$\eta_{Net\ Electric}$: Power block net electric efficiency
$\eta_{el,mech}$: Electromechanical efficiency of the turbine and the pump
G: Mass velocity [$kg/s/m^2$]
NTU: Number of transfer units of the HX
Nu: Nusselt number
Pr: Prandtl number
P: Pressure [bar]
ΔP : Pressure drop [bar]
T: Temperature [°C]
ΔT : Temperature difference [°C]
ΔT_{lm} : Mean logarithmic temperature difference of the HX [°C]
$\Delta T_{Cycle-Ambient}$: Cold-end temperature difference of the condenser [°C]
$\dot{Q}$: Thermal power [MW_{th}]
$\dot{Q}_{PHE}$: Thermal power of the primary heat exchanger [MW_{th}]
$\dot{Q}_{PCHE}$: Thermal power of the recuperator [MW_{th}]
$\dot{Q}_{Recuperator}$: Thermal power of the recuperator [MW_{th}]
$\dot{Q}_{COND}$: Thermal power of the condenser [MW_{th}]
Re: Reynolds number
ρ: Density of a fluid [kg/m^3]
$w_{specific}$: Specific Work of the power cycle [kJ/kg]
$\dot{V}_{air}$: Air volumetric flow rate delivered by the air-cooled condenser [m^3/s]
$\frac{V}{L}$: Ratio between the volume of vapor and the liquid phase in the hotwell
U: Overall Heat Transfer Coefficient of a Heat Exchanger [$W/m^2/K$]
UA: Product between U and A of a Heat Exchanger [W/K]
Z: Compressibility factor of a fluid

Thesis contributions to literature

The following literature works have been submitted, or will be submitted in the following months, to journals or conference proceedings to partially fulfil the requirements for the PhD degree.

Journal articles

• Experimental characterization of CO_2 + C_6F_6 mixture: thermal stability and vapor liquid equilibrium test for its application in transcritical power cycles

Authors: Gioele Di Marcoberardino, Ettore Morosini et al
Journal: Applied Thermal Engineering – DOI: 10.1016/j.applthermaleng.2022.118520

• Adoption of the CO_2+SO_2 mixture as working fluid for transcritical cycles: A thermodynamic assessment with optimized equation of state

Authors: Ettore Morosini, Abubakr Ayub et al
Journal: Energy conversion and management - DOI: 10.1016/j.enconman.2022.115263

• Preliminary investigation of the influence of equations of state on the performance of CO_2 + C_6F_6 as innovative working fluid in transcritical cycles

Authors: Gioele Di Marcoberardino, Ettore Morosini, Giampaolo Manzolini
Journal: Energy - DOI: 10.1016/j.energy.2021.121815

• Solar tower CSP plants with transcritical cycles based on CO_2 mixtures: a sensitivity on storage and power block layout

Authors: Ettore Morosini, Enrico Villa, Guglielmo Quadrio, Marco Binotti, Giampaolo Manzolini
Journal: Solar Energy – DOI: 10.1016/j.solener.2023.05.054

• Off-design of a transcritical cycle working with the CO_2+C_6F_6 mixture in a CSP environment: analysis at part load and variable ambient temperature

Authors: Ettore Morosini, Dario Alfani et al
Journal: Applied Thermal Engineering – Under review

• Experimental characterization of the CO_2+$SiCl_4$ mixture: Densities, thermal stability and bubble conditions

Authors: Michele Doninelli, Ettore Morosini et al
Journal: Energy – To be submitted

• Experimental characterization of the CO_2+C_2Cl_4 mixture: Densities, thermal stability and excess volumes

Authors: Ettore Morosini, Michele Doninelli et al
Journal: Energy – To be submitted

Conference Proceedings

- Adoption of CO_2 Blended with C_6F_6 as Working Fluid in CSP Plants

Authors: Giampaolo Manzolini, Marco Binotti, Ettore Morosini et al
International conference SOLARPACES 2020 – DOI: 10.1063/5.0086520

- Design of an air-cooled condenser for CO_2-based mixtures: Model Development, Validation and heat exchange gain with internal microfins

Authors: Viktoria Illyés, Ettore Morosini, Michele Doninelli et al
International conference ASME TurboExpo 2022 – DOI: 10.1115/GT2022-82438

- Adoption of CO_2 Mixtures as Working Fluid for CSP Cycles with Linear Collectors and Molten Salts as HTF

Authors: Ettore Morosini, Marco Binotti et al
International conference SOLARPACES 2021 – In press

The following literature works have been submitted to journals or conference proceedings. They are not considered part of this thesis but include studies on tCO_2-mixtures for power cycles and analysis of CSP plants that are inherent to the content the PhD thesis.

- Thermal desalination from rejected heat of power cycles working with CO_2-based working fluids in CSP application: a focus on the MED technology

Authors: Michele Doninelli, Ettore Morosini et al
Journal: Sustainable Energy Technologies and Assessments – Accepted

- Techno-economic assessment of small-scale solar tower plants with modular billboard receivers and innovative power cycles

Authors: Ettore Morosini, Giancarlo Gentile, Marco Binotti, Giampaolo Manzolini
Conference: ATI 2022 – DOI: 10.1088/1742-6596/2385/1/012109

- Analysis of the potential of CO_2 based mixtures to improve the efficiency of cogenerative waste heat recovery power plants

Authors: Ettore Morosini, Michele Doninelli, Dario Alfani et al
Conference: European sCO_2 Conference 2023 – In press

- Potential of trigenerative waste heat recovery CO_2-mixture transcritical power plants for increasing the sustainability of district heating and cooling networks

Authors: Mattia Baiguini, Michele Doninelli, Ettore Morosini et al
Conference: ORC 2023 International seminar – In press

Appendix

Appendix A: Analysis of the innovative working fluids

Appendix A.1: Thermal stability of the CO_2-mixtures at UNIBS

The thermal stability of the mixtures CO_2+C_6F_6, CO_2+SO_2, CO_2+C_2Cl_4, CO_2+$SiCl_4$ and CO_2+$TiCl_4$ have been investigated from an experimental point of view within the SCARABEUS and the DESOLINATION H2020 EU project by the partners at University of Brescia (UNIBS). The methodology adopted in the analysis is proposed in literature as carried out in UNIBS [57], [149]: the results are already available in literature for some mixtures and still to be published for other mixtures.

Figure 66 briefly depicts the steps carried out for the thermal stability assessment: at first, the working fluid is charged in a vessel (made by either SS316 or INC625), its temperature-pressure behavior of the fresh working fluid is measured in a wide temperature range. Then, the vessel and the fluid are heated for 100 hours in an electric oven, continuously monitoring the temperature and pressure of the charged mixture, and subsequently cooled down. By measuring the temperature and pressure of the cooled mixture and comparing the new results with the ones of the virgin mixture, the stability of the working fluid can be assessed, since a higher pressure can be representative of a dissociation of heavy compounds into lighter ones. If, on the other hand, the volumetric behavior of the mixture mimics the one of the fresh mixture, the test indicates a good thermal stability of the fluid after a long-term static thermal stress: the vessel can be heated in the oven at a higher temperature, repeating the procedure, up to the onset of thermal degradation of the working fluid.

For a correct assessment of the mixture stability, a significant fraction of dopant must be charged in the vessel: if only impurities are present in CO_2, the decomposition of the dopant will not be visible monitoring the pressure of the mixture. Moreover, if the pressure after the thermal stress decreases drastically, either a leakage or a reaction between the fluid and the metals are foreseeable.

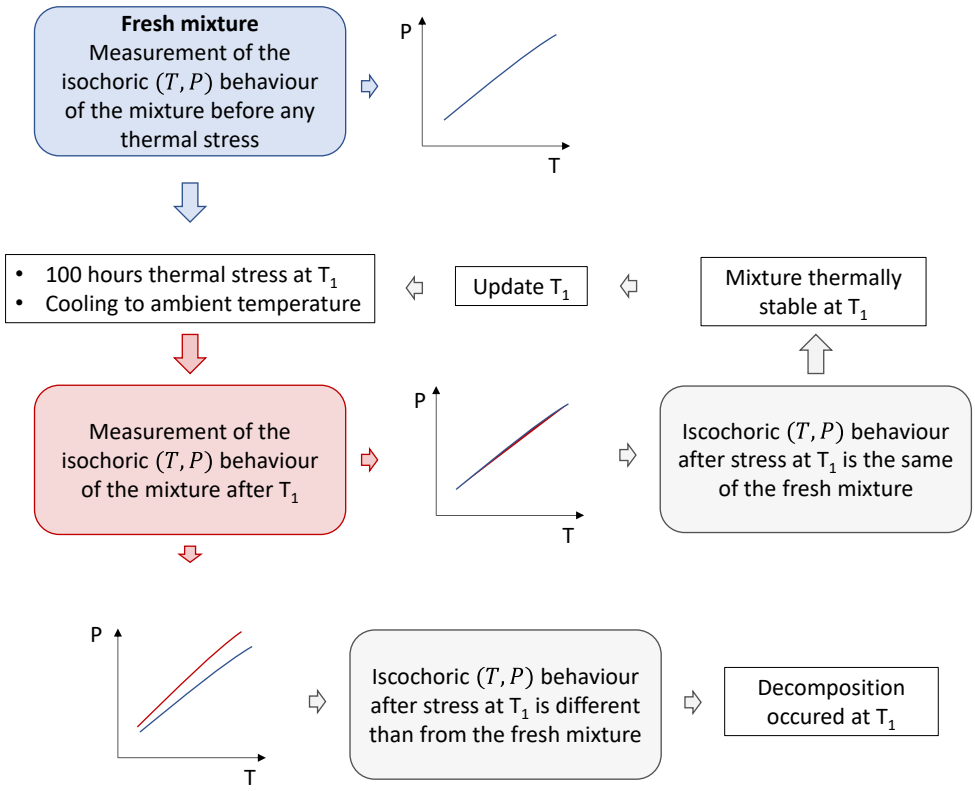

Figure 66. Flowchart of the methodology adopted in the SCARABEUS project in UNIBS to determine the thermal stability of CO_2-based mixtures

Appendix A.2: Potentialities of transcritical cycles with CO_2-mixtures and additional unconventional dopants

The table proposed in this appendix is taken from a literature work developed within the SCARABEUS project by master students of PoliMi under the direct supervision of the author of this thesis [119]. The dopants listed in Table 52 are only a subset of more than 300 dopants considered.

For each CO_2-dopant the critical temperature of the pure fluid is proposed, along with its melting and boiling point at ambient pressure. Then, the health, flammabilty and reactiveness indexes are listed according to the NFPA 704 classification, and some qualitative information about the dopant cost, thermal stability and the efficiency of the respective CO_2-mixture in a transcritical power cycle are also reported.

Table 52. List of hypothetical CO_2-dopants for transcritical cycles [119]

CAS	Dopant	Melting / Boiling [°C]		T_c[°C]	Health	Flamm.	React.	Efficiency w/r/t sCO_2	Cost	Stability [°C]
355-25-9	C_4F_{10}	-84	-2	113	1	0	0	+	Very High	500
431-89-0	C_3HF_7	-126	-16	102	1	0	1	+ +	Very High	>400
79-34-5	$C_2H_2Cl_4$	-43	147	371	3	1	1	+ +	Not High	No Info
95-50-1	$C_6H_4Cl_2$-o	-15	179	401	2	2	0	+ + +	Low	400
7646-78-8	$SnCl_4$	-33	114	319	3	0	3	+ + +	Not High	700
75-62-7	CBrCl3	-6	105	326	1	0	0	+ +	High	<350
100-54-9	$C_6H_4N_2$	50	201	440	2	1	1	+ + +	High	No Info
116-15-4	C_3F_6	-153	-28	122	2	0	0	+	Very High	550
120-82-1	$C_6H_3Cl_3$	16	214	452	2	1	0	+ + +	Low	No Info
100-47-0	C_7H_5N	-13	191	428	2	2	0	+ + +	Low	>400
634-66-2	$C_6H_2Cl_4$	44	245	501	1	1	0	+	High	<400
79-00-5	$C_2H_3Cl_3$	-37	110	329	2	1	0	+ +	High	350
87-68-3	C_4Cl_6	-19	220	499	3	1	0	+ + +	High	350
42532-60-5	C_4F_7N	-118	3	113	3	0	0	+ +	Very High	No Info
10025-67-9	S_2Cl_2	-80	136	386	3	1	1	+ + +	Not High	No Info

Appendix A.3: CO_2-mixtures experimental data taken within this work

Within this PhD thesis, two experimental campaigns were carried out by the author on three promising CO_2-based mixtures:

- A campaign on the CO_2+C_6F_6 mixture, from November 2019 to October 2020, at LEAP laboratories in Piacenza (Italy). The experimental campaign was supervised and engineered by Daniele Di Bona, senior researcher at LEAP scarl. The campaign focused on the measurement of the VLE behaviour of the mixture in the temperature range between 50 °C and 90 °C. For sake of brevity, in this thesis the campaign is not described, and the author refers to the respective literature work [57] for a detailed description: only the experimental data are listed in the sub-chapter below.
- A campaign on the CO_2+$SiCl_4$ and on the CO_2+C_2Cl_4 mixture, carried out from September 2022 to December 2022, at the Centre Thermodynamique des Procédés (CTP) of Mines ParisTech in Fontainebleau (Île-de-France). The experimental campaign was supervised by Paolo Stringari (head of CTP) and Mauro Riva (researcher at CTP), with the support from Alain Valtz (researcher at CTP). In this period, the CO_2+$SiCl_4$ mixture was analysed in a variable volume P-V-T cell and in a vibrating tube densimeter. The CO_2+C_2Cl_4 mixture, instead, only in the densimeter.

The next sub-chapter provides a brief description of the experimental campaign carried out on the CO_2+$SiCl_4$ and on the CO_2+C_2Cl_4 mixture at CTP in Fontainebleau, as the obtained experimental data are not yet published in the open literature the moment this thesis is submitted.

Appendix A.3.1: Overview of the experimental campaign at CTP

Two apparatus were adopted in this experimental campaign: a vibrating tube densimeter (VTD) and a variable volume P-V-T cell. In both cases, the mixture is prepared in a separated dedicated variable volume, as both test rigs share the same procedure for the mixture preparation.

- Preparation of the mixture from the separated two pure components

The mixture is charged directly in the variable volume cylinder accordingly to the relative volatility of the two components, starting from the heavier component to the lighter. Considering the CO_2+C_2Cl_4 mixture, carbon dioxide is the most volatile component, and it is stored in two-phase conditions in a gas bottle (>99.99% purity) at ambient temperature (approximately 20 °C and 57 bar), while C_2Cl_4 is liquid at ambient temperature and pressure, available in a vessel

with a purity above 99%. Analogous considerations are valid for $SiCl_4$ (but with a purity above 98%).

At first, a magnetic agitator with the volume of about 0.5 cm^3 is filled in the variable volume cylinder: during the measurement period it is used to homogenize the composition of the mixture in the cylinder. Then, vacuum is created in the variable volume cylinder with a vaccum pump, up to a condition of around 5.5 Pa. Then, the empty charging cylinder is weighted. Afterwards, the dopant is injected in the cylinder manually with a syringe through a sealing cap, avoiding the contamination with air: the system is weighted again to measure the mass of the dopant entered in the volume, by difference with the previous value. Once the dopant is charged in the cylinder, the CO_2 is introduced into the cylinder not directly from the CO_2 reservoir but trough an additional variable volume cylinder that can be pressurized to reach the desired mass of carbon dioxide inside the mixture cylinder. Initially, vacuum conditions are imposed into the auxiliary variable-volume cylinder and into the connecting ducts to avoid the presence of atmospheric air, then the CO_2 is transferred from the 57 bar gas bottle into the dedicated vessel, occupying the maximum volume.

Once the CO_2 is charged in the auxiliary cylinder, the bottom of the vessel is connected to the pressurizing N_2 bottle (at pressures typically higher than 110 bars). The carbon dioxide is then pressurized inside the auxiliary vessel at an arbitrary constant pressure level at which the CO_2 is charged in the variable volume cylinder containing the dopant. Knowing the volume of CO_2 in the auxiliary vessel, its pressure and temperature, it is possible to know with a good accuracy the amount of carbon dioxide transferred into the mixture cylinder by monitoring the displacement of the piston with an encoder. Once the mixture is prepared in the main variable volume cyclinder, it is weighetd again to compute by difference the mass of CO_2 in the mixture. Knowing the mass of both CO_2 and the dopant, the molar composition of the mixture is determined, as proposed in literature. The system mass is measured with a Mettler Toledo CC3000 balance, with an accuracy of ±0.0001 g (six order of magnitude lower than the mass of the charged mixture), as an average of three subsequent measures.

The variable volume cylinder containing the prepared mixture is brought to the apparatus of interest (either the VTD or the P-V-T cell), where the piston is pressurized with the high-pressure nitrogen reservoir at a pressure higher than the expected bubble condition at ambient temperature: afterward, an electromagnetic field is created externally to the variable volume cylinder, to move the magnetic agitator submerged in the mixture, improving the mixing of the two components. After few minutes the equilibrium is supposedly reached, with the mixture in the volume at liquid condition. Vacuum is created in the whole circuit of the test rig, before injecting for pressure difference the mixture from the charge to the measurement circuit.

- Vibrating tube densimeter: description, characteristics and operation

The vibrating tube densimeter manufactured by Anton Paar (model DMA 512) is already described in literature [76]. The scheme of the apparatus is shown in Figure 67. A detail of the apparatus (the variable volume cylinder, the open thermostatic bath and the pressure transducers of the VTD) is also proposed in Figure 68.

The measurement technique consists in determining the density of the liquid mixture from the variation of the period of vibration of a U-shaped tube when it is filled with liquid with respect to the period of vibration measured when vacuum is created. The VTD is immersed in a thermostatic liquid bath for maintaining its temperature at the target value of the measurement. The operating range of the densimeter is from -10 °C to 200 °C in temperature, and over 1000 bar in pressure. The vibrating tube is made in Hastelloy, and its temperature is controlled by a heat transfer fluid flowing in a jacket with a temperature stability of 0.02 °C. Additional information about the VTD adopted can be found in a previous literature work [150]: as reported, during the operation, when the pressure of the fluid decreases and before the advent of the bubble point, starting from subcooled liquid conditions, the temperature of the thermostatic bath should be around 0.2 °C lower than the heat transfer fluid flowing in the jacket of the densimeter, as the first bubble of CO_2-mixture must occur precisely into the densimeter in the vibrating tube.

The densimeter does not allow for a direct measurement of density. What is measured is the period of vibration of the U-shaped tube when it contains the mixture of interest. To convert the period of vibration measured into density values, the period of vibration of a fluid with a known density must be measured, defining the correlation between the period of vibration and the density. As this relation is temperature-dependent, the period of vibration of the reference fluid must be measured at each temperature of interest.

At first, vacuum is done in the whole circuit up to valves V2 and V4, then the nitrogen reservoir is put in contact with the variable volume cylinder (V1 and V3 are opened) and the mixture is instantly pushed into the TDV through the movement of the piston of the variable volume cylinder, due to pressure difference between the nitrogen and the mixture. Finally, also valve V6 is opened and the mixture flows also in the variable volume cell. Once thermal and mechanical equilibria are achieved (pressure and temperature are stable within the uncertainties of their measurements), the variable volume cylinder is closed (V4 is closed): in fact, during measurements valves V5 and V6 are closed too.

The variable volume cell after the outlet of the VTD is added in order to manually modify the volume (and the pressure) of the measured fluid in the vibrating tube, without influencing the fresh charge in the variable volume cylinder: the modification has been proposed specifically for mixtures, since it is crucial to definitively fix the composition of the measured fluid, for various pressure levels. Accordingly, the position of the piston of the variable volume cell

is manually modified (with valve V6 open) to match the pressure into the VTD to the desired value: once equilibrium is reached the valve V6 is closed and another acquisition can be carried out, at the same temperature but different pressure than the previous ones. The described procedure is repeated for each temperature at which measurements are carried out.

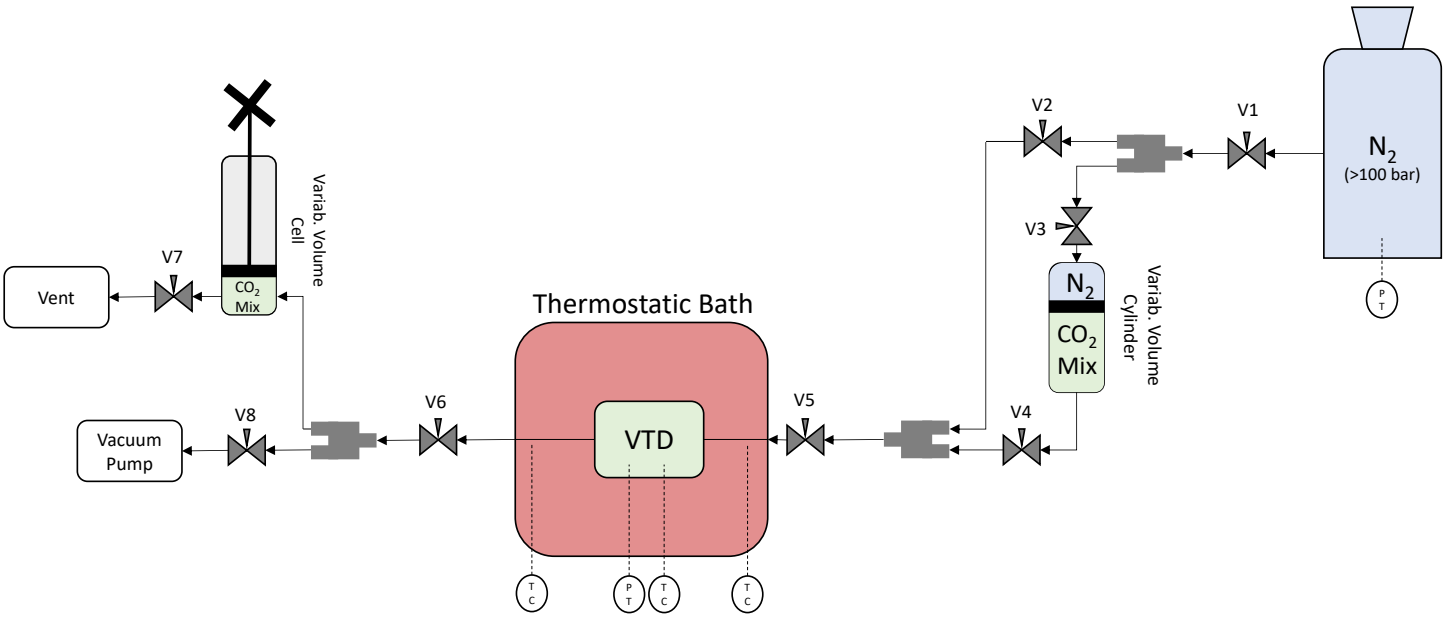

Figure 67. Simplified layout of the VTD adopted at CTP (Mines ParisTech)

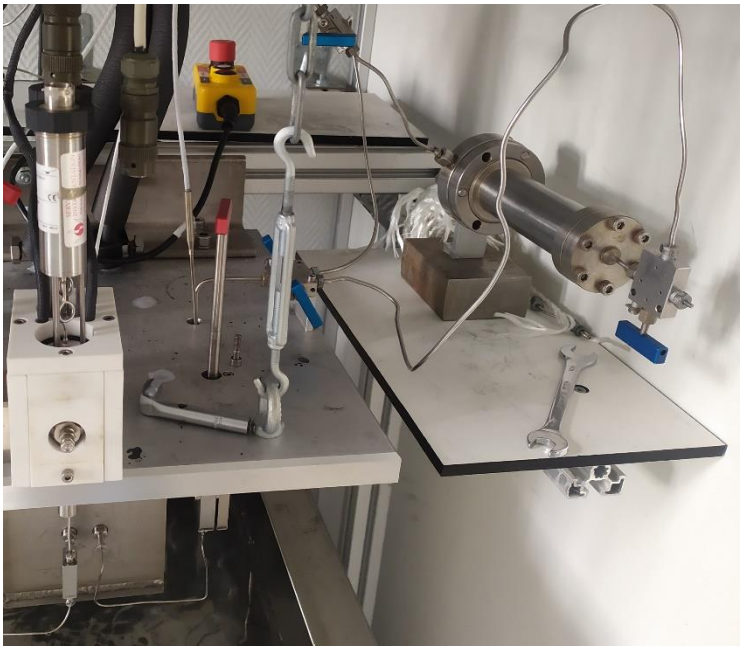

Figure 68. Details of the VTD test rig including the variable volume cylinder, pressure transducers and the thermostatic bath

Densities are measured calibrating the vibrating tube period (τ) with the behavior of pure carbon dioxide (adopted as refence fluid) at 40 °C, 60 °C and 80 °C, with a linear correlation as reported in Equation (44):

$$\rho|_T = f\,(\tau)_\mathrm{T} = A \cdot \tau + \mathrm{B} \tag{44}$$

To build the correlations of Equation (44) at each temperature, the results of the equation of state by Span and Wagner have been assumed as reference values of the densities to be associated with the measured vibrating periods, in order to find the numerical values of A and B for each temperature investigated with a linear interpolation.

For the uncertainty calculation, associated to pressure, temperature and the density, the approach reported in Equation (45) has been followed: as each single thermodynamic condition of temperature and pressure has been investigated only once, the contribution to the uncertainty of the repeatability is not present.

$$u_{Expanded}(X) = 2 \cdot \sqrt{(u_{Calibration}(X))^2 + (u_{Acquisition}(X))^2} \tag{45}$$

In the uncertainty formulation, each of the two contributions have been estimated as:

$$u_{Calibration}(X) = \max\big(Measured\,(X) - Reference\,(X)\big) \tag{46}$$

$$u_{Acquisition}(X) = \sigma(X) \tag{47}$$

Where the deviation standard of the variable, $\sigma(X)$, is directly computed with the data acquisition unit, in a wide range of at least 60 acquisitions, with a frequency of one acquisition per second.

The contribution of the calibration in the uncertainty calculations, instead, is evaluated accounting for the calibration curve of the instrument, compared with a reference value: it is 0.03 °C for the temperature and 0.02 bar for the pressure at any temperature considered (40 °C, 60 °C and 80 °C), while for the density it is 2.95 kg/m^3 at 40 °C, 1.19 kg/m^3 at 60 °C and 1.27 kg/m^3 at 80 °C. These values of uncertainties are computed with respect to reference thermocouples and pressure transducers, while the value of density of the Span and Wagner EoS are assumed as reference for the calibration of the density, as mentioned. The pressure transducer (PT) used for the measurement is a PAA-35HXTC (operating range up to 700 bar), and the temperature sensor (TC) are four-wire 100- Ω platinum resistance probes (Pt100). The reference pressure transducer used during calibration instead is a GE Sensing PACE 5000. During the measurements, the pressure and temperature were recorded thanks to the Agilent HP34970A data

acquisition unit, while the vibration period is recorded with the HP53131A data acquisition unit, as specified in literature [150].

- Variable volume P-V-T cell: description, characteristics and operation

The second test rig adopted in the CTP at Mines ParisTech is a variable volume cell, chosen as a method to measure bubble points of a pressurized mixture, alternative to a conventional VLE cell with a gas chromatographer.

The apparatus is schematized in Figure 69 and it is already described in literature by Coquelet [151]. In the figure, the nomenclature for the components correspond to the following: DAU stands for Data Acquisition Unit, DDD for Digital Displacement Display, DT for Displacement Transducer, GC for Gas Cylinder, LB for Liquid Bath; LVi for Loading Valve; P for Piston; PD for Piston Monitoring; PN for Pressurized Nitrogen; PP for Platinum Probe; PT for Pressure Transducer; PV (VP) for Vacuum Pump; R for Gas Reservoir; SD for Stirring Device; SB for Stirring Bar; ST for Sapphire Tube; TR for Thermal Regulator; Vi for Valve; VVCM for Variable Volume Cell.

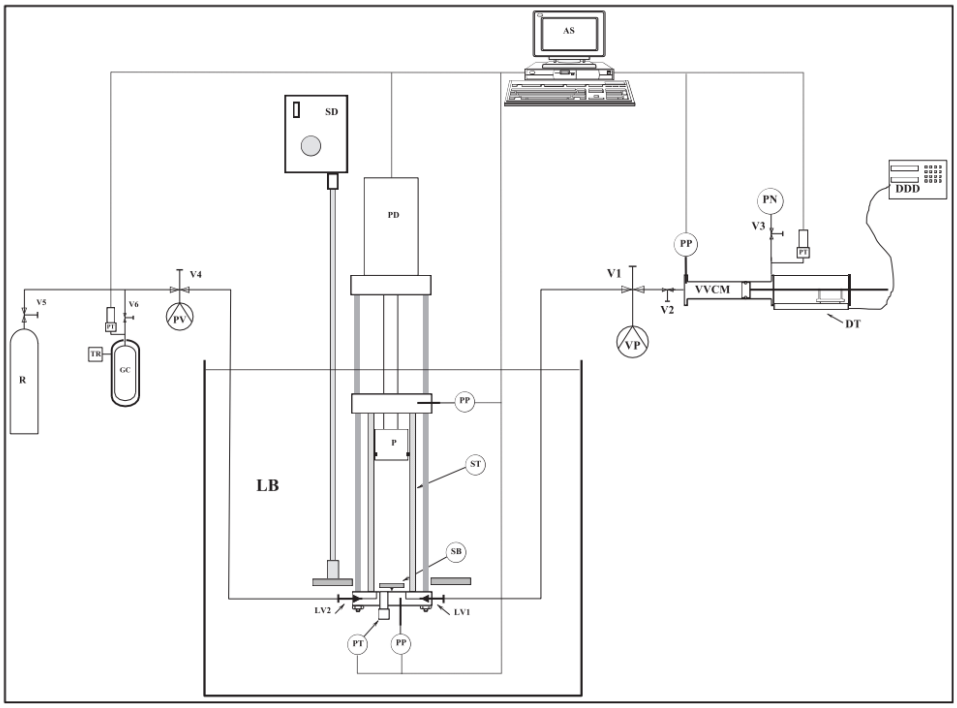

Figure 69. Diagram of the variable volume P-V-T apparatus [151]

A detail of the variable volume cell can be seen in Figure 70: the piston and the sapphire cell are visible in the center, the two agitators (one inside the cell and the second one, the actuator, out of the cell) are at the bottom of the picture.

Figure 70. Picture of the variable volume cell at CTP (Mines ParisTech) loaded with the CO_2+$SiCl_4$ mixture in liquid phase

Referring to an additional literature work by Neyrolles [152] dealing with this test rig at CTP, a brief description of the system is provided: the core of the apparatus is the variable volume equilibrium cell that consists of a sapphire tube held between two titanium flanges with suitable O-rings. The volume of the cell can be varied by controlling the position of a piston at the top of the cell, set in motion by a motorized lead screw actuator. The pressure and the temperature, as well as the piston position, are monitored in continuous. A 100 Ω platinum thermoresistance is adopted to measure the temperature in the lower part of the cell: it has been calibrated compared with a reference 25Ω platinum probe, with a resulting accuracy of ±0.03 °C. The pressure is measured with a cryogenic miniature ruggedized Kulite pressure transducer placed at the bottom of the cell. The transducer is calibrated with a numerical standard and the resulting average accuracy was estimated to be ±0.003 bar.

The signals from the temperature and pressure sensors are recorded via a software developed for the specific apparatus, called PVT Cell Controller. Within the software, the acquisitions are recorded with an acceptable standard deviation for the temperature and the pressure. The measurements are carried out in isothermal conditions, since the cell is placed in a thermostatic water-based Tamson bath and the temperature set-point is guaranteed by a PID controller.

The bath is equipped with a glass window that allows to see the sapphire equilibrium cell in order to visually confirm the presence of the meniscus in vapour-liquid conditions and to control the piston displacement. The equilibrium conditions of the fluid inside the cell are favoured by the presence of a corrosion-resistant magnetic stirrer placed at the cell bottom, which is coupled with an external agitator placed inside the bath. By regulating the rotation speed of the external agitator, it is possible to reach the required agitation level inside the cell. Two valves are present at the cell bottom for the fluid charging and venting.

While operating this test rig with the mixture CO_2+$SiCl_4$, the vented mixture was rejected under hood after passing through a solution of water and NaOH, neutralizing the formation of hydrochloric acid.

Figure 70 shows the charged mixture at high-pressure liquid phase: since the equilibrium cell is initially completely evacuated, before charging the mixture at high pressure (typically around 120 bars) an initial flash is unavoidable during the charging process from the cylinder to the variable volume P-V-T cell. Nevertheless, it is considered negligible and the composition of the mixture in the equilibrium cell is reasonably assumed to be the same of the charge in the cylinder.

The identification of the bubble point of the mixture at a given temperature and composition is obtained analytically by interpolating two linear equations: the first is obtained with a regression from all the experimental data measured in the liquid phase and the second from the experimental data measured in the VLE phase, since the two sets of data presents different slopes. Figure 71 describes a set of two different measures of a single bubble point of the mixture, the first in red and the second in blue: in the liquid region, at high pressure, the derivative of the pressure with respect to the volume is high, as the liquid tends to behave as an incompressible fluid. On the other hand, in the VLE region, below a certain pressure, the compressibility of the mixture increases drastically and no variation in pressure occurs for large range of volumes: in fact, the gaseous phase can compensate for all the volume left by the piston movement, without influencing the pressure.

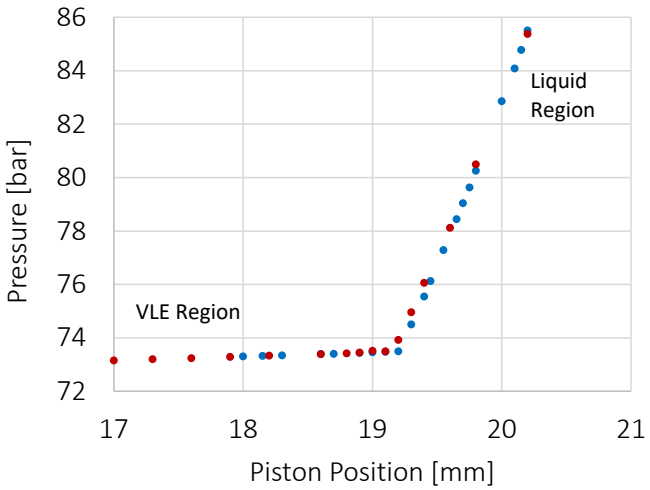

Figure 71. Experimental characterization of a bubble point of a mixture after two (blue and red) sets of measurement

The experimental data acquired in this way, by varying the piston position, have been collected at least three times for each bubble point measured. The contribution of the repeatability of the bubble pressure and temperature measured is accounted for in the uncertainty calculations.

Appendix A.3.2: Experimental data from the campaign at CTP

In the following three tables are listed the experimental data of the campaign carried out by the author of this work on the CO_2+$SiCl_4$ and CO_2+C_2Cl_4 mixtures.

Table 53. Experimental bubble points of the CO_2+$SiCl_4$ mixture taken with the variable volume P-V-T cell

CO_2 Molar Fraction [%]	Temperature [°C]	$U(T)$ [°C]	Pressure [bar]	$U(P)$ [bar]
80.28	35.01	0.08	57.11	0.10
80.28	50.11	0.07	72.46	0.03
80.28	60.01	0.17	82.92	0.19
80.28	70.09	0.11	93.44	0.08
84.95	35.02	0.09	60.41	0.20
84.95	49.98	0.08	76.73	0.33
84.95	59.93	0.09	87.82	0.23
84.95	69.99	0.14	98.45	0.14
87.69	34.78	0.08	63.38	0.16
87.69	49.92	0.09	80.53	0.19
87.69	59.94	0.15	92.02	0.51
87.69	69.97	0.14	101.59	0.36

Table 54. Experimental densities of the CO_2+C_2Cl_4 mixture taken with the vibrating tube densimeter (VTD)

CO_2 Molar Fraction [%]	Temperature [°C]	Pressure [bar]	Density [kg/m^3]	$U(T)$ [°C]	$U(P)$ [bar]	$U(\rho)$ [kg/m^3]
93.25	40.27	189.19	957.6	0.06	0.04	5.9
		167.09	942.1	0.06	0.05	5.9
		143.02	921.9	0.06	0.05	5.9
		131.75	910.6	0.06	0.04	5.9
		115.23	891.7	0.06	0.04	5.9
		124.48	901.8	0.06	0.05	5.9
		132.52	910.4	0.06	0.05	5.9
		141.71	919.5	0.06	0.04	5.9
		156.30	932.4	0.06	0.04	5.9
		179.62	950.4	0.06	0.05	5.9
		169.56	943.6	0.06	0.04	5.9
		160.20	936.5	0.06	0.08	5.9
		152.26	929.8	0.06	0.06	5.9
		125.91	904.3	0.06	0.04	5.9
93.25	59.98	185.20	864.8	0.06	0.08	2.4
		169.63	845.3	0.06	0.06	2.4
		160.23	831.6	0.06	0.05	2.4
		150.00	814.5	0.06	0.05	2.4
		138.32	791.1	0.06	0.04	2.4
		124.14	753.4	0.06	0.05	2.4
		140.62	796.9	0.06	0.04	2.4
		154.49	822.7	0.06	0.06	2.4
		171.99	848.6	0.06	0.05	2.4
93.25	79.84	191.86	743.4	0.06	0.06	2.5
		170.63	700.5	0.06	0.05	2.5

		159.19	670.1	0.06	0.05	2.5
	79.99	154.63	657.1	0.06	0.05	2.5
		178.24	718.5	0.06	0.04	2.5
		187.58	736.7	0.06	0.04	2.5
		183.82	730.2	0.06	0.05	2.5
83.82	40.08	171.61	1065.6	0.06	0.05	5.9
		158.41	1058.4	0.06	0.05	5.9
		134.50	1044.1	0.06	0.05	5.9
		116.23	1031.3	0.06	0.05	5.9
		99.21	1017.6	0.06	0.04	5.9
		90.08	1009.3	0.06	0.06	5.9
90.80	40.22	162.38	977.0	0.07	0.05	5.9
		149.77	967.8	0.07	0.04	5.9
		139.22	959.3	0.07	0.04	5.9
		118.93	941.0	0.07	0.04	5.9
		101.31	921.8	0.07	0.05	5.9
		130.06	951.4	0.07	0.05	5.9
		156.08	972.4	0.07	0.04	5.9
85.69	40.17	160.87	1056.5	0.06	0.05	5.9
		140.88	1045.1	0.06	0.05	5.9
		120.58	1031.9	0.06	0.05	5.9
		99.97	1016.4	0.06	0.04	5.9
		110.20	1024.0	0.06	0.07	5.9
		129.81	1037.6	0.06	0.05	5.9
		183.83	1068.1	0.06	0.11	5.9
85.69	59.96	197.11	1013.8	0.06	0.05	2.4
		169.79	993.9	0.06	0.09	2.4
		149.54	976.1	0.06	0.05	2.4
		125.13	949.4	0.06	0.05	2.4
		138.22	964.7	0.06	0.05	2.4
		159.80	985.3	0.06	0.04	2.4
		184.28	1004.5	0.06	0.12	2.4
85.69	79.95	220.43	929.7	0.09	0.05	2.5
		200.09	911.5	0.09	0.07	2.5
		180.18	890.4	0.09	0.12	2.5
		170.03	877.6	0.09	0.05	2.5
		149.72	846.4	0.09	0.05	2.5
		160.92	864.7	0.09	0.04	2.5
		188.22	899.0	0.09	0.04	2.5
		133.41	808.0	0.09	0.04	2.5
		131.43	800.8	0.09	0.04	2.5
70.31	40.18	160.30	1227.3	0.06	0.13	5.9
		140.07	1220.5	0.06	0.04	5.9
		119.36	1213.1	0.06	0.26	5.9
		99.15	1205.3	0.06	0.08	5.9
		76.84	1196.1	0.06	0.11	5.9
		91.41	1202.1	0.06	0.23	5.9
		110.05	1209.5	0.06	0.22	5.9
		128.87	1216.4	0.06	0.12	5.9
70.31	59.93	193.95	1197.5	0.07	0.05	2.4
		179.32	1191.7	0.07	0.05	2.4
		150.66	1179.5	0.07	0.07	2.4
		119.12	1164.1	0.07	0.04	2.4
		95.24	1150.7	0.07	0.04	2.4
		103.96	1155.6	0.07	0.10	2.4
		137.78	1172.9	0.07	0.08	2.4
		160.41	1183.2	0.07	0.12	2.4
70.47	40.28	147.49	1224.2	0.06	0.23	5.9
		130.59	1218.2	0.06	0.16	5.9

		105.17	1208.8	0.06	0.27	5.9
		73.95	1195.9	0.06	0.14	5.9
		87.61	1201.7	0.06	0.07	5.9
		114.76	1212.4	0.06	0.06	5.9
		162.66	1229.3	0.06	0.09	5.9
70.47	59.97	164.90	1187.0	0.06	0.05	2.4
		145.58	1178.6	0.06	0.05	2.4
		125.33	1168.8	0.06	0.13	2.4
		97.89	1153.9	0.06	0.12	2.4
		103.68	1157.2	0.06	0.11	2.4
		115.00	1163.4	0.06	0.18	2.4
		134.86	1173.5	0.06	0.14	2.4
		152.43	1181.6	0.06	0.07	2.4
		173.68	1190.8	0.06	0.04	2.4
70.47	79.91	199.36	1117.2	0.06	0.07	2.5
		180.92	1107.8	0.06	0.04	2.5
		161.74	1097.3	0.06	0.13	2.5
		140.29	1084.0	0.06	0.08	2.5
		120.79	1069.9	0.06	0.05	2.5
		129.32	1076.3	0.06	0.04	2.5
		148.13	1089.1	0.06	0.05	2.5
		167.22	1100.5	0.06	0.05	2.5
		183.50	1109.3	0.06	0.08	2.5

Table 55. Experimental densities of the CO_2+$SiCl_4$ mixture taken with the vibrating tube densimeter (VTD)

CO_2 Molar Fraction [%]	**Temperature [°C]**	**Pressure [bar]**	**Density [kg/m^3]**	**$U(T)$ [°C]**	**$U(P)$ [bar]**	**$U(\rho)$ [kg/m^3]**
80.20	40.09	157.58	1058.6	0.06	0.05	5.9
		141.64	1048.7	0.06	0.06	5.9
		125.61	1037.9	0.06	0.05	5.9
		100.24	1018.1	0.06	0.16	5.9
		85.06	1003.8	0.06	0.14	5.9
		111.88	1027.3	0.06	0.05	5.9
		134.88	1044.1	0.06	0.04	5.9
		195.18	1079.3	0.06	0.07	5.9
80.20	59.87	189.19	1016.2	0.06	0.05	2.4
		170.74	1002.0	0.06	0.07	2.4
		149.94	983.3	0.06	0.04	2.4
		129.49	961.5	0.06	0.04	2.4
		110.41	936.3	0.06	0.05	2.4
		95.06	910.0	0.06	0.08	2.4
		119.77	949.4	0.06	0.04	2.4
		160.33	993.0	0.06	0.04	2.4
		200.87	1024.4	0.06	0.06	2.4
80.20	79.90	235.43	954.6	0.06	0.05	2.5
		214.33	937.5	0.06	0.05	2.5
		190.65	914.9	0.06	0.05	2.5
		170.98	892.4	0.06	0.05	2.5
		150.70	863.9	0.06	0.04	2.5
		129.91	824.8	0.06	0.04	2.5
		141.79	848.7	0.06	0.04	2.5
		159.84	877.6	0.06	0.05	2.5
90.67	40.28	154.77	934.5	0.06	0.05	5.9
		139.47	920.2	0.06	0.04	5.9

		119.73	898.1	0.06	0.05	5.9
		95.60	862.4	0.06	0.04	5.9
		104.79	877.7	0.06	0.04	5.9
		129.09	909.3	0.06	0.05	5.9
		145.06	925.7	0.06	0.04	5.9
90.67	59.98	162.36	847.3	0.06	0.05	2.4
		144.97	818.7	0.06	0.05	2.4
		131.23	789.6	0.06	0.04	2.4
		115.58	742.9	0.06	0.04	2.4
		122.98	767.6	0.06	0.04	2.4
		137.73	804.4	0.06	0.05	2.4
		154.22	834.8	0.06	0.05	2.4
		169.38	857.1	0.06	0.04	2.4
		180.66	871.4	0.06	0.05	2.4
90.67	79.90	213.13	792.1	0.06	0.04	2.5
		199.03	772.1	0.06	0.08	2.5
		170.59	719.3	0.06	0.05	2.5
		150.55	665.6	0.06	0.04	2.5
		140.01	626.8	0.06	0.05	2.5
		120.52	523.8	0.06	0.04	2.5
		129.50	577.6	0.06	0.04	2.5
		159.12	690.9	0.06	0.04	2.5
		179.58	737.9	0.06	0.04	2.5
72.73	40.29	148.34	1123.6	0.06	0.05	5.9
		129.24	1113.4	0.06	0.11	5.9
		110.01	1102.2	0.06	0.11	5.9
		85.52	1086.1	0.06	0.12	5.9
		97.73	1094.2	0.06	0.12	5.9
		119.20	1107.6	0.06	0.05	5.9
		138.20	1118.2	0.06	0.04	5.9
		170.58	1134.5	0.06	0.05	5.9
72.73	59.95	199.09	1098.1	0.06	0.05	2.4
		180.58	1087.3	0.06	0.06	2.4
		160.48	1074.3	0.06	0.07	2.4
		140.00	1059.4	0.06	0.05	2.4
		111.67	1035.3	0.06	0.14	2.4
		123.98	1046.1	0.06	0.04	2.4
		149.76	1066.6	0.06	0.05	2.4
		170.26	1080.6	0.06	0.05	2.4
72.73	79.90	165.80	979.1	0.06	0.08	2.5
		145.04	957.8	0.06	0.05	2.5
		125.64	933.4	0.06	0.04	2.5
		135.25	946.1	0.06	0.05	2.5
		154.95	968.4	0.06	0.06	2.5
		180.34	993.8	0.06	0.05	2.5
		114.82	919.1	0.06	0.05	2.5

Appendix A.3.3: Experimental data from the campaign at LEAP

The data in Table 56 refer to the experimental campaign carried out within this thesis at LEAP laboratory on the CO_2+C_6F_6 mixture. A conventional VLE cell was adopted, analyzing the composition of the two phases with a gas chromatograph. As mentioned, details about the experimental campaign are not reported but they can be found in literature [57].

Table 56. Experimental VLE data of the CO_2+C_6F_6 mixture

Temperature [°C]	**Pressure [bar]**	x_{CO2}	y_{CO2}
89.93	9.97	0.0698	0.8901
89.93	15.38	0.1219	0.9320
89.93	20.05	0.1654	0.9426
89.93	25.62	0.2101	0.9529
89.93	30.19	0.2542	0.9578
89.93	35.26	0.3023	0.9619
89.93	40.23	0.3612	0.9637
89.93	45.16	0.3848	0.9653
89.93	50.05	0.4341	0.9699
89.93	55.20	0.4547	0.9682
89.93	60.06	0.4938	0.9681
89.93	65.63	0.5290	0.9687
89.93	70.79	0.5596	0.9691
89.93	75.74	0.5962	0.9672
89.93	80.81	0.6219	0.9662
89.93	86.01	0.6612	0.9652
89.93	90.13	0.6913	0.9656
89.93	95.20	0.7220	0.9574
89.93	100.05	0.7467	0.9526
89.93	105.06	0.7745	0.9520
89.93	110.14	0.8116	0.9374
89.93	114.03	0.8442	0.9199
70.10	10.44	0.1027	0.9286
70.10	15.00	0.1538	0.9467
70.10	20.03	0.2045	0.9572
70.10	25.30	0.2538	0.9656
70.10	30.69	0.3063	0.9681
70.10	35.09	0.3571	0.9700
70.10	40.24	0.4033	0.9728
70.10	45.20	0.4538	0.9742
70.10	50.22	0.4945	0.9747
70.10	55.25	0.5334	0.9771
70.10	60.22	0.5756	0.9763
70.10	66.01	0.6207	0.9757
70.10	69.90	0.6534	0.9758
70.10	75.00	0.6876	0.9764
70.10	80.08	0.7229	0.9746
70.10	86.44	0.7687	0.9672
70.10	90.06	0.7862	0.9633
70.10	94.53	0.8161	0.9585
70.10	99.47	0.8523	0.9564
70.10	104.67	0.8890	0.9431
50.00	10.31	0.1441	0.9662
50.00	20.15	0.2635	0.9812
50.00	30.09	-	0.9863
50.00	40.08	-	0.9883
50.00	50.14	-	0.9892
50.00	60.06	-	0.9906
50.00	69.96	0.7930	0.9895
50.00	80.02	0.8722	0.9873
50.00	85.03	0.9070	0.9853

Appendix B: Analysis of the heat exchangers

Appendix B.1: Bell and Delaware model for S&T

In this appendix the Bell and Delaware method used to model the S&T HX is briefly presented. As mentioned, the method allows to compute the shell-side HTC of the S&T HX as function of the characteristic of the flow field and the geometrical assumption on both the shell and the tubes. Therefore, in the design model of the S&T HX, the Bell and Delaware method is exploited both to fix the geometrical characteristics of the overall HX and to compute, consequently, the shell-side HTC (that influence the geometry, according to the methodology reported in Figure 33). In the off-design model of the HX the method is only run to compute the HTC on the shell-side.

The shell-side convective HTC is computed as in Equation (48):

$$HTC_{shell} = \left(j_{col} \cdot C_{P,shell} \cdot Pr_{shell}^{\frac{2}{3}} \cdot \frac{\dot{m}_{shell}}{A_{shell}} \cdot \left(\frac{\mu_{shell}}{\mu_{shell,wall}} \right)^{0.14} \right) \cdot J_c \cdot J_l \cdot J_b \cdot J_s \quad (48)$$

Where A_{shell} is the bundle cross-flow area at the centre of the shell, j_{col} is the Colburn factor for and ideal tube bank, and the correction factors J_i account for a set of non-idealities described below. The quantities with the "shell" subscript refer to the fluid on the shell side (in this case the HTF), computed with polynomial functions from literature depending only on local temperatures [25].

The Colburn factor is expressed as evidenced in literature [106] [104] as function of the Reynolds number on the shell-side and the pitch ratio between the centre of two adjacent tubes, shown in Figure 72.

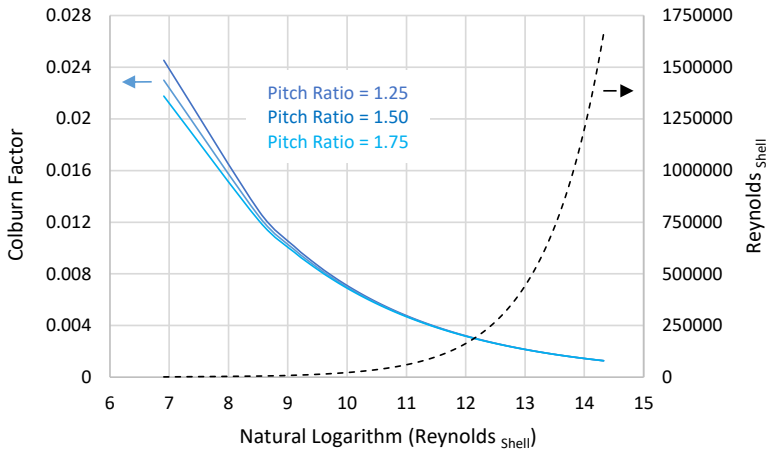

Figure 72. Colburn factor for an ideal tube bank of 45° staggered tubes, as considered in this work in Figure 32

The various correction factors J_i are computed according to literature [104], in particular: i) the segmental baffle window correction factor J_c depends on the shell diameter and the baffle cut spacing, as reported in Figure 32 (for large baffle cuts can be below 0.6, and it is 1 for HX with no tubes in the window [107]), ii) the correction factor J_l accounts for the streams leaking between the tubes and the baffles and between the shell and the baffles, which depends mainly on the tube number and the various clearances, iii) the bundle bypass correction factor J_b is influenced by the outermost tubes and the shell and pass dividers (sealing strips can decrease the value of J_b), while iv) the correction factor J_s is related to the variable baffle spacing at the inlet and outlet of the S&T (set at 1 in this work, as the baffle spacing is constant for each finite volume).

The expression for J_c, J_l and J_b are considered as proposed in the model of Guccione [104], while assuming the set of clearances proposed by in the thesis of Waleaven [108].

Appendix B.2: Validation of the PHE model with Thermoflex

The results of this appendix refer to the comparison between the MATLAB tool adopted within this work for the design of S&T HX, detailed in Figure 33, and the results of Thermoflex v.29 [112] (exploiting the Bell and Delaware model itself for the calculation of the external convective coefficient): a comparison which is reported mainly for validation purposes.

The comparison has been carried out varying the baffle number in the MATLAB model, minimizing the deviation in overall heat transfer area between the two models. The calculations have done with the pure CO_2 as working fluid for sake of simplicity while adopting Thermoflex: nevertheless, the validity of the MATLAB model can be extended to any working fluid. The comparison proposes both the cases with S&T adopted as PHE in CSP applications with solar salts as HTF (Case 1 and 2) and for a case of S&T used as gas cooler (HRU) of the power cycle, with water as cooling medium (Case 3), described in Table 57. The comparison offers optimal deviations (in the range around 2%) between the main geometrical results of two models for cases of PHEs, as shown in Table 58. Moreover, a good comparison is still possible for the case study where the S&T is used as gas cooler. The highest deviations are computed for the frictional pressure drop on the tube side, as Thermoflex adopts a different correlation than the one of this work for the frictional friction factor.

Table 57. Inputs for the comparison of this work and Thermoflex S&T models

Parameter	Case 1	Case 2	Case 3
S&T in the sCO_2 cycle	PHE	PHE	HRU
HTF (shell) / Working fluid (tube)	Solar Salts / CO_2	Solar Salts / CO_2	Water / CO_2
CO_2 pressure [bar]	254	254	100
Temperature range HTF [°C]	575-400	575-400	80-20
Temperature range working fluid [°C]	550-380	500-350	100-50
Mass flow rate working fluid / HTF [kg/s]	1000 / 795.6	100 / 70.24	100 / 47.82
Tube material	Inconel 617	Inconel 617	Carbon Steel
Tube outer diameter / Thickness [mm]	20 / 3	18 / 3	20 / 3
Shell diameter-to-Baffle spacing ratio	0.5	0.5	0.5
Tube-to-Pitch ratio / Tube arrangement angle	1.6 / 45 °	1.6 / 45 °	1.6 / 45 °
Thermal Power [MW_{th}]	212.6	18.8	12.0

Table 58. Results of the comparison between this work MATLAB model and Thermoflex model for the design of S&T

Parameter	Case 1 (MATLAB)	Case 1 (THERMOFLEX)	Deviation [%]
Tube external HX area [m^2]	11 501	11 370	1.2
Tube number	5 495	5 430	1.2
Tube length [m]	33.31	33.33	0.1
Shell diameter [m]	2.70	2.78	3.0
Baffle number	23	24	4.2
Tube side pressure drop [bar]	1.49	1.25	16.1
Average tube side HTF [$W/m^2/K$]	2 676	2 946	9.2
Overall HTC [$W/m^2/K$]	834	825	1.1

Parameter	Case 2 (MATLAB)	Case 2 (THERMOFLEX)	Deviation [%]
Tube external HX area [m^2]	368	372	1.1
Tube number	676	691	2.2
Tube length [m]	9.64	9.51	1.4
Shell diameter [m]	0.88	0.89	1.1
Baffle number	21	22	4.5
Tube side pressure drop [bar]	0.48	0.68	29.4
Average tube side HTF [$W/m^2/K$]	2 962	3 162	6.3
Overall HTC [$W/m^2/K$]	828	815	1.6

Parameter	Case 3 (MATLAB)	Case 3 (THERMOFLEX)	Deviation [%]
Tube external HX area [m^2]	791	856	7.6
Tube number	1 551	1 480	4.8
Tube length [m]	8.11	9.21	11.9
Shell diameter [m]	1.47	1.43	2.8
Baffle number	10	12	16.7
Tube side pressure drop [bar]	0.01	0.06	83.3
Average tube side HTF [$W/m^2/K$]	1 581	1 415	11.7
Overall HTC [$W/m^2/K$]	602	568	6.0

Appendix B.3: Cost correlation of Inconel S&T PHE from Thermoflex

The resulting cost function of the sCO_2-to-Solar Salts PHEs computed by Thermoflex are graphically reported in Figure 73: higher tube side pressure drops entail higher velocities, lower heat transfer area and therefore lower capital costs, assuming the UA size parameter to be constant. The figure also shows the same cost function for large scale PHE according to Carlson [111]: as the Carlson correlation is not dependent on the PHE pressure drop it overestimates (assuming this working fluid, storage fluid and Inconel 617 as tube material), the capital cost of the heat exchanger with respect to the results from Thermoflex v29, especially at higher tube side pressure drops.

The cost correlation adopted in Equation (26), generated interpolating Thermoflex results, is expressed in Equation (49) and Equation (50) for two sizes of heat exchangers.

Figure 73 directly reports Thermoflex results, but in this work the cost function adopted are overestimated by a factor $f_{inst+eng}$ (equal to 2), to move from the capital cost of the materials to the overall cost, including the engineering and installation costs. No correction terms have been included in cases the fluid on the shell side is advanced molten salts, different than solar salts, de facto adopting the cost correlation presented also in conditions where the cycle maximum temperature is above 550 °C, since the selected material (Inconel 617) is compatible with these temperatures.

$C_{PHE,CO2}(\ f\ (\mathrm{UA}, \Delta P_{Tube}, Material)\ )\ [M\$] =$		
$= f_{inst+eng}\ \cdot UA \left[\frac{MW}{K}\right] \cdot 2.116 \cdot \Delta P_{Tube}\ [bar]^{-0.2705}$	$for\ \dot{Q}_{PHE} > 100\ MW_{th}$	(49)
$= f_{inst+eng}\ \cdot UA \left[\frac{MW}{K}\right] \cdot 2.262 \cdot \Delta P_{Tube}\ [bar]^{-0.2176}$	$for\ \dot{Q}_{PHE} > 10\ MW_{th}$	(50)

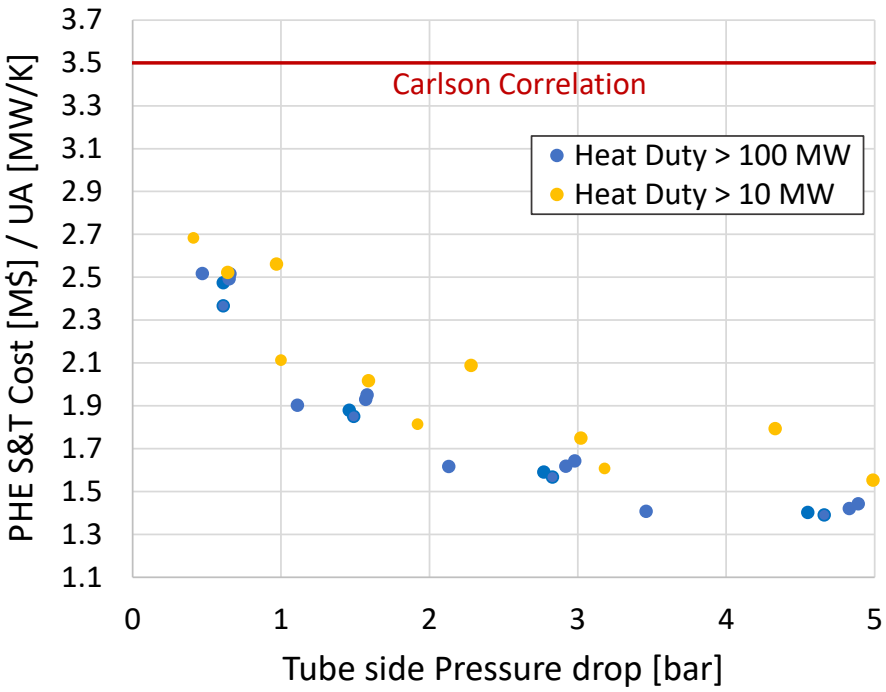

Figure 73. Thermoflex v29 cost of the S&T for the sCO_2-to-solar salts PHE assuming Inconel 617 as tube material, excluding installation and engineering cost

Appendix C: Results of solar plants for the case study in Las Vegas

The results of this Appendix refer to the case study proposed in Chapter 6, detailing the four different CSP plants located in Las Vegas.

Appendix C.1: Solar fields and receiver characteristics

The solar fields modelled in Solarpilot are proposed in Figure 74 through their aerial view. Moreover, each heliostat is described by its optical efficiency at design condition. In the figure, the field (a) refers to the direct 550 °C plant, field (b) refers to indirect 550 °C plant, field (c) represent the indirect 625 °C plant, while field (d) is the field of the indirect 700 °C solar plant. The denomination of each plant refers to the ones reported in Table 37.

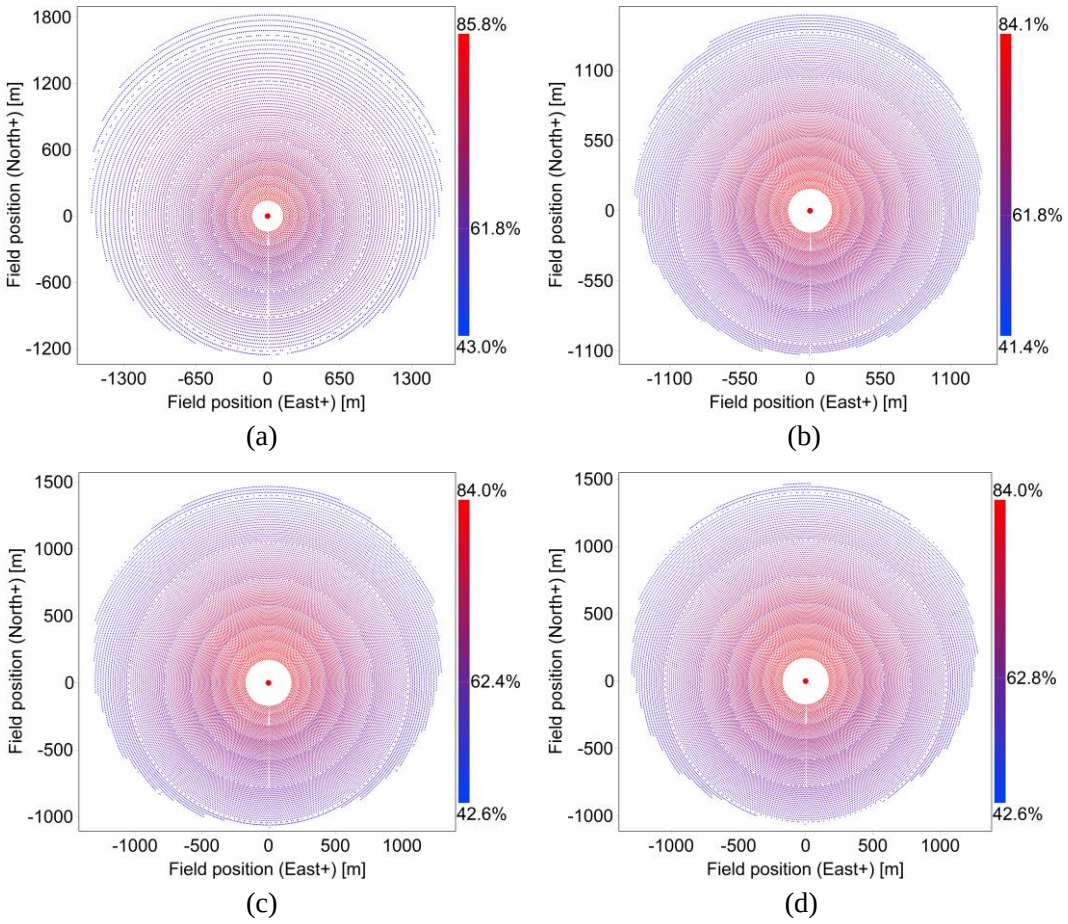

Figure 74. Solar plants designed for the case study in Las Vegas

The optical efficiency maps of the four solar plants are reported in Figure 75: they are adopted in the annual analysis to compute the thermal power hitting the receiver, as indicated in Figure 42. Finally, the maps of the concentrated solar flux hitting the receiver at design condition, used as input for the thermal model of the receiver, are shown in Figure 76.

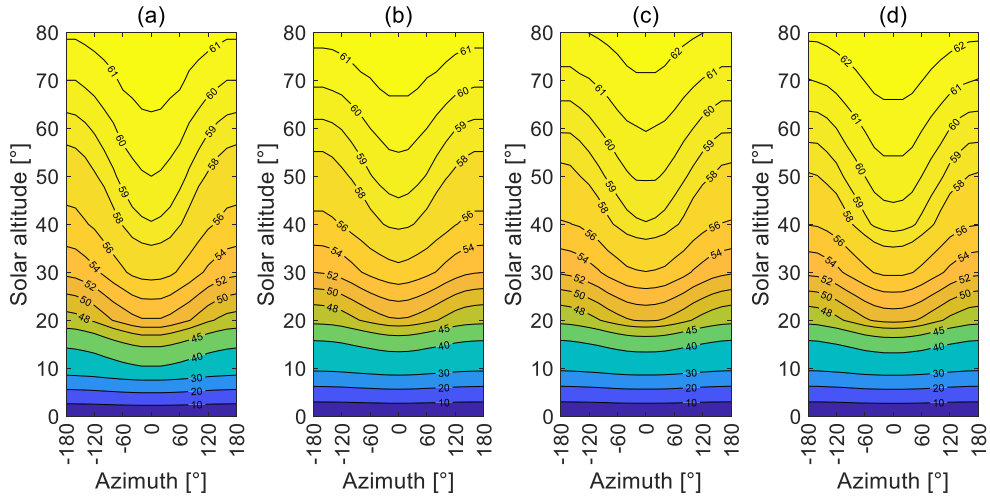

Figure 75. Maps of the optical efficiencies of the CSP plants considered for the CSP plants considered in the case study in Las Vegas

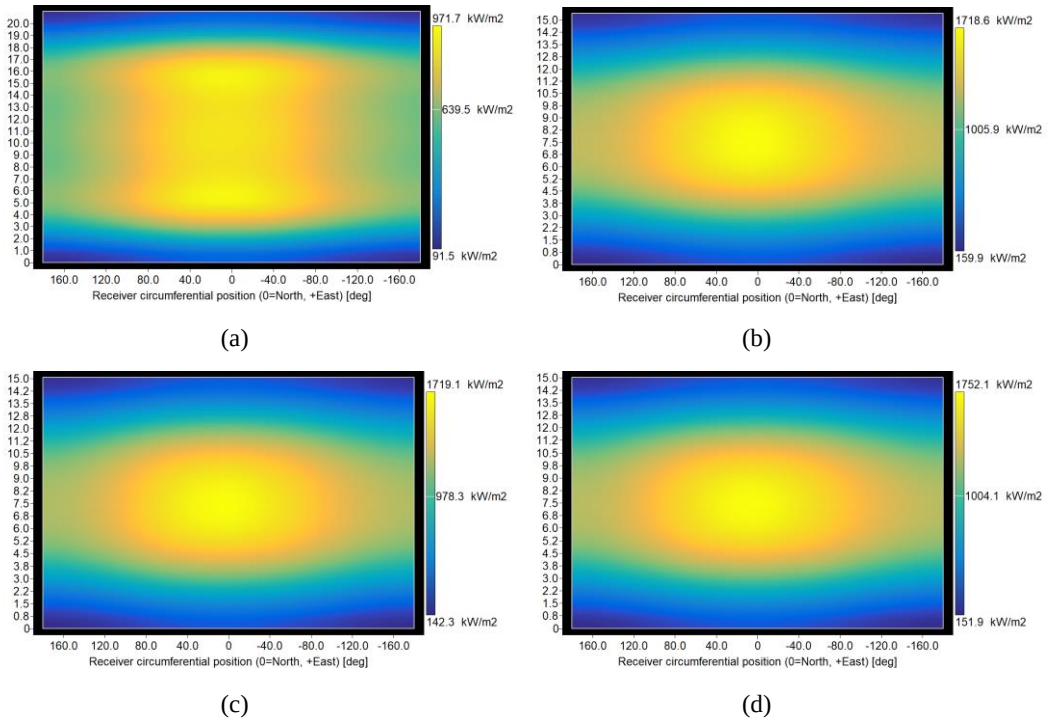

Figure 76. Power flux incident on the receiver at design conditions for the CSP plants considered in the case study in Las Vegas

Appendix C.2: Yearly results and economic analysis

The results shown in this appendix refer to the economic analysis of the solar plants for the case study of the large scale CSP plant in Las Vegas, discussed in Chapter 6.6.

Table 59. Capital cost analysis and LCOE of the various configurations of power cycles reported in Table 40 adopted to the direct 550 °C solar field

Power Cycle 550 °C Direct Storage		Cycle Specific [$/kW$_{el}$]	Heliostats [M$]	Tower [M$]	Receiver and HTF subsystems [M$]	TES [M$]	Cycle [M$]	TOTAL [M$]	LCOE [$/MWh$_{el}$]
sCO$_2$	Simple	860	174.5	23.7	82.8	71	70	506	106.4
	Recompressed	1086	174.5	23.7	82.8	87	98	560	106.3
	Precompressed	1074	174.5	23.7	82.8	82	93	547	107.9
	Cascade	1002	174.5	23.7	82.8	48	78	488	105.7
CO$_2$ + C$_6$F$_6$	Simple	879	174.5	23.7	82.8	80	79	528	101.7
	Recompressed	-	-	-	-	-	-	-	-
	Precompressed	1017	174.5	23.7	82.8	78	93	542	101.8
	Cascade	1072	174.5	23.7	82.8	48	92	505	99.8
CO$_2$ + C$_4$F$_8$	Simple	839	174.5	23.7	82.8	82	75	525	102.0
	Recompressed	1112	174.5	23.7	82.8	92	105	573	104.7
	Precompressed	992	174.5	23.7	82.8	80	91	542	102.2
	Cascade	1035	174.5	23.7	82.8	49	88	501	99.9
CO$_2$ + C$_2$H$_3$N	Simple	757	174.5	23.7	82.8	64	68	496	95.7
	Recompressed	-	-	-	-	-	-	-	-
	Precompressed	864	174.5	23.7	82.8	63	79	508	96.0
	Cascade	835	174.5	23.7	82.8	48	72	481	95.6

Table 60. Capital cost analysis and LCOE of the various configurations of power cycles reported in Table 41 adopted to the indirect 550 °C solar field

Power Cycle 550 °C Indirect Storage		Cycle Specific [$/kW$_{el}$]	Heliostats [M$]	Tower [M$]	Receiver and HTF subsystems [M$]	TES [M$]	Cycle [M$]	TOTAL [M$]	LCOE [$/MWh$_{el}$]
sCO$_2$	Simple	861	167.6	37.4	69.1	70	69	504	105.3
	Recompressed	1088	167.6	37.4	69.1	86	97	557	105.2
	Precompressed	1076	167.6	37.4	69.1	81	92	545	106.8
	Cascade	1003	167.6	37.4	69.1	48	77	487	105.3
CO$_2$ + C$_6$F$_6$	Simple	881	167.6	37.4	69.1	80	78	526	100.7
	Recompressed	-	-	-	-	-	-	-	-
	Precompressed	1020	167.6	37.4	69.1	77	92	540	100.9
	Cascade	988	167.6	37.4	69.1	48	91	503	99.6
CO$_2$ + C$_4$F$_8$	Simple	841	167.6	37.4	69.1	81	74	522	101.0
	Recompressed	1115	167.6	37.4	69.1	91	104	570	103.7
	Precompressed	994	167.6	37.4	69.1	79	90	539	101.2
	Cascade	1036	167.6	37.4	69.1	48	87	499	99.7
CO$_2$ +	Simple	758	167.6	37.4	69.1	64	67	494	95.0
	Recompressed	-	-	-	-	-	-	-	-

C_2H_3N	Precompressed	866	167.6	37.4	69.1	63	78	505	95.5
	Cascade	836	167.6	37.4	69.1	48	71	479	95.5

Table 61. Capital cost analysis and LCOE of the various configurations of power cycles reported in Table 42 adopted to the indirect 625 °C solar field

Power Cycle 625 °C Indirect Storage		**Cycle Specific [$/kW$_{el}$]**	**Heliostats [M$]**	**Tower [M$]**	**Receiver and HTF subsystems [M$]**	**TES [M$]**	**Cycle [M$]**	**TOTAL [M$]**	**LCOE [$/MWh$_{el}$]**
sCO_2	Simple	821	157.6	37.4	66.7	66	66	485	102.2
	Recompressed	1030	157.6	37.4	66.7	77	91	529	101.0
	Precompressed	986	157.6	37.4	66.7	71	84	513	101.7
	Cascade	1006	157.6	37.4	66.7	54	77	483	105.3
CO_2 + C_6F_6	Simple	847	157.6	37.4	66.7	73	74	504	98.4
	Recompressed	-	-			-	-	-	-
	Precompressed	988	157.6	37.4	66.7	71	89	518	98.0
	Cascade	1030	157.6	37.4	66.7	62	87	506	100.4

Table 62. Capital cost analysis and LCOE of the various configurations of power cycles reported in Table 43 adopted to the indirect 700 °C solar field

Power Cycle 700 °C Indirect Storage		**Cycle Specific [$/kW$_{el}$]**	**Heliostats [M$]**	**Tower [M$]**	**Receiver and HTF subsystems [M$]**	**TES [M$]**	**Cycle [M$]**	**TOTAL [M$]**	**LCOE [$/MWh$_{el}$]**
sCO_2	Simple	924	153.6	37.4	66.3	67	80	505	99.3
	Recompressed	1114	153.6	37.4	66.3	79	105	550	99.4
	Precompressed	931	153.6	37.4	66.3	66	85	510	96
	Cascade	941	153.6	37.4	66.3	51	79	484	98.2

Appendix D: Off-design of the $tCO_2+C_6F_6$ simple cycle

The information reported in this appendix refer to the analysis of the off-design behavior of the simple recuperative transcritical cycle working with the $CO_2+C_6F_6$ mixture, described at design conditions in Table 47 and Figure 55, and covered in Chapter 8.

Appendix D.1: Axial turbine model by CITY University

In this appendix it is proposed the sizing and the off-design map of the turbine provided by the SCARABEUS partners from CITY University in London. The axial turbine described is used in the analysis of the off-design performance of the simple recuperative transcritical cycle working with $CO_2+C_6F_6$. For a more detailed description of this turbine, it is possible to refer to the respective literature work of the SCARABEUS consortium [145].

The turbine design process is initiated using a mean-line in-house design tool (1D) to create the flow path and to set the base for the 3D numerical simulations [153], [154]. The preliminary flow path design aims at achieving the highest aerodynamic performance while complying with a set of mechanical and rotodynamic considerations. In addition, the number of design stages and rotor blades are selected to allow for a higher aerodynamic performance alongside with complying to the mechanical and rotodynamic design criteria. The turbine performance is evaluated in the 1D mean-line methodology using the Aungier loss model correlations where profile, secondary flow, tip clearance and trailing edge losses are included [155]. Given that the machine is designed to operate for a 100 MW_{el} plant, a synchronous generator is selected due to the difficulty of incorporating a gearbox for such turbine scales.

Following the 1D flow path designed, the 3D blades are generated assuming several geometric parameters to fully define the 3D blade shape such as leading-edge thickness, inlet/outlet wedge angles, airfoil curvature control points, and blade base fillet, based on a previous blade shape optimization study [156]. The 3D analysis in CFD is carried out using ANSYS workbench. In the developed design, total pressure and total temperature are used to model the stator inlet conditions whereas the static pressure is defined at the turbine outlet.

As a result of the 1D modeling of the turbine, a flow path with nine stages is designed with a hub diameter of 628 mm as shown in Figure 77. A total-to-total efficiency of 92.1% is achieved for the design conditions of the turbine reported in Chapter 8 and for a turbine rotational speed of 3000 rpm. In this work, the turbine total-to-total efficiency is expected to mimic the trend of the isentropic efficiency, assuming to adopt an ideal diffuser at the outlet of the last stage.

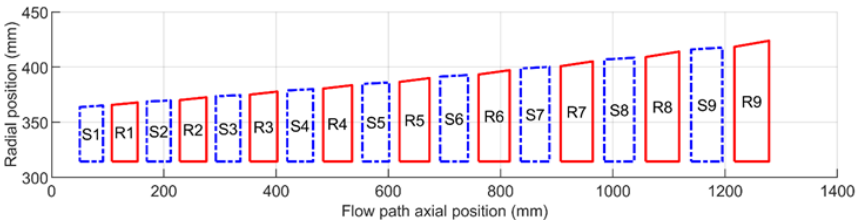

Figure 77. Meridian view of the axial turbine designed by CITY University for the CO_2+C_6F_6 cycle of Chapter 8

The off-design performance of the defined flow path is then evaluated to investigate the turbine performance over a wide range of operating conditions by varying the turbine inlet pressure while maintaining a fixed outlet pressure and turbine maximum temperature, equal to the nominal ones. The performance map of the considered flow path is presented in Figure 78, coherent with the form described in the off-design methodology reported in Figure 53.

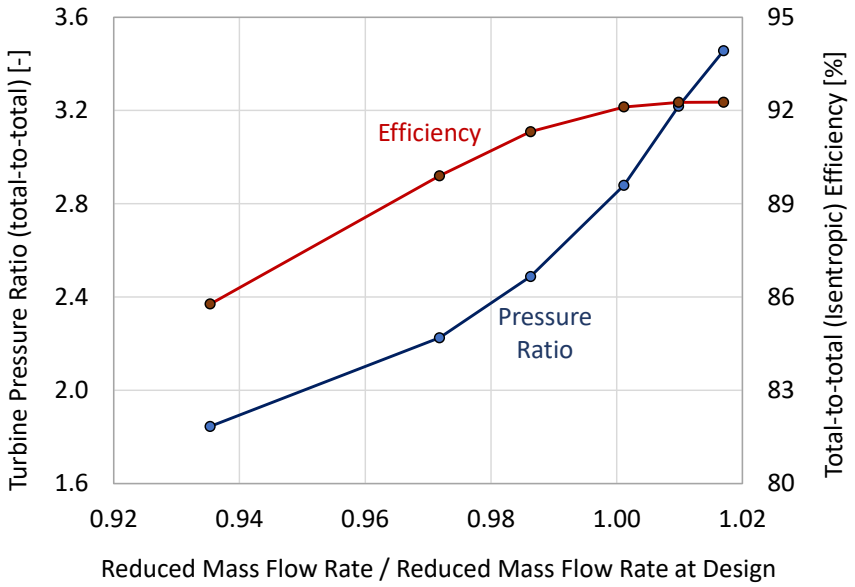

Figure 78. Off-design map of the axial turbine used in this work in Chapter 8

The presented range of reduced mass flow rate corresponds to a working fluid mass flow rate variation from 61 to 100% of the design flow rate. A decrease of the reduced mass flow rate, from 100% to 93.5% of the design value (minimum value of the map), results in a reduction in the operating total-to-total pressure ratio which passes from 2.88 to approximately 1.85. This results in a reduction in the total-to-total turbine efficiency from approximately 92.1% to 85.8%. On the other hand, for reduced mass flow rates higher than the nominal value, it is possible to notice an almost flat trend of the turbine efficiency.

Appendix D.2: Simplified modeling of the PHE off-design

An additional information is retrieved from the simulations presented in Figure 61, which it can help identifying a simplified and quicker solution to the overall off-design simulations of the power cycle. As the PHE off-design is built as a complex and computationally expensive code, its results are more carefully categorized and analyzed: the goal of this analysis is to propose a correlation for the overall HTC of the HX without running the whole MATLAB model across each finite-volume.

This correlation can have the form expressed in Equation (51), neglecting the dependency on the HTF pressure, since it is modelled as an ideal liquid according to literature [25]:

$$U_{PHE} = f(\,PHE_{design}, \dot{m}_{HTF}, Temperature_{HTF}, \dot{m}_{Working\ Fluid}, Pressure_{Working\ Fluid}, Temperature_{Working\ Fluid}) \quad (51)$$

Analyzing the case-specific S&T PHE of this work for CSP applications (with a CO_2-based working fluid and solar salts on the HTF side), it is possible to conclude that the HTF temperature range is approximately always constant in off-design conditions, and the temperature range of the working fluid shows only limited variations. Under these assumptions, the overall HTC is proposed in adimensional terms according to Equation (52):

$$U_{PHE\ Off-Design}/U_{PHE\ Design} = f(\dot{m}_{HTF}, \dot{m}_{Working\ Fluid}, Pressure_{Working\ Fluid}) \quad (52)$$

The simulations carried out in this work (plotted in Figure 61) are organized to build a single correlation, proposed as a polynomial function of the product between the HTF mass flow rate and the working fluid mass flow rate ($\dot{m}_{HTF} \cdot \dot{m}_{Working\ Fluid}$), neglecting the dependency on the pressure of the working fluid. The resulting correlation to model Equation (52) is proposed in Figure 79, built upon four additional sets of simulations (denominated Case A, B, C and D): they are run as stand-alone off-design simulations of the PHE, with no connection to any other part of the power cycle, simulating more generalized conditions.

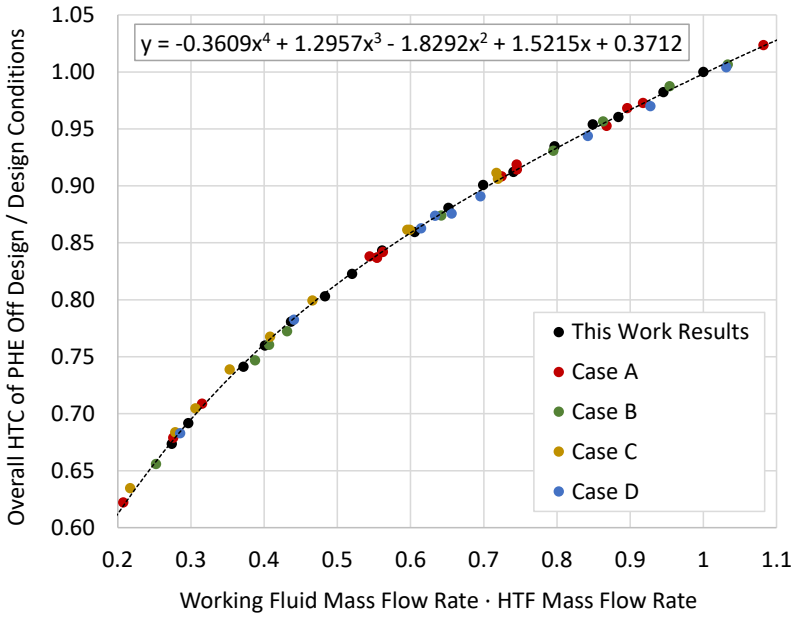

Figure 79. Resulting overall HTC of the PHE computed by the MATLAB model, for various operating conditions and design of PHE reported in Table 63

The other four sets of simulations of Figure 79 are characterized by various design of the PHE and different HTF outlet temperature (described in Table 63), to widen the validity of the correlation. Case B is proposed for a different design of the PHE, in a condition with 4 bar of tube-side pressure drop and a heat exchange area lower than the one of the PHE in this work. On the other hand, Case C and D evaluates the PHE performance at different HTF outlet temperature, to understand the influence of this variable. For the four sets of simulations of Table 63, which do not correspond to solutions of the overall off-design model of the cycle, the working fluid conditions are varied randomly in a range coherent with the simulations carried out in this work in Figure 61. In particular: the mass flow rate on the tube side is varied randomly between 35% and 105% of the design value, the temperature at the outlet of the PHE randomly varied between 560 °C and 530 °C, the pressure of the working fluid is also varied randomly between 140 bar and 250 bar and the temperature at PHE inlet is varied randomly between 370 °C and 415 °C.

Table 63. Characteristics of the four additional sets of simulations for the off-design of the PHE proposed in Figure 79

	PHE Design	**HTF Outlet Temperature**
Case A	This Work Design	This Work Value
Case B	Pressure Drop x 2, Area x 0.88 w/r/t This Work	This Work Value
Case C	This Work Design	This Work Value + 15 °C
Case D	This Work Design	This Work Value – 15 °C

The correlation proposed in this work to compute the off-design value of the HTC of a S&T PHE for CSP applications has the form of Equation (53), fitted on the simulations of Figure 79 with an R^2 of 0.9993. In order to adopt this correlation in other conditions it is important to assume molten salts as HTF, a CO_2-based working fluid and to adopt Inconel 617 (or a similar alloy) as tube material, suitable to CSP applications at high temperature.

$$\frac{U_{PHE\ Off-Design}}{U_{PHE\ Design}} = -0.3609 \cdot \left(\dot{m}_{HTF} \cdot \dot{m}_{Working\ Fluid}\right)^4 + 1.2957 \cdot \left(\dot{m}_{HTF} \cdot \dot{m}_{Working\ Fluid}\right)^3 - 1.8292 \cdot \left(\dot{m}_{HTF} \cdot \dot{m}_{Working\ Fluid}\right)^2 + 1.5215 \cdot \left(\dot{m}_{HTF} \cdot \dot{m}_{Working\ Fluid}\right) + 0.3712 \quad (53)$$

Appendix D.3: Cycle conditions at constant condenser fan speed

The results in Figure 80 describe the performance in off-design of the transcritical simple recuperative power cycle working with the CO_2+C_6F_6 mixture investigated in this work in Figure 55 for state-of-the-art CSP plants.

In the figures the dependency of each variable on both the thermal input and the ambient temperature is clearly underlined, proposing only solutions where the speed of the air condenser fans is fixed at design value and the cycle is regulated in sliding pressure as described in Figure 51.

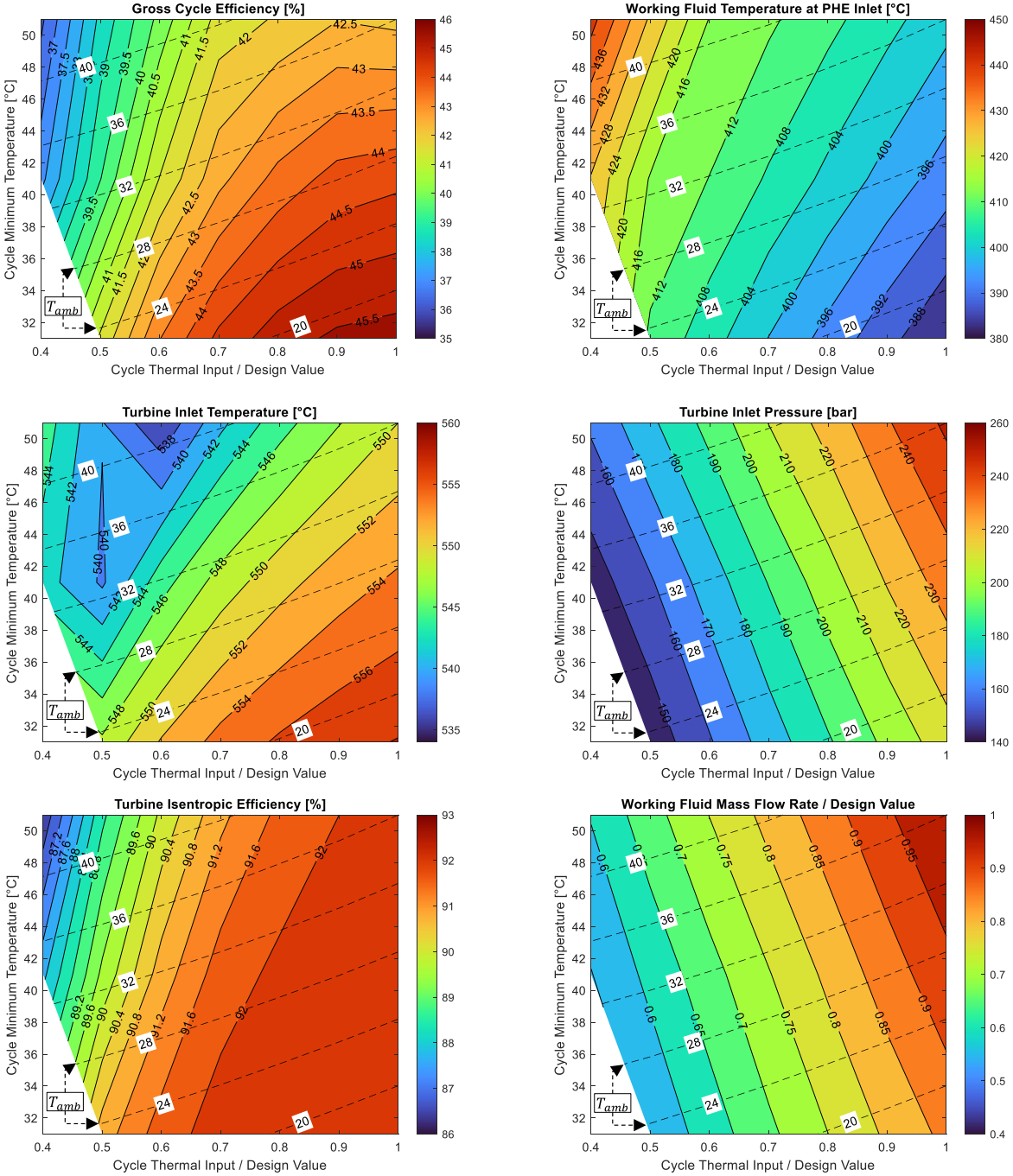

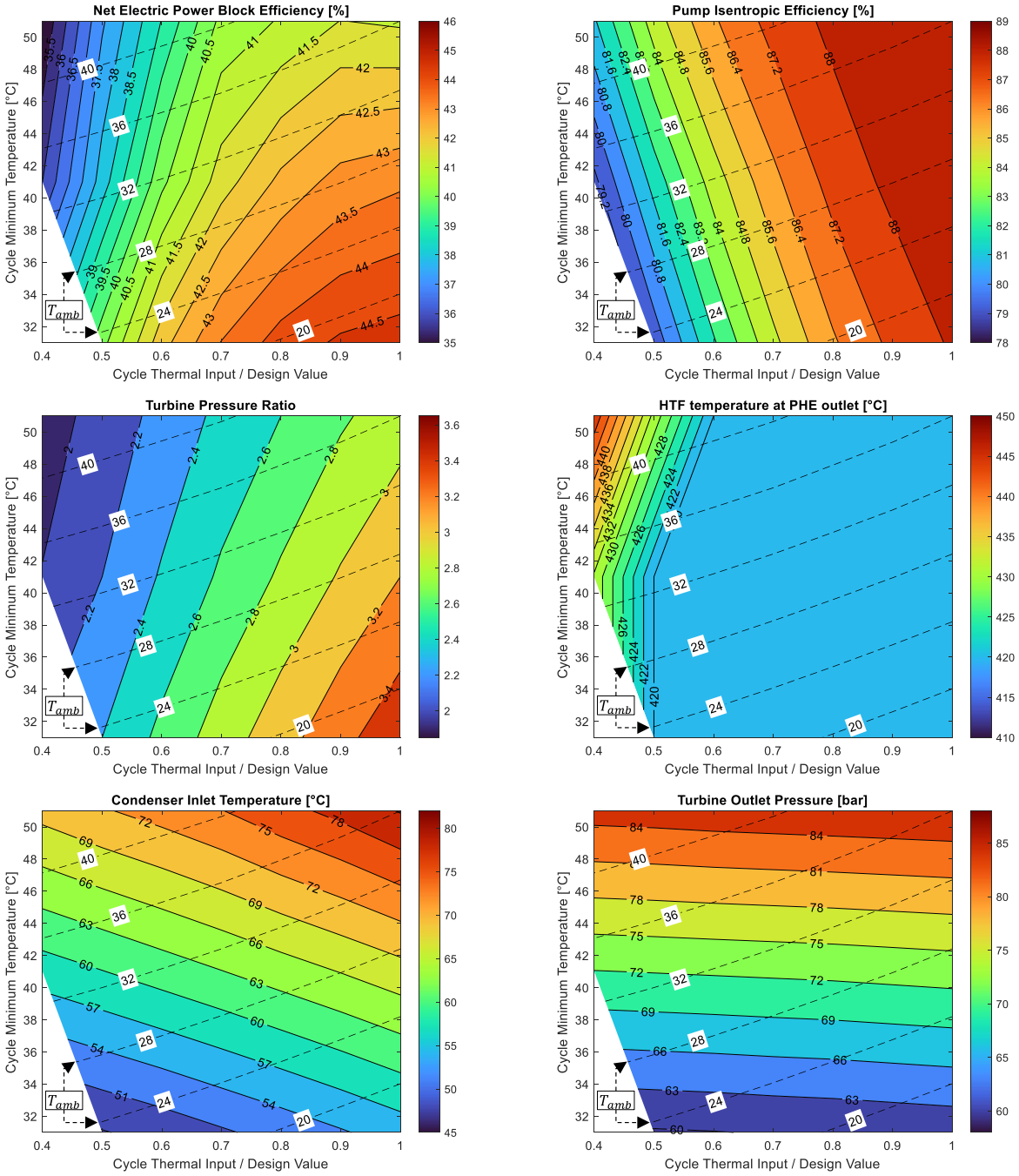

Figure 80. Off-design characteristics of the cycle investigated in Figure 55 operating in sliding pressure, at design speed of the air-cooled condenser fans